



THE UNIVERSITY
of ADELAIDE

Flame Structure and Stability for Improved Fuel Flexibility in Practical Combustion Devices

DOUGLAS B. PROUD

School of Mechanical Engineering
The University of Adelaide
South Australia 5005
Australia

*Thesis submitted in fulfillment of the
requirements for the degree of Ph. D. in
Engineering on Monday 24th October, 2022.*

Ph. D. Thesis

Monday 24th October, 2022

School of Mechanical Engineering
The University of Adelaide
South Australia 5005
Australia

Copyright © 2022 Douglas B. Proud, and The University of Adelaide, Australia.

All right reserved. No part of this report may be used or reproduced in any form or by any means, or stored in a database or retrieval system without prior written permission of the copyright holders except in the case of brief quotations embodied in critical articles and reviews.

Abstract

If it is to be achieved successfully, the rapid transition towards a low-carbon future requires the development of flexible, efficient and low-emissions combustion systems. A comprehensive understanding of fundamental combustion processes—such as flame structure and stability—is necessary to optimise the operation of such systems. While these phenomena have been investigated in detail in the past, the studies have typically been focussed on relatively “conventional” flames in open environments. There has also been significant attention towards the combustion of fuels under hot and low-oxygen conditions, such as those which would occur with intense recirculation or re-use of exhaust gases. An important concept in this regard is mild combustion, a particular combustion regime which can lead to numerous benefits such as improved fuel-flexibility and emissions reductions. While mild combustion has been studied previously, the range of conditions and fuel types investigated has remained relatively narrow, limiting the uptake of the technology in certain practical applications, such as gas turbines.

To address the knowledge gaps relating to fuel-flexible combustion under conditions of practical interest, a series of experimental investigations have been performed to encompass different burner configurations, fuel types, operating pressures and boundary conditions. The first set of these experiments—upon which the first two papers of this thesis-by-publication are based—relates to a novel combustion apparatus which enables the study of jet flames issuing into a hot and low-oxygen coflow at elevated pressures. Using this configuration, the independent effects of jet Reynolds number, coflow oxygen concentration and operating pressure on the structure, stability and sooting behaviour of the flames are investigated. The flames are studied in terms of their chemiluminescence behaviour, providing a useful comparison against the results of a series of computational fluid dynamics (CFD) simulations. The validity of this CFD model in predicting the trends with increasing pressure is investigated, while the chemiluminescence mechanism is further studied via laminar flame simulations.

The combustion of liquid sprays under hot and low-oxygen conditions was also studied experimentally as part of this research. A combination of laser diagnostic techniques were implemented to simultaneously image the location of key reaction zone species, fuel droplets and soot, for dilute spray flames of differing fuel compositions. A range of different boundary conditions were again investigated for these spray flames, enabling the

change in stabilisation behaviour and the effect that this has on the structure of the reaction zones to be studied. The combined imaging of droplets and reaction zone structures offers unique insights regarding the complex and highly coupled interactions between chemistry, droplet evaporation and flow phenomena which influence these flames. These experiments also led to the publication of two journal papers, in which a thorough analysis of the key features of the flames and the sensitivity to changes in jet and coflow boundary conditions is performed.

As an extension to the experiments based on a “jet-in-hot-coflow” configuration, a series of flames using fuel blends of predominately hydrogen were also studied experimentally. The focus of this phase of the research is on improving the visibility and radiative heat transfer characteristics of hydrogen flames, which is motivated by the potential substitution of natural gas with hydrogen for the decarbonisation of a range of processes. The results of this testing indicate a significant increase in thermal radiation and flame luminosity with the addition of toluene (a highly sooting fuel) in concentrations of up to 1% by mole. Furthermore, the spectral imaging of these flames showed a strong emission band at 589 nm, confirming the importance of sodium from the surrounding environment on the visual appearance of hydrogen flames.

The fundamental reaction zone structures and stabilisation features relating to the combustion of fuels under practically relevant conditions are examined in this thesis. Particular emphasis has been placed on the experimental imaging of flames under a wide range of independently controllable boundary conditions, to isolate the effects of pressure, oxidant composition, fuel flowrate and fuel type. In addition to providing important insights in their own right, these results will enable numerical modelling capabilities to be further developed, which will in-turn facilitate the optimisation of fuel-flexible and low-emissions combustion devices.

Contents

Abstract	i
Contents	iii
Acknowledgements	v
Declaration	vi
1 Introduction	1
1.1 Motivation and current challenges for the energy transition	1
1.2 Thesis outline and details of publications	3
1.3 References	5
2 Literature Review	9
2.1 Turbulence-chemistry interactions in combustion	9
2.2 Combustion under hot and low-oxygen conditions	10
2.3 Pressurised combustion	15
2.4 Combustion of liquid sprays	20
2.5 Hydrogen as a fuel in practical combustion systems	24
2.6 Research gaps	27
2.7 References	28
3 Aims and Objectives	41
4 Characteristics of Turbulent Flames in a Confined and Pressurised Jet-in-hot-coflow Combustor	44
5 The Effects of Pressure and Oxygen Concentration on the Structure and Stability of Turbulent Flames	61
6 Experimental Investigation of the Flame Structure of Dilute Sprays Issuing into a Hot and Low-oxygen Coflow	104
7 Dilute Spray Flames of Ethanol and <i>n</i>-heptane in the Transition to Mild Combustion	129

8	Effect of Dopants on Hydrogen Flames for Improved Safety and Performance	149
9	Discussion	186
9.1	Decoupling of boundary conditions for the study of flame stabilisation	186
9.2	Imaging of flame structure and sooting behaviour under variable operating conditions	188
9.3	Flame spectrometry and chemiluminescence	189
9.4	References	191
10	Summary	192
10.1	Conclusions	192
10.2	Future work	194
	Appendix A Work Related to this Thesis	197

Acknowledgements

This thesis would not have been possible without the guidance, assistance, and general support of a range of individuals and groups. I am forever grateful to A/Prof. Paul Medwell and Dr. Michael Evans, both of whom have invested their time and energy to a far greater extent than they were obligated. I have benefited immensely from Paul's tutelage and the level of care he has shown for my development as a researcher, whether it be ensuring that I understand the correct use of an en-dash and an em-dash—or the differences between NPT and BSP threads (and why both are inferior to Swagelok). I am extremely fortunate to have had a principal supervisor who is not only an expert in the field of combustion, but is also willing to join his students in the lab and offer his knowledge in that regard. In a similar fashion, the technical knowledge and skills that I have gained through working alongside Michael cannot be overstated. I am particularly appreciative of his commitment to passing on his expertise, be it in relation to the operation of pulsed lasers and the alignment of optics, or patiently explaining the theory behind the eddy dissipation concept. I am also very lucky to have had the support of Dr. Shaun Chan, whose outside perspectives have been of particular importance in the drafting and refining of journal manuscripts.

There are many people from The University of Adelaide, both staff and students, to whom I am indebted. I wish to extend my thanks to the numerous workshop staff who have facilitated the construction, installation and operation of the various experimental burners; particularly the efforts of Jason Peake, Phil Schmidt, Marc Simpson and Darren Faulkner. Additionally, the advice and wisdom of Prof. Bassam Dally and Drs. Neil Smith, Kae Ken Foo and Alfonso Chinnici is gratefully acknowledged. I have also enjoyed working collaboratively with a range of fellow HDR students during my time, including Jordan Kildare, Adam Gee, Ian Shaw and Yilong Yin, as well as the various honours groups who made the operation of the CP-JHC possible.

I never would have made it to this point without the love and support from my family and friends. Thank you especially to Tony—for always fostering my inquisitive attitude and putting up with my countless questions as a child, and Jenny—for always making sure I had a book to read and strengthening my love of language. Thanks also to Max, Madeleine (×2), Chris, Zac and Leroy, and the countless others who have given me a (sometimes) much-needed distraction and helped to keep me sane throughout the last few years.

Declaration

I certify that this work contains no material which has been accepted for the award of any other degree or diploma in my name, in any university or other tertiary institution and, to the best of my knowledge and belief, contains no material previously published or written by another person, except where due reference has been made in the text. In addition, I certify that no part of this work will, in the future, be used in a submission in my name, for any other degree or diploma in any university or other tertiary institution without the prior approval of the University of Adelaide and where applicable, any partner institution responsible for the joint award of this degree.

The author acknowledges that copyright of published works contained within the thesis resides with the copyright holder(s) of those works.

I give permission for the digital version of my thesis to be made available on the web, via the University's digital research repository, the Library Search and also through web search engines, unless permission has been granted by the University to restrict access for a period of time.

I acknowledge the support I have received for my research through the provision of an Australian Government Research Training Program Scholarship.

Douglas B. Proud

Chapter 1

Introduction

1.1 Motivation and current challenges for the energy transition

It is no secret that there is mounting pressure around the world to transition away from the combustion of fossil fuels and towards low-carbon, sustainable sources of energy. In terms of electricity generation, there has been an enormous increase in the contribution from renewable energy sources in recent years, particularly from wind and solar energy [1], facilitating the phase-out of many coal-fired power plants globally. Despite this, combustion still remains the dominant source of energy, accounting for more than 90% of the world's primary energy supply in 2019 [2]. Although there is significant potential for further increases in the capacity of renewables for electricity generation, the decarbonisation of other sectors such as transport and manufacturing is much more challenging, since alternatives to combustion are not always feasible [3, 4]. The long- and short-term fluctuations in output from wind and solar also presents additional challenges. Addressing this inherent variability requires either a highly developed storage infrastructure within the electricity grid, or alternatively (or in conjunction with), generation sources that are often referred to as “dispatchable power” which can respond to these fluctuations. Consequently, gas turbine combustors are predicted to play an increasingly important role during the transition to renewables [5]. This includes both land-based (or stationary) gas turbines used for electricity generation, and those used for propulsion in aerospace applications.

It is well documented that combustion—in particular the combustion of fossil fuels—can lead to significant environmental consequences, most notably in terms of CO₂ emissions and the associated greenhouse effect [6]. It is therefore important that new combustion systems facilitate the use of alternative, low- or zero-carbon fuels, such as biodiesel or hydrogen (H₂), while maintaining high efficiencies. In addition to CO₂, other harmful emissions which can be formed during combustion include nitrogen oxides (NO_x), carbon monoxide (CO) and soot [7, 8]. In many practical devices, such as gas turbines and reciprocating engines, limiting these emissions to comply with regulations is often accompanied by a reduction in operating efficiency,

and it can also lead to a reduction in stability or increased sensitivity to fuel composition [9, 10]. Moderate or intense low-oxygen dilution combustion, or “mild” combustion, is a promising solution in this regard.

Mild combustion refers to a particular mode of combustion which can provide a range of benefits over conventional combustion. Mild combustion occurs when fuel is burnt in sufficiently hot and low-oxygen conditions, such that the fuel undergoes autoignition and there is a modest increase in temperature [11]. The required conditions are typically achieved using hot exhaust gases to dilute the oxidant stream and raise the temperature, either through exhaust gas recirculation (EGR) or sequential combustion. In this context, sequential combustion refers to a configuration in which the exhaust gases from an initial or upstream combustion zone pass through to a secondary or downstream combustor, providing the necessary conditions for mild combustion. Not only does the use of exhaust gas heat allow an increase in thermodynamic efficiency, mild combustion also offers considerable reductions in CO, NO_x and soot emissions [12], and can improve fuel flexibility [13]. The technology has been successfully implemented in industrial furnaces, with the resultant uniform temperature distribution leading to increased performance [14].

Mild combustion can also be implemented in gas turbines, for both electricity generation and transport applications. This can be achieved via the EGR technique, although such designs tend to involve a trade-off between achieving good mixing (and hence low emissions) and avoiding excessive pressure losses (which reduces efficiency) [5]. Gas turbines which employ the concept of sequential combustion are an alternative option for the application of mild combustion. In a sequential gas turbine (SGT), a primary (typically lean-premixed) combustion chamber generates the hot and low-oxygen exhaust gases which pass through to a secondary combustion zone, into which the secondary fuel stream is injected [15]. Depending on the specific design architecture, the SGT may incorporate a high- and low-pressure turbine, with the secondary combustion zone located between the two turbines, or the two combustors may operate at approximately the same pressure to drive a single turbine stage [15–18]. In terms of land-based/stationary gas turbines, the former configuration has been implemented in the Ansaldo GT24/26 family of gas turbines (originally developed by ABB/Alstom) [15, 19], while the latter is used in the more recent GT36 design [20, 21]. A similar concept has been implemented in the context of aerospace propulsion systems, where it is referred to as an inter-turbine burner or ITB [22, 23].

Although commercial gas turbines which incorporate hot and low-oxygen combustion have been developed, further exploration is necessary to facilitate

design improvements and optimisation, particularly in terms of obtaining the benefits of the mild combustion regime [5]. Specifically, there is a lack of understanding regarding mild combustion under the elevated-pressure conditions which are encountered in gas turbines [24]. Additionally, the fundamental combustion processes relating to spray-injected liquid fuels and hydrogen-based fuels are other areas which require a higher level of understanding for practical implementation [5, 25]. It should be noted that hydrogen-compatible gas turbines are currently in development [26, 27], and the ability to retrofit existing natural gas systems to run on both blended and pure hydrogen has been demonstrated [28–30]. In saying this, there remains significant potential for the optimisation of hydrogen-fired gas turbines in terms of efficiency and emissions reductions [31].

The possibility of using hydrogen and hydrogen-based fuels for practical combustion processes is a topic which has received significant attention in recent years. This has largely been stimulated by the growing interest from governments and industries in developing a so-called “hydrogen economy” [32], in which hydrogen becomes a key energy carrier to enable the decarbonisation of a range of sectors, while also acting as a storage medium and providing a method of exporting renewable energy. In terms of combustion, the substitution of natural gas with hydrogen is a particularly attractive option which can enable rapid reductions in carbon emissions in a range of areas [33, 34]. Potential applications include power generation via implementation in gas turbines (as mentioned previously) and combined heat and power (CHP) plants, industrial burners such as those used in high-temperature manufacturing processes, and in domestic appliances such as cookers, boilers, water heaters and space heaters.

1.2 Thesis outline and details of publications

This thesis takes the form of a thesis-by-publication. Specifically, the body of the thesis is composed of three papers that have been published in peer-reviewed scientific journals and one which is currently under review, as well as a technical report based on research aligned with the Future Fuels Cooperative Research Centre (FF-CRC); these are each presented as separate chapters in the thesis. Prior to presenting these chapters, a comprehensive review of the relevant literature is provided, with a focus on the research efforts in relation to the development of low-emissions and fuel-flexible practical combustion systems. Five key research gaps are identified from this analysis, which leads directly into the aims and objectives of the research, which are in-turn addressed within the five publications. This is followed

by a summary chapter which presents the key outcomes of this work in a cohesive manner and provides additional discussion. The submission and publication details of the papers and the associated chapters are as follows:

Paper 1 (Chapter 4)

D. B. Proud, M. J. Evans, Q. N. Chan & P. R. Medwell (2022). "Characteristics of turbulent flames in a confined and pressurised jet-in-hot-coflow combustor." *Journal of the Energy Institute*, vol. 105, pp.103–113.

Paper 2 (Chapter 5)

D. B. Proud, M. J. Evans, J. A. Kildare, Q. N. Chan & P. R. Medwell. "The effects of pressure and oxygen concentration on the structure and stability of turbulent flames." Submitted Oct. 2022 to: *Fuel*.

Paper 3 (Chapter 6)

D. B. Proud, M. J. Evans, P. R. Medwell & Q. N. Chan (2021). "Experimental investigation of the flame structure of dilute sprays issuing into a hot and low-oxygen coflow." *Combustion and Flame*, vol. 230, Article 111439.

Paper 4 (Chapter 7)

D. B. Proud, M. J. Evans, Q. N. Chan & P. R. Medwell (2022), "Dilute spray flames of ethanol and *n*-heptane in the transition to mild combustion." *Combustion and Flame* vol. 238, Article 111918.

Paper 5 (Chapter 8)

D. B. Proud, P. R. Medwell, N. Smith, M. J. Evans (2022), "Effect of Dopants on Hydrogen Flames for Improved Safety and Performance." Report published by Future Fuels Cooperative Research Centre (Project RP1.10-04).

1.3 References

- [1] International Energy Agency (2021). *Renewables 2021 - Analysis and Forecast to 2026*. Technical Report. <https://www.iea.org/reports/renewables-2021> [Accessed: 24/10/2022].
- [2] International Energy Agency (2021). *Key World Energy Statistics 2021*. Technical Report. <https://www.iea.org/reports/key-world-energy-statistics-2021> [Accessed: 24/10/2022].
- [3] Napp, T. A., A. Gambhir, T. P. Hills, N. Florin, and P. S. Fennell (2014). "A Review of the Technologies, Economics and Policy Instruments for Decarbonising Energy-Intensive Manufacturing Industries". *Renewable and Sustainable Energy Reviews* 30, pp. 616–640.
- [4] Fridell, E. (2019). "Emissions and Fuel Use in the Shipping Sector". *Green Ports*. Elsevier, pp. 19–33.
- [5] Perpignan, A. A. V., A. G. Rao, and D. J. E. M. Roekaerts (2018). "Flameless Combustion and Its Potential towards Gas Turbines". *Progress in Energy and Combustion Science* 69, pp. 28–62.
- [6] Quadrelli, R. and S. Peterson (2007). "The Energy–Climate Challenge: Recent Trends in CO₂ Emissions from Fuel Combustion". *Energy Policy* 35 (11), pp. 5938–5952.
- [7] Bowman, C. T. (1992). "Control of Combustion-Generated Nitrogen Oxide Emissions: Technology Driven by Regulation". *Symposium (International) on Combustion*. Twenty-Fourth Symposium on Combustion 24 (1), pp. 859–878.
- [8] Myung, C. L. and S. Park (2011). "Exhaust Nanoparticle Emissions from Internal Combustion Engines: A Review". *International Journal of Automotive Technology* 13 (1), p. 9.
- [9] Dowling, A. P. and S. Hubbard (2000). "Instability in Lean Premixed Combustors". *Proceedings of the Institution of Mechanical Engineers, Part A: Journal of Power and Energy* 214 (4), pp. 317–332.
- [10] Lammel, O., H. Schütz, G. Schmitz, R. Lücknerath, M. Stöhr, B. Noll, M. Aigner, M. Hase, and W. Krebs (2010). "FLOX[®] Combustion at High Power Density and High Flame Temperatures". *Journal of Engineering for Gas Turbines and Power* 132 (12).
- [11] Cavaliere, A. and M. de Joannon (2004). "Mild Combustion". *Progress in Energy and Combustion Science* 30 (4), pp. 329–366.

-
- [12] Joannon, M. de, G. Langella, F. Beretta, A. Cavaliere, and C. Noviello (2000). "Mild Combustion: Process Features and Technological Constraints". *Combustion Science and Technology* 153 (1), pp. 33–50.
- [13] Galletti, C., A. Parente, M. Derudi, R. Rota, and L. Tognotti (2009). "Numerical and Experimental Analysis of NO Emissions from a Lab-Scale Burner Fed with Hydrogen-Enriched Fuels and Operating in MILD Combustion". *International Journal of Hydrogen Energy* 34 (19), pp. 8339–8351.
- [14] Colorado, A. F., B. A. Herrera, and A. A. Amell (2010). "Performance of a Flameless Combustion Furnace Using Biogas and Natural Gas". *Bioresource Technology* 101 (7), pp. 2443–2449.
- [15] Joos, F., P. Brunner, B. Schulte-Werning, K. Syed, and A. Eroglu (1996). "Development of the Sequential Combustion System for the ABB GT24/GT26 Gas Turbine Family". *Volume 4: Heat Transfer; Electric Power; Industrial and Cogeneration*. Birmingham, UK: American Society of Mechanical Engineers, V004T10A022. ISBN: 978-0-7918-7875-0.
- [16] Rao, A. G., F. Yin, and J. P. van Buijtenen (2014). "A Hybrid Engine Concept for Multi-Fuel Blended Wing Body". *Aircraft Engineering and Aerospace Technology: An International Journal* 86 (6). Ed. by R. Singh, pp. 483–493.
- [17] Levy, Y., V. Erenburg, V. Sherbaum, and I. Gaissinski (2016). "Flameless Oxidation Combustor Development for a Sequential Combustion Hybrid Turbofan Engine". *ASME Turbo Expo 2016: Turbomachinery Technical Conference and Exposition*. American Society of Mechanical Engineers Digital Collection.
- [18] Ballal, D. and J. Zelina (2004). "Progress in Aeroengine Technology (1939–2003)". *Journal of Aircraft* 41 (1), pp. 43–50.
- [19] Güthe, F., J. Hellat, and P. Flohr (2008). "The Reheat Concept: The Proven Pathway to Ultralow Emissions and High Efficiency and Flexibility". *Journal of Engineering for Gas Turbines and Power* 131 (2).
- [20] Pennell, D. A., M. R. Bothien, A. Ciani, V. Granet, G. Singla, S. Thorpe, A. Wickstroem, K. Oumejjoud, and M. Yaquinto (2017). "An Introduction to the Ansaldo GT36 Constant Pressure Sequential Combustor". *ASME Turbo Expo 2017: Turbomachinery Technical Conference and Exposition*. American Society of Mechanical Engineers Digital Collection.

-
- [21] Bothien, M. R., A. Ciani, J. P. Wood, and G. Fruechtel (2019). "Toward Decarbonized Power Generation With Gas Turbines by Using Sequential Combustion for Burning Hydrogen". *Journal of Engineering for Gas Turbines and Power* 141 (12).
- [22] Zelina, J., G. Sturgess, and D. Shouse (2004). "The Behavior of an Ultra-Compact Combustor (UCC) Based on Centrifugally-Enhanced Turbulent Burning Rates". *40th AIAA/ASME/SAE/ASEE Joint Propulsion Conference and Exhibit*. Joint Propulsion Conferences. American Institute of Aeronautics and Astronautics.
- [23] Mawid, M., H. Thornburg, B. Sekar, and J. Zelina (2005). "Numerical Analysis of Inter-Turbine Burner (ITB) Concepts For Improved Gas Turbine Engine Performance". *43rd AIAA Aerospace Sciences Meeting and Exhibit*. American Institute of Aeronautics and Astronautics.
- [24] Kruse, S., B. Kerschgens, L. Berger, E. Varea, and H. Pitsch (2015). "Experimental and Numerical Study of MILD Combustion for Gas Turbine Applications". *Applied Energy* 148, pp. 456–465.
- [25] Ye, J., P. R. Medwell, E. Varea, S. Kruse, B. B. Dally, and H. G. Pitsch (2015). "An Experimental Study on MILD Combustion of Prevaporised Liquid Fuels". *Applied Energy* 151, pp. 93–101.
- [26] *Turbines Driven Purely by Hydrogen in the Pipeline* (n.d.). <https://www.nature.com/articles/d42473-020-00545-7>. [Accessed: 24/10/2022].
- [27] *Hydrogen-Fueled Gas Turbines | GE Gas Power* (n.d.). <https://www.ge.com/gas-power/future-of-energy/hydrogen-fueled-gas-turbines>. [Accessed: 24/10/2022].
- [28] Burke, J. (2022). *Gas Turbine Power Plant Getting Hydrogen Retrofit*. <https://www.diesलगasturbine.com/news/gas-turbine-power-plant-getting-hydrogen-retrofit/8020456.article>. [Accessed: 24/10/2022].
- [29] Carusotto, S., P. Goel, M. Baratta, D. A. Misul, S. Salvadori, F. Cardile, L. Forno, M. Toppino, and M. Valsania (2022). "Combustion Characterization in a Diffusive Gas Turbine Burner for Hydrogen-Compliant Applications". *Energies* 15 (11), p. 4117.
- [30] Cappelletti, A. and F. Martelli (2017). "Investigation of a Pure Hydrogen Fueled Gas Turbine Burner". *International Journal of Hydrogen Energy* 42 (15), pp. 10513–10523.

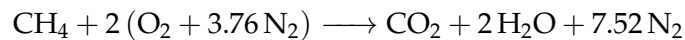
- [31] Beita, J., M. Talibi, S. Sadasivuni, and R. Balachandran (2021). “Thermoacoustic Instability Considerations for High Hydrogen Combustion in Lean Premixed Gas Turbine Combustors: A Review”. *Hydrogen* 2 (1), pp. 33–57.
- [32] Crabtree, G. W., M. S. Dresselhaus, and M. V. Buchanan (2004). “The Hydrogen Economy”. *Physics Today* 57 (12), pp. 39–44.
- [33] Melaina, M. W., O. Antonia, and M. Penev (2013). “Blending Hydrogen into Natural Gas Pipeline Networks: A Review of Key Issues”.
- [34] Haeseldonckx, D. and W. D’haeseleer (2007). “The Use of the Natural-Gas Pipeline Infrastructure for Hydrogen Transport in a Changing Market Structure”. *International Journal of Hydrogen Energy* 32 (10), pp. 1381–1386.

Chapter 2

Literature Review

2.1 Turbulence-chemistry interactions in combustion

Although the study of combustion phenomena pre-dates recorded human history, and despite its widespread application, there remain many areas in the field of combustion science which are not well-understood. This is largely a result of the inherent complexity associated with combustion—particularly turbulent combustion. Not only is the study of turbulence notoriously complex in its own right, but the coupling of turbulent flow phenomena with the chemical reactions which occur within a flame further complicates this behaviour. To illustrate this, consider the chemistry involved in the combustion of methane (CH_4), a relatively simple fuel. The combustion of methane in air is often expressed in its simplest form, via the global reaction:



However, the actual process of forming the major products of CO_2 and H_2O from the reactants is much more complex in terms of chemistry, involving a number of elementary reactions and intermediate species. A commonly used and well-validated chemical mechanism to describe this process—namely, GRI-Mech 3.0 [1]—consists of more than 300 individual elementary reactions (many of which are reversible), with an additional 48 intermediate chemical species [2]. While it is not always necessary to understand this behaviour in detail, certain situations—specifically those in which there is strong coupling between the intermediate species and the underlying flow-field—are heavily influenced by these “finite-rate chemistry” effects [3]. The rate at which the various reactions take place at different regions in a flame is dependent on the localised conditions—such as temperature and species’ concentrations—which are influenced by the turbulent transport properties, both at large scales via eddy transport, and at very fine scales. The heat released from these reactions subsequently affects the fluid properties, such as viscosity, which leads to changes in turbulence [4]. This coupled behaviour between the turbulent flow properties and the finite-rate chemistry is referred to as the turbulence-chemistry interaction, or TCI [5]

The understanding of TCI phenomena is particularly important from a computational modelling perspective. Typically, computational fluid dynamics (CFD) models of combustion prioritise the accurate and detailed description of either the flow behaviour or the chemical kinetics, with one at the expense of the other, to enable simulations to be performed with reasonable computational resources [6]. This leads to TCI models such as the conserved scalar equilibrium model, which assumes that the individual chemical reactions occur at a much faster rate than the transport phenomena (referred to as the “infinitely fast chemistry” assumption) [7], such that the chemistry can be simplified and the flow described in greater detail. At the other end of the spectrum are TCI models such as the well-stirred reactor model, which facilitates calculation of the intermediate species concentrations and individual reaction rates under the assumption of a simplified flow-field [8]. A useful parameter for characterising different combustion scenarios is the Damköhler number (Da), a dimensionless number defined as the ratio of the characteristic flow and chemical timescales [7]. For cases where reactions occur relatively quickly (in comparison to the rate of turbulent mixing), Da is large, and approaches such as the laminar flamelet model [9] are valid, while combustion systems with low Da —due to either slower chemistry or increased levels of turbulence—require additional computational resources to be assigned to describe the coupling between the finite-rate chemistry and the flow-field [3, 10].

2.2 Combustion under hot and low-oxygen conditions

2.2.1 Mild combustion and related concepts

As mentioned in §1.1, the re-use of exhaust gases via either EGR or sequential combustion can lead to a range of benefits, including increased thermal efficiency and reductions in emissions. The dilution of the reactants with exhaust gases leads to an increased temperature of the reactants and a lower oxygen (O_2) concentration, which significantly alters the combustion process in comparison to “conventional” combustion. In particular, the reduced O_2 concentration causes the reactions to proceed at a slower rate, while the increased temperature of the reactants can—in some instances—lead to autoignition of the fuel. The characteristic features of combustion under these hot and low- O_2 conditions has been a key focus of research in the field of combustion, with various regimes identified based on the specific behaviour observed.

An important concept related to EGR and sequential combustion is a specific regime referred to as “mild combustion”. In general terms, the mild regime may be characterised by a hot and highly diluted reactant stream, which results in a distributed reaction zone, reduced maximum temperatures, and the lack of a clearly visible or defined flame front [11, 12]. The use of preheated reactants is not unique to mild combustion; the high temperature air combustion (HiTAC) technique has been studied in-depth [13, 14], along with the more general concept of high temperature combustion technology (HiCOT), of which mild can be considered a subset [12]. An important distinction for mild combustion is the low O_2 concentration, with the maximum allowable mole fraction of O_2 in the oxidant stream typically ranging from 0.06–0.1 based on previous studies [15, 16]. This reduced O_2 concentration results in a relatively gradual transition from reactants to products (both spatially and temporally), in contrast to the intense reactions typically associated with combustion. In this sense, the term mild is not only an acronym which stands for “moderate or intense low-oxygen dilution”, but is also descriptive of the combustion process itself. The term “flameless” is often used interchangeably with mild [6], along with “flameless oxidation”, or FLOX[®], with the latter actually referring to a specific, trademarked burner technology rather than a combustion regime [17]. Figure 2.1 illustrates graphically the various modes of combustion, classified in terms of the concentration of O_2 in the reactants, and temperature of the reactants.

In Figure 2.1, the mild combustion regime (referred to in the figure as flameless) is depicted in the upper-left corner, corresponding to a significant preheating of reactants and a depleted level of O_2 . The most practical method of attaining such conditions is via dilution of the reactants with the exhaust products of combustion, which has the added benefit of enabling an increase in thermal efficiency, since the exhaust gas heat would otherwise be wasted in a conventional combustor. Despite the high initial temperature of the reactants, the low O_2 concentration limits the increase in temperature during combustion, such that the maximum temperature is reduced in comparison to conventional combustion. Consequently, NO_x emissions are significantly reduced through mild combustion, since the formation of thermal NO_x (typically the dominant NO_x formation mechanism in a flame [19]) is extremely sensitive to high temperatures [20].

The precise definition of mild combustion and the boundaries of the regime have been the subject of review and debate, further complicated by the existence of the previously mentioned similar and/or overlapping combustion modes. A commonly cited definition of mild combustion is based upon the notion of a minimum “self-ignition” (or autoignition) temperature

2.2 Combustion under hot and low-oxygen conditions

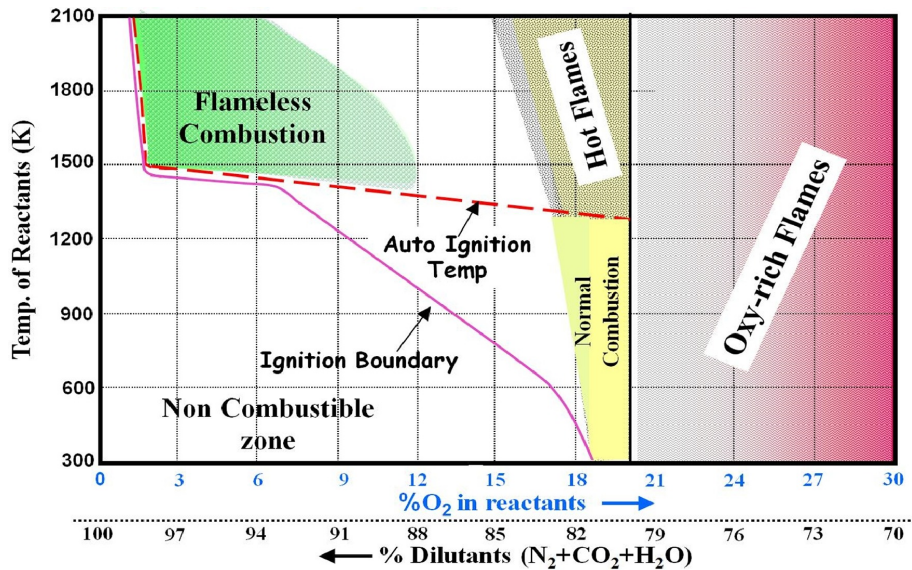


Figure 2.1: High temperature combustion regimes, including mild (described as flameless) combustion. Reproduced from Perpignan et al. [6] (originally produced by Rao & Levy [18]). Creative Commons License (CC BY NC ND): <https://creativecommons.org/licenses/by-nc-nd/4.0/>

of a given fuel-air mixture in a premixed reactor, and requires that the temperature increase within the reactor remain below this temperature [12]. This definition—while convenient—is somewhat arbitrary, and is not readily applied to nonpremixed configurations. A more theoretical approach based on the analysis of the so-called “S-shaped curve” (which relates the temperature of a reactor to Da) leads to an alternative definition of mild combustion, predicated upon the absence of the typical ignition and extinction phenomena associated with conventional combustion [15]. This is consistent with the previously mentioned characteristics of the mild regime; that is, a less clearly defined flame structure and more distributed reaction zones, which are a consequence of the increased chemical timescales. In the context of this project, the precise definition and classification of the mild regime is not a major focus, instead focussing on the flame properties and boundary conditions which are characteristic of mild combustion and similar/overlapping regimes.

2.2.2 Fundamental studies in mild combustion

Burner designs which limit the formation of NO_x , while maintaining high efficiencies, have long been considered a priority in the field of combustion. EGR is a well-known technique in this regard, having been applied in many

practical devices [21, 22]. Under regular conditions with ambient air, EGR combustion tends to become unstable when the recirculation rate—defined as the mass ratio of exhaust gas to fresh fuel and air in the reactant stream—exceeds 30% [23]. It was found, however, that with sufficient preheating of the reactants (that is, above auto-ignition temperature), much higher levels of recirculation can be achieved [24]. Under such conditions, a region of stable combustion, generally lacking a visible or audible flame, was observed [24]. The concept of a stable combustion mode which enables both emissions reductions and efficiency improvements is obviously very attractive, leading to significant interest in the development of a fundamental understanding of mild combustion.

Since the initial conception of mild combustion, a number of experimental and numerical studies have been carried out to investigate the fundamental behaviour of flames in this regime. To study the effect of O₂ concentration on the structure of turbulent, nonpremixed flames in the mild regime, the jet-in-hot-coflow (JHC) burner was developed [25]. This burner essentially emulates the recirculation of exhaust gases typically associated with mild combustion, without the need for this recirculation. The JHC configuration involves a central jet stream of fuel, which issues into the products of a secondary burner located upstream of the jet exit plane. Air and nitrogen (N₂) can also be injected into the coflow, allowing temperature, O₂ concentration and flow rate to be independently controlled, which is not possible for burners which use recirculation [6]. It was found that a reduction in O₂ concentration from 9% to 3% resulted in a decrease in peak temperature of up to 400 K, as well as reductions in CO and NO levels. Additionally, the results indicated a change in the NO formation mechanism at very low (~3%) O₂ concentrations [25].

The transition from the high-temperature, auto-ignitive combustion regime to the mild regime is of importance for the development of adaptive CFD models, as well as for implementation in practical systems. The JHC configuration was used to study this transition for ethylene flames, again with coflow O₂ concentrations of 3% and 9% [26]. Laser diagnostic measurements of the hydroxyl radical (OH) indicated a broader and less intense reaction zone for the 3% O₂ case, which results in a higher level of partial premixing prior to combustion. Another study, using a similar experimental setup, examined the reaction zone structures at the bases of these flames in more detail [27]. Flames with 9% O₂ appeared to be lifted from the jet exit, while in the 3% O₂ case, a faint outline attaching the flame base to the jet was observed. For the visually lifted flames, laser diagnostic data pointed towards the occurrence of a “weak” reaction upstream of the apparent lift-off height, and this height was found to decrease with increasing jet exit velocity, both of which indicate

a fundamentally different behaviour to that of conventional lifted flames [27]. The transient autoignition behaviour of flames based on a similar JHC burner was investigated in further detail, by implementing a pulsed fuel injection technique combined with high-speed chemiluminescence imaging and Rayleigh scattering measurements [28]. This configuration enables the detection of ignition kernels and quantification of the associated temperature and mixture fraction fields, providing insights that are particularly useful for the validation of models [28, 29].

The experimental data collected in the aforementioned studies—and indeed others using similar configurations [30–32]—have facilitated significant progress in the modelling of mild combustion and autoignition processes. In general, mild combustion is notoriously difficult to model, since the low O_2 concentration in the reactant stream and the corresponding reduction in reaction rates leads to a lower value of Da under mild combustion conditions in comparison to conventional combustion [33]. In many cases, Da is of the order of unity, which means that both the turbulent flow-field and the finite-rate chemistry must be captured in detail in order to accurately model the combustion process [33]. As a result, many commonly used TCI models—such as the flamelet model—either fail to describe the mild regime accurately or require significant computational resources, thus limiting their practicality [34]. Additionally, the changes in flame stabilisation with variations in O_2 concentration, Reynolds number, and fuel composition [6] add to the difficulty of developing a robust model. The TCI model known as the eddy dissipation concept (EDC) has been identified as a promising technique in this respect, as it allows both the turbulent transport of individual species and detailed chemical kinetics to be captured with relatively low computational expense [35]. The EDC model operates under the assumption that reactions occur within localised regions represented by the smallest turbulent structures, and these regions are approximated as a perfectly stirred reactor (PSR) [36]. Modification of the standard parameters of this model has been shown to be successful in terms of reproducing experimental results of mild combustion [37–39]. However, these modified models are limited to describing specific flame cases by adjusting the values of the parameter constants, hindering their use for practical simulations [6]. Much of the recent work in this area has therefore focused on the development of more generalised models, using locally-evaluated model constants [10, 40]. While such models have been proven successful in predicting a range of experimental results, this has largely been limited to flames at atmospheric pressures, likely due to a lack of validation data at elevated pressures.

2.3 Pressurised combustion

2.3.1 Fundamental studies at elevated pressure

Many practical combustion devices, such as reciprocating engines and gas turbines, operate at pressures significantly above that of the surrounding atmosphere. Combustion at high pressures is advantageous for such devices because it allows a reduction in the size of the combustion chamber while maintaining the same power output; similarly, it enables the power output to be increased without the need to increase the size of the device [41]. Despite the high combustion pressures associated with many practical devices, there is a comparative lack in understanding of the behaviour of flames at elevated pressures in relation to what is known of flames at atmospheric conditions [42]. This is largely due to the added cost and complexity of pressurised experimental burners, and the challenges associated with optical diagnostics for high-pressure configurations [41]. As a result, many studies of combustion at elevated pressures—particularly those relating to the development of practical combustors—have historically been carried out with the goal of optimising the performance of a specific type of device, by fine-tuning the performance and analysing the output and emissions under varying conditions, without necessarily investigating the underlying physics and chemistry involved [43]. Nevertheless, a number of important observations have been made regarding the fundamental effects of pressure on flame behaviour and emissions.

Much of the research based on flames at elevated pressures has involved the investigation of soot formation, as it has long been recognised as a harmful pollutant as well as being important for radiative heat transfer [44, 45]. For laminar diffusion flames, soot formation was initially studied in terms of a maximum smoke-free flow rate [46], whereby the flow rate of various fuels was gradually increased until smoke was observed, and the process repeated for a range of pressures up to 4 atm. It was observed that, for all fuel types considered, the maximum smoke-free flow rate of fuel is inversely proportional to pressure [46], indicating that elevated pressure leads to an increase in the formation of soot. This increase in soot was attributed to the decrease in diffusion coefficient with pressure, which results in less mixing between fuel and oxidant and therefore less opportunity for soot to be oxidised. This explanation appears to be insufficient, however, since an increase in soot formation at higher pressures has also been observed with a constant mass flow rate (and hence a constant rate of diffusion) [47]. Additionally, experiments with premixed, laminar flames also show

an increase in soot volume fraction with pressure [48, 49], indicating that there is a change in soot formation chemistry with pressure, rather than it being simply a mixing phenomenon. These experiments clearly indicate a change in combustion behaviour at elevated pressures, for both premixed and nonpremixed (diffusion) flames.

A major limitation of the aforementioned findings is that the experiments were performed for the case of laminar flames only. Although such results are certainly important in terms of providing a fundamental understanding and enabling the development of simplified models, they are not directly translatable to practical combustion scenarios, which almost always involve turbulence [50]. Experiments based on turbulent, nonpremixed flames of kerosene—both in prevaporised form [51] and as a liquid [52]—suggest that the soot formation rate in such flames increases approximately linearly with pressure. Interestingly, the study which focussed on prevaporised flames attributed this trend to the increase in the carbon content per unit volume as pressure is increased [51], while the latter study concluded that there is a broadly linear underlying pressure-dependence of soot chemistry [52]. Soot measurements based on methane flames in the same experimental configuration observed an order-of-magnitude increase in soot volume fraction when increasing the pressure from 1–3 bar, indicating that the pressure-dependence of soot formation is very sensitive to the fuel used [53]. More recently, highly turbulent (Reynolds number up to 50,000), nonpremixed flames were studied at pressures of up to 5 bar, with a particular focus on measurements in the near-field sooting region to facilitate model development and validation [54]. These experiments reveal a reduction in the length of the non-sooting region of the flames with increasing pressure, even when the bulk velocity of the fuel at the jet exit was held constant.

Combustion experiments which focus on the analysis of flame structure and reaction zone features are particularly challenging at elevated pressure, since the requirement of a confined and sealed vessel tends to limit optical access for flame diagnostics. In this context, an attractive option for studying elevated-pressure combustion is via the detection of chemiluminescence emitted from the flame—that is, the light which is emitted from excited species (specifically, those excited via a chemical reaction) upon their decay back to the ground state [55]. Chemiluminescence-based sensors have also been identified as a potential tool to be implemented in practical combustion systems, both for detecting the presence of a flame [56], as well as providing an active control signal to sense changes in key combustion parameters, such as equivalence ratio [57–59]. The major contributors to chemiluminescence in a flame are the OH^* , CH^* , C_2^* and CO_2^* species [60], where the asterisk

(*) superscript denotes the excited-state nature of the various species. The OH^* and CH^* species are of particular interest in the investigation of flame structure, as they tend to be correlated with regions of high heat release and radical concentrations [61]. It has previously been observed for laminar, premixed flames that the chemiluminescence intensity of both OH^* and CH^* tends to decrease as a function of pressure, with this intensity also being very sensitive to equivalence ratio [58, 62]. This study again highlights the potential for the determination of equivalence ratio based on the relative signal intensities, using the known pressure-dependence of the OH^* and CH^* signals [58]. With regard to turbulent flames, it has been observed that the presence OH^* and CH^* is particularly sensitive to the local strain rate, with regions of very high strain heavily diminishing the chemiluminescence signal [63, 64]. It is worth noting that there have been very few experimental studies of chemiluminescence involving turbulent, nonpremixed flames [65], and even fewer relating to elevated-pressure conditions.

It should be mentioned that laser-based imaging of turbulent, non-premixed flames at elevated pressures has been performed previously. Planar laser induced fluorescence (PLIF) imaging of the OH radical was performed in the near-field region for a series of sooting flames at pressures of up to 5 bar and Reynolds numbers up to 50,000 [54], allowing the structure and stabilisation features to be investigated at increased levels of turbulence than that which is possible at atmospheric pressure, due to the increased stability of the flames as the pressure is increased. Using the same burner configuration, turbulent, nonpremixed flames with a mixture of H_2 , CO and N_2 in the fuel stream were investigated at pressures up to 12 bar [66]. It was observed in this study that increasing the pressure while maintaining constant Reynolds number leads to a reduced probability of local extinction events, which is believed to be a consequence of the reduced strain rate at the burner exit. Additionally, it was found that Reynolds number is the dominating factor in terms of the degree of corrugation of the flame front, with pressure alone having relatively little impact at sufficiently high levels of turbulence [66]. These studies have provided important and unique insights regarding the near-field structure of well-defined and practically-relevant flames at elevated pressure, which is particularly important for the validation of CFD models.

With the continuous rise in computational processing capabilities, coupled with the difficulty and cost of developing suitable experimental rigs, numerical modelling is a useful tool for the analysis of pressurised combustion. In general, the simulation of practical cases of combustion—such as those relevant to gas turbines and engines—requires the use of a simplifying tur-

bulence model, since the processing power required to resolve the fine-scale flow structures is not feasible for repeated simulations of detailed geometries [42]. Due to the complex interaction between turbulence and chemistry, the use of a turbulence model can often lead to erroneous simulation results [4], so validation of the model against experimental results under a range of boundary conditions is necessary. Significant progress has been made in the development of experimental data sets for this reason, such as the “Turbulent Nonpremixed Flames” and “International Sooting Flames” workshops [67, 68]. However, these flames have largely been limited to atmospheric pressure, since optical access is generally prioritised. The previously mentioned recent laser diagnostics experiments of highly turbulent flames at pressure (e.g., [54, 66]) therefore provide much needed data for model validation in this regard. There still, however, remains a lack of detailed data at pressure, particularly regarding the effect of the surrounding conditions on combustion behaviour, including the hot and low-O₂ conditions encountered in mild combustion [6, 42].

2.3.2 Mild combustion at elevated pressures

A promising application of mild combustion is in gas turbines (which can operate at pressures on the order of 50 bar), both for electricity generation and aircraft propulsion [69]. From a theoretical standpoint, it is expected that pressure would have a noticeable impact on the mild regime, since reactions occur at a faster rate due to the higher concentration of reactants at increased pressure [6]. Additionally, mild combustion is known to suppress soot [70], while increased pressure tends to promote it, so it is difficult to predict the outcome of these competing effects. Despite the importance of pressure and the need to understand its impact, the vast majority of fundamental studies on mild combustion have been limited to atmospheric pressure [6].

Experimental investigations of combustion in general tend to involve a compromise between how closely a certain configuration represents practical conditions—such as high pressures and realistic burner geometries—and the ability to gather detailed experimental data suitable for model validation. A prime example is the JHC burner (see §2.2.2), which facilitates the use of laser diagnostic measurement techniques and is a relatively simple flame for computational modelling, but the results cannot be directly applied to practical burners which have complex geometries and operate at increased pressure [6]. There have, however, also been a number of investigations using confined burners with more complex geometries, which often allow the effect of pressure to be studied.

Measurements made in enclosed burners without optical access typically focus on the final products of combustion, including pollutant emissions, rather than intermediate species and flame structure. In experiments performed with a burner geometry which promotes a strong recirculation of exhaust gases, interesting changes in NO_x and CO emissions were observed for increasing pressure with a constant level of recirculation [71]. The formation of NO_x was found to increase with pressure due to the longer residence times, while the opposite was true for CO, ultimately resulting in a narrowing of the range in which both low NO_x and CO emissions can be achieved. Interestingly, when pressure was increased with velocity held constant (by decreasing the nozzle diameter), both NO_x and CO emissions were found to be reduced, emphasising the importance of mixing processes on mild combustion [71]. Pre-vapourised fuels have also been studied with the same experimental configuration [72], with results indicating that at elevated pressures, the shorter ignition delay times can lead to less mixing prior to combustion, such that a higher jet velocity (or another method of promoting mixing) is required to achieve mild combustion. Although these studies provide important insights regarding the effects of pressure, the lack of data regarding flame structure and ignition processes—as well as the strong coupling between flow rate and O_2 concentration—makes it difficult to draw any generalised conclusions regarding mild combustion at pressure.

Despite the relative lack of understanding regarding the fundamental features of mild combustion at elevated pressure, there are some exploratory designs for gas turbines operating in the mild regime (or similar), that have been manufactured and tested. Many of these designs employ the FLOX[®] burner technology, which was originally developed for industrial furnaces [24]. The feasibility of extending this technology to gas turbines has been demonstrated experimentally [73], and modified designs have since been developed [74–76]. Even with optimisation, there are some inherent challenges associated with the FLOX[®] concept for gas turbines, primarily related to the trade-off between achieving good mixing (and hence low emissions) and avoiding excessive pressure losses (which reduces efficiency) [6]. Gas turbines which employ the concept of sequential combustion are an alternative option for the application of mild combustion. In such designs, a primary, lean combustion chamber generates the hot gases to drive a high-pressure turbine, and the flue gases pass through to a secondary combustion zone, located between the high-pressure and low-pressure turbines [77]. This secondary combustion process could operate in the mild regime, with the flue gases from the upstream combustion providing the hot and diluted environment without the need for recirculation—much like the JHC concept

[12]. Some recent designs based on this concept have been developed [78–80]; however, further exploration is necessary for these to become commercially viable [6].

Due to the cost of developing prototypes for testing, and the fact that in-depth analyses of flame structure and intermediate species are experimentally challenging at elevated pressures, computational modelling is particularly important in the design and optimisation of gas turbines. Although significant progress has been made in the modelling of mild combustion, it has not yet reached the level at which design decisions can be made in confidence based off of simulation results, particularly with limited computational resources [6]. Furthermore, optimisation of models is largely based on comparisons with experimental results at atmospheric pressure, due to the lack of suitable data pertaining to flames in a pressurised environment [40, 42]. Preliminary experimental results clearly indicate a change in behaviour at elevated pressure, although these studies do not facilitate the individual variation in parameters such as reactant O_2 concentration, Reynolds number and temperature, nor the visualisation of flame structure and reaction zones, which limits their usefulness in terms of model validation. This highlights the need for high-quality experimental data relating to canonical flames at elevated pressure, under well-defined operating conditions whereby key parameters—such as jet Reynolds number and coflow O_2 concentration—can be independently varied, to emulate the range of conditions that may be encountered in the secondary combustor of a sequential gas turbine.

2.4 Combustion of liquid sprays

2.4.1 Fundamental studies in spray combustion

Liquid fuels are the most common form of fuel for transport applications, due to their high energy density and relative ease of storage [81]. Since evaporation must occur prior to combustion, liquid fuels are commonly injected in the form of a high-momentum spray which breaks up to form droplets, increasing the surface area and therefore enhancing the evaporation/combustion process [82]. When studying sprays, and the combustion of sprays in particular, it is convenient to divide the spray into two regions; namely the “dense” and “dilute” regions [83]. The fuel is typically injected directly into the reaction zone as a dense spray in practical burners, whereby droplets are clustered together and form “ligaments”. This dense region then undergoes spray break-up, with droplets becoming smaller and more dispersed, ultimately forming a dilute sprays when the interactions between

individual droplets become negligible [84]. The droplets in this dilute region then undergo the processes of vaporisation and combustion. The presence of a secondary phase adds another layer of complexity to the already complicated process of turbulent combustion, due to the coupling between spray break-up/evaporation processes, transport phenomena and chemistry [85]. Consequently, spray combustion is another area in which there remain gaps in the fundamental understanding, despite its widespread implementation in practice [83].

In order to focus on the fundamental combustion processes in spray flames in an experimental setting, it is often useful to form a dilute spray directly. This can be achieved by forming the droplets upstream of the reaction zone (via an atomiser, for example), with the droplets then transported to the reaction zone via a carrier gas [86]. Not only does this allow greater control over the boundary conditions (since the dense region is much more difficult to characterise), it also facilitates the use of non-intrusive laser diagnostic techniques, the usefulness of which is limited in regions with high droplet densities despite recent progress being made in this regard [83, 87]. These “dilute spray burners” are a particular focus of The International Workshop on Turbulent Combustion of Sprays (TCS) [83, 88], which has been established to assist in the development of numerical models of spray combustion. The TCS has facilitated the provision of experimental data on the flow and droplet fields, as well as reactive scalars, for a series of well-defined target flames.

Experiments based on the TCS target flames have revealed important insights relating to the structure and stabilisation mechanisms of pilot-stabilised dilute spray flames. In order to examine the turbulence-droplet-chemistry interactions, measurements of the velocity and droplet fields were performed for both reacting and non-reacting sprays [86]. In addition to highlighting the interactions between the flame and the underlying droplet dynamics, these measurements provide much-needed data for model development and validation. Simultaneous imaging of both droplets and the reaction zones (via OH-PLIF) was performed for a range of flame cases with the same burner configuration, with the results indicating that the flames displayed characteristics of both premixed and non-premixed flames [89]. This is related to the development of double flame structures in certain cases, in which there is a distinct inner reaction zone due to premixing between fuel vapour and the carrier air [89]. The effect of droplets on the sooting behaviour has also been investigated, for dilute sprays using hydrogen as a carrier gas, with a notable increase in soot formation in the near-field region in comparison to otherwise equivalent prevaporised mixtures [90].

The concept of dual-fuelling—which refers to the combined use of both a

liquid and gaseous fuel—has also been studied in the context of a swirling flow burner configuration [91, 92]. Dual-fuelling can offer advantages in engine performance, by allowing the timing of auto-ignition to be precisely controlled, or prevented in the case of an SI engine, through variation of the relative proportion of the two fuels [93]. The results from the swirl burner investigations, which used both H₂ and natural gas (predominantly CH₄) in the gaseous stream, suggested a significant change in flame structure due to both the high temperature oxidant stream and the change in chemistry associated with the addition of gaseous fuel [91, 92]. It would therefore also be expected that spray flames would show a different behaviour under conditions relating to mild combustion, since this also involves a change in temperature and composition of the oxidant stream.

2.4.2 Liquid fuels and mild combustion

In order to assess the viability of mild combustion for transport applications, particularly for aerospace gas turbines, knowledge of the behaviour of liquid fuel combustion in a hot and low-oxygen environment is required. Since much of the work on mild combustion has been focussed on developing a fundamental understanding and obtaining datasets for model validation, experiments have typically involved relatively simple, gaseous fuels. There are, however, a limited number of studies which have investigated the behaviour of liquid fuels in the mild regime.

To isolate the chemical effects of different liquid fuels and to simplify the analysis, the combustion of pre vapourised fuels was investigated using the previously mentioned JHC configuration [94–96]. Similar to previous studies with this type of burner, a fundamental change in behaviour in terms of flame structure was observed when reducing the coflow O₂ concentration from 9% to 3%, indicating a transition toward the mild regime [95]. When using both ethanol and dimethyl ether (DME) as a fuel, the resulting flames exhibited similar structures when issuing into a 3% O₂ coflow [95], while *n*-heptane—which tends to involve a more complex combustion pathway—displayed a notably different behaviour, with a shift away from the features typical of mild combustion under the same conditions [94].

To analyse the effect of the surrounding conditions on the spray atomisation and evaporation processes, high-speed imaging and laser diagnostics of ethanol spray flames was performed for coflows of both air and a hot and low-O₂ oxidant [97]. The results indicated a much more rapid break-up and vaporisation of the liquid jet in the hot and diluted coflow, leading to an interesting change in the overall structure and propagation of the flame. In

particular, it was found that in the case of an air coflow, there were distinct peaks in the temperature profile on either side of the centreline, which is indicative of dual reaction zones, often referred to as a “double flame structure”. This was attributed to the tendency for large droplets to spread radially outwards (noting that these experiments used a pressure-swirl atomiser to generate the spray), while fuel vapour mixes with air to form an inner flame which propagates towards the centreline [97]. Under the hot and low-O₂ conditions, this behaviour was less prominent, since the stoichiometry of the inner flame was shifted toward the fuel-rich side. The structure of these flames was also investigated via numerical simulations, in which a high sensitivity to the relative evaporative and chemical timescales was observed [98]. This highlights the challenges associated with the modelling of spray combustion, and the importance of detailed experimental results under a range of operating conditions to test the robustness of these models.

Dilute spray flames have also been studied under hot and low-O₂ conditions. The autoignition and heat release behaviour of such flames was investigated experimentally [99, 100], using a burner design which combines the features of the JHC with the previously mentioned piloted dilute spray burner [86]. This facilitates the study of the independent effects of fuel loading and coflow properties on flame structure and stabilisation mechanisms. A double flame structure was observed for cases in which the droplets were carried by air, with a more typical nonpremixed behaviour when using nitrogen as the carrier gas, again emphasising the importance of mixing between air and fuel vapour on the development of the flame structure [100]. A change in the autoignition behaviour was also observed for these flames in comparison to gaseous flames, with the presence of localised ignition kernels observed over a larger range of axial locations for the spray flames [99]. One of the limitations of these studies—and the previously mentioned investigations involving pressure-swirl injected sprays [97]—is the absence of simultaneous imaging of both fuel droplets and intermediate species indicative of preheat regions within the flames (such as CH₂O). Additionally, it is of interest to extend the range of boundary conditions investigated, particularly to coflows of lower O₂ concentration to further explore the behaviour under conditions relevant to mild combustion and sequential gas turbines.

2.5 Hydrogen as a fuel in practical combustion systems

2.5.1 Hydrogen and mild combustion

Hydrogen has been identified as a promising carbon-free energy source of the future, with the capability to be produced via the electrolysis of water using excess renewable energy in the electricity grid [101]. This hydrogen can then be used in fuel cells to produce electricity, or it can be used directly in combustion systems. As a fuel for combustion, hydrogen has the potential to be used in a range of domestic, transport and industrial applications [102, 103]. In particular, it is anticipated that hydrogen will displace (or in some cases, supplement) the use of natural gas in a range of areas, including power generation [104] and high-temperature industrial processes [105]. There is also potential for it to be used in commercial and domestic appliances in instances where electric alternatives are either cost-prohibitive, do not meet requirements of end-users, or place an excessive load on the wider power generation and storage infrastructure [102, 106]. There are, however, a range of key differences between hydrogen and natural gas in terms of their fundamental combustion properties [107], leading to challenges in terms of adapting existing burner technologies to operate safely and effectively with hydrogen. These differences include a reduced volumetric energy density, wider flammability limits, higher flame speed, higher adiabatic flame temperature, and reduced levels of visible and thermal radiation [108–111].

One of the key advantages of hydrogen as a fuel is that it is essentially emissions-free, with the only product ideally being water vapour. However, the relatively high adiabatic flame temperature of hydrogen can result in significant thermal NO_x production [112, 113]. The most common method of preventing NO_x formation in devices such as gas turbines is by premixing the fuel with air at very low equivalence ratios—that is, with much more air than is required. The excess air essentially increases the thermal mass of the reactants, resulting in a lower flame temperature. Due to the wide flammability limits of hydrogen, this technique can be very effective, since extremely fuel-lean conditions can be reached. Incidentally, the wide flammability limits are also one of the issues with this technique, due to the risk of pre-ignition which is both a safety and performance concern for devices [114, 115]. H_2 combustion in the mild regime is therefore an attractive option, since it facilitates a reduction in NO_x emissions without the need for lean, premixed combustion.

Hydrogen has been used as a fuel in several studies of mild combustion, primarily in blends with hydrocarbon fuels [6]. Experiments using the JHC

setup indicated that the addition of H_2 can cause a significant change in flame structure, particularly with regards to ignition and stabilisation; in fact, hydrogen blending is often necessary to avoid flame blow-off [27, 30, 116]. Although hydrogen addition can aid in flame stabilisation, measurements indicate that it also leads to higher flame temperature (and therefore potentially higher NO_x emissions), possibly indicating a narrowing or shifting of the mild regime with the change in fuel composition [6, 117]. As mentioned, there has recently been a much larger emphasis placed on the adoption of hydrogen as a fuel for the decarbonisation of combustion processes. There is particular interest in the potential for operating existing combustion devices—such as gas turbines—on blends of hydrogen in natural gas [118, 119]. It is therefore important to extend the understanding of mild combustion to fuels with higher hydrogen content, as well as investigating the impact of elevated pressures on these flames.

2.5.2 Visibility and radiative properties of hydrogen flames

One of the concerns related to the transition from natural gas to hydrogen is the supposed “invisible” nature of hydrogen flames, due to the potential safety implications and acceptance by end-users [111, 120]. While it is true that hydrogen tends to produce a less intense flame appearance compared with conventional hydrocarbon fuels (including natural gas), the combustion of hydrogen in air does, in fact, lead to the emission of light in the visible spectrum [111]. Although the majority of the light emitted is in the ultraviolet (UV) and infra-red (IR) regions, analysis of the spectra of hydrogen flames reveals a relatively low-intensity blue continuum in the 412–510 nm range, as well as emissions in the red region of the visible spectrum due to vibrationally excited H_2O molecules [111]. In other experiments, a relatively intense visual appearance of hydrogen flames has been observed, which has been attributed to various sources such as carbon impurities in the fuel or piping system, as well as from metal or metal-oxide particles stemming from hydrogen embrittlement during storage [121]. It is also possible that the presence of sodium in the atmosphere could contribute to this phenomenon, as it has previously been found to produce interference in measurements of flame spectra [122], and has an emission wavelength at 589 nm which appears to match the experimental observations. It is worth noting that there is very little information on this topic in the literature, with no clear consensus regarding the source of the light.

In addition to visibility, the emission of electromagnetic radiation from hydrogen flames—particularly in the UV to IR range—is of interest more

generally. In many practical combustion applications, radiative heat transfer from flames is particularly important, either as a desired or unwanted feature of the process, depending on the application. Industrial combustion processes often rely heavily on thermal radiation to operate effectively; for example, to enable efficient heating of refractory walls in furnaces and rotary kilns [123, 124]. In contrast, for applications in which the aim is to maximise the temperature of the combustion products (i.e., to drive a piston in a reciprocating engine or a turbine in a gas turbine), thermal radiation is generally considered a negative feature as it results in radiative heat losses, and can also lead to overheating of the combustor walls [123]. For hydrocarbon fuels, the emissivity of the flame is largely dependent on the amount of soot particles within the flame, with this soot producing black-body radiation proportional to the fourth power of the temperature [125]. In non-sooting flames, the thermal radiation is dominated by the excitation of CO_2 and H_2O molecules [110]. Since the combustion of hydrogen produces both no soot and no CO_2 , the thermal radiation from such flames is much lower. Consequently, applications in which thermal radiation provides a significant proportion of the heat transfer require either design modifications to the furnace or kiln, for example, or a method for improving radiative heat transfer.

Methods of improving the radiative heat transfer characteristics of fuels which would otherwise produce minimal thermal radiation have been investigated previously. The addition of chemically inert nano-particles of alumina to LPG fuel was found to significantly enhance the radiative heat transfer from the resulting flames, although the practical concerns of introducing nano-particles to industrial combustion systems places several limitations on this approach [126]. In terms of fuel additives, a review of existing combustion data accompanied by a theoretical analysis suggested that the addition of solid, liquid and gaseous hydrocarbons to hydrogen in varying proportions can produce a highly radiating, luminous flame, with pulverised bituminous coal being particularly effective due to its high sooting propensity [110]. If such a technique is to be applied in practice, it is important to understand the fundamental physical and chemical phenomena relating to soot formation and its subsequent oxidation in a predominately hydrogen flame, both to maximise the thermal radiation and to ensure that the emission of unburnt hydrocarbons and particulate matter is avoided [110]. These phenomena have been investigated in a recent investigation focussing on the impact of the addition of toluene—a particularly highly sooting aromatic hydrocarbon—to hydrogen in the liquid and gaseous phases [90]. Experimental measurements of the soot volume fraction revealed a highly non-linear dependence of soot formation on the ratio between toluene and hydrogen in the fuel mixture,

as well as an increased tendency for localised regions of soot to be formed when the toluene is injected as a liquid [90]. This study (i.e., ref. [90]) was performed in a project closely related to the work presented in this thesis, and is therefore included in Appendix A. Generally, these different methods aim to increase the total radiative heat flux via either the direct introduction of solid particles, or the use of a fuel additive which promotes the formation of particles within the flame—that is, via the formation of soot. These particles emit broadband radiation within the flame, which also results in a luminous flame with increased visibility. It is therefore of interest to explore the feasibility of using these techniques to simultaneously improve the safety and performance of hydrogen as a fuel.

2.6 Research gaps

Following a review of the literature, five key gaps have been identified, which relate to the improvement of fuel-flexibility in practical combustion systems—these are summarised below:

1. There is a lack of experimental data relating to flames at elevated pressures under sequential combustion conditions. Most high pressure configurations do not facilitate the decoupling of temperature, flow-rate and composition of the oxidant stream. Consequently, understanding of combustion under such conditions is limited, as are validation options for computational models.
2. Numerical simulations have great potential for improving understanding of mild combustion at pressure; however, the implementation of combustion models typically used to describe the mild regime—such as the EDC model—has not been extended to elevated pressures.
3. The flame structure of dilute liquid sprays in a hot and low-oxygen environment is significantly different to that of conventional spray flames, yet there is a lack of understanding regarding the sensitivity of this structure to changes in boundary conditions for such flames.
4. The stabilisation mechanisms of liquid sprays under sequential combustion conditions are not well-understood, particularly in the transition to the mild regime.
5. The effects of fuel blending with a liquid “dopant” on the structure, appearance and radiative properties of predominately hydrogen flames

is another subject which requires further investigation. Further understanding of these effects will facilitate the transition towards low-carbon and fuel-flexible combustion.

2.7 References

- [1] Smith, G. P., D. M. Golden, M. Frenklach, N. W. Moriarty, B. Eiteneer, M. Goldenberg, C. T. Bowman, R. K. Hanson, S. Song, W. C. G. Jr., V. V. Lissianski, and Z. Qin (2000). *GRI-Mech 3.0*. <http://combustion.berkeley.edu/gri-mech/version30/text30.html>. [Accessed: 24/10/2022].
- [2] Turns, S. (2020). *An Introduction to Combustion: Concepts and Applications*. McGraw-Hill US Higher Ed ISE. ISBN: 978-1-260-59033-3.
- [3] Dunn, M. J., A. R. Masri, and R. W. Bilger (2007). "A New Piloted Premixed Jet Burner to Study Strong Finite-Rate Chemistry Effects". *Combustion and Flame* 151 (1), pp. 46–60.
- [4] Poinso, T. and D. Veynante (2012). *Theoretical and Numerical Combustion*. ISBN: 978-2-7466-3990-4.
- [5] Zhang, Y. Z., E. H. Kung, and D. C. Haworth (2005). "A PDF Method for Multidimensional Modeling of HCCI Engine Combustion: Effects of Turbulence/Chemistry Interactions on Ignition Timing and Emissions". *Proceedings of the Combustion Institute* 30 (2), pp. 2763–2771.
- [6] Perpignan, A. A. V., A. G. Rao, and D. J. E. M. Roekaerts (2018). "Flameless Combustion and Its Potential towards Gas Turbines". *Progress in Energy and Combustion Science* 69, pp. 28–62.
- [7] Peters, N. (2000). *Turbulent Combustion*. Cambridge, United Kingdom: Cambridge University Press. ISBN: 978-0-511-15320-4.
- [8] Glarborg, P., R. Kee, J. Grcar, and J. Miller (1986). *PSR: A Fortran Program for Modeling Well-Stirred Reactors*. Technical Report SAND-86-8209.
- [9] Peters, N. (1988). "Laminar Flamelet Concepts in Turbulent Combustion". *Symposium (International) on Combustion*. Twenty-First Symposium (International on Combustion) 21 (1), pp. 1231–1250.
- [10] Parente, A., M. R. Malik, F. Contino, A. Cuoci, and B. B. Dally (2016). "Extension of the Eddy Dissipation Concept for Turbulence/Chemistry Interactions to MILD Combustion". *Fuel* 163, pp. 98–111.

-
- [11] Joannon, M. de, G. Langella, F. Beretta, A. Cavaliere, and C. Noviello (2000). "Mild Combustion: Process Features and Technological Constraints". *Combustion Science and Technology* 153 (1), pp. 33–50.
- [12] Cavaliere, A. and M. de Joannon (2004). "Mild Combustion". *Progress in Energy and Combustion Science* 30 (4), pp. 329–366.
- [13] Rafidi, N. and W. Blasiak (2006). "Heat Transfer Characteristics of HiTAC Heating Furnace Using Regenerative Burners". *Applied Thermal Engineering* 26 (16), pp. 2027–2034.
- [14] Tsuji, H., A. K. Gupta, T. Hasegawa, M. Katsuki, K. Kishimoto, and M. Morita (2002). *High Temperature Air Combustion : From Energy Conservation to Pollution Reduction*. CRC Press. ISBN: 978-0-429-12261-3.
- [15] Evans, M. J., P. R. Medwell, H. Wu, A. Stagni, and M. Ihme (2017). "Classification and Lift-off Height Prediction of Non-Premixed MILD and Autoignitive Flames". *Proceedings of the Combustion Institute* 36 (3), pp. 4297–4304.
- [16] Mi, J., P. Li, F. Wang, K.-P. Cheong, and G. Wang (2021). "Review on MILD Combustion of Gaseous Fuel: Its Definition, Ignition, Evolution, and Emissions". *Energy & Fuels* 35 (9), pp. 7572–7607.
- [17] Flamme, M. (2004). "New Combustion Systems for Gas Turbines (NGT)". *Applied Thermal Engineering*. Industrial Gas Turbine Technologies 24 (11), pp. 1551–1559.
- [18] Rao, A. and Y. Levy (2010). "A New Combustion Methodology for Low Emission Gas Turbine Engines". *8th International Symposium on High Temperature Air Combustion and Gasification*, pp. 177–185.
- [19] Correa, S. M. and M. D. Smooke (1991). "NO_x in Parametrically Varied Methane Flames". *Symposium (International) on Combustion*. Twenty-Third Symposium (International) on Combustion 23 (1), pp. 289–295.
- [20] Correa, S. M. (1993). "A Review of NO_x Formation Under Gas-Turbine Combustion Conditions". *Combustion Science and Technology* 87 (1-6), pp. 329–362.
- [21] Abd-Alla, G. H. (2002). "Using Exhaust Gas Recirculation in Internal Combustion Engines: A Review". *Energy Conversion and Management* 43 (8), pp. 1027–1042.

- [22] Nishimura, M., T. Suzuki, R. Nakanishi, and R. Kitamura (1997). "Low-NO_x Combustion under High Preheated Air Temperature Condition in an Industrial Furnace". *Energy Conversion and Management*. International Symposium on Advance Energy Conversion Systems and Related Technologies 38 (10), pp. 1353–1363.
- [23] Katsuki, M. and T. Hasegawa (1998). "The Science and Technology of Combustion in Highly Preheated Air". *Symposium (International) on Combustion* 27 (2), pp. 3135–3146.
- [24] J.A.Wünning and J.G.Wünning (1997). "Flameless Oxidation to Reduce Thermal No-Formation". *Progress in Energy and Combustion Science* 23 (1), pp. 81–94.
- [25] Dally, B. B., A. N. Karpetis, and R. S. Barlow (2002). "Structure of Turbulent Non-Premixed Jet Flames in a Diluted Hot Coflow". *Proceedings of the Combustion Institute* 29 (1), pp. 1147–1154.
- [26] Medwell, P. R., P. A. Kalt, and B. B. Dally (2007). "Simultaneous Imaging of OH, Formaldehyde, and Temperature of Turbulent Non-premixed Jet Flames in a Heated and Diluted Coflow". *Combustion and Flame* 148 (1-2), pp. 48–61.
- [27] Medwell, P. R., P. A. M. Kalt, and B. B. Dally (2008). "Imaging of Diluted Turbulent Ethylene Flames Stabilized on a Jet in Hot Coflow (JHC) Burner". *Combustion and Flame* 152 (1-2), pp. 100–113.
- [28] Papageorge, M. J., C. Arndt, F. Fuest, W. Meier, and J. A. Sutton (2014). "High-Speed Mixture Fraction and Temperature Imaging of Pulsed, Turbulent Fuel Jets Auto-Igniting in High-Temperature, Vitiated Co-Flows". *Experiments in Fluids* 55 (7), p. 1763.
- [29] Arndt, C. M., M. J. Papageorge, F. Fuest, J. A. Sutton, W. Meier, and M. Aigner (2016). "The Role of Temperature, Mixture Fraction, and Scalar Dissipation Rate on Transient Methane Injection and Auto-Ignition in a Jet in Hot Coflow Burner". *Combustion and Flame* 167, pp. 60–71.
- [30] Cabra, R., T. Myhrvold, J. Y. Chen, R. W. Dibble, A. N. Karpetis, and R. S. Barlow (2002). "Simultaneous Laser Raman-Rayleigh-Lif Measurements and Numerical Modeling Results of a Lifted Turbulent H₂/N₂ Jet Flame in a Vitiated Coflow". *Proceedings of the Combustion Institute* 29 (2), pp. 1881–1888.
- [31] Oldenhof, E., M. J. Tummers, E. H. van Veen, and D. J. E. M. Roekaerts (2010). "Ignition Kernel Formation and Lift-off Behaviour of Jet-in-Hot-Coflow Flames". *Combustion and Flame* 157 (6), pp. 1167–1178.

-
- [32] Arndt, C. M., M. J. Papageorge, F. Fuest, J. A. Sutton, and W. Meier (2019). "Experimental Investigation of the Auto-Ignition of a Transient Propane Jet-in-Hot-Coflow". *Proceedings of the Combustion Institute* 37 (2), pp. 2117–2124.
- [33] Galletti, C., A. Parente, and L. Tognotti (2007). "Numerical and Experimental Investigation of a Mild Combustion Burner". *Combustion and Flame* 151 (4), pp. 649–664.
- [34] Evans, M. J. (2017). "Flame Stabilisation in the Transition to MILD Combustion". Thesis. The University of Adelaide, South Australia.
- [35] De, A. and A. Dongre (2015). "Assessment of Turbulence-Chemistry Interaction Models in MILD Combustion Regime". *Flow, Turbulence and Combustion* 94 (2), pp. 439–478.
- [36] Magnussen, B. (1981). "On the Structure of Turbulence and a Generalized Eddy Dissipation Concept for Chemical Reaction in Turbulent Flow". *19th Aerospace Sciences Meeting*. American Institute of Aeronautics and Astronautics.
- [37] Evans, M. J., P. R. Medwell, and Z. F. Tian (2015). "Modeling Lifted Jet Flames in a Heated Coflow Using an Optimized Eddy Dissipation Concept Model". *Combustion Science and Technology* 187 (7), pp. 1093–1109.
- [38] De, A., E. Oldenhof, P. Sathiah, and D. Roekaerts (2011). "Numerical Simulation of Delft-Jet-in-Hot-Coflow (DJHC) Flames Using the Eddy Dissipation Concept Model for Turbulence–Chemistry Interaction". *Flow, Turbulence and Combustion* 87 (4), pp. 537–567.
- [39] Aminian, J., C. Galletti, and L. Tognotti (2016). "Extended EDC Local Extinction Model Accounting Finite-Rate Chemistry for MILD Combustion". *Fuel* 165, pp. 123–133.
- [40] Evans, M. J., C. Petre, P. R. Medwell, and A. Parente (2019). "Generalisation of the Eddy-Dissipation Concept for Jet Flames with Low Turbulence and Low Damköhler Number". *Proceedings of the Combustion Institute* 37 (4), pp. 4497–4505.
- [41] Boyette, W. (2018). "Experiments on Turbulent Nonpremixed Flames at Elevated Pressures". Thesis. King Abdullah University of Science and Technology, Saudi Arabia.
- [42] Hochgreb, S. (2019). "Mind the Gap: Turbulent Combustion Model Validation and Future Needs". *Proceedings of the Combustion Institute* 37 (2), pp. 2091–2107.

-
- [43] Finger, S. N. and T. L. Dubell (2015). "Gas Turbine Combustor Development Tools for Production Designs". *ASME 1985 International Gas Turbine Conference and Exhibit*. American Society of Mechanical Engineers Digital Collection.
- [44] Parker, W. G. and H. G. Wolfhard (1950). "Carbon Formation in Flames". *Journal of the Chemical Society (Resumed)*, pp. 2038–2049.
- [45] Chakraborty, B. B. and R. Long (1968). "The Formation of Soot and Polycyclic Aromatic Hydrocarbons in Diffusion Flames— Part One". *Combustion and Flame* 12 (3), pp. 226–236.
- [46] Schalla, R. L. and G. E. McDonald (1955). "Mechanism of Smoke Formation in Diffusion Flames". *Symposium (International) on Combustion* 5 (1), pp. 316–324.
- [47] McArragher, J. S. and K. J. Tan (1972). "Soot Formation at High Pressures: A Literature Review". *Combustion Science and Technology* 5 (1), pp. 257–261.
- [48] Mätzing, H. and H. G. Wagner (1988). "Measurements about the Influence of Pressure on Carbon Formation in Premixed Laminar C₂H₄-Air Flames". *Symposium (International) on Combustion* 21 (1), pp. 1047–1055.
- [49] Böhm, H., D. Hesse, H. Jander, B. Lüers, J. Pietscher, H. G. G. Wagner, and M. Weiss (1989). "The Influence of Pressure and Temperature on Soot Formation in Premixed Flames". *Symposium (International) on Combustion* 22 (1), pp. 403–411.
- [50] Peters, N. (2001). "Turbulent Combustion". *Measurement Science and Technology* 12 (11).
- [51] Young, K. J., C. D. Stewart, and J. B. Moss (1994). "Soot Formation in Turbulent Nonpremixed Kerosine-Air Flames Burning at Elevated Pressure: Experimental Measurement". *Symposium (International) on Combustion* 25 (1), pp. 609–617.
- [52] Fischer, B. A. and J. B. Moss (1998). "The Influence of Pressure on Soot Production and Radiation in Turbulent Kerosine Spray Flames". *Combustion Science and Technology* 138 (1-6), pp. 43–61.
- [53] Brookes, S. J. and J. B. Moss (1999). "Measurements of Soot Production and Thermal Radiation from Confined Turbulent Jet Diffusion Flames of Methane". *Combustion and Flame* 116 (1-2), pp. 49–61.

-
- [54] Boyette, W. R., A. M. Elbaz, T. F. Guiberti, and W. L. Roberts (2019). "Experimental Investigation of the near Field in Sooting Turbulent Nonpremixed Flames at Elevated Pressures". *Experimental Thermal and Fluid Science* 105, pp. 332–341.
- [55] Vasil'ev, R. F. (1970). "Chemiluminescence Excitation Mechanisms". *Russian Chemical Reviews* 39 (6), p. 529.
- [56] Brown, D. M., E. Downey, J. Kretchmer, G. Michon, Emily Shu, and D. Schneider (1998). "SiC Flame Sensors for Gas Turbine Control Systems". *Solid-State Electronics* 42 (5), pp. 755–760.
- [57] Docquier, N., S. Belhafaoui, F. Lacas, N. Darabiha, and C. Rolon (2000). "Experimental and Numerical Study of Chemiluminescence in Methane/Air High-Pressure Flames for Active Control Applications". *Proceedings of the Combustion Institute* 28 (2), pp. 1765–1774.
- [58] Higgins, B., M. Q. McQuay, F. Lacas, and S. Candel (2001). "An Experimental Study on the Effect of Pressure and Strain Rate on CH Chemiluminescence of Premixed Fuel-Lean Methane/Air Flames". *Fuel* 80 (11), pp. 1583–1591.
- [59] Güthe, F., D. Guyot, G. Singla, N. Noiray, and B. Schuermans (2012). "Chemiluminescence as Diagnostic Tool in the Development of Gas Turbines". *Applied Physics B* 107 (3), pp. 619–636.
- [60] Samaniego, J.-M., F. N. Egolfopoulos, and C. T. Bowman (1995). "CO₂* Chemiluminescence in Premixed Flames". *Combustion Science and Technology* 109 (1-6), pp. 183–203.
- [61] Nori, V. and J. Seitzman (2008). "Evaluation of Chemiluminescence as a Combustion Diagnostic Under Varying Operating Conditions". *46th AIAA Aerospace Sciences Meeting and Exhibit*. American Institute of Aeronautics and Astronautics.
- [62] Higgins, B., M. Q. McQuay, F. Lacas, J. C. Rolon, N. Darabiha, and S. Candel (2001). "Systematic Measurements of OH Chemiluminescence for Fuel-Lean, High-Pressure, Premixed, Laminar Flames". *Fuel* 80 (1), pp. 67–74.
- [63] Najm, H. N., P. H. Paul, C. J. Mueller, and P. S. Wyckoff (1998). "On the Adequacy of Certain Experimental Observables as Measurements of Flame Burning Rate". *Combustion and Flame* 113 (3), pp. 312–332.

- [64] Bedard, M. J., T. L. Fuller, S. Sardeshmukh, and W. E. Anderson (2020). "Chemiluminescence as a Diagnostic in Studying Combustion Instability in a Practical Combustor". *Combustion and Flame* 213, pp. 211–225.
- [65] Merotto, L., M. Sirignano, M. Commodo, A. D'Anna, R. Dondè, and S. De Iuliis (2017). "Experimental Characterization and Modeling for Equivalence Ratio Sensing in Non-premixed Flames Using Chemiluminescence and Laser-Induced Breakdown Spectroscopy Techniques". *Energy & Fuels* 31 (3), pp. 3227–3233.
- [66] Boyette, W., T. Guiberti, G. Magnotti, and W. Roberts (2019). "Structure of Turbulent Nonpremixed Syngas Flames at High Pressure". *Proceedings of the Combustion Institute* 37 (2), pp. 2207–2214.
- [67] TNF Workshop | International Workshop on Measurement and Computation of Turbulent Flames (n.d.). <https://tnfworkshop.org/>. [Accessed: 24/10/2022].
- [68] International Sooting Flame (ISF) Workshop | University of Adelaide (n.d.). <https://www.adelaide.edu.au/cet/isfworkshop/>. [Accessed: 24/10/2022].
- [69] Lefebvre, A. H., D. R. Ballal, and D. R. Ballal (2010). *Gas Turbine Combustion : Alternative Fuels and Emissions, Third Edition*. CRC Press. ISBN: 978-0-429-14104-1.
- [70] Noor, M. M., A. P. Wandel, and T. Yusaf (2012). "A Review of MILD Combustion and Open Furnace Design Consideration". *International Journal of Automotive and Mechanical Engineering* 6, pp. 730–754.
- [71] Kruse, S., B. Kerschgens, L. Berger, E. Varea, and H. Pitsch (2015). "Experimental and Numerical Study of MILD Combustion for Gas Turbine Applications". *Applied Energy* 148, pp. 456–465.
- [72] Ye, J., P. R. Medwell, E. Varea, S. Kruse, B. B. Dally, and H. G. Pitsch (2015). "An Experimental Study on MILD Combustion of Pre-vaporised Liquid Fuels". *Applied Energy* 151, pp. 93–101.
- [73] Lückcrath, R., W. Meier, and M. Aigner (2008). "FLOX[®] Combustion at High Pressure With Different Fuel Compositions". *Journal of Engineering for Gas Turbines and Power* 130 (1), p. 011505.
- [74] Lammel, O., H. Schütz, G. Schmitz, R. Lückcrath, M. Stöhr, B. Noll, M. Aigner, M. Hase, and W. Krebs (2010). "FLOX[®] Combustion at High Power Density and High Flame Temperatures". *Journal of Engineering for Gas Turbines and Power* 132 (12).

- [75] Schütz, H., O. Lammel, G. Schmitz, T. Rödiger, and M. Aigner (2013). “EZEE[®]: A High Power Density Modulating FLOX[®] Combustor”. *ASME Turbo Expo 2012: Turbine Technical Conference and Exposition*. American Society of Mechanical Engineers Digital Collection, pp. 701–712.
- [76] Zanger, J., T. Monz, and M. Aigner (2015). “Experimental Investigation of the Combustion Characteristics of a Double-Staged FLOX[®] -Based Combustor on an Atmospheric and a Micro Gas Turbine Test Rig”. *ASME Turbo Expo 2015: Turbine Technical Conference and Exposition*. American Society of Mechanical Engineers Digital Collection.
- [77] Joos, F., P. Brunner, B. Schulte-Werning, K. Syed, and A. Eroglu (1996). “Development of the Sequential Combustion System for the ABB GT24/GT26 Gas Turbine Family”. *Volume 4: Heat Transfer; Electric Power; Industrial and Cogeneration*. Birmingham, UK: American Society of Mechanical Engineers, V004T10A022. ISBN: 978-0-7918-7875-0.
- [78] Yin, F. and A. G. Rao (2017). “Off-Design Performance of an Inter-stage Turbine Burner Turbofan Engine”. *Journal of Engineering for Gas Turbines and Power* 139 (8).
- [79] Perpignan, A. A. V., M. G. Talboom, Y. Levy, and A. G. Rao (2018). “Emission Modeling of an Interturbine Burner Based on Flameless Combustion”. *Energy & Fuels* 32 (1), pp. 822–838.
- [80] Levy, Y., V. Erenburg, V. Sherbaum, and I. Gaissinski (2016). “Flameless Oxidation Combustor Development for a Sequential Combustion Hybrid Turbofan Engine”. *ASME Turbo Expo 2016: Turbomachinery Technical Conference and Exposition*. American Society of Mechanical Engineers Digital Collection.
- [81] Agrawal, R., N. R. Singh, F. H. Ribeiro, and W. N. Delgass (2007). “Sustainable Fuel for the Transportation Sector”. *Proceedings of the National Academy of Sciences* 104 (12), pp. 4828–4833.
- [82] Wu, J. S., Y. J. Liu, and H. J. Sheen (2001). “Effects of Ambient Turbulence and Fuel Properties on the Evaporation Rate of Single Droplets”. *International Journal of Heat and Mass Transfer* 44 (24), pp. 4593–4603.
- [83] Masri, A. R. (2016). “Turbulent Combustion of Sprays: From Dilute to Dense”. *Combustion Science and Technology* 188 (10), pp. 1619–1639.
- [84] Faeth, G. M. (1987). “Mixing, Transport and Combustion in Sprays”. *Progress in Energy and Combustion Science* 13 (4), pp. 293–345.

- [85] Jenny, P., D. Roekaerts, and N. Beishuizen (2012). "Modeling of Turbulent Dilute Spray Combustion". *Progress in Energy and Combustion Science* 38 (6), pp. 846–887.
- [86] Gounder, J. D., A. Kourmatzis, and A. R. Masri (2012). "Turbulent Piloted Dilute Spray Flames: Flow Fields and Droplet Dynamics". *Combustion and Flame* 159 (11), pp. 3372–3397.
- [87] Dunn, M. J., A. R. W. Macfarlane, R. S. Barlow, D. Geyer, K. Dieter, and A. R. Masri (2021). "Spontaneous Raman–LIF–CO–OH Measurements of Species Concentration in Turbulent Spray Flames". *Proceedings of the Combustion Institute* 38 (1), pp. 1779–1786.
- [88] Merci, B., D. Roekaerts, and A. Sadiki, eds. (2011). *Experiments and Numerical Simulations of Diluted Spray Turbulent Combustion*. Vol. 17. ERCOFTAC Series. Dordrecht: Springer Netherlands. ISBN: 978-94-007-1408-3 978-94-007-1409-0.
- [89] Masri, A. R. and J. D. Gounder (2010). "Turbulent Spray Flames of Acetone and Ethanol Approaching Extinction". *Combustion Science and Technology* 182 (4-6), pp. 702–715.
- [90] Evans, M. J., D. B. Proud, P. R. Medwell, H. Pitsch, and B. B. Dally (2021). "Highly Radiating Hydrogen Flames: Effect of Toluene Concentration and Phase". *Proceedings of the Combustion Institute* 38 (1), pp. 1099–1106.
- [91] Sidey, J. and E. Mastorakos (2017). "Visualisation of Turbulent Swirling Dual-Fuel Flames". *Proceedings of the Combustion Institute* 36 (2), pp. 1721–1727.
- [92] Evans, M. J., J. A. M. Sidey, J. Ye, P. R. Medwell, B. B. Dally, and E. Mastorakos (2019). "Temperature and Reaction Zone Imaging in Turbulent Swirling Dual-Fuel Flames". *Proceedings of the Combustion Institute* 37 (2), pp. 2159–2166.
- [93] Hegab, A., A. La Rocca, and P. Shayler (2017). "Towards Keeping Diesel Fuel Supply and Demand in Balance: Dual-Fuelling of Diesel Engines with Natural Gas". *Renewable and Sustainable Energy Reviews* 70, pp. 666–697.
- [94] Ye, J., P. R. Medwell, M. J. Evans, and B. B. Dally (2017). "Characteristics of Turbulent n-Heptane Jet Flames in a Hot and Diluted Coflow". *Combustion and Flame* 183, pp. 330–342.

-
- [95] Ye, J., P. R. Medwell, K. Kleinheinz, M. J. Evans, B. B. Dally, and H. G. Pitsch (2018). "Structural Differences of Ethanol and DME Jet Flames in a Hot Diluted Coflow". *Combustion and Flame* 192, pp. 473–494.
- [96] Evans, M. J., P. R. Medwell, Z. Sun, A. Chinnici, J. Ye, Q. N. Chan, and B. B. Dally (2019). "Downstream Evolution of N-Heptane/Toluene Flames in Hot and Vitiated Coflows". *Combustion and Flame* 202, pp. 78–89.
- [97] Rodrigues, H. C., M. J. Tummers, E. H. van Veen, and D. J. E. M. Roekaerts (2015). "Spray Flame Structure in Conventional and Hot-Diluted Combustion Regime". *Combustion and Flame* 162 (3), pp. 759–773.
- [98] Ma, L. and D. Roekaerts (2017). "Numerical Study of the Multi-Flame Structure in Spray Combustion". *Proceedings of the Combustion Institute* 36 (2), pp. 2603–2613.
- [99] O’Loughlin, W. and A. Masri (2011). "A New Burner for Studying Auto-Ignition in Turbulent Dilute Sprays". *Combustion and Flame* 158 (8), pp. 1577–1590.
- [100] O’Loughlin, W. and A. R. Masri (2012). "The Structure of the Auto-Ignition Region of Turbulent Dilute Methanol Sprays Issuing in a Vitiated Co-flow". *Flow, Turbulence and Combustion* 89 (1), pp. 13–35.
- [101] Crabtree, G. W., M. S. Dresselhaus, and M. V. Buchanan (2004). "The Hydrogen Economy". *Physics Today* 57 (12), pp. 39–44.
- [102] Dodds, P. E. and S. Demoullin (2013). "Conversion of the UK Gas System to Transport Hydrogen". *International Journal of Hydrogen Energy* 38 (18), pp. 7189–7200.
- [103] Taamallah, S., K. Vogiatzaki, F. M. Alzahrani, E. M. A. Mokheimer, M. A. Habib, and A. F. Ghoniem (2015). "Fuel Flexibility, Stability and Emissions in Premixed Hydrogen-Rich Gas Turbine Combustion: Technology, Fundamentals, and Numerical Simulations". *Applied Energy* 154, pp. 1020–1047.
- [104] Pilavachi, P. A., S. D. Stephanidis, V. A. Pappas, and N. H. Afgan (2009). "Multi-Criteria Evaluation of Hydrogen and Natural Gas Fuelled Power Plant Technologies". *Applied Thermal Engineering* 29 (11), pp. 2228–2234.

-
- [105] Neuwirth, M., T. Fleiter, P. Manz, and R. Hofmann (2022). "The Future Potential Hydrogen Demand in Energy-Intensive Industries - a Site-Specific Approach Applied to Germany". *Energy Conversion and Management* 252, p. 115052.
- [106] Cooper, S. J., G. P. Hammond, M. C. McManus, and D. Pudjianto (2016). "Detailed Simulation of Electrical Demands Due to Nationwide Adoption of Heat Pumps, Taking Account of Renewable Generation and Mitigation". *IET Renewable Power Generation* 10 (3), pp. 380–387.
- [107] Schefer, R. W., C. White, and J. Keller (2008). "Chapter 8 - Lean Hydrogen Combustion". *Lean Combustion*. Ed. by D. Dunn-Rankin. Burlington: Academic Press, pp. 213–VIII. ISBN: 978-0-12-370619-5.
- [108] Nagalingam, B., F. Duebel, and K. Schmillen (1983). "Performance Study Using Natural Gas, Hydrogen-Supplemented Natural Gas and Hydrogen in AVL Research Engine". *International Journal of Hydrogen Energy* 8 (9), pp. 715–720.
- [109] Mishra, S. K. and R. P. Dahiya (1989). "Adiabatic Flame Temperature of Hydrogen in Combination with Gaseous Fuels". *International Journal of Hydrogen Energy* 14 (11), pp. 839–844.
- [110] Hutny, W. P. and G. K. Lee (1991). "Improved Radiative Heat Transfer from Hydrogen Flames". *International Journal of Hydrogen Energy* 16 (1), pp. 47–53.
- [111] Schefer, R. W., W. D. Kulatilaka, B. D. Patterson, and T. B. Settersten (2009). "Visible Emission of Hydrogen Flames". *Combustion and Flame* 156 (6), pp. 1234–1241.
- [112] Kim, S.-H., Y. Yoon, and I.-S. Jeung (2000). "Nitrogen Oxides Emissions in Turbulent Hydrogen Jet Non-Premixed Flames: Effects of Coaxial Air and Flame Radiation". *Proceedings of the Combustion Institute* 28 (1), pp. 463–471.
- [113] Rørtveit, G. J., K. Zepter, Ø. Skreiberg, M. Fossum, and J. E. Hustad (2002). "A Comparison of Low-NO_x Burners for Combustion of Methane and Hydrogen Mixtures". *Proceedings of the Combustion Institute* 29 (1), pp. 1123–1129.
- [114] White, C. M., R. R. Steeper, and A. E. Lutz (2006). "The Hydrogen-Fueled Internal Combustion Engine: A Technical Review". *International Journal of Hydrogen Energy* 31 (10), pp. 1292–1305.

-
- [115] Yip, H. L., A. Srna, A. C. Y. Yuen, S. Kook, R. A. Taylor, G. H. Yeoh, P. R. Medwell, and Q. N. Chan (2019). "A Review of Hydrogen Direct Injection for Internal Combustion Engines: Towards Carbon-Free Combustion". *Applied Sciences* 9 (22), p. 4842.
- [116] Medwell, P. R. and B. B. Dally (2012). "Effect of Fuel Composition on Jet Flames in a Heated and Diluted Oxidant Stream". *Combustion and Flame* 159 (10), pp. 3138–3145.
- [117] Arteaga Mendez, L. D., M. J. Tummers, E. H. van Veen, and D. J. E. M. Roekaerts (2015). "Effect of Hydrogen Addition on the Structure of Natural-Gas Jet-in-Hot-Coflow Flames". *Proceedings of the Combustion Institute* 35 (3), pp. 3557–3564.
- [118] Melaina, M. W., O. Antonia, and M. Penev (2013). "Blending Hydrogen into Natural Gas Pipeline Networks: A Review of Key Issues".
- [119] Carusotto, S., P. Goel, M. Baratta, D. A. Misul, S. Salvadori, F. Cardile, L. Forno, M. Toppino, and M. Valsania (2022). "Combustion Characterization in a Diffusive Gas Turbine Burner for Hydrogen-Compliant Applications". *Energies* 15 (11), p. 4117.
- [120] Scott, M. and G. Powells (2020). "Sensing Hydrogen Transitions in Homes through Social Practices: Cooking, Heating, and the Decomposition of Demand". *International Journal of Hydrogen Energy* 45 (7), pp. 3870–3882.
- [121] Zhao, Y., K. N. Soto Leytan, V. McDonnell, and S. Samuelsen (2019). "Investigation of Visible Light Emission from Hydrogen-Air Research Flames". *International Journal of Hydrogen Energy* 44 (39), pp. 22347–22354.
- [122] Webster III, H. A. (1985). "Visible Spectra of Standard Navy Colored Flares". *Propellants, Explosives, Pyrotechnics* 10 (1), pp. 1–4.
- [123] Sarofim, A. F. (1988). "Radiative Heat Transfer in Combustion: Friend or Foe". *Symposium (International) on Combustion* 21 (1), pp. 1–23.
- [124] Gorog, J. P., J. K. Brimacombe, and T. N. Adams (1981). "Radiative Heat Transfer in Rotary Kilns". *Metallurgical Transactions B* 12 (1), pp. 55–70.
- [125] Colombo, U. and M. W. Thring (1972). "Soot in Flames: The Technological Significance of the Problems of Soot and Other Particles Formed in Flames". *Combustion Science and Technology* 5 (1), pp. 189–191.

- [126] Waheed, K., S. W. Baek, I. Javed, and Y. Kristiyanto (2015). "Investigations on Thermal Radiative Characteristics of LPG Combustion: Effect of Alumina Nanoparticles Addition". *Combustion Science and Technology* 187 (6), pp. 827–842.

Chapter 3

Aims and Objectives

The overarching aim of this research is to advance the fundamental understanding of combustion under hot, low-oxygen and elevated-pressure conditions. This in-turn facilitates the development of fuel-flexible, low-emissions and efficient combustion systems, such as sequential combustion gas turbines. More specifically, five individual aims have been identified; these are aligned with the five gaps outlined in §2.6, and are addressed by the five publications which constitute the following chapters of this thesis.

Aim 1

To investigate the flame structure, stability and chemiluminescence features of jet flames issuing into a low-oxygen and high-temperature coflow, within a confined burner operating at elevated pressures.

Jet flames in hot and low-oxygen environments have been widely studied at atmospheric pressures, using burner configurations such as the jet-in-hot-coflow (JHC) which enable the independent variation of parameters such as jet Reynolds number, coflow temperature and oxygen concentration. In contrast, most studies of mild combustion at elevated pressures are based on recirculation designs, which inherently involve the coupling of these variables. Therefore, the focus of Aim 1 is to address this gap in knowledge by performing a series of chemiluminescence imaging experiments based on turbulent flames in a confined-and-pressurised jet-in-hot-coflow (CP-JHC) combustor. The results of these experiments offer several key insights relating to the effects of pressure under conditions that are particularly relevant to practical combustion devices. Paper 1 (Chapter 4) presents the commissioning and characterisation of the CP-JHC and a selection of experimental results, which are expanded upon in Paper 2 (Chapter 5).

Aim 2

To assess the validity of an atmospheric-pressure numerical model for mild combustion at elevated pressures.

Numerical modelling is an important tool for the development and optimisation of practical combustion systems, and can also provide fundamental insights not available experimentally. Significant progress has been made in the development of computational fluid dynamics (CFD) models in the context of mild combustion, although the lack of experimental data at pressure has limited the applicability of these models. Recently, the eddy dissipation concept (EDC) has proved particularly useful for modelling turbulence-chemistry interactions in conditions associated with the mild regime. Consequently, it is of interest to extend the use of this model to elevated pressures and assess its suitability in predicting trends with increasing pressure. The validity of the kinetics mechanisms which describe chemiluminescence (OH^* and CH^*) are also explored within the the context of this modelling. The CFD modelling results are presented in Paper 2 (Chapter 5), which also includes the experimental results against which comparisons are made.

Aim 3

To examine the effect of variations in the jet boundary conditions on the flame structure of dilute sprays in a sequential combustion environment.

The combustion of liquid sprays is an inherently complex phenomenon, due to the coupled interactions between droplet evaporation, turbulence and chemistry. To provide fundamental insights and aid in the development of computational models, it is useful to investigate the impact of variations in boundary conditions on the structure and evolution of the resulting flames. This has been achieved through a series of experiments based on a dilute spray JHC burner, which enables the independent variation in jet and coflow parameters, with instantaneous imaging of reaction zones and radical species via laser diagnostic techniques. Paper 3 of this thesis, presented in Chapter 6, investigates in detail the effects of fuel type, fuel loading, and the jet Reynolds number on the reaction zone features of dilute sprays issuing into a hot and low-oxygen coflow, emulating the secondary stage of a sequential gas turbine.

Aim 4

To investigate the stabilisation mechanisms of dilute spray flames under hot and low-oxygen conditions.

Expanding on the scope of Aim 3, the fourth aim of this thesis relates to the mechanisms involved in the stabilisation of the flames studied via the dilute spray JHC burner. In particular, the effect of the coflow oxygen concentration and temperature on the evaporation and subsequent combustion of the droplets is investigated, and comparisons are drawn against previous observations for gaseous flames. These results, which are presented in Paper 4 (Chapter 7), highlight the complexity of turbulent spray combustion, while providing a number of important insights to advance the understanding of the fundamental nature of such flames.

Aim 5

To assess the effects of toluene addition on the appearance and radiative properties of hydrogen flames, in the context of the practical implementation of hydrogen as a fuel source.

As an extension to the experiments involving liquid spray flames, blends of hydrogen and prevaporised toluene were also investigated as the final aim of the thesis. The motivation behind this aspect of the research is to improve the applicability of hydrogen as a fuel source in practical combustion devices, including in domestic applications such as gas cookers. This aim has been addressed through a series of experiments involving both a simple jet burner configuration as well as two practical domestic (Type A) appliances, in which the flames were studied in terms of their visual appearance and their radiative and spectral properties. The key outcomes of these experiments were presented in a report for the Future Fuels Cooperative Research Centre (CRC), which is included in Chapter 8. This investigation was also accompanied by experiments of a more fundamental nature, the results of which were included in a separate journal paper. Although this paper does not directly contribute to this thesis-by-publication, it has been included in the appendices for reference (Appendix A).


Chapter 4

Characteristics of Turbulent Flames in a Confined and Pressurised Jet-in-hot-coflow Combustor

Statement of Authorship

Title of Paper	Characteristics of turbulent flames in a confined and pressurised jet-in-hot-coflow combustor.
Publication Status	<input checked="" type="checkbox"/> Published <input type="checkbox"/> Accepted for Publication <input type="checkbox"/> Submitted for Publication <input type="checkbox"/> Unpublished and Unsubmitted work written in manuscript style
Publication Details	D. B. Proud , M. J. Evans, Q. N. Chan & P. R. Medwell (2022). "Characteristics of turbulent flames in a confined and pressurised jet-in-hot-coflow combustor." <i>Journal of the Energy Institute</i> 105, pp.103–113.

Principal Author

Name of Principal Author (Candidate)	Douglas B. Proud		
Contribution to the Paper	<p>Performed initial commissioning of a pressurised combustion apparatus, to understand the range of operating conditions that could be achieved, and the inlet flowrates required achieve the desired conditions.</p> <p>Developed and executed an experimental plan for operating the apparatus and collecting data in the form of temperature measurements and filtered flame photography, and identified a range of boundary conditions/flame cases to be investigated.</p> <p>Performed numerical simulations and processed, analysed and interpreted experimental and numerical data. Generated figures from data and wrote manuscript.</p>		
Overall percentage (%)	80		
Certification:	This paper reports on original research I conducted during the period of my Higher Degree by Research candidature and is not subject to any obligations or contractual agreements with a third party that would constrain its inclusion in this thesis. I am the primary author of this paper.		
Signature	 <table border="1" style="float: right; margin-left: 20px;"> <tr> <td>Date</td> <td>24-OCT-2022</td> </tr> </table>	Date	24-OCT-2022
Date	24-OCT-2022		

Co-Author Contributions

By signing the Statement of Authorship, each author certifies that:

- i. the candidate's stated contribution to the publication is accurate (as detailed above);
- ii. permission is granted for the candidate to include the publication in the thesis; and
- iii. the sum of all co-author contributions is equal to 100% less the candidate's stated contribution.

Name of Co-Author	Michael J. Evans			
Contribution to the Paper	Assisted in initial design/commissioning of experimental apparatus, provided assistance with numerical simulations, edited and provided feedback on manuscript.			
Signature	<table border="1" style="float: right; margin-left: 20px;"> <tr> <td>Digitally signed by Michael Evans Date: 2022.10.17 14:12:32 +10'30'</td> <td>Date</td> <td>17-Oct-2022</td> </tr> </table>	Digitally signed by Michael Evans Date: 2022.10.17 14:12:32 +10'30'	Date	17-Oct-2022
Digitally signed by Michael Evans Date: 2022.10.17 14:12:32 +10'30'	Date	17-Oct-2022		

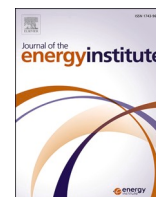
Name of Co-Author	Qing N. Chan		
Contribution to the Paper	Involved in initial concept generation and supervised direction of the work. Provided feedback on manuscript relating to discussion and presentation of results.		
Signature	<table border="1" style="float: right; margin-left: 20px;"> <tr> <td>Date</td> <td>17/10/2022</td> </tr> </table>	Date	17/10/2022
Date	17/10/2022		

Name of Co-Author	Paul R. Medwell		
Contribution to the Paper	Supervised the initial conception and construction of the experimental apparatus. Assisted in data collection and troubleshooting, oversaw the direction of the work, and provided feedback on manuscript (presentation of methods/results, discussion/interpretation).		
Signature		Date	17-OCT-2022



Contents lists available at ScienceDirect

Journal of the Energy Institute

journal homepage: www.elsevier.com/locate/joei

Characteristics of turbulent flames in a confined and pressurised jet-in-hot-coflow combustor

D.B. Proud^{a,*}, M.J. Evans^{a,b}, Q.N. Chan^c, P.R. Medwell^a

^a School of Mechanical Engineering, The University of Adelaide, Adelaide, SA 5005, Australia

^b UniSA STEM, University of South Australia, Mawson Lakes, SA 5095, Australia

^c School of Mechanical and Manufacturing Engineering, University of New South Wales, Sydney, NSW 2052, Australia

ARTICLE INFO

Keywords:

Elevated pressure combustion
Mild combustion
Turbulent flames
Jet-in-hot-coflow
Chemiluminescence

ABSTRACT

Combustion in hot and low oxygen environments—such as those encountered in practical devices including inter-turbine burners and sequential gas turbines—is not yet fully understood at a fundamental level, particularly in terms of the effects of pressure. To meet this gap in understanding, a confined-and-pressurised jet-in-hot-coflow (CP-JHC) combustor has been developed to facilitate optical diagnostics of turbulent flames in hot and vitiated coflows for the studies of flame stabilisation, structure and soot formation at elevated pressures. The CP-JHC burner has been designed for steady operation at 10 bar with internal temperatures of up to 1975 K, with a water-cooled central jet issuing into a hot oxidant stream of combustion products from a non-premixed natural gas/H₂ burner. This work describes the key features and operational capabilities of the CP-JHC burner and presents a selection of experimental results showing characteristics not previously available. Specifically, temperature measurements of the hot coflow are used to estimate the enthalpy deficit of the stream, revealing an increase in thermal efficiency with increasing heat input, and a decrease with increasing pressure. Chemiluminescence imaging of OH* and CH* is performed for turbulent jet flames to study the flame structure under various operating conditions, and true-colour imaging results are also included to highlight the change in soot formation under elevated pressures. The mean images indicate a change in stabilisation behaviour with changes in pressure and jet Reynolds number (Re_{jet}), which is further investigated by a statistical analysis of the short-exposure CH* images. This analysis reveals that an increase in Re_{jet} from 10,000 to 15,000 leads to an increase in the mean lift-off height (from the jet exit plane) from approximately 1.5 to 6 jet diameters at atmospheric pressure, while the flames at elevated pressures show significantly less variation and tend to stabilise at the jet exit for $P > 3.5$ bar(a). The experimental findings are complemented by numerical simulations of laminar opposed flow flames, providing additional insights into the fundamental chemical kinetics effects which influence these flames. In particular, a monotonic reduction in both the maximum and integrated OH* and CH* mass fractions is observed with increasing pressure. This reduction is particularly pronounced at lower pressures, with a reduction to 10% of the atmospheric-pressure value at 3 bar(a) for the integrated OH* mass fraction. Additionally, this behaviour is shown to be related to the combined effects of a shift in the formation pathways and the increased impact of collisional quenching.

1. Introduction

The reduction of pollutant emissions, in conjunction with improvements in efficiency and operational flexibility, are major challenges in the development of new combustion devices. A promising technology in this regard is “mild” combustion, which, in addition to describing the nature of the combustion process, is an acronym for moderate or intense low-oxygen dilution combustion. This mode of combustion, which is

also referred to as flameless combustion and flameless oxidation [1,2], is characterised by a highly diluted oxidant stream which is above the auto-ignition temperature of the fuel [3]. In practice, such conditions are typically achieved via exhaust gas recirculation (EGR) or the use of a secondary combustion stage. The use of exhaust gas heat allows an increase in the thermal efficiency, while the low oxygen concentration results in lower peak temperatures, thus limiting the production of NO_x, a major pollutant associated with combustion. Another important

* Corresponding author.

E-mail address: douglas.proud@adelaide.edu.au (D.B. Proud).

<https://doi.org/10.1016/j.joei.2022.07.007>

Received 10 May 2022; Received in revised form 16 July 2022; Accepted 19 July 2022

Available online 16 August 2022

1743-9671/© 2022 Energy Institute. Published by Elsevier Ltd. All rights reserved.

feature of mild combustion is the reduced tendency for soot formation in this regime, which is attributed to a shift in the heat release profile such that pyrolytic regions of negative heat release are suppressed [4].

A potential application of mild combustion is in gas turbines, for both electricity generation and aerospace propulsion applications [1]. The most common approach for practical implementations of mild combustion is via the EGR method, using either internal recirculation (e.g. with a high-momentum jet to generate recirculation zones) or the external recirculation of flue gases. Another potential option which is particularly relevant for gas turbines is the use of a sequential combustion configuration, in which the exhaust products of a primary or initial combustor pass through to a downstream combustion zone into which a secondary fuel stream is injected. Such a configuration—which is referred to as either a sequential gas turbine (SGT) or inter-turbine burner (ITB) depending on the geometry [5–9]—may be beneficial as it can provide additional fuel-flexibility while avoiding the issue of pressure loss, an inherent challenge of EGR-based gas turbines [1]. There are, however, a number of complexities involved in the implementation of mild combustion in a gas turbine, largely due to the requirement of a variable output and the need to operate at a range of pressures and temperatures. While mild combustion is relatively well understood for the case of atmospheric pressure (such as in a furnace), the impact of increased pressure on the formation of emissions and stability of the mild regime requires further investigation [10], to enable the extension of its application to devices such as gas turbines.

Due to the relevance of the topic to practical applications, the effect of pressure on combustion has remained an active area of investigation for some time. An inherent challenge associated with experiments at elevated pressure is the difficulty in obtaining data relating to flame structure and stabilisation, since the need for confinement tends to limit optical access for diagnostics. A useful technique in this regard is chemiluminescence imaging, which facilitates the investigation of flame structure and reaction zone features through a single viewing window. This imaging is typically focussed on the excited-state OH and CH species (termed OH* and CH*), as they tend to be correlated with regions of high heat release and radical concentrations [11]. One of the challenges associated with chemiluminescence imaging is the difficulty in extracting quantitative information (such as heat release rate) from the measurements, since several factors—including pressure—can influence the excitation and subsequent relaxation of the species [12,13]. Recently, laser diagnostic measurements have been performed for turbulent flames at pressures up to 12 bar for turbulent nonpremixed flames with a CO/H₂/N₂ fuel mixture issuing into a coflow of air [14]. Imaging of the near-field reaction zone revealed both a narrowing of the OH layer and a reduced probability of local extinction with increasing pressure [14]. The formation of soot is also known to be particularly sensitive to pressure, with previous studies suggesting a linear relationship between soot volume fraction and operating pressure [15], as well as a shift in the onset of the sooting region further upstream for elevated pressures, even when velocity is held constant [16]. Although mild conditions are known to suppress soot formation, this is primarily based on observations at atmospheric pressures; it is therefore imperative to explore the competing effects of pressure and dilution by exhaust products on the formation of soot.

There have also been a number of important studies based on conditions relevant to mild and sequential combustion at elevated pressures. A particular configuration that has been studied in-depth is the FLOX[®] combustor [17,18], which is based on a high-momentum, recirculation concept. Optically accessible experiments with the FLOX[®] combustor highlighted the importance of the jet exit conditions on the mixing processes and the resulting emissions characteristics, with OH* chemiluminescence and OH-PLIF reaction-zone imaging confirming the existence of distributed reaction zones (typical of mild combustion) in the low-emissions operating range [17]. Turbulent jets issuing into a hot cross-flow of combustion products under pressurised conditions have also been investigated, with high-speed imaging

revealing that the flame stabilisation process is particularly sensitive to the addition of natural gas to hydrogen, as well as highlighting the importance of isolated ignition kernels on the overall autoignition process [19]. The ignition and stabilisation features of flames in conditions relevant to sequential gas turbines have also been studied, with a numerical analysis involving both 1-D simulations and LES modelling by Schulz and Noiray [20] identifying a range of possible combustion modes which can co-exist in such a configuration. Additionally, Guethe et al. [21] provide a comprehensive overview of the potential of chemiluminescence to aid in the development, control and optimisation of gas turbines, including as a diagnostic tool to further understand the flame dynamics in sequential combustors. While these studies provide valuable insights into the behaviour of flames under hot and low-oxygen conditions at pressure, they tend to feature relatively complex geometries which—although beneficial in terms of demonstrating the viability of the technology—leads to coupling between boundary conditions and limits the applicability of the results for model validation [10].

In contrast to the aforementioned studies at elevated pressures, there have been several studies performed in open-flame burners at atmospheric pressure which facilitate the decoupling of chemistry, mixing and flow-field effects. Many of these experiments have been carried out using so-called jet-in-hot-coflow (JHC) burners [22,23], or similar designs such as the vitiated coflow burner [24,25]. In these burners, mild combustion conditions are achieved using an additional burner upstream of the main combustion zone, with the primary fuel jet issuing into the hot and low-O₂ coflow of combustion products. This configuration emulates EGR conditions, or the secondary stage of an SGT or ITB. The advantage of the JHC and similar designs is the fact that the upstream combustion zone can be controlled independently of the jet, allowing the coflow properties, such as O₂ concentration and temperature, to be varied while maintaining constant jet boundary conditions, such as Reynolds number and fuel type.

To enhance the fundamental understanding of mild combustion in conditions relevant to devices such as gas turbines, the current investigation is focussed on the structure, stability and sooting behaviour of turbulent flames at elevated pressures, in a hot and low-O₂ coflow. Experiments have been performed using a unique burner which combines the advantages of the well-studied JHC configuration with the ability to operate at pressure. The design and operation of this “confined and pressurised jet-in-hot-coflow” combustor (CP-JHC) is described in this paper, along with a series of experimental results. This includes a characterisation of the coflow, in terms of the effect of pressure, equivalence ratio and heat input on the downstream temperature of the coflow stream. Chemiluminescence and true-colour imaging is performed to examine the effect of pressure on the characteristics of jet flames with Reynolds numbers of 10,000 and 15,000 issuing into a 9% O₂ coflow. These results are supplemented by laminar flame simulations, which facilitate the detailed analysis of the change in chemical kinetics with increasing pressure, and its implications regarding chemiluminescence intensity. This is of particular importance to guide future research efforts in developing the ability to extract quantitative information from chemiluminescence imaging, which will in turn aid in the development and validation of CFD models.

2. Methods

2.1. Burner description

A cross-sectional schematic which highlights the key features of the CP-JHC combustor is shown in Fig. 1. The jet flame and hot coflow are contained within a 100-mm-diameter cylindrical quartz tube, which is surrounded by a section of DN300 (O.D. of 324 mm), 304 stainless steel seamless pipe with a wall thickness of 12.7 mm. The void between the quartz and the pipe wall is filled with thermal insulation to allow steady operation at 10 bar with internal temperatures up to 1975 K without a requirement for cooling the main pressure vessel walls. This

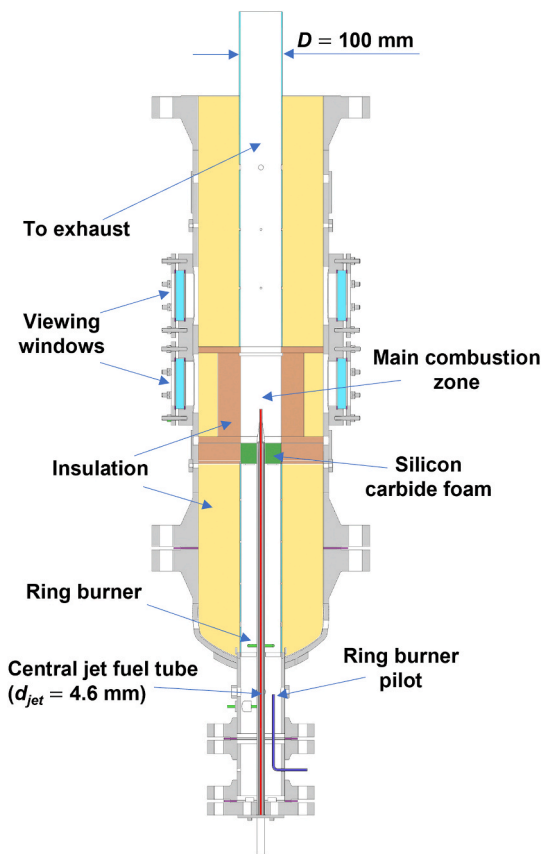


Fig. 1. CP-JHC cross section with main components labelled. Note: the exhaust section of the combustor has been omitted from this figure.

configuration minimises heat losses in the system, allowing for the investigation of hotter coflow conditions and with minimal thermal boundary layer. The hot combustion products from the jet and coflow are then cooled via water jackets, allowing the pressure in the vessel to be controlled with a back-pressure regulator (cooling/exhaust system is not shown in Fig. 1).

The hot and low- O_2 coflow is produced using a ring burner, via the nonpremixed combustion of a natural gas (NG) and H_2 fuel mixture with an air stream which enters upstream of the ring burner. The ring burner is initially ignited with a pilot flame, which is then extinguished following stabilisation. The flowrates of NG, H_2 and air can be independently varied to provide a range of coflow conditions, with the option of diluting the air stream with N_2 to obtain specific O_2 concentrations and temperatures with constant coflow velocity [22,23]. The main fuel stream issues into the coflow of combustion products from a 4.6-mm-diameter jet, which is readily interchangeable to facilitate measurements with other jet diameters. The central jet is water-cooled to avoid structural damage or thermal decomposition of the fuel, and the length of the jet is nearly 300 times its internal diameter to ensure fully-developed flow at the exit plane. The combustor has the capability for 8 windows to be installed at two different heights (as shown in Fig. 1), although the current configuration features a single quartz window (48 mm \times 107 mm) positioned level with the jet exit plane, with the others blanked-off with thermal insulation. This viewing window facilitates the optical analysis of the jet flames issuing into the hot coflow of combustion products. An annulus composed of porous silicon carbide foam is positioned below the viewing window, upstream of the jet exit plane in order to improve the uniformity of the flow. It is worth noting that the CP-JHC is a research burner developed for the investigation of flame structure and stabilisation in a specific location within

the burner; consequently, the emissions characteristics—which are a global feature of the combustor—are not a focus of the experiments.

2.2. Boundary conditions and experimental techniques

Turbulent flames were stabilised in a hot and low- O_2 coflow in the CP-JHC burner. The ring burner fuel is NG blended with H_2 in a 1:1 volumetric ratio to improve stability and reduce formation of soot at increased pressures. Air was used as the oxidant, and the air-fuel ratio and total fuel flowrate were modified to provide a range of coflow O_2 concentrations (X_{O_2}) and heat inputs (Q_{in}), respectively. Coflow temperatures (T_{meas}) were monitored *in-situ* with an R-type thermocouple which was located level with the jet exit plane, halfway between the central axis and the inner wall of the insulation. As mentioned previously, the insulation surrounding the combustor walls minimises the prominence of the thermal boundary layer. Similarly, the water-cooled jet is covered with an alumina sheath to minimise heat transfer. With these features, the impacts of a thermal boundary layer are ameliorated. Additionally, the temperature across the core of the coflow is homogenised by the silicon carbide foam which is positioned upstream of the jet exit. Ultimately, the spatial variations in the coflow temperature are at most 10%, and the effect of these variations is reflected in the experimental uncertainty that is reported throughout the paper. Presented temperature measurements for coflow characterisation were taken without a jet flame to minimise additional incident radiation on the thermocouple. The coflow characterisation results presented in this paper correspond to equivalence ratios (Φ) ranging from 0.3 to 0.85 (excess O_2 of 3–14% vol.), with heat inputs ranging from approximately 4–22 kW; these two variables in turn correspond to variations in the temperature, O_2 concentration and velocity (\bar{U}) of the coflow.

Turbulent jet flames with a 1:1 (by volume) blend of NG ($\geq 92\%$ CH_4) and H_2 issuing into the hot coflow were also investigated. Two different jet Reynolds numbers (Re_{jet}) of 10,000 and 15,000 were used throughout the investigation; these were maintained across the different pressures to examine the effects of pressure and Re_{jet} independently. The chemiluminescence imaging results presented for the turbulent jet flames herein correspond to constant coflow conditions at the various pressures; these are shown in Table 1.

Images of the jet flames were captured using both a DSLR camera and an intensified CCD camera with a UV lens. The DSLR camera was fitted with a 430 nm bandpass filter (FWHM of 10 nm), enabling the imaging of CH^* chemiluminescence. True-colour photographs (i.e. without the filter installed) were also captured with the DSLR camera to study the broadband luminescence. The UV-ICCD camera was also fitted with a bandpass filter, centred at 310 nm with a FWHM of 10 nm to target the chemiluminescence from OH^* radicals. Both cameras were manually focussed, and images were captured with a range of exposure times, f-numbers and ISO-speeds/gains—these settings are reported in this paper where appropriate, and consistency is ensured when directly comparing images from different flame cases. A series of short-exposure CH^* images were also captured with the DSLR camera, facilitating the statistical analysis of the flames in greater detail.

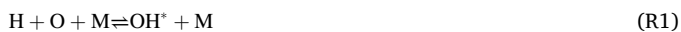
Table 1
Coflow boundary conditions and equilibrium species concentrations (X) for the NG: H_2 jet flame results.

P	\bar{U}	T_{meas}	T_{ad}	Q_{in}	X_{O_2}	X_{CO_2}	X_{H_2O}	X_{N_2}
[bar (a)]	[m/s]	[K]	[K]	[kW]	[%]	[%]	[%]	[%]
1.1–7	3.6–0.57	1025 \pm 25	1595	8.7	9.0	4.3	13	73

2.3. Numerical simulations

Numerical simulations were performed for 1-D, laminar opposed flow flames under a range of conditions, using the OPPDIF code available in CHEMKIN-PRO. The GRI-Mech 3.0 chemical kinetics mechanism was used to model the combustion of a 1:1 mixture of CH₄ and H₂, with a hot and low-O₂ oxidant stream ($T = 1050$ K, $X_{O_2} = 0.09$) to match the experimental conditions. GRI-Mech 3.0 is a well-established detailed kinetics mechanism available for natural gas combustion under a range of conditions, including pressures up to 20 atm [26]. The rate constant parameters for GRI-Mech are informed by laboratory experiments and theoretical formulations, with the resulting mechanism subjected to a series of sensitivity analyses and parameter optimisations, and the final parameter set then checked against validation datasets available in the literature. This mechanism has been used extensively in the context of CFD modelling, to reproduce the behaviour observed for JHC flames at atmospheric pressure [27–29], as well as in laminar flame simulations [30]. It is also worth noting that GRI-Mech 3.0 is a more sophisticated version of its predecessors in GRI-Mech 2.11 and GRI-Mech 1.2, which have also been used previously in combustion models involving hot and low-oxygen conditions, including studies based the JHC configuration [31], and similar burners such as the vitiated coflow burner [32,33]. These mechanisms have also been used to develop reduced mechanisms such as DRM19 and DRM22 [34], as well as in comparisons against other, less detailed mechanisms such as KEE [35]. These reduced mechanisms—particularly DRM19—have again been used successfully to model combustion under similar hot and low-oxygen conditions [36–39], further validating the use of GRI-Mech 3.0 in the current study.

The strain rate was held constant for the simulations at different pressures, with a mean normal strain rate of approximately 40 s^{-1} . In order to compare against the experimental observations, additional reactions for OH* and CH* formation were included in the kinetics mechanism. The sub-mechanism used for OH* formation is based on the following two formation reactions, with rate coefficients obtained from Hall & Petersen [40]:



The CH* sub-mechanism is based on the following two reactions, with rate coefficients from Elsamra et al. [41]:



Additionally, quenching reactions were included in the model, using the rate coefficients from Tamura et al. [42]. For the OH* sub-mechanism, an additional reaction was included in order to model the spontaneous emission process, that is:



For this reaction, a spontaneous emission rate coefficient of 1.45×10^6 was assumed [43]. It is worth noting that R5 is the mechanism by which light is emitted and therefore corresponds to the experimental chemiluminescence imaging, so its inclusion provides additional insights in comparing the numerical and experimental results.

Although GRI-Mech 3.0 is valid at elevated pressures, the excited-state OH* and CH* sub-mechanisms have only been validated at atmospheric pressures. Nevertheless, it is still of interest to investigate how the model behaves as the pressure is increased, particularly in terms of the underlying species which participate in the excitation reactions. Additionally, the simulations enable the modelling of heat release rate (HRR) as a function of pressure. Since OH* and CH* chemiluminescence are often used as indicators for regions of intense heat release in a flame [13,44], it is useful to compare the trends in HRR with pressure—based

on the simulations—with the experimental observations relating to chemiluminescence.

3. Results and discussion

3.1. Coflow characterisation and operational limits

To facilitate the precise control of the coflow conditions for the current and future experiments, it is important to characterise the behaviour of the coflow under a range of operating conditions. To ensure that the coflow exhibited a consistent and predictable behaviour, temperature measurements were performed for a range of equivalence ratios, heat inputs, and operating pressures. In addition to these measurements, qualitative observations via the viewing window were made to assess the stability of the coflow, in addition to monitoring the integrity of the combustor itself in the form of wall-temperature measurements. Fig. 2 maps the measured coflow temperatures at 1 and 5 bar (a) to combinations of coflow heat input (calculated using the lower heating value of the fuel mixture) and equivalence ratio, producing an “operational window” for the coflow burner. This window is limited by: (i) the requirement for a lean, soot-free coflow; (ii) minimum temperature to ensure self-ignition of the jet; and (iii) maximum operating temperature to avoid overheating the pressure vessel.

The temperature maps shown in Fig. 2 highlight some interesting results regarding the behaviour of the coflow, particularly when comparing the two different pressures. First of all, both maps show a general increase in the coflow temperature from the bottom-left of the map to the top-right. The increase from left-to-right is expected, since the adiabatic flame temperature increases the closer the equivalence ratio is to unity. The increase in coflow temperature with increasing heat input is due to heat losses to the walls of the combustor, since—despite the insulation surrounding the combustion zone—there is expected to be a departure from the adiabatic flame temperature, emphasising the importance of characterising the coflow. Based on Fig. 2, it appears that

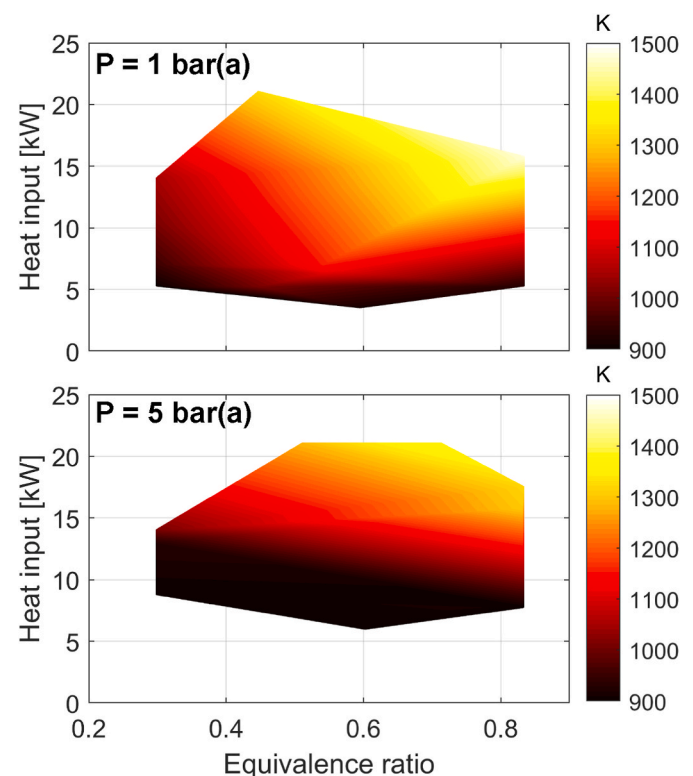


Fig. 2. Temperature maps for combinations of coflow heat input and equivalence ratio at 1 and 5 bar(a).

the heat loss is in general greater under the elevated pressure conditions, with a lower coflow temperature for corresponding locations on the map in comparison to the atmospheric case; this is most apparent at low heat inputs and equivalence ratios.

To investigate the heat loss from the coflow under different operating conditions, it is useful to quantify this behaviour using the enthalpy deficit (Δh), defined by the following:

$$\Delta h = c_p \times (T_{ad} - T_{meas}) \quad (1)$$

where c_p is the specific heat capacity, T_{ad} is the adiabatic flame temperature, and T_{meas} the measured coflow temperature. Fig. 3 displays the enthalpy deficits calculated using Eq. (1) as a function of operating pressure, from 1 to 5 bar(a). The values were calculated for three different coflow initial conditions, corresponding to three different heat inputs, all with an adiabatic flame temperature of 1595 K and an equilibrium O₂ concentration of 9% by mole. The plots shown in Fig. 3 display a clear trend in the enthalpy deficit with both operating pressure and heat input. A consistent decrease in the coflow temperature can be seen with increasing pressure, leading to an approximately linear relationship between enthalpy deficit and operating pressure for all three heat inputs. The increase in heat loss is likely a consequence of the greater residence times as pressure is increased, since the coflow velocity is inversely proportional to operating pressure for coflows of equivalent heat input. This also explains the reduction in enthalpy deficit with increasing heat input, noting that the coflow fuel composition is the same for all three heat inputs, such that the mass flow-rate—and therefore the coflow velocity for a given pressure and equivalence ratio—is directly proportional to the heat input. Referring back to Fig. 2, a reduction in equivalence ratio (that is, an increase in the amount of excess air) can actually be seen to lead to an increase in coflow temperature for equivalent heat inputs for certain regions of the map, for example when moving directly right-to-left from $\Phi = 0.8$ to 0.65 with a heat input of approximately 10 kW in the case of the 1 bar map in Fig. 2. This again indicates that the heat losses are related to the coflow velocity, such that the excess air can lead to the heat from the coflow being more effectively transferred downstream despite the reduced flame temperature under certain conditions.

3.2. Mean chemiluminescence imaging

To examine the effect of pressure on the behaviour of turbulent flames issuing into the hot coflow, chemiluminescence imaging of OH* and CH* was performed. Fig. 4 displays the results of this imaging for H₂/NG flames with $Re_{jet} = 10,000$ and $Re_{jet} = 15,000$, at operating pressures ranging from 1.1 to 7 bar(a). The flames shown in Fig. 4 correspond to a coflow of constant heat input and equivalence ratio across the various operating pressures, producing the conditions shown

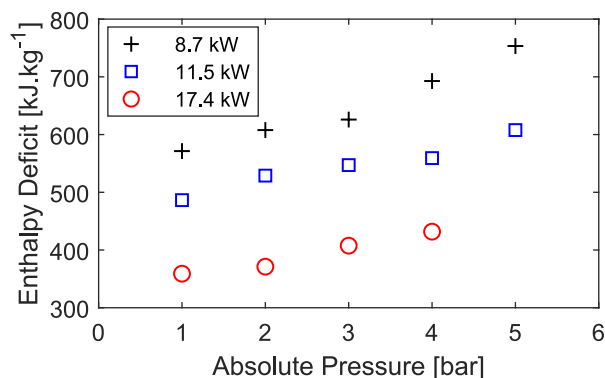


Fig. 3. Enthalpy deficits based on measured coflow temperatures, for coflows with three different heat inputs at operating pressures from 1 to 5 bar(a).

in Table 1. It is worth noting that, although Fig. 3 shows that the operating temperature tends to decrease with increasing pressure if the heat input is held constant, it is possible to exploit the large thermal mass of the system to maintain quasi-constant temperature for the short duration of each individual measurement at different pressures. This is useful as it enables the effect of pressure to be examined for a coflow of constant momentum. Some interesting changes in flame structure and stability with increasing pressure can be seen from the chemiluminescence imaging results in Fig. 4. For the $Re_{jet} = 10,000$ case at near-atmospheric pressure (i.e. at 1.1 bar), the flame can be seen to be slightly lifted from the jet exit, by approximately half a jet-diameter, based on the OH* image. It is worth noting that this behaviour is consistent with previous observations based on a flame of equivalent Re_{jet} , fuel mixture and coflow O₂ concentration in an open JHC burner [23]. At 2.0 bar, the flame again appears lifted at first glance; however, upon closer inspection a very faint flame front can be seen to extend to the jet exit. It should be noted that the images shown correspond to long exposure times (20 s in the case of the OH* images), such that it represents the mean rather than the instantaneous flame structure. The statistical features relating to flame liftoff and stabilisation are presented and analysed in §3.3, in addition to a series of short-exposure OH* images which are included in Fig. S1 of the Supplementary Material.

The $Re_{jet} = 15,000$ case displays a similar behaviour to the $Re_{jet} = 10,000$ case at 2.0 bar in Fig. 4, although the faint region appears to extend further downstream for the higher Re_{jet} case. At 1.1 bar, the $Re_{jet} = 15,000$ case shows a significant departure, with a less clearly defined flame structure and lift-off location in the near-field which suggests a change in flame stability; this is explored further in §3.3. Interestingly, the 10,000 and 15,000 Re_{jet} flames studied in the open JHC burner both exhibited similar structures, with no noticeable change in stability or lift-off in the near-field [23]. It should be mentioned that the CP-JHC flames presented in Fig. 4 correspond to an approximately 75 K lower coflow temperature to that of the JHC, as well as an increased coflow velocity. These differences—in addition to the absence of entrainment of surrounding air in the confined configuration—are likely responsible for the increased sensitivity to Re_{jet} . For $P > 2.0$ bar, a shift to a flame that is stabilised at the jet exit can be seen for both the 10,000 and 15,000 Re_{jet} cases; this is evident from both the OH* and CH* images.

In general, the OH* and CH* imaging results both show a similar flame structure for the various cases, with a consistent jet spreading angle of $\approx 7^\circ$ from the jet centreline. It is, however, important to note the change in intensity of the images at different pressures shown in Fig. 4. Specifically, a reduction in intensity with increasing pressure is apparent for both the OH* and CH* imaging results in Fig. 4, with a particularly noticeable shift from 2.0 to 3.5 bar for both Reynolds numbers. This is also evident for the $Re_{jet} = 10,000$, 7 bar case, which displays very faint CH* and OH* signals which are difficult to distinguish from the background. Interestingly, the $Re_{jet} = 15,000$ case at 7 bar shows a stronger signal, and there does not appear to be a significant reduction in intensity from 3.5 to 7 bar for the higher Re_{jet} flames. This suggests that changes due to flow effects and flame stability have at least a partial impact on the chemiluminescence detected, although the much stronger signal at 1.1 and 2 bar hints at a fundamental change in behaviour at elevated pressures. The change in chemical kinetics behaviour with increasing pressure is examined in §3.5.

3.3. Statistical analysis of short-exposure images

The statistical behaviour of the flames can be examined in greater detail by analysing the short-exposure CH* images. A series of greater than 200 video frames for each case were included in the analysis, enabling the calculation of the mean and variation in the liftoff height. An adaptive thresholding algorithm was applied to each individual frame, which effectively isolates the flame base such that the liftoff height can be determined. This process, in-turn, enables the mean location of the liftoff height (x_{-L}^*) above the jet exit to be calculated, as

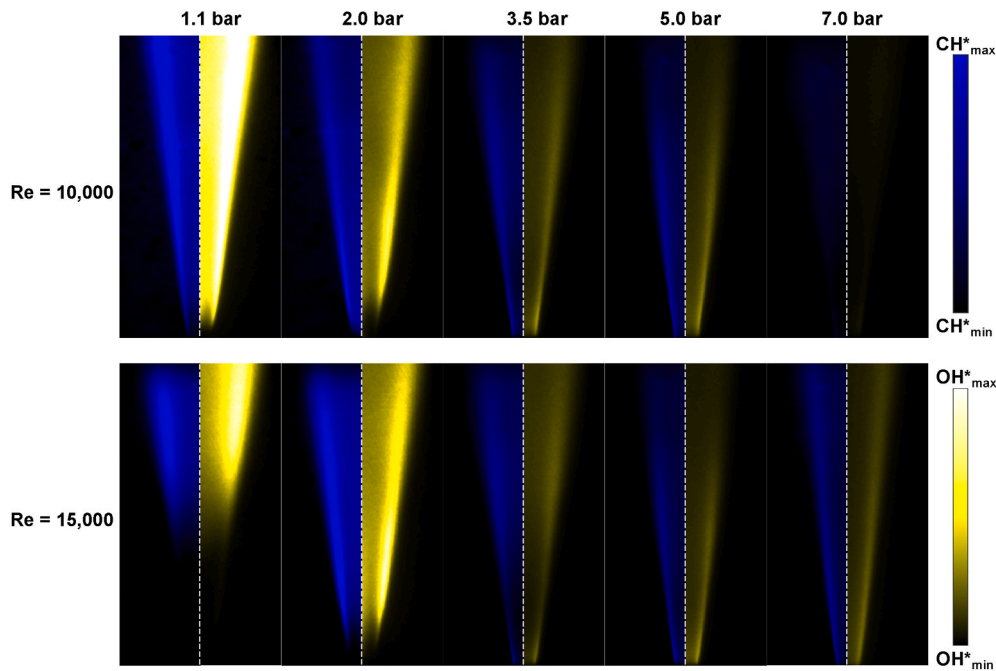


Fig. 4. Chemiluminescence imaging of 10,000 and 15,000 Reynolds number CH_4/H_2 flames (1:1 blend) at 5 different operating pressures, showing CH^* (left) and OH^* (right). All flames correspond to a 9% O_2 coflow and a nominal coflow temperature of 1025 K (± 25 K). Note: jet exit is located at the bottom of the images, issuing towards the top, and each photograph is 4 jet diameters (18.4 mm) in width and 13 jet diameters (59.5 mm) in height.

well as the standard deviation. These results are plotted as a function of pressure in Fig. 5, with the standard deviation (σ_L) about the mean represented by the vertical bars; these and the mean values are also included in Table 2. The minimum and maximum liftoff heights (following removal of outliers) from the series of images are also displayed in Fig. 5 on the same set of axes.

In the discussion surrounding the mean images shown in Fig. 4, the lack of a clearly defined flame base for the $Re_{jet} = 15,000$, 1.1 bar case was noted. The statistical results shown in Fig. 5 and Table 2 confirm the hypothesis that this is related to fluctuations in the liftoff height, with this case displaying not only an increased liftoff height, but significantly greater variation in this value in comparison to the other cases. This is also evident in the short-exposure (1–2.5 ms) OH^* images which may be found in Fig. S1 of the Supplementary Material. It has previously been observed that flames in the transition from the attached to the lifted regimes can show a sudden change in liftoff location with changes in the jet and coflow velocity [45], so it is possible that small fluctuations in the relative velocity are responsible for the variability of the flame base. It has also been observed previously that inhomogeneities in the temperature profile can have a significant effect on the liftoff height of JHC

Table 2

Standard deviation values of liftoff height based on CH^* video frames.

P [bar]	$\sigma_L[x/D]$		$\bar{x}_L[x/D]$	
	$Re_{jet} = 10k$	$Re_{jet} = 15k$	$Re_{jet} = 10k$	$Re_{jet} = 15k$
1.1	0.35	2.4	1.5	5.5
2.0	0.21	0.23	0.88	0.90
3.5	0.06	0.40	0.32	0.50
5.0	0.03	0.06	0.04	0.14
7.0	–	0.02	–	0.02

flames [46], which could also be responsible for this variability. Regardless of the mechanism, it can be seen that increasing the pressure from 1.1 to 2 bar has a significant effect for the $Re_{jet} = 15,000$ flames, with the 2 bar case displaying a very similar liftoff behaviour to the corresponding $Re_{jet} = 10,000$ flame. As the pressure is increased beyond 2 bar, the flames become stabilised at the jet exit, with a tendency for less fluctuation in the flame base; again, the instantaneous OH^* images shown in Fig. S1 support this. This change in stabilisation with pressure

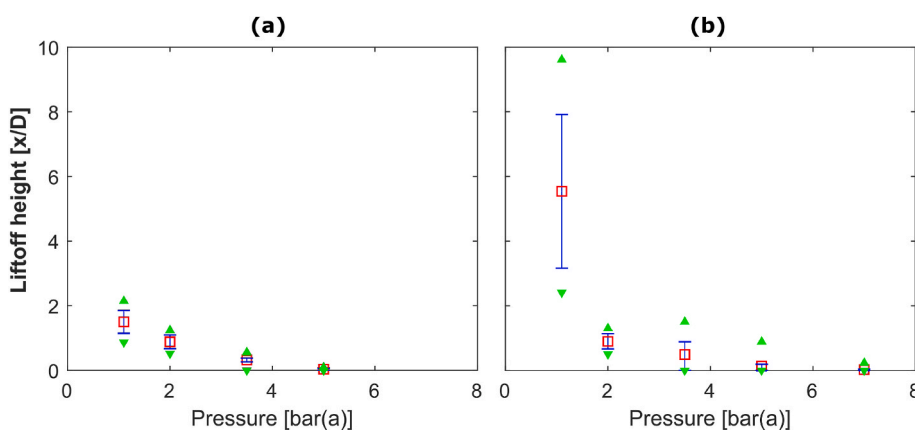


Fig. 5. Mean liftoff height (indicated by red boxes) as a function of pressure for $Re_{jet} = 10,000$ (a) and $Re_{jet} = 15,000$ (b) flames, with vertical bars representing the standard deviation from the mean. Minimum and maximum liftoff heights from the series of images are also shown by the green markers, noting that the same axis limits are used for subfigures (a) and (b). Statistical values were calculated from a series of > 200 CH^* video frames for each case. (For interpretation of the references to colour in this figure legend, the reader is referred to the Web version of this article.)

can be explained by the reduced velocity of the fuel stream at higher pressures, since velocity is inversely proportional to pressure for the flames with constant Re_{jet} .

3.4. Broadband flame imaging

To compare the broadband appearance of the flames at different pressures, true-colour images are shown in Fig. 6. These images correspond to jet flames with $Re_{jet} = 10,000$ and a coflow of 9% O_2 similar to Fig. 4, although with an increased coflow temperature of 1200 K. The typical flame photographs at $Re_{jet} = 15,000$ show very similar features and trends with pressure to those presented in Fig. 6 and are not included for brevity. All photographs were captured with an exposure time of 1/250 s in order to capture the turbulent sooting behaviour, and two photographs are shown for each operating pressure. Reduced ISO-speed settings on the camera were required to avoid saturation as the operating pressure was increased; these values are also displayed in the figure.

The true-colour images in Fig. 6 display a noticeable change in the sooting behaviour of the flames as the pressure is increased. For the 1.1 and 2.0 bar cases, a very faint blue/violet outline can be observed, while there is no evidence of soot formation. The lack of soot at 1.1 bar is consistent with observations for similar flames at atmospheric pressure, whereby soot formation is suppressed within the coflow-controlled region (which extends approximately 120 mm from the jet exit); this is true for flames of 1:1 NG:H₂ [23] as well as for unblended NG in a 9% O_2 coflow [47]. Notably, soot can be seen to form well within this region for the 5.0 and 7.0 bar cases shown in Fig. 6, which is a significant departure from the behaviour observed for low-pressure flames, particularly considering the fuel mixture being used. This is likely a result of a shift towards pyrolytic reactions at elevated pressure, which is examined further via laminar flame simulations in §3.5.

3.5. Laminar flame simulation results

To determine whether the changes in chemiluminescence intensity (§3.2) and sooting behaviour (§3.4) are a result of mixing/flow-field effects or purely chemical phenomena, laminar opposed-flow simulations were performed. Although the OH* and CH* sub-mechanisms that were used in the simulations are tailored for atmospheric-pressure combustion, they can be implemented in combination with the underlying kinetics mechanism, which is valid for elevated pressures. This facilitates comparisons against the experimental chemiluminescence results, to assess the suitability of the model in regard to predicting the underlying trends with increasing pressure. Fig. 7 displays the variation in the mass fraction of both OH* and CH* as a function of pressure, with strain rate held constant for the different pressures. Both the maximum

and integrated values over the simulation domain are shown in Fig. 7, in order to account for the narrowing of the reaction zone as pressure is increased.

Both OH* and CH* show a noticeable reduction with pressure based on the simulation results presented in Fig. 7. The reduction is particularly pronounced at lower pressures, in particular for the integrated OH* values up to $P \approx 3.0$ bar, at which point the mass fraction is reduced by a factor of 10 from the atmospheric-pressure value, after which further increases in pressure appear to be less significant. This generally supports the experimental observations, in which the most noticeable

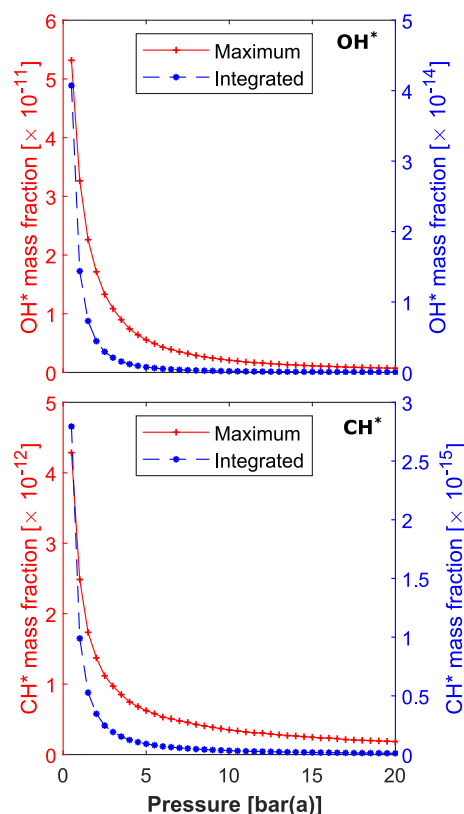


Fig. 7. Variation in OH* (top) and CH* (bottom) for pressures ranging from 0.5 to 20 bar(a). Results are shown for the maximum mass fraction (in red) and integrated mass fraction (in blue) over the simulation domain. (For interpretation of the references to colour in this figure legend, the reader is referred to the Web version of this article.)

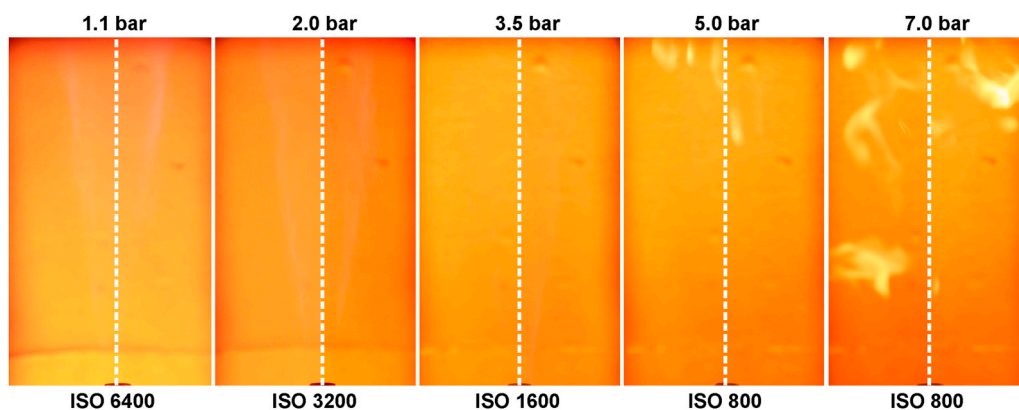


Fig. 6. True-colour images of $Re_{jet} = 10,000$ CH₄/H₂ flames (1:1 blend) at 5 different operating pressures. All flames correspond to a 9% O_2 coflow and heat input of 15 kW. Note that a constant exposure time and aperture were used, and each photograph has a width of 5 jet diameters (23 mm) and height of 17 jet diameters (78 mm). (For interpretation of the references to colour in this figure legend, the reader is referred to the Web version of this article.)

reduction in intensity was from 1.1 to 3.5 bar, although the 7 bar case was also seen to be of significantly lower intensity for the $Re_{jet} = 10,000$ case. The fact that there is a monotonic decrease in both the maximum and integrated values indicates that this reduction is not a direct consequence of a narrowing of the reaction zone, suggesting instead that it could be related to a change in the consumption and/or formation pathways as the pressure is increased. For OH^* , this can be investigated by studying the rates of the two reactions which lead to OH^* formation—that is, R1 and R2 (§2.3)—as a function of pressure, as shown in Fig. 8 (see Fig. 9)

The plots shown in Fig. 8 show that reaction R2 is the main contributor to OH^* formation at all pressures (in terms of both the maximum and mean formation rate), although R1 becomes more significant as the pressure is increased. Despite the clear reduction in the OH^* mass fraction with pressure shown in Fig. 7, the maximum formation rate is seen to increase with pressure for both reactions; this is also the case for the mean rate of R1, while the mean rate of R2 shows a non-monotonic behaviour. These results indicate that, although the pressure does have an impact on the OH^* formation pathways, this does not explain the reduced mass fractions observed in Fig. 7. It is important to note that, due to the short-lived nature of excited-state radicals such as OH^* in a flame, the formation rate does not completely capture the overall behaviour in terms of the steady-state species concentrations. Therefore, it is important to understand the total or net rate of production (ROP), which in this analysis includes both formation and consumption (largely due to collisional quenching). The trends in net ROP as a function of pressure are shown in Fig. 9, along with the values of heat release rate (HRR) and OH^* concentration ($[OH^*]$), noting that the mass fraction and not the concentration was shown in Fig. 7. As mentioned in §2.3, the spontaneous emission process and associated relaxation to the ground state was included in the OH^* sub-mechanism; this emission rate is also shown in Fig. 9. To facilitate comparison in terms of the trends with pressure, all of the values are normalised against their respective maxima across all pressures in Fig. 9. It should also be mentioned that the HRR values correspond to specific (i.e. density-normalised) heat release, to account for the increased mass flow as the pressure is increased.

The normalised values shown in Fig. 9 provide a number of interesting insights regarding the chemiluminescence behaviour. First of all, it is worth noting that the plots for the OH^* decay rate and the OH^* concentration are essentially coincident, both in terms of the maximum and integrated values; this is expected, since a constant rate coefficient was prescribed for reaction R5. The increase in the maximum OH^* concentration at low pressures ($P \leq 1.5$) suggests that there are

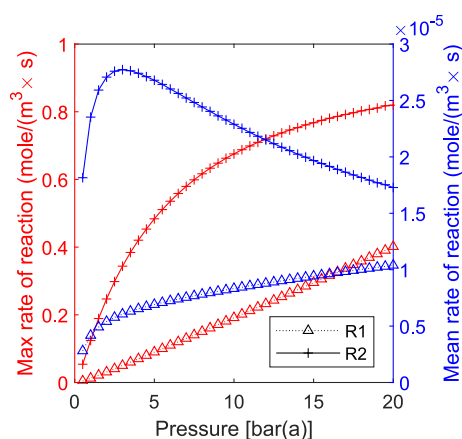


Fig. 8. Variation in the formation rates of OH^* for pressures ranging from 0.5 to 20 bar(a). Results are shown for the maximum rates (in red) and mean rates (in blue), with the contribution from R1 and R2 shown separately. (For interpretation of the references to colour in this figure legend, the reader is referred to the Web version of this article.)

competing effects taking place in terms of the effect of pressure, noting that higher peak values of species concentrations are expected as the pressure is increased due to the narrowing of the reaction zone and the increase in density. This initial increase with pressure can also be seen for the maximum and integrated net ROP values, with the maximum ROP showing a significant increase up to approximately 7 bar and then decreasing slightly, while the integrated ROP only shows a slight increase from 0.5 to 1.0 bar. Interestingly, the maximum OH^* concentration and the integrated ROP both show a similar trend with pressure. Since the formation rates show a general increase with pressure (at least for lower pressures in the case of R2) as shown in Fig. 8, it follows that the more rapid reduction in the net ROP—and the corresponding reduction in $[OH^*]$ —is related to the increased impact of collisional quenching at higher pressures. Indeed, the mixture-fraction-space profiles of formation and consumption—included in Figs. 2 and 3 of the Supplementary Material—show that an increase in formation is accompanied by an increase in consumption via quenching, which ultimately leads to a reduction in the net ROP at elevated pressures.

The normalised plots of specific heat release rate shown in Fig. 9 are also important to analyse, since chemiluminescence is commonly used as a practical method of indicating heat release. While the maximum HRR is seen to increase with pressure, the integrated values—which essentially represent the total heat release across the 1-D flame zone—show a reduction with pressure due to the narrowing of the reaction zone. It can also be seen that the integrated OH^* concentration shows a similar trend with pressure to HRR, although the former shows a more rapid reduction. These results highlight the importance of understanding the effects of pressure on chemiluminescence, particularly in terms of developing a quantitative relationship between chemiluminescence and HRR. It is also worth noting that it has previously been observed that changes in heat release rate with pressure are heavily dependent on flow characteristics, particularly when comparing the behaviour of laminar and turbulent flames [48]. Therefore, further efforts in developing the relationship between chemiluminescence and HRR should consider these effects, which can be achieved using both computational fluid dynamics (CFD) and more detailed experimental measurements via laser diagnostics, for example.

In the photographs shown in Fig. 6, it was observed that there is a significant increase in soot formation near the jet exit as the pressure is increased. Although the detailed chemistry relating to soot formation was not modelled in the simulations, it is possible to analyse the presence of regions of negative heat release; these regions are indicative of pyrolysis within the flame, which leads to the production of soot precursors [4]. Mixture-fraction-space profiles of net HRR are shown in Fig. 10, for five different pressures ranging from 1 to 7 bar(a). At 1 bar (a), two distinct positive peaks are observed in the heat release profile, which is typical of combustion with a high-temperature oxidant stream [4]. As the pressure is increased, this dual-peak behaviour is suppressed, with the cases at 5 and 7 bar(a) displaying a “shoulder” feature rather than a distinct secondary peak. The reaction-specific plots—which are included in the Supplementary Material for 1 and 7 bar(a)—show that this is due to an increase in the spatial overlap between the exothermic reactions as the pressure is increased, accompanied by a general narrowing of the positive heat release region. This is accompanied by an increased tendency for negative heat release as the pressure is increased, both in terms of net HRR and the reaction-specific profiles.

The results of these laminar flame simulations highlight the importance of understanding the effect of pressure on combustion under hot and low- O_2 conditions. The narrowing of the reaction zone and reduced chemical time-scales which occur with increasing pressure appears to promote a transition away from features typically associated with the mild combustion regime, such as a broadening of the OH profile and an absence of negative heat release regions [4]. The chemiluminescence behaviour is shown to be particularly sensitive to pressure, with both the OH^* and CH^* maximum and integrated mass fractions displaying a monotonic reduction with pressure. Further analysis of the OH^*

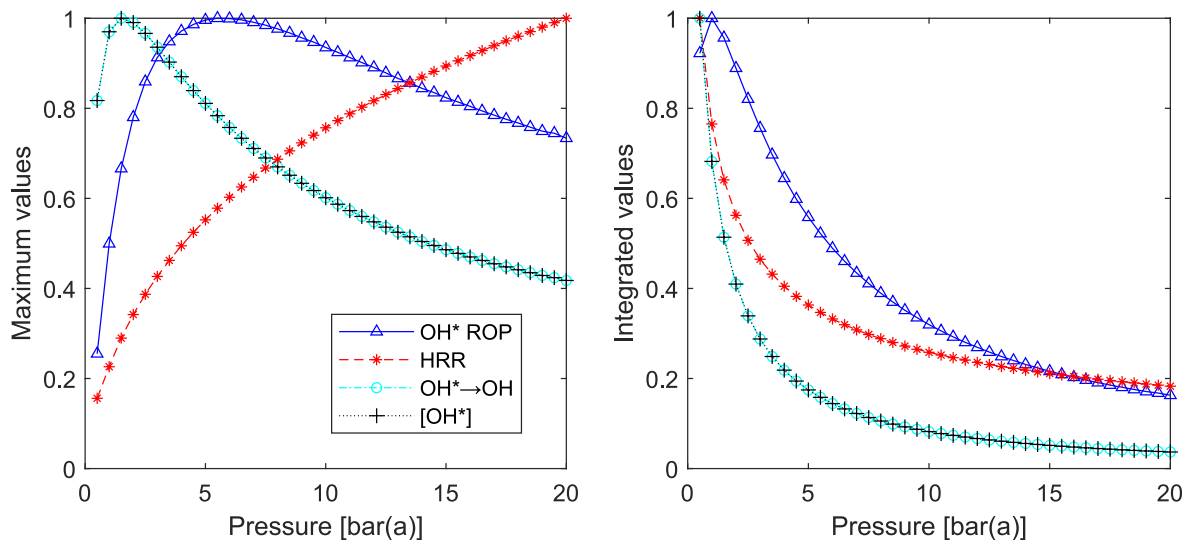


Fig. 9. Normalised results displaying OH^* concentration and spontaneous decay rate, as well as net ROP and heat release rate (HRR), for pressures ranging from 0.5 to 20 bar(a). Results are shown for the maximum values (left) and integrated values (right). Note that for ROP, the integrated values are calculated over the regions of positive net ROP only.

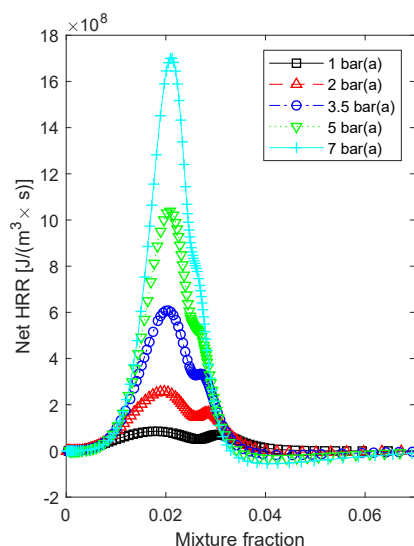


Fig. 10. Profiles of net HRR as a function of mixture fraction, for pressures ranging from 1 to 7 bar(a).

formation reactions and net ROP rates suggests that there are competing effects present leading to non-monotonic trends, particularly at lower pressures. Furthermore, the analysis indicates that the general reduction in OH^* with pressure is due to a combination of a shift in the formation pathways and an increased impact of collisional quenching at elevated pressures. These findings are particularly important for informing future research directions, which will involve extending the 1-D simulations to a more realistic CFD model with geometry and flow conditions matching those of the CP-JHC.

4. Conclusions

The characteristics of confined-and-pressurised, turbulent jet flames have been investigated, using a novel burner configuration which facilitates the control of coflow conditions. The CP-JHC enables the parametric analysis of the effects of coflow temperature and oxygen

concentration, as well as turbulent and chemical timescales and how these change with elevated pressure. A detailed description of the key features and capabilities of the apparatus has been provided in this paper. Temperature measurements of the coflow stream indicate an increase in enthalpy deficit as the pressure is increased, due to increased heat losses to the combustor walls. Turbulent jet flames of NG/ H_2 were examined in terms of both targeted chemiluminescence and broadband imaging. Changes in flame stability were observed for variations in both Reynolds number and pressure, with an increased tendency for flame attachment at elevated pressures, as well as a reduction in OH^* and CH^* and an increase in soot formation.

The effect of pressure on the chemiluminescence behaviour and heat release rate was examined numerically via laminar flame simulations, which highlighted a fundamental change in behaviour at elevated pressures. In particular, both the OH^* and CH^* mass fractions were observed to show a reduction with pressure in line with the experimental observations, suggesting that the atmospheric-pressure chemiluminescence sub-mechanisms can provide at least a qualitative indication of the trends with increasing pressure. Further analysis in regards to the OH^* behaviour indicates that this reduction is related to an increase in collisional quenching, which counteracts the increase in the rate of formation at lower pressures. Additionally, a narrowing of the reaction zone and a more prominent negative heat release region is observed with pressure, highlighting the challenges associated with the adoption of mild combustion in practical configurations such as gas turbines. This in-turn emphasises the need for further investigation into the fundamental combustion behaviour under such conditions, which the CP-JHC apparatus will facilitate.

Declaration of competing interest

The authors declare that they have no known competing financial interests or personal relationships that could have appeared to influence the work reported in this paper.

Acknowledgements

The authors would like to acknowledge the multitude of individuals and groups who have contributed to the design, construction and commissioning of the CP-JHC apparatus. While it is not possible to mention each of the contributors by name, the design team of Michael

De Duonni, Jakeob Clarke-Kennedy, Luke Ross, and Tomas Zott deserve particular recognition. Thanks also go to Chan Han Zheng, Haoling Li, Kiing Yean Wong, and Yong Sern Chee for their experimental efforts in characterising the coflow behaviour, and to Ian Shaw and Jordan Kildare for their assistance during data collection. Finally, the generous financial support from the Australian Research Council (ARC), the United States Asian Office for Aerospace Research and Development (AOARD), the Future Fuels Cooperative Research Centre (FF-CRC), and the Australian Government Research Training Program Scholarship (RTPS) is gratefully acknowledged.

Appendix A. Supplementary data

Supplementary data to this article can be found online at <https://doi.org/10.1016/j.joei.2022.07.007>.

References

- [1] A. Perpignan, A. Gangoli Rao, D. Roekaerts, Flameless combustion and its potential towards gas turbines, *Prog. Energy Combust. Sci.* 69 (2018) 28–62.
- [2] J.A. Wünnig, J.G. Wünnig, Flameless oxidation to reduce thermal NO-formation, *Prog. Energy Combust. Sci.* 23 (1) (1997) 81–94.
- [3] A. Cavaliere, M. de Joannon, Mild Combustion, *Progress in Energy and Combustion Science* 30, 2004, pp. 329–366, 4.
- [4] M. de Joannon, P. Sabia, G. Cozzolino, G. Sorrentino, A. Cavaliere, Pyrolytic and oxidative structures in hot oxidant diluted oxidant (HODO) MILD combustion, *Combust. Sci. Technol.* 184 (7–8) (2012) 1207–1218, <https://doi.org/10.1080/00102202.2012.664012>.
- [5] F. Joos, P. Brunner, B. Schulte-Werning, K. Syed, A. Eroglu, Development of the Sequential Combustion System for the ABB GT24/GT26 Gas Turbine Family, in: Volume 4: Heat Transfer; Electric Power; Industrial and Cogeneration, AMSE, Birmingham, UK, 1996.
- [6] D. Ballal, J. Zelina, Progress in aeroengine technology (1939–2003), *J. Aircraft* 41 (1) (2004) 43–50.
- [7] F. Güthe, J. Hellat, P. Flohr, The reheat concept: the proven pathway to ultralow emissions and high efficiency and flexibility, *J. Eng. Gas Turbines Power* 131 (2) (2009).
- [8] Y. Levy, V. Erenburg, V. Sherbaum, I. Gaissinski, Flameless oxidation combustor development for a sequential combustion hybrid turbofan engine, in: ASME Turbo Expo 2016: Turbomachinery Technical Conference and Exposition, AMSE Digital Collection, 2016.
- [9] A.a.v. Perpignan, A.G. Rao, Effects of chemical reaction mechanism and NOx formation pathways on an inter-turbine burner, *Aeronaut. J.* 123 (1270) (2019) 1898–1918.
- [10] J. Ye, P. Medwell, E. Varea, S. Kruse, B. Dally, H. Pitsch, An experimental study on MILD combustion of prevaporised liquid fuels, *Appl. Energy* 151 (2015) 93–101.
- [11] V. Nori, J. Seitzman, Evaluation of chemiluminescence as a combustion diagnostic under varying operating conditions, in: 46th AIAA Aerospace Sciences Meeting and Exhibit, American Institute of Aeronautics and Astronautics. doi:10.2514/6.2008-953.
- [12] B. Higgins, M.Q. McQuay, F. Lacas, J.C. Rolon, N. Darabiha, S. Candel, Systematic measurements of OH chemiluminescence for fuel-lean, high-pressure, premixed, laminar flames, *Fuel* 80 (1) (2001) 67–74, [https://doi.org/10.1016/S0016-2361\(00\)00069-7](https://doi.org/10.1016/S0016-2361(00)00069-7).
- [13] S. Sardeshmukh, M. Bedard, W. Anderson, The use of OH* and CH* as heat release markers in combustion dynamics, *Int. J. Spray Combust. Dyn.* 9 (4) (2017) 409–423, <https://doi.org/10.1177/1756827717718483>.
- [14] W. Boyette, A. Elbaz, T. Guiberti, W. Roberts, Experimental investigation of the near field in sooting turbulent nonpremixed flames at elevated pressures, *Exp. Therm. Fluid Sci.* 105 (2019) 332–341, <https://doi.org/10.1016/j.exthermfluidsci.2019.04.008>.
- [15] K. Young, C. Stewart, J. Moss, Soot formation in turbulent nonpremixed kerosene-air flames burning at elevated pressure: experimental measurement, *Symp. (Int.) on Combust.* 25 (1) (1994) 609–617, [https://doi.org/10.1016/S0082-0784\(06\)80692-2](https://doi.org/10.1016/S0082-0784(06)80692-2).
- [16] W. Boyette, T. Guiberti, G. Magnotti, W. Roberts, Structure of turbulent nonpremixed syngas flames at high pressure, *Proc. Combust. Inst.* 37 (2) (2019) 2207–2214, <https://doi.org/10.1016/j.proci.2018.09.004>.
- [17] R. Lücklerath, W. Meier, M. Aigner, FLOX[®] combustion at high pressure with different fuel compositions, *J. Eng. Gas Turbines Power* 130 (1) (2008), 011505, <https://doi.org/10.1115/1.2749280>.
- [18] H. Schütz, R. Lücklerath, T. Kretschmer, B. Noll, M. Aigner, Analysis of the pollutant formation in the FLOX[®] combustion, *J. Eng. Gas Turbines Power* 130 (1) (2008), <https://doi.org/10.1115/1.2747266>.
- [19] J.M. Fleck, P. Griebel, A.M. Steinberg, C.M. Arndt, M. Aigner, Auto-ignition and flame stabilization of hydrogen/natural gas/nitrogen jets in a vitiated cross-flow at elevated pressure, *Int. J. Hydrogen Energy* 38 (36) (2013) 16441–16452, <https://doi.org/10.1016/j.ijhydene.2013.09.137>.
- [20] O. Schulz, N. Noiray, Combustion regimes in sequential combustors: flame propagation and autoignition at elevated temperature and pressure, *Combust. Flame* 205 (2019) 253–268, <https://doi.org/10.1016/j.combustflame.2019.03.014>.
- [21] F. Guethe, D. Guyot, G. Singla, N. Noiray, B. Schuermans, Chemiluminescence as diagnostic tool in the development of gas turbines, *Appl. Phys. B* 107 (3) (2012) 619–636, <https://doi.org/10.1007/s00340-012-4984-y>.
- [22] B. Dally, A. Karpets, R. Barlow, Structure of turbulent non-premixed jet flames in a diluted hot coflow, in: Proceedings of the Combustion Institute, 29, 2002, pp. 1147–1154, 1.
- [23] P. Medwell, P. Kalt, B. Dally, Simultaneous imaging of OH, formaldehyde, and temperature of turbulent nonpremixed jet flames in a heated and diluted coflow, *Combust. Flame* 148 (1–2) (2007) 48–61.
- [24] R. Cabra, T. Myhrvold, J. Chen, R. Dibble, A. Karpets, R. Barlow, Simultaneous laser Raman-Rayleigh-LIF measurements and numerical modeling results of a lifted turbulent H₂/N₂ jet flame in a vitiated coflow, *Proc. Combust. Inst.* 29 (2) (2002) 1881–1888.
- [25] R. Gordon, A. Masri, E. Mastorakos, Simultaneous Rayleigh temperature, OH- and CH₂O-LIF imaging of methane jets in a vitiated coflow, *Combust. Flame* 155 (1) (2008) 181–195.
- [26] G.P. Smith, D.M. Golden, M. Frenklach, N.W. Moriarty, B. Eiteneer, M. Goldenberg, C.T. Bowman, R.K. Hanson, S. Song, W.C.G. Jr, V.V. Lissianski, Z. Qin, GRI-Mech 3.0. <http://combustion.berkeley.edu/gri-mech/version30/text30.html>, 2000.
- [27] F.C. Christo, B.B. Dally, Modeling turbulent reacting jets issuing into a hot and diluted coflow, *Combust. Flame* 142 (1) (2005) 117–129, <https://doi.org/10.1016/j.combustflame.2005.03.002>.
- [28] M.J. Evans, P.R. Medwell, Z.F. Tian, Modeling lifted jet flames in a heated coflow using an optimized eddy dissipation concept model, *Combust. Sci. Technol.* 187 (7) (2015) 1093–1109.
- [29] S.R. Shabanian, P.R. Medwell, M. Rahimi, A. Frassoldati, A. Cuoci, Kinetic and fluid dynamic modeling of ethylene jet flames in diluted and heated oxidant stream combustion conditions, *Appl. Therm. Eng.* 52 (2) (2013) 538–554, <https://doi.org/10.1016/j.applthermaleng.2012.12.024>.
- [30] J.A.M. Sidey, E. Mastorakos, Simulations of laminar non-premixed flames of methane with hot combustion products as oxidiser, *Combust. Flame* 163 (2016) 1–11, <https://doi.org/10.1016/j.combustflame.2015.07.034>.
- [31] M. Ihme, Y. C. See, LES flamelet modeling of a three-stream MILD combustor: analysis of flame sensitivity to scalar inflow conditions, *Proc. Combust. Inst.* 33 (1) (2011) 1309–1317, <https://doi.org/10.1016/j.proci.2010.05.019>.
- [32] M. Ihme, Y. C. See, Prediction of autoignition in a lifted methane/air flame using an unsteady flamelet/progress variable model, *Combust. Flame* 157 (10) (2010) 1850–1862, <https://doi.org/10.1016/j.combustflame.2010.07.015>.
- [33] R.N. Roy, S. Kumar, S. Sreedhara, A new approach to model turbulent lifted CH₄/air flame issuing in a vitiated coflow using conditional moment closure coupled with an extinction model, *Combust. Flame* 161 (1) (2014) 197–209, <https://doi.org/10.1016/j.combustflame.2013.08.007>.
- [34] A. Kazakov, M. Frenklach, Reduced Reaction Sets based on GRI-Mech 1.2, <http://combustion.berkeley.edu/drm/>.
- [35] A. Parente, M.R. Malik, F. Contino, A. Cuoci, B.B. Dally, Extension of the Eddy Dissipation Concept for turbulence/chemistry interactions to MILD combustion, *Fuel* 163 (2016) 98–111, <https://doi.org/10.1016/j.fuel.2015.09.020>.
- [36] M.T. Lewandowski, Z. Li, A. Parente, J. Pozorski, Generalised Eddy Dissipation Concept for MILD combustion regime at low local Reynolds and Damköhler numbers. Part 2: validation of the model, *Fuel* 278 (2020), 117773, <https://doi.org/10.1016/j.fuel.2020.117773>.
- [37] N. Romero-Anton, X. Huang, H. Bao, K. Martin-Eskudero, E. Salazar-Herran, D. Roekaerts, New extended eddy dissipation concept model for flameless combustion in furnaces, *Combust. Flame* 220 (2020) 49–62, <https://doi.org/10.1016/j.combustflame.2020.06.025>.
- [38] A. De, E. Oldenhof, P. Sathiah, D. Roekaerts, Numerical simulation of delft-jet-in-hot-coflow (DJHC) flames using the eddy dissipation concept model for turbulence-chemistry interaction, *Flow, Turbul. Combust.* 87 (4) (2011) 537–567, <https://doi.org/10.1007/s10494-011-9337-0>.
- [39] C. Galletti, A. Parente, M. Derudi, R. Rota, L. Tognotti, Numerical and experimental analysis of NO emissions from a lab-scale burner fed with hydrogen-enriched fuels and operating in MILD combustion, *Int. J. Hydrogen Energy* 34 (19) (2009) 8339–8351, <https://doi.org/10.1016/j.ijhydene.2009.07.095>.
- [40] J.M. Hall, E.L. Petersen, An optimized kinetics model for OH chemiluminescence at high temperatures and atmospheric pressures, *Int. J. Chem. Kinet.* 38 (12) (2006) 714–724, <https://doi.org/10.1002/kin.20196>.
- [41] R.M.I. Elsamra, S. Vranckx, S.A. Carl, C.H. (A2Δ), formation in hydrocarbon combustion: the temperature dependence of the rate constant of the reaction C₂H + O₂ → CH(A²Δ) + CO₂, *J. Phys. Chem.* 109 (45) (2005) 10287–10293, <https://doi.org/10.1021/jp053684b>.
- [42] M. Tamura, P.A. Berg, J.E. Harrington, J. Luque, J.B. Jeffries, G.P. Smith, D. R. Crosley, Collisional quenching of CH(A), OH(A), and NO(A) in low pressure hydrocarbon flames, *Combust. Flame* 114 (3) (1998) 502–514, [https://doi.org/10.1016/S0010-2180\(97\)00324-6](https://doi.org/10.1016/S0010-2180(97)00324-6).
- [43] W.L. Dimpfl, J.L. Kinsey, Radiative lifetimes of OH(A²Σ) and Einstein coefficients for the A-X system of OH and OD, *J. Quant. Spectrosc. Radiat. Transf.* 21 (3) (1979) 233–241, [https://doi.org/10.1016/0022-4073\(79\)90014-1](https://doi.org/10.1016/0022-4073(79)90014-1).
- [44] Y. Liu, J. Tan, H. Wang, L. Lv, Characterization of heat release rate by OH* and CH* chemiluminescence, *Acta Astronaut.* 154 (2019) 44–51, <https://doi.org/10.1016/j.actaastro.2018.10.022>.
- [45] S.D. Terry, K.M. Lyons, Turbulent lifted flames in the hysteresis regime and the effects of coflow, *J. Energy Resour. Technol.* 128 (4) (2006) 319–324, <https://doi.org/10.1115/1.2358147>.

- [46] E. Oldenhof, M.J. Tummers, E.H. van Veen, D.J.E.M. Roekaerts, Role of entrainment in the stabilisation of jet-in-hot-coflow flames, *Combust. Flame* 158 (8) (2011) 1553–1563, <https://doi.org/10.1016/j.combustflame.2010.12.018>.
- [47] M. Evans, A. Chinnici, P. Medwell, J. Ye, Ignition features of methane and ethylene fuel-blends in hot and diluted coflows, *Fuel* 203 (2017) 279–289.
- [48] X. Wang, T. Jin, Y. Xie, K.H. Luo, Pressure effects on flame structures and chemical pathways for lean premixed turbulent H₂/air flames: three-dimensional DNS studies, *Fuel* 215 (2018) 320–329, <https://doi.org/10.1016/j.fuel.2017.10.094>.

Characteristics of turbulent flames in a confined and pressurised jet-in-hot-coflow combustor

Douglas B. Proud^{a,*}, Michael J Evans^{a,b}, Qing N Chan^c, Paul R Medwell^a

^a*School of Mechanical Engineering, The University of Adelaide, Adelaide, SA 5005, Australia*

^b*UniSA STEM, University of South Australia, Mawson Lakes, SA 5095, Australia*

^c*School of Mechanical and Manufacturing Engineering, University of New South Wales, Sydney, NSW 2052, Australia*

Supplementary Material

1. Short-exposure OH^* imaging

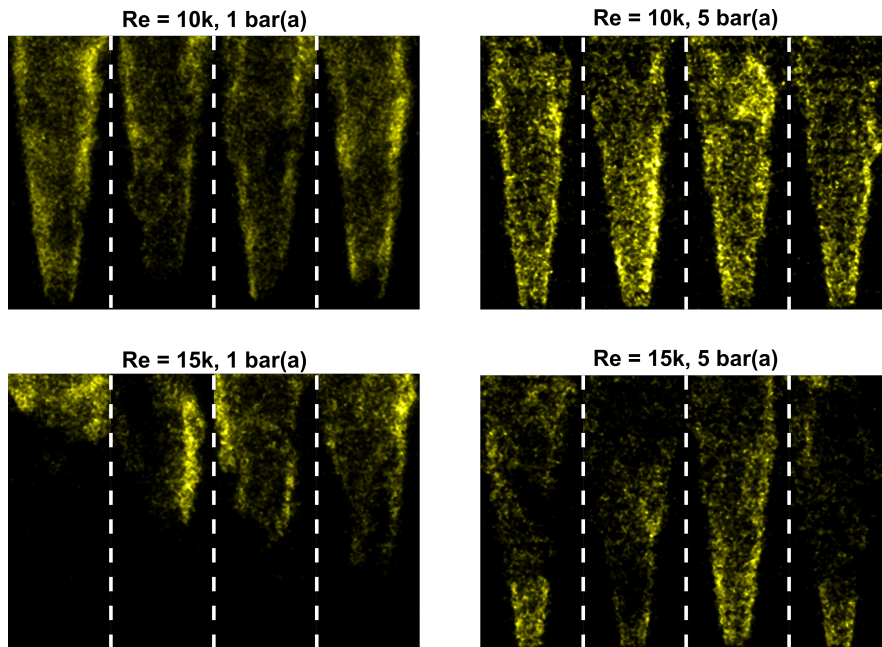


Figure 1: Short-exposure example images of OH^* for the 10,000 and 15,000 Reynolds number jet flames issuing into a 9% O_2 , 1025 K (± 25 K) coflow, at near-atmospheric pressure (1 bar(a)) and at 5 bar(a). Exposure time is 1 ms for the 1 bar(a) cases and 2.5 ms for the 5 bar(a) cases, due to the lower signal-to-noise ratio at elevated pressures.

*Corresponding author. E-mail: douglas.proud@adelaide.edu.au

2. OH* formation and consumption profiles

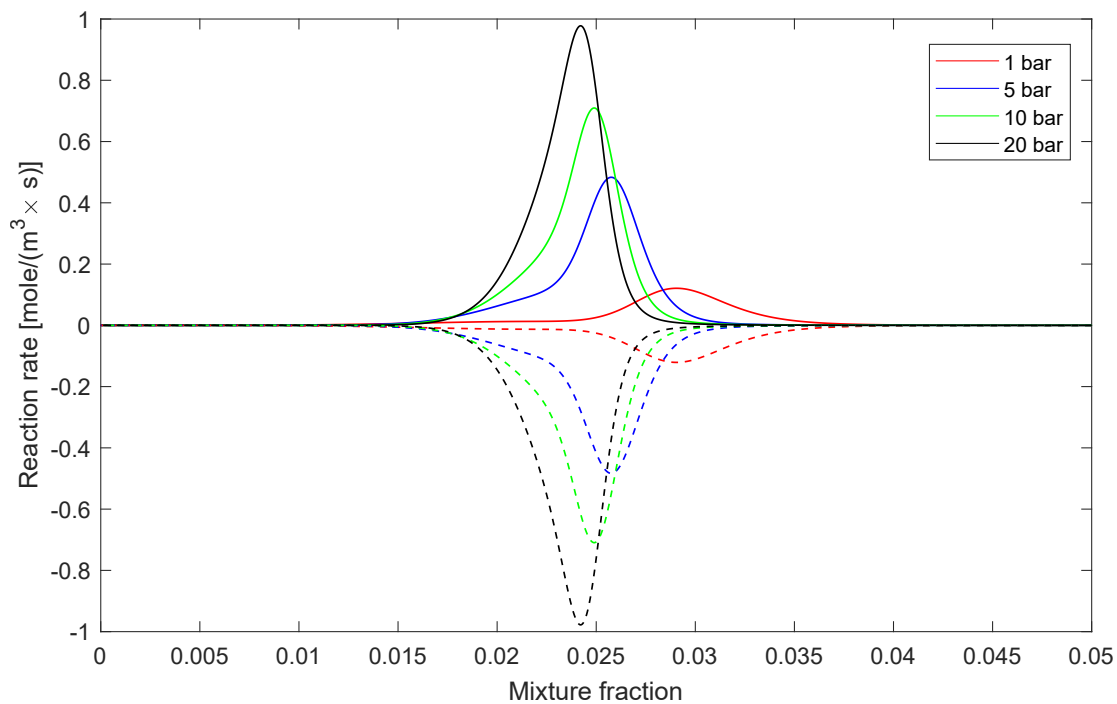


Figure 2: OH* total formation and quenching rates for pressures of 1, 5, 10 and 20 bar. Formation rates are shown as positive with solid lines, while quenching rates are shown as negative with dashed lines.

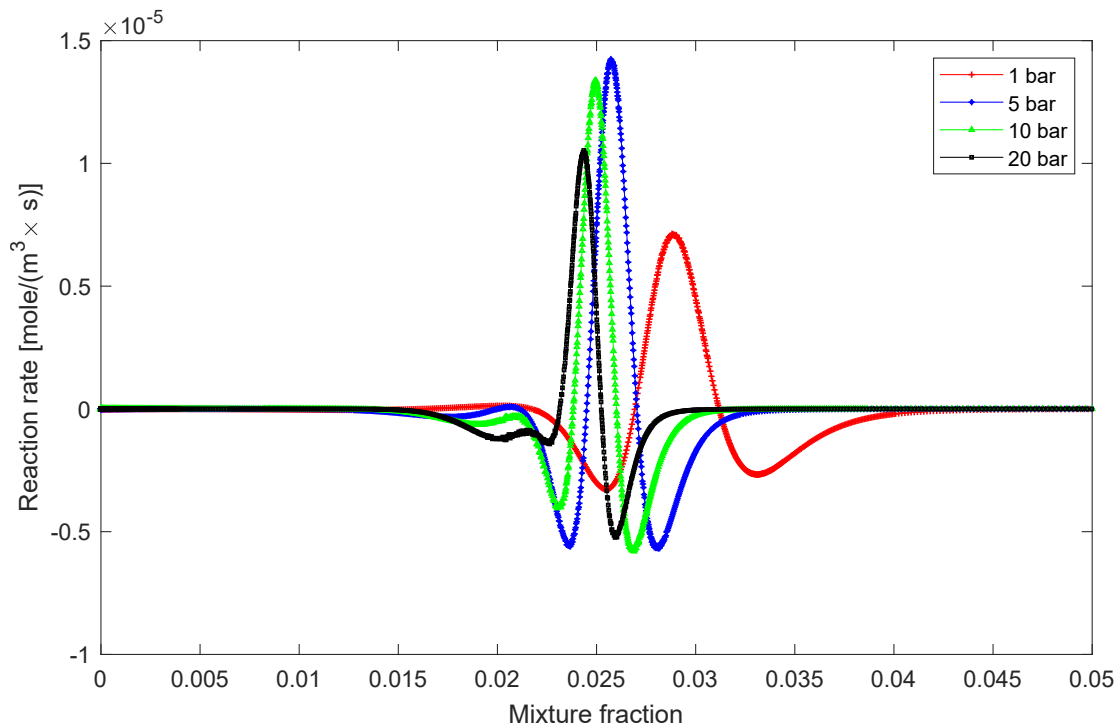


Figure 3: OH* total ROP from all reactions, shown for pressures of 1, 5, 10 and 20 bar.

3. Profiles of heat release for specific reactions

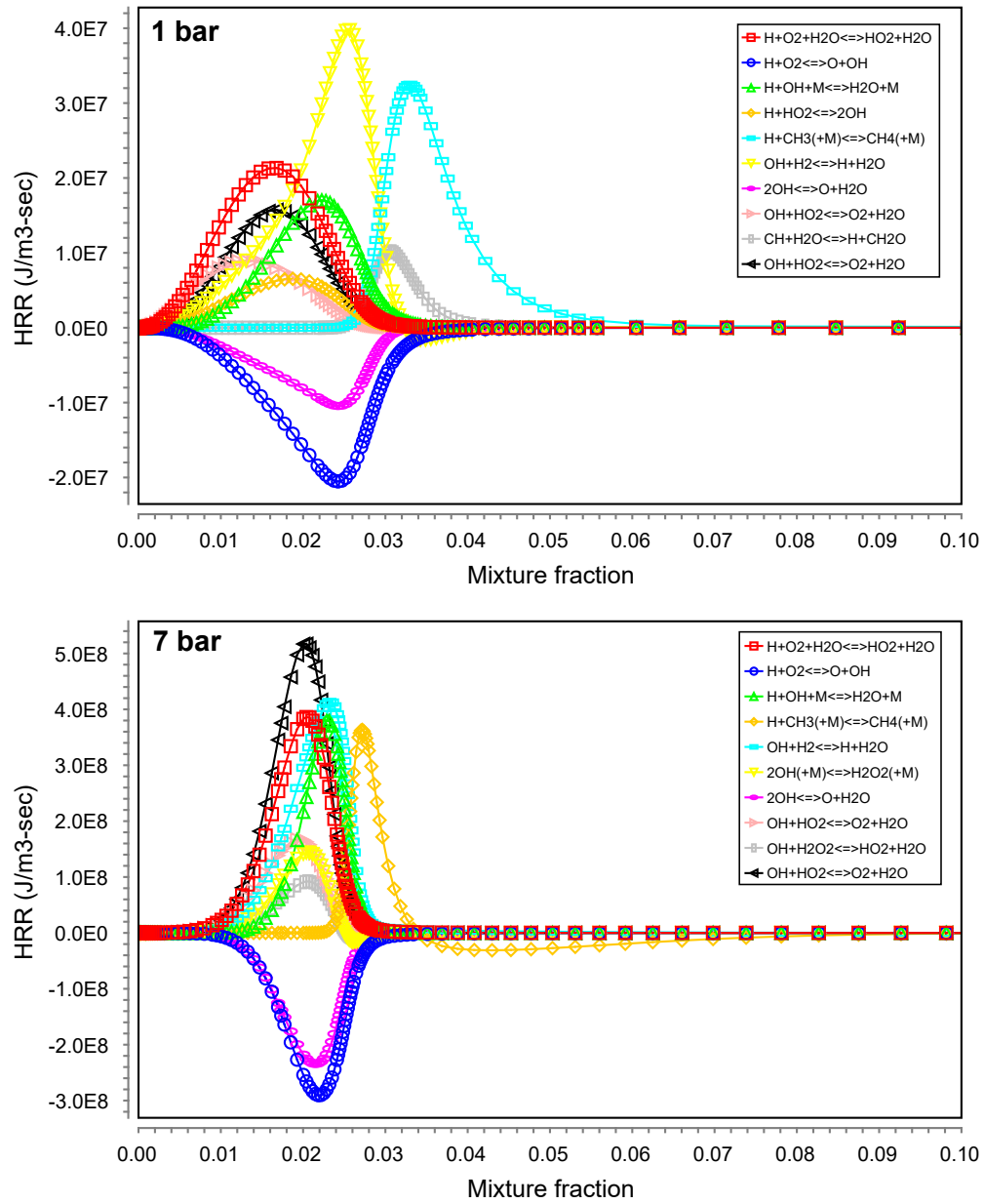


Figure 4: Profiles of heat release from individual reactions, for 1 bar and 7 bar.


Chapter 5

The Effects of Pressure and Oxygen Concentration on the Structure and Stability of Turbulent Flames

Statement of Authorship

Title of Paper	The effects of pressure and oxygen concentration on the structure and stability of turbulent flames.
Publication Status	<input type="checkbox"/> Published <input type="checkbox"/> Accepted for Publication <input checked="" type="checkbox"/> Submitted for Publication <input type="checkbox"/> Unpublished and Unsubmitted work written in manuscript style
Publication Details	D. B. Proud , M. J. Evans, J. A. Kildare, Q. N. Chan & P. R. Medwell. " The effects of pressure and oxygen concentration on the structure and stability of turbulent flames." Submitted Oct 2022 to: <i>Fuel</i> .


Principal Author


Name of Principal Author (Candidate)	Douglas B. Proud
Contribution to the Paper	Developed and executed an experimental plan for operating a pressurised combustion apparatus, collected data in the form of temperature measurements and filtered flame photography, and identified a range of boundary conditions/flame cases to be investigated. Generated a computational fluid dynamics (CFD) model to simulate the experimental cases, and performed the simulations. Also performed a series of 1-D laminar flame simulations to complement the CFD modelling. Processed, analysed, interpreted and compared the experimental and numerical data, generated figures from data and wrote manuscript.
Overall percentage (%)	75
Certification:	This paper reports on original research I conducted during the period of my Higher Degree by Research candidature and is not subject to any obligations or contractual agreements with a third party that would constrain its inclusion in this thesis. I am the primary author of this paper.
Signature	
Date	24-OCT-2022


Co-Author Contributions

By signing the Statement of Authorship, each author certifies that:

- i. the candidate's stated contribution to the publication is accurate (as detailed above);
- ii. permission is granted for the candidate to include the publication in the thesis; and
- iii. the sum of all co-author contributions is equal to 100% less the candidate's stated contribution.

Name of Co-Author	Michael J. Evans
Contribution to the Paper	Involved in initial design/commissioning of experimental apparatus, provided guidance to aid in the development of the CFD model, edited and provided feedback on manuscript.
Signature	
Date	17-Oct-2022

Name of Co-Author	Qing N. Chan
Contribution to the Paper	Involved in initial concept generation and supervised direction of the work. Provided feedback on manuscript relating to discussion and presentation of results.
Signature	
Date	21-10-2022

Name of Co-Author	Jordan A.C. Kildare		
Contribution to the Paper	Assisted with experimental data collection and provided feedback/editing of manuscript.		
Signature		Date	23-OCT-2022

Name of Co-Author	Paul R. Medwell		
Contribution to the Paper	Supervised the initial conception and construction of the experimental apparatus. Assisted in data collection and troubleshooting, oversaw the direction of the work, and provided feedback on manuscript (presentation of methods/results, discussion/interpretation).		
Signature		Date	17-OCT-2022

1 Pressurised combustion in hot and low-oxygen environments:
2 chemiluminescence imaging and modelling

3 D.B. Proud^a, M.J. Evans^{a,b}, J.A. Kildare^a, Q.N. Chan^c, P.R. Medwell^a

4 ^a*School of Mechanical Engineering, The University of Adelaide, Adelaide, SA 5005, Australia*

5 ^b*UniSA STEM, University of South Australia, Mawson Lakes, SA 5095, Australia*

6 ^c*School of Mechanical and Manufacturing Engineering, University of New South Wales, Sydney, NSW*
7 *2052, Australia*

8 **Abstract**

9 Turbulent flames in a confined and pressurised jet-in-hot-coflow combustor, under a range
10 of pressures and coflow conditions, are investigated in this study. The investigation in-
11 volves both experimental and numerical analyses, with the central focus on extending
12 the use of an atmospheric-pressure computational fluid dynamics (CFD) model to de-
13 scribe hot and low-oxygen combustion at elevated pressures. A series of CFD simulations
14 are compared against experimental images, in terms of both flame structure and chemi-
15 luminescence behaviour. The imaging of OH* and CH* is performed experimentally
16 for flames with Reynolds numbers of 10,000 and 15,000, issuing into coflows with O₂
17 concentrations ranging from 3–9%. The experimental results show a reduction in OH*
18 and CH* intensity with increasing pressure under the various coflow conditions, while
19 the CFD results display some key differences in the trends with pressure and O₂. The
20 computational analysis is complemented by a series of one-dimensional laminar flame
21 simulations at a range of pressures and oxidant O₂ concentrations. These simulations
22 enable the changes in chemical kinetics with pressure and O₂ concentration to be studied
23 in greater detail, and several key differences in comparison with the CFD results are
24 observed. Ultimately, the results highlight the importance of accurately predicting both
25 the flow-field and finite-rate chemistry to reproduce the trends observed under hot and
26 low-oxygen combustion conditions at elevated pressures.

27 *Keywords:* Elevated pressure combustion, Mild combustion, Turbulent flames

28 **1. Introduction**

29 Combustion at elevated pressures is encountered in a range of applications due to the
30 thermodynamic and practical advantages of burning fuels under such conditions. While
31 devices such as internal combustion engines and gas turbines have been continually opti-
32 mised for improved performance, there remain significant knowledge gaps relating to the
33 effects of pressure on the fundamental combustion phenomena which govern the perfor-
34 mance of these devices [1, 2, 3]. This is particularly true for “non-standard” combustion
35 regimes, such as those encountered under conditions associated with sequential combus-
36 tion [4] and exhaust gas recirculation (EGR) [5]. Not only can these techniques enable
37 improvements in thermal efficiency, they can also effectively reduce emissions of NO_x ,
38 CO and soot, while improving fuel flexibility if implemented correctly. With the growing
39 need to shift towards low-emissions and carbon-neutral fuels—such as hydrogen-based
40 and synthetic fuels—the understanding of these combustion phenomena is of paramount
41 importance.

42 The techniques of sequential combustion and EGR are closely related to the concept
43 of mild combustion. In this context, the term “mild” refers to a specific combustion
44 regime that is characterised by a highly diluted (i.e. low-oxygen) and high-temperature
45 oxidant stream [6]. Under these conditions, reactions proceed more slowly and with lower
46 peak temperatures, accompanied by the absence of distinct ignition and extinction events
47 that are associated with conventional combustion [7]. In practice, mild conditions are
48 typically achieved via dilution with exhaust gases—either via recirculation or by passing
49 the products from an initial combustor into a downstream reaction zone—this latter
50 technique can be referred to as sequential combustion. To date, most fundamental studies
51 of mild combustion have been performed in “open” burners operating at atmospheric
52 pressures. Many of these experiments have been carried out using so-called “jet-in-hot-
53 coflow” (JHC) burners [8, 9], or similar designs such as the “vitiated coflow” burner [10,
54 11]. In these burners, mild combustion conditions are achieved using an additional burner

*Corresponding author. E-mail: douglas.proud@adelaide.edu.au

55 upstream of the main combustion zone, with the primary fuel jet issuing into the hot and
56 low-oxygen coflow of combustion products, such that there are two distinct combustion
57 processes which happen sequentially. The advantage of the JHC and similar designs is
58 the fact that the upstream combustion zone can be controlled independently of the jet,
59 allowing the coflow properties, such as O₂ concentration and temperature, to be varied
60 while maintaining constant jet boundary conditions, such as Reynolds number and fuel
61 type, and vice-versa. On the other hand, studies of mild combustion at elevated pressures
62 generally involve more complex geometries, such that the separation of chemistry, mixing
63 and flow-field effects is not possible [12, 13]; this is a general limitation of many studies
64 of elevated-pressure combustion.

65 The effect of pressure on combustion phenomena has long been a topic of great interest
66 in the field of combustion science. Typically, combustion experiments involve a trade-off
67 between the level of detail of the results which can be obtained for the flames, and the
68 similarity to practical configurations, such as high pressures and realistic burner geome-
69 tries [14]. Consequently, investigations relating to confined environments and elevated
70 pressures are often focussed on the analysis of exhaust gases and pollutant emissions, for
71 example, rather than more fundamental aspects such as flame structure and stabilisation
72 [2]. While such studies at pressure have provided a wealth of knowledge to enable the
73 development of more efficient and reliable engine and gas turbine designs, a higher level
74 of understanding is necessary to produce more accurate and robust numerical models. It
75 should be noted that significant research efforts have been dedicated to obtaining data
76 for model validation under well-defined and engine-relevant conditions in recent years,
77 with much of this research being guided by the Engine Combustion Network (ECN), a
78 collaboration between experimentalists and computational modellers [15, 16]. This work
79 acts as an important link between purely performance-based experiments (for example,
80 measurements of power output and exhaust emissions) and the more fundamental ap-
81 proaches involving detailed measurements of relatively simple flames. These experiments
82 and their associated models are primarily concerned with the measurement and predic-

83 tion of parameters that are specific to internal combustion engine designs and concepts,
84 such as spray penetration and ignition delay [16]. As a result, the knowledge gained and
85 the validation data are not directly applicable to other high-pressure combustion config-
86 urations, such as those found in gas turbines, for example. Therefore, to further develop
87 modelling capabilities for such combustors—and to in-turn enable design improvements
88 in regards to operational and fuel flexibility—it is pertinent to obtain data relating to
89 flame structure and reaction zones under a range of boundary conditions.

90 It should also be mentioned that *in situ* measurements and reaction zone imaging
91 of flames at elevated pressures has indeed been performed. Recently, turbulent non-
92 premixed flames of CO/H₂/N₂ issuing into a coflow of air at pressures up to 12 bar
93 were investigated experimentally, with OH imaging revealing both a narrowing of the
94 reaction zone and a reduced probability of local extinction with increasing pressure [17].
95 Additional experiments based on a similar configuration were aimed at characterising
96 flame height for a range of fuel compositions, Reynolds numbers and pressures, with the
97 results suggesting that—in general—the prediction of flame height based on the well-
98 established “Delichatsios’ model” is valid at elevated pressure, with pressure having no
99 noticeable impact on flame height in the momentum-controlled region [18]. These exper-
100 iments have provided key insights pertaining to the change in combustion behaviour at
101 pressure, as well as enabling advances in modelling capabilities via validation datasets.
102 However, to further develop this understanding and to test the robustness of the mod-
103 els, a greater range of operating conditions is required. This includes combustion under
104 high-temperature and low-oxygen conditions, such as those encountered in sequential
105 combustors and EGR configurations.

106 Chemiluminescence imaging is a particularly useful diagnostic technique for burn-
107 ers featuring confinement and/or pressurisation, as it enables the investigation of flame
108 structure and reaction zone features through a single viewing window. It is also particu-
109 larly attractive from the perspective of implementation in practical combustion systems;
110 for example, flame detectors which rely on chemiluminescence have been developed [19],

111 with a major advantage being that such devices—particularly those which detect the
112 chemiluminescence via a photodiode—can be used in harsh environments (such as the
113 high temperatures encountered in a furnace or combustor) [20]. In addition to detection
114 of flames (i.e. whether or not a flame is present), there is also ongoing research into
115 developing techniques for chemiluminescence-based active control systems to optimise
116 combustion performance; for example, by correlating the measured signals to equivalence
117 ratio in premixed systems [21, 22, 23, 24].

118 Typically, chemiluminescence imaging of hydrocarbon flames targets one or both of
119 the excited-state OH and CH species (termed OH* and CH*), which are associated with
120 regions of high heat release and radical concentrations [25]. Consequently, significant ef-
121 forts have been made to develop methods of obtaining quantitative data relating to heat
122 release rate from chemiluminescence intensity [26, 27]. There are several factors which
123 influence both the excitation of the radical species and the resulting chemiluminescence
124 that is detected, making a generalised relationship difficult to formulate. In particular,
125 pressure is expected to have a significant impact on chemiluminescence intensity. For
126 example, a monotonic reduction in both OH* and CH* with increasing pressure has been
127 observed for laminar premixed methane flames at pressures ranging from 5–25 bar(a),
128 although the measured intensity was also found to be very sensitive to equivalence ra-
129 tio [28, 22]. Interestingly, this study found that equivalence ratio can be correlated to
130 the product of the OH* and CH* signal intensities independently of the mass flowrate
131 (provided that the pressure is known) [22], which has important implications for imple-
132 mentation in control systems. While the equivalence ratio parameter is generally reserved
133 for the description of premixed flames, the concept can also be extended to nonpremixed
134 configurations in which there is rapid mixing between fuel and oxidiser (e.g. via turbu-
135 lence), such that a “local equivalence ratio” can be used to describe certain regions of
136 the flame [29]. In this context, an experimental investigation was performed to assess the
137 potential for local equivalence ratio sensing in diffusion flames, although the results in-
138 dicated that this technique is ill-suited for such flames when compared to measurements

139 made via the laser-induced breakdown spectroscopy (LIBS) technique [29]. Again, these
140 findings relate only to a relatively narrow range of operating conditions and tend to be
141 focussed on the development of specific techniques; it is therefore important to inves-
142 tigate the fundamental chemiluminescence behaviour under combustion conditions that
143 are of particular practical interest, such as jet flames issuing into hot and low-oxygen
144 coflows.

145 To enable the investigation of elevated-pressure combustion under a range of condi-
146 tions relevant to practical devices, a confined and pressurised jet-in-hot-coflow (CP-JHC)
147 combustor has been developed. This apparatus facilitates the parametric analysis of the
148 effect of pressure on the behaviour of jet flames issuing into an independently controlled
149 coflow. This paper builds upon a previous study with the same apparatus in which the
150 coflow conditions were characterised and preliminary jet flame imaging results were pre-
151 sented [30]. Specifically, the current study focusses on the flame structure and stability
152 of turbulent flames under a range of coflow O_2 concentrations up to pressures of 7 bar(a),
153 emulating the conditions likely to be encountered in the secondary stage of a sequential
154 gas turbine. Chemiluminescence imaging of the flames is performed, to investigate the
155 changes in OH^* and CH^* under the various operating conditions, and providing a useful
156 resource to test the applicability of atmospheric-pressure numerical models at elevated
157 pressures. The results of a series of computational fluid dynamics (CFD) simulations
158 under conditions matching those of the CP-JHC combustor are also presented, with par-
159 ticular focus on the changes in chemiluminescence behaviour with pressure and coflow O_2
160 concentration, and the mechanisms responsible for these changes. The CFD modelling
161 is accompanied by one-dimensional, opposed-flow laminar flame simulations to provide
162 additional insights regarding the effect of pressure and O_2 concentration on the reactions
163 which lead to chemiluminescence.

164 **2. Experimental details**

165 *2.1. Burner configuration and operating conditions*

166 The confined and pressurised jet-in-hot-coflow (CP-JHC) combustor used for the ex-
167 perimental investigation has been described in detail in a previous publication [30], which
168 includes characterisation of the coflow behaviour and a limited set of jet-flame imaging
169 results. In brief, the CP-JHC consists of a 4.6-mm water-cooled jet, through which a
170 fuel stream issues into a hot and low-oxygen coflow of combustion products formed from
171 an upstream ring burner. The jet and coflow are contained within a cylindrical quartz
172 tube with a diameter of 100 mm, which is surrounded by a 100-mm thick layer of ther-
173 mal insulation, thus minimising the effect of the thermal boundary layer at high coflow
174 temperatures. This apparatus facilitates the analysis of elevated-pressure flames under
175 a range of jet and coflow boundary conditions, with optical access to the flames via a
176 quartz viewing window.

177 A range of different operating conditions have been investigated in this study, corre-
178 sponding to changes in the combustor pressure, as well as the jet and coflow parameters.
179 The composition of the fuel stream in the jet remained consistent throughout the exper-
180 iments, with a 1:1 (by volume) mixture of H₂ and NG, while two different jet Reynolds
181 numbers (Re_{jet}) were used. Using previously obtained measurements which characterised
182 the coflow behaviour [30], the flowrates of fuel and air into the ring burner were varied
183 to control the coflow conditions at the height of the viewing window, including the mole
184 fraction of O₂ (X_{O_2}), temperature (T_{cofl}), mass flowrate (\dot{m}_{cofl}) and the coflow heat
185 input (\dot{Q}_{in}). The ranges of these different parameters for the results presented herein
186 are displayed in Tables 1 and 2.

Table 1: Range of jet boundary conditions used in the current study.

Fuel	Re_{jet}	\dot{m}_{jet} [g/s]
1:1 NG/H ₂	10,000	6.14
1:1 NG/H ₂	15,000	7.44

Table 2: Range of coflow operating conditions used in the current study.

X_{O_2} [%]	\dot{m}_{cofl} [g/s]	T_{meas} [K]	\dot{Q}_{in} [kW]
3.0	6.14	1200±25	14.8
6.0	7.44	1200±25	14.8
9.0	9.36	1200±25	14.8
5.2	7.33	1300±25	14.8
7.8	10.1	1300±25	17.6

187 *2.2. Diagnostic techniques & image processing*

188 Images of the jet flames were captured using both a DSLR camera and an intensified
189 CCD camera with a UV lens. The DSLR camera was fitted with a 430 nm bandpass
190 filter (FWHM of 10 nm), enabling the imaging of CH* chemiluminescence. True-colour
191 photographs (i.e. without the filter installed) were also captured with the DSLR cam-
192 era to study the broadband luminescence. The UV-ICCD camera was also fitted with
193 a bandpass filter, centred at 310 nm with a FWHM of 10 nm to target the chemilumi-
194 nescence from OH* radicals. Both cameras were manually focussed, and images were
195 captured with a range of exposure times and ISO-speeds/gains to account for changes
196 in intensity between cases. For flame cases with sufficient signal-to-noise ratio (SNR), a
197 series of high-speed, low-exposure images were captured to enable the visualisation of the
198 instantaneous behaviour of the flames, as well as statistical analyses. A gain correction
199 based on a calibration curve was also performed to enable direct comparisons between
200 images captured with different camera settings. A 3×3 median filter was applied to the
201 OH* images in order to improve the SNR.

202 A background correction algorithm was applied to both the OH* and CH* images in
203 post-processing. This algorithm generates a background profile graduated in the axial
204 direction, based on the intensity of the pixels outside of the flame boundary, which is
205 then applied to the entire image. The OH* and CH* images were then cropped and
206 scaled to achieve pixel-to-pixel matching between the images from the two cameras. It
207 is worth noting that the two cameras were aligned with the jet centreline, mounted on
208 top of one another and at a sufficient distance from the flame such that the difference in
209 the viewing angle was negligible—thus no spatial transformation other than scaling was

210 required; this was confirmed by comparisons of the jet spreading angle between the OH*
 211 and CH* camera.

212 To enable comparison of the line-of-sight-integrated photographs with the 2-D CFD
 213 results, an Abel inversion (inverse Abel transformation) was applied to the rows of the
 214 chemiluminescence images. This inversion algorithm operates under the assumption of
 215 cylindrical symmetry, to reconstruct the underlying radial profile (akin to that obtained
 216 from planar LIF imaging, for example) from the integrated data. The results of this
 217 inversion are shown in Figure 1, for an entire flame image and for a radial profile at
 218 $x/D = 6.0$.

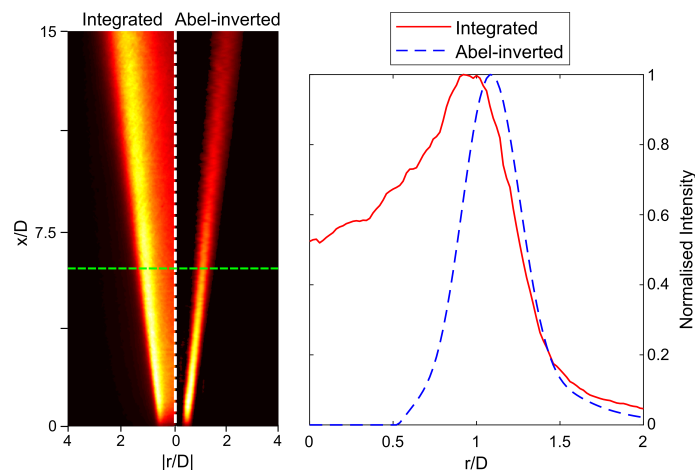


Figure 1: Comparison of line-of-sight-integrated and Abel-inverted chemiluminescence images, with radial profiles at $x/D = 6.0$ also shown (axial location of radial profiles indicated by dashed line on images).

219 3. Numerical modelling approach

220 3.1. Model overview

221 The mild combustion regime can be characterised by a near-unity Damköhler number
 222 (Da), limiting the applicability of commonly used models which describe the turbulence-
 223 chemistry interactions (TCI), such as the flamelet model [31]. Previously, the eddy
 224 dissipation concept (EDC) [32] has been found to be promising in this regard [33, 34],
 225 facilitating the detailed modelling of both turbulent mixing and finite-rate chemistry. The

226 simulation results presented throughout this paper extend the use of this EDC model—
 227 which has previously been optimised for moderately-turbulent diffusion flames in hot and
 228 low-oxygen conditions at atmospheric pressures [34, 35]—to describe elevated-pressure
 229 mild combustion.

230 Similar to a previous study [34], a reduced form of the GRI-Mech 3.0 chemical ki-
 231 netics mechanism (with N-O reactions excluded) is implemented to model the finite-rate
 232 chemistry. The simulations were performed using the ANSYS Fluent 19.2 CFD software,
 233 with a 2-D, axisymmetric domain. An optimised form of the $k - \epsilon$ turbulence model
 234 was implemented for closure of the Reynolds-averaged Navier-Stokes (RANS) equations,
 235 with the $C_{1,\epsilon}$ constant set to 1.6, a value which has previously been shown to correct for
 236 the so-called “round-jet anomaly” in axisymmetric flows [36, 37]. Initially, the geometry
 237 of the well-studied JHC configuration was maintained, to enable direct comparisons to
 238 the results of Dally et al. [8], for which detailed species compositions and temperature
 239 measurements are available at atmospheric pressure for a 1:1 NG/H₂ fuel mixture in the
 240 jet. The geometry was then updated to model the combustion chamber of the CP-JHC
 241 burner, facilitating comparisons with the experimental results at elevated pressures.

242 To compare the simulation results with those obtained experimentally with the CP-
 243 JHC, chemiluminescence modelling of OH* and CH* was also performed. This was
 244 implemented as a post-processing step based on the converged results of the simulation,
 245 since these excited-state radicals have a negligible effect on the concentrations of other
 246 species. The sub-mechanism used for OH* formation uses the following two formation
 247 reactions, with rate coefficients obtained from Hall & Petersen [38]:



248 The CH* sub-mechanism is based on the following formation reaction, with rate
 249 coefficients from Elsamra et al. [39]:



250 Additionally, quenching reactions were included in the model, using the rate coef-
 251 ficients from Tamura et al. [40]. Including these quenching reactions, a total of 12
 252 reactions were included for OH*, and 9 included for CH*. It is worth noting that these
 253 sub-mechanisms have not been validated at elevated pressures, so the analysis of the
 254 current chemiluminescence modelling requires careful interpretation, as discussed in the
 255 presentation of the results. To complement the CFD results, an additional set of chemical
 256 kinetics simulations based on 1-D, laminar opposed flow flames was carried out. These
 257 simulations were performed using the OPPDIF code available in the Chemkin-Pro soft-
 258 ware, which allows the reaction pathways and kinetics effects to be explored in more
 259 detail under the assumption of a simplified flow field. The same kinetics and chemilu-
 260 minescence mechanism to that described above was used for these simulations, and a
 261 constant mean strain rate of approximately 40 s^{-1} was used.

262 3.2. Validation and comparison cases

263 To confirm the validity of the CFD model under open, atmospheric conditions, com-
 264 parisons were made against the experimental results obtained with the JHC configura-
 265 tion, under similar operating conditions to those implemented in the CP-JHC. Specifi-
 266 cally, the HM2 and HM3 flames from Dally et al. [8] were used for validation purposes;
 267 these correspond to $Re_{jet} = 10,000$ flames with a 1:1 (by volume) NG/H₂ fuel blend
 268 issuing into a 1300 K coflow, with a coflow O₂ mole fraction of 5.2% and 7.8%, respec-
 269 tively. The CFD and experimental results were compared in terms of the radial profiles
 270 of OH concentration at two different axial locations; this is shown in Figure A1 of the
 271 Supplementary Material. This comparison yields a mean error of 5% in terms of the ra-
 272 dial location of peak OH, and 10% in terms of the peak magnitude of OH mass fraction.
 273 Specifically, the CFD model under-predicts the peak OH magnitude for the 5.2% O₂ case
 274 at $x = 30 \text{ mm}$, and also slightly over-predicts the radial location of peak OH for both

275 cases at $x = 30$ mm; these observations are consistent with previous studies relating to
276 the simulation of JHC flames using the EDC model [35, 41].

277 To assess the effect of confinement on the behaviour and validity of the model, simu-
278 lations at atmospheric pressure were performed with a modified geometry and boundary
279 conditions to match those of the CP-JHC. As shown in the last two rows in Table 2,
280 coflows with a measured temperature of approximately 1300 K with a molar O₂ concen-
281 tration of 5.2% and 7.8% were generated under near-atmospheric pressure conditions in
282 the CP-JHC, facilitating comparisons with the experimental results based on the JHC
283 configuration. It is worth noting that, due to the heat losses to the walls of the com-
284 bustor, an increased heat input (and hence coflow velocity) was required to produce a
285 coflow of the same temperature as that of the JHC, since the coflow temperature in the
286 near-field can be closely approximated by the adiabatic flame temperature for the JHC.
287 The various results are compared in terms of the jet spreading rate in §4.1, based on the
288 radial location at which OH* is at a maximum, using the Abel-inverted experimental
289 results as described in §2.2.

290 Following these comparisons at atmospheric pressure, the behaviour of the model
291 at elevated pressures is then investigated. Simulations were performed at a range of
292 operating conditions to match those shown in Tables 1 and 2, and the results were
293 compared with those of the experiments in terms of the change in chemiluminescence
294 behaviour with pressure and O₂ concentration.

295 4. Results and discussion

296 4.1. Effect of confinement

297 The model used in this study has been validated for atmospheric-pressure combus-
298 tion under the hot and low-oxygen conditions associated with the JHC/CP-JHC burner
299 configurations (see §3.2). To assess the effect of confinement, comparisons are made
300 between the CFD (with geometry matching the CP-JHC) and experimental results at
301 near-atmospheric pressure initially, for the cases displayed in the bottom two rows of

302 Table 2. This comparison is shown in Figure 2 for the jet spreading rate based on the
 303 location of maximum OH^* , as well as the location of maximum OH concentration for
 304 the open JHC results (i.e. flames HM2 and HM3 [8]). For the JHC spreading rates, the
 305 plots shown are based on the radial data available at the three axial locations of 4 mm,
 306 30 mm and 60 mm from the jet exit.

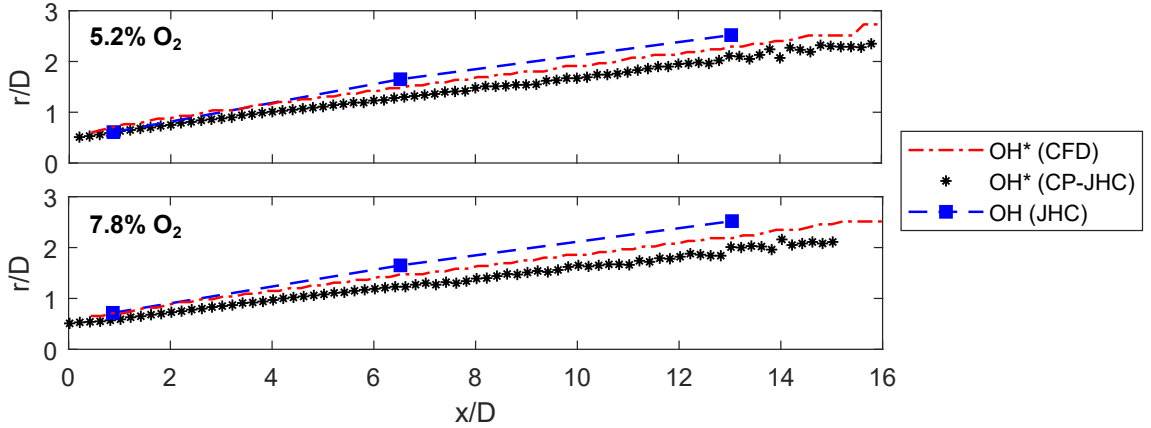


Figure 2: Jet spreading comparison between confined CFD and experimental results at atmospheric pressure, based on location of maximum OH^* . Jet spreading is also shown for open-JHC case based on OH data from Dally et al. [8] for comparison.

307 From Figure 2, it appears that there is a slight discrepancy in the radial location of
 308 maximum OH^* between the CFD and experimental results, with the CFD OH^* values
 309 occurring at radial distances further from the centreline. It is worth noting that the two
 310 curves have approximately the same gradient, with the largest differences occurring in the
 311 near-field ($x/D \lesssim 2$). It should also be mentioned that the difference in radial location
 312 between OH and OH^* in the CFD simulations is relatively minor, with the OH^* maxima
 313 occurring at slightly reduced radial distances. Similar results have also been observed
 314 experimentally, with general agreement in terms of visualisation of the flame structure
 315 based on OH and OH^* imaging [42, 43]. It follows then that the reduced gradients of
 316 the CP-JHC plots (both from the experiments and CFD) in comparison to those of the
 317 JHC suggests a reduction in the jet spreading rate as a result of confinement, a trend
 318 which is reasonably well-predicted by the CFD model, although the CFD still slightly

319 over-predicts the spreading rate in comparison to the experimental data.

320 *4.2. General observations at elevated pressures*

321 The jet flames issuing into the 3%, 6% and 9% O₂ coflows were imaged via both
322 unfiltered (i.e. true-colour) and spectrally filtered photography, to study both the broad-
323 band light emission and chemiluminescence behaviour, as described in §2.2. In terms
324 of their visible appearance, the flames were generally difficult to distinguish from the
325 background radiation, as shown by the unfiltered images displayed in Figure A2 of the
326 Supplementary Material. The 3% and 6% O₂ flames are virtually indistinguishable from
327 the background both at 1 bar and 7 bar, although a very faint blue-violet outline can
328 be observed for the 6% O₂ case at 1 bar; this lack of a clearly visible flame front is a
329 common feature of combustion under hot and low-oxygen conditions [2, 44]. The 9%
330 O₂ atmospheric-pressure case also displays a faint flame boundary in Figure A2, while
331 luminous radiation due to the presence of soot is observed for the 7 bar case at this
332 O₂ concentration. It is particularly interesting to note that neither the 3% nor the 6%
333 O₂ images indicate the presence of any soot in the region of interest; indeed, none of
334 the photographs captured for these O₂ concentrations suggest any soot formation in this
335 region under such conditions. This highlights the soot suppression characteristics of the
336 mild combustion regime, which has previously been attributed to a reduced tendency for
337 pyrolytic reactions to occur under hot and low-oxygen conditions [45, 46, 47].

338 Chemiluminescence images obtained experimentally for a series of flames at pressures
339 ranging from atmospheric pressure (1 bar) to 7 bar are displayed in Figure 3. The images
340 correspond to jet flames with two different Reynolds numbers ($Re_{jet} = 10,000$ and
341 $Re_{jet} = 15,000$), with a constant coflow O₂ concentration of 6% by mole and measured
342 coflow temperatures of 1200 ± 25 K. The OH* and CH* images are shown side-by-side for
343 each flame case, with the OH* images reflected about the centreline such that the same
344 half of the flame is shown. The images were generated based on multiple long-exposure
345 (> 1 s) photographs, such that they represent the mean behaviour. These images also

346 correspond to the line-of-sight-integrated photographs, that is, prior to implementing the
 347 Abel inversion algorithm.

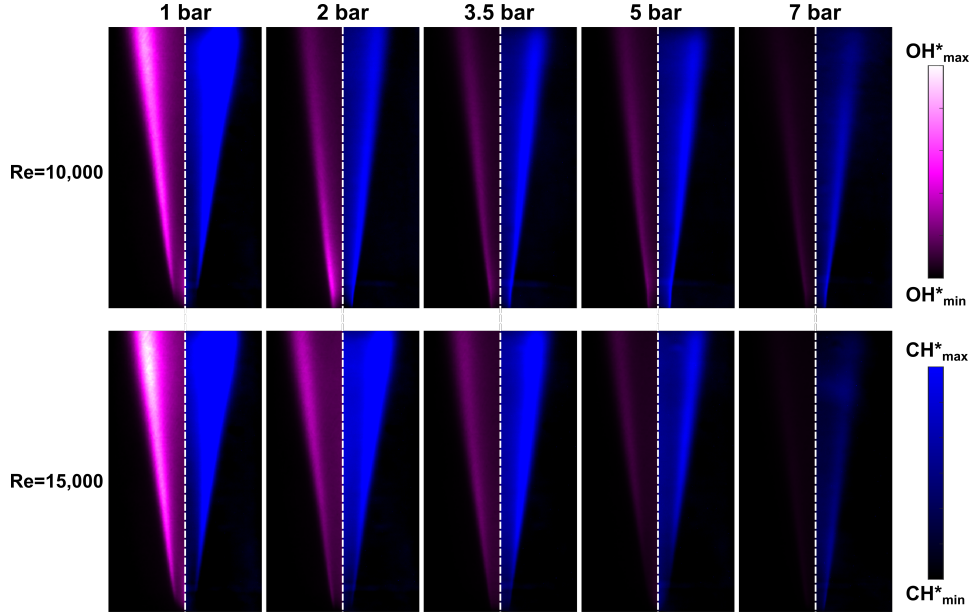


Figure 3: OH^* (left) and CH^* (right) chemiluminescence images for flames with $Re_{jet} = 10000$ and $Re_{jet} = 15000$ issuing into a 6% O_2 coflow with $T_{coflow} = 1200 \pm 25$ K, at absolute pressures ranging from 1–7 bar. Each image has a width of 4 jet diameters (18.4 mm) and height of 15 jet diameters (67 mm).

348 The key observation in Figure 3 is the notable reduction in chemiluminescence in-
 349 tensity with increasing pressure, in terms of both of OH^* and CH^* , for both Reynolds
 350 number series shown. It is worth noting that a consistent colour scale was used for all of
 351 the flames at different pressures and Reynolds numbers in order to highlight this change
 352 in intensity; hence the difficulty in distinguishing the flames in some images, particularly
 353 the OH^* for the 7 bar cases. In previous studies involving both premixed [28] and non-
 354 premixed [48] flames, a reduction in OH^* chemiluminescence with increasing pressure has
 355 been observed, and attributed to increased frequency of collisional quenching at elevated
 356 pressures. This behaviour and the mechanisms responsible for it are further explored in
 357 §4.3.

358 In general, all of the flames shown in Figure 3 display similar overall structures,

359 although some differences in the flame bases are worth discussing. For both the $Re_{jet} =$
 360 10000 and $Re_{jet} = 15000$ flames at near-atmospheric pressure, the flame base appears to
 361 be slightly lifted from the jet exit plane, although closer inspection of the OH^* images
 362 indicates that the flame base is not clearly defined. Since these images represent the
 363 mean, not the instantaneous behaviour, the ill-defined flame base indicates that there is
 364 some variation in its location with respect to time for these cases. At elevated pressures,
 365 this behaviour is not apparent, with the flames all appearing to be stabilised at the jet
 366 exit. In order to quantify these differences, statistical analyses were performed for a series
 367 of more than 200 short-exposure images (obtained with the CH^* camera) for the various
 368 cases. This enables the mean liftoff height to be determined, as well as the unsteadiness
 369 at the flame base as quantified by the standard deviation of the liftoff height—these
 370 results are displayed in Figure 4 for the $Re = 15000$ flames with a 6% O_2 coflow.

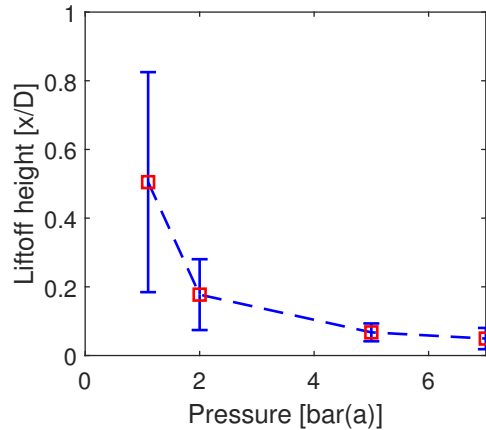


Figure 4: Effect of pressure on liftoff height and stability, for the $Re = 15000$, 6% O_2 cases. Note that the vertical bars shown on the plot represent one standard deviation above and below the mean, providing an indication of the time-dependent fluctuations in the liftoff height.

371 The results shown in Figure 4 show a general reduction in liftoff and more stabilised
 372 flame base at elevated pressures. The change from 1 to 2 bar is the most notable observa-
 373 tion, with a significant reduction in both the mean and the variation of the liftoff height.
 374 For $P > 2$ bar, the variation in the location of the flame base is seen to be significantly
 375 reduced, and there is relatively little change from 5 to 7 bar. The tendency for the flames

376 to stabilise nearer to the jet exit at elevated pressures can be explained by the reduced
 377 velocity of the fuel stream at higher pressures, since the cases shown all correspond to a
 378 constant mass flowrate, such that velocity is inversely proportional to pressure.

379 4.3. OH^* and CH^* intensity

380 To further explore the changes in chemiluminescence behaviour under different oper-
 381 ating conditions, Figure 5 displays the intensity of OH^* and CH^* as a function of pressure
 382 for the various coflow cases, based on the experimental imaging. For this analysis, the
 383 intensity values for each case were calculated based on the peak signals along each row
 384 of pixels from the jet exit to $x/D = 10$, which were then averaged.

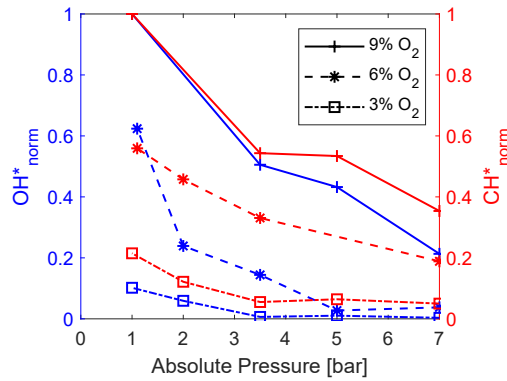


Figure 5: OH^* and CH^* row-averaged maximum chemiluminescence intensity (based on the experiments) as a function of pressure for $Re_{jet} = 10000$ flames with 3%, 6% and 9% O_2 coflows. OH^* signals are shown on the left vertical axis (blue) and CH^* signals are shown on the right (red).

385 In Figure 5, it is apparent that there is a general reduction in chemiluminescence
 386 intensity as the pressure is increased and the O_2 concentration reduced. In terms of
 387 pressure-dependence, the OH^* intensity appears to show greater sensitivity, with an
 388 approximate order-of-magnitude decrease as the absolute pressure is increased from 1 bar
 389 to 7 bar. There is also a tendency for CH^* to decrease with pressure, although the trend
 390 is less consistent, particularly for the 3% O_2 coflow where the curve is seen to level
 391 out and even slightly increase for $P > 3.5$ bar. As mentioned in §4.2, the reduction in
 392 intensity with increasing pressure has previously been attributed to a greater likelihood

393 of third-body or collisional quenching of the excited-state radicals [28], which is expected
394 to increase with density and therefore pressure. Additionally, it is possible that there is
395 a shift in chemical kinetics pathways at elevated pressures which leads to a change on
396 OH* formation. The greater relative intensities for the CH* results at elevated pressures
397 suggests that either quenching has a reduced effect in comparison to OH*, or there is
398 indeed a difference due to chemical kinetics as the pressure is increased; this is explored
399 further in §4.4.

400 Figure 6 compares the experimental and numerical modelling (both CFD and Chemkin)
401 results, in terms of the change in chemiluminescence behaviour with pressure and coflow
402 O₂ concentration. The intensity values shown for the experiments correspond to the
403 maximum radial values averaged over $x/D < 10$ (i.e. the results from Figure 5 are repro-
404 duced), while the molar concentration was used for the CFD and Chemkin results. Both
405 sets of results were normalised against the maximum value over the entire dataset, which
406 corresponds to the 9% O₂, 1 bar case for the experiments, CFD and Chemkin results.
407 The results corresponding to the same coflow are shown together on a single set of axes,
408 with a separate set of axes for each of the 3, 6 and 9% O₂ coflow cases.

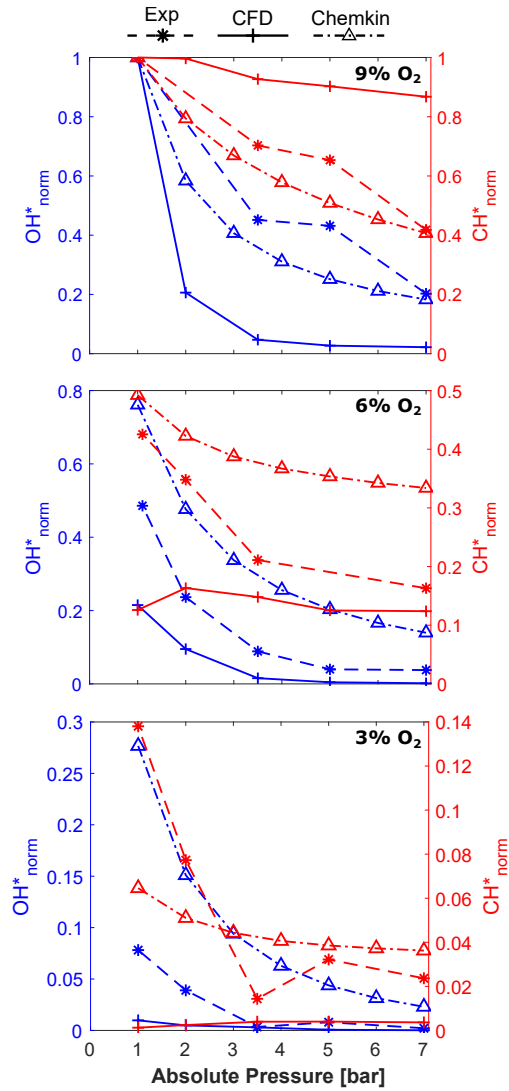


Figure 6: OH^* and CH^* radially-averaged chemiluminescence intensity (experiments) and molar concentration (CFD and Chemkin) as a function of pressure for $Re_{jet} = 10000$ flames for three different coflows. The experimental, CFD and Chemkin results are normalised against their highest respective values across all pressures and O_2 concentrations. Also note the change in the scale of the y-axis for the separate plots corresponding to the different O_2 concentrations.

409 In Figure 6, some key differences between the results of the CFD and Chemkin simu-
 410 lations and those from the experiments can be seen. First of all, it can be seen that—for
 411 the 9% O_2 case—both the CFD and Chemkin simulations appear to over-predict the
 412 reduction in OH^* with pressure, although the Chemkin results match the experimental

413 observations much more closely. Interestingly, the pressure-dependence of CH^* based on
414 the CFD results appears to be minimal, while the 1-D simulations predict a consistent
415 reduction in CH^* with pressure which is similar to that observed for the experimental
416 results—at least at 9% O_2 . The large discrepancy between the Chemkin and CFD results
417 in terms of CH^* suggests that the flow field plays an important role on the predicted
418 trends, that is, it is not simply a matter of kinetics. Although the OH^* intensity is seen
419 to decrease with pressure slightly more rapidly than CH^* based on the experiments, the
420 CFD results predict a major difference between the two. This is further explored in terms
421 of the reaction pathways in §4.4.

422 In comparison to the experimental chemiluminescence imaging, the CFD results show
423 a much greater reduction in both OH^* and CH^* as the O_2 concentration is decreased.
424 Considering the 1 bar cases in isolation, it can be seen that the OH^* and CH^* chemilumi-
425 nescence intensities based on the photographs are reduced by approximately 50% as the
426 O_2 concentration is reduced from 9% to 6%, noting the change in vertical axis scales be-
427 tween the sub-figures. The CFD concentrations, however, are reduced to approximately
428 20% and 10% of the maximum OH^* and CH^* values, respectively. The difference is even
429 more pronounced for the 3% O_2 coflow, particularly for the CH^* results, which have
430 normalised values of less than 0.01 (i.e., < 1% of the maximum radially-averaged value)
431 based on the CFD concentration at all pressures, while the experimental case at 1 bar and
432 3% O_2 is approximately 25% of the maximum value. It is particularly interesting that the
433 CH^* concentrations based on the CFD simulations do not appear to show any noticeable
434 pressure-dependence, yet are very sensitive to changes in O_2 concentration. Considering
435 now the Chemkin results, it is interesting to note that the OH^* concentration shows less
436 sensitivity to O_2 concentration, with all of the normalised values at 6% and 3% O_2 based
437 on the Chemkin analysis being greater than the corresponding CFD and experimental
438 values. Interestingly, the Chemkin-derived CH^* values show a similar reduction from
439 9% to 6% O_2 to the behaviour observed based on the experiments, yet there is then a
440 more pronounced reduction from 6% to 3% O_2 for the Chemkin results, particularly at

441 lower pressures. These results indicate that the trends in chemiluminescence behaviour
442 which occur with both pressure and O₂ concentration are highly sensitive to both chem-
443 ical kinetics and flow phenomena. The following section explores this in more detail by
444 comparing the simulation results of the CFD and Chemkin models, in terms of formation
445 mechanisms and the sensitivities of the underlying chemical species.

446 4.4. OH* and CH* reaction pathways

447 Although there is some agreement in the general trends between the modelling and
448 experiments based on the results shown in §4.3, it is apparent that the simulations do
449 not accurately predict all of the changes in chemiluminescence as the pressure and O₂
450 concentration are varied. It is therefore of interest to analyse in more detail the individual
451 reactions and species which are relevant to OH* and CH* formation and consumption,
452 based on both the Chemkin and CFD simulations. This is important not only to provide
453 insight into the mechanisms responsible for the experimental observations, but also to
454 highlight which aspects of the model should be prioritised in future investigations—
455 particularly since the kinetics mechanism used for chemiluminescence has been applied
456 beyond the conditions for which it has previously been validated.

457 Figure 7 shows the effect of pressure on the rates of formation and consumption of
458 OH* based on both the CFD and laminar opposed-flow flame (Chemkin) simulations.
459 The formation rates are determined based on the forward-reactions of R1 and R2 (see
460 §3.1), with the contribution from each reaction shown separately. The rates of the reverse
461 reactions are also displayed, although these are much lower. Also shown in Figure 7 is
462 the total collisional quenching rate, based on the summation of all of the quenching
463 reactions. The values shown in the plots correspond to the mean reaction rates for
464 the region $x/D < 10$, to maintain consistency with the results shown in the previous
465 section. Similar to Figure 6, the results for the three different coflow O₂ concentrations
466 are displayed on separate axes.

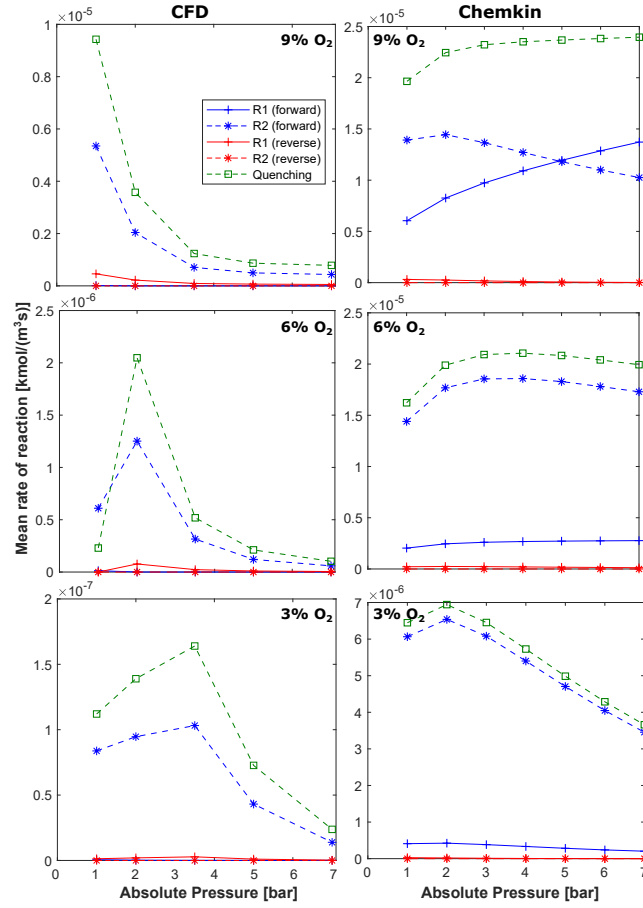


Figure 7: Mean rates of reactions R1 and R2 based on the CFD and Chemkin simulations (evaluated for axial distances $x/D < 10$ for the CFD). Forward reactions (i.e. OH* formation) shown in blue, while reverse (i.e. consumption) shown in red. OH* quenching rate also shown in green.

467 Figure 7 highlights some interesting behaviour with regards to OH* formation. It
 468 is evident that—at least for the CFD results—reaction R2 is the dominant formation
 469 pathway in the near-field region for all pressures and coflow O₂ cases, with a mean rate
 470 that is multiple orders of magnitude greater than that of reaction R1. Interestingly, the
 471 Chemkin simulations predict a relatively greater contribution from reaction R1, partic-
 472 ularly for the 9% O₂ case as the pressure is increased, where it is seen to become the
 473 dominant pathway for $P > 5.0$ bar. It can also be seen in the CFD results that the
 474 R1 reaction favours the reverse pathway in this region (although this is still significantly

475 lower than the formation rate from R2), which suggests that the concentration of O and
476 H radicals is relatively low. In general, the CFD and Chemkin results predict signifi-
477 cantly different trends, both in terms of the effects of pressure and O₂ concentration.
478 For example, the quenching and total formation rates show a slight increase with in-
479 creasing pressure for the 9% O₂ Chemkin results (noting that the total formation rate
480 essentially matches the quenching rate), while the CFD predicts a monotonic reduction
481 with pressure at the same O₂ concentration. This difference appears to be largely related
482 to the increased prominence of R1, whose mean rate is seen to increase with pressure
483 based on the Chemkin analysis, although it is also seen that the rate of R2 also shows an
484 initial increase with pressure which is not evident in the CFD results at 9% O₂. These
485 differences highlight the influence of the flow field on the resulting chemiluminescence
486 behaviour, as explored further in this section.

487 A noticeable change in behaviour can also be seen by comparing the results for the
488 different O₂ concentrations in Figure 7. Focussing on the CFD results in isolation, it
489 is interesting to note that while the 9% O₂ cases show a monotonic trend in terms of
490 pressure-dependence of the various reaction rates, both the 6% and 3% O₂ cases show a
491 departure from this. Firstly, it is worth noting that the trends are essentially the same
492 for the 6% and 9% plots if the 1 bar data points are excluded (i.e. for $P \geq 2$ bar), and
493 similarly for the 3% O₂ case for $P \geq 3.5$ bar. This suggests that there are competing
494 effects occurring as the pressure is varied, which are more pronounced at lower pressures
495 and O₂ concentrations. Since the reaction R2 is the dominant OH* formation pathway
496 in the CFD simulations, it is useful to investigate the CH radical to provide additional
497 insight. This analysis is included in the Supplementary Material (Figure A3), and shows
498 that—although there is a monotonic decrease in the mean CH concentration with pressure
499 for all O₂ cases—the spatial overlap between CH and O₂ (the two reactants of R2)
500 increases from 1.0–2.0 bar for the 6% O₂ case and from 1–3.5 bar for the 3% O₂ case.
501 Additionally, this change in overlap can be attributed to the flames stabilising nearer to
502 the jet exit as the pressure is increased, as was observed from the experimental imaging

503 results (§4.2). This emphasises the importance of accurately modelling both the flow-
504 field and the finite-rate chemistry for the flames studied, particularly when simulating
505 chemiluminescence behaviour. It is also worth noting that, despite the non-monotonic
506 behaviour of the 3% and 6% cases in terms of formation rate, the OH* concentration
507 displays a consistent reduction with pressure for all cases, as seen in Figure 6. This
508 suggests that quenching does, in fact, have an increased impact at elevated pressures in
509 conjunction with the change in formation rate.

510 The Chemkin simulations also predict a shift in pressure-dependence with regard to
511 OH* formation as the O₂ is varied. Comparing the 9% and 6% Chemkin plots and
512 noting that they share the same vertical axis scale, it can be seen—somewhat counter-
513 intuitively—that reaction R2 actually shows a slightly increased mean rate at all pressures
514 for the 6% O₂ case. Further reducing the O₂ concentration to 3% then leads to a reduction
515 in both the R1 and R2 reaction rates, as well as a more significant decrease with pressure
516 for $P > 2$ bar as seen in the 3% O₂ plot in Figure 7. These trends, in addition to others
517 discussed in this section, can be explored further by analysing the sensitivity of the OH*
518 species, in terms of the reactions which have the greatest influence on formation and
519 consumption. These sensitivity results are shown in Figure A4 of the Supplementary
520 Material, in the form of normalised charts displaying the key reactions at the location of
521 maximum OH* at a range of pressures and O₂ concentrations.

522 The sensitivity results indicate that, for all of the cases shown, the key reactions
523 which influence the OH* concentration at its peak remain largely the same. For all cases
524 shown except for the 7 bar, 3% O₂ case, the behaviour is consistent in terms of the
525 three reactions which produce the greatest sensitivity. In general, the key reaction is
526 R2, as would be expected based on Figure 7, although the 7 bar cases at 9% and 3%
527 O₂ show a departure from this. For the higher O₂ case, the sensitivity to reaction R2 is
528 significantly reduced in comparison to the other cases, with a normalised value of 0.75,
529 with the other cases all having sensitivities of greater than 0.95. It is also interesting to
530 note that reaction R1 does not appear in the list for any of the cases other than the 7 bar,

531 9% O₂ case, which appears to be a result of the narrower reaction zone which occurs at
532 higher pressures and O₂ concentration. Interestingly, Figure 7 shows that the mean rate
533 of R1 exceeds that of R2 for the 7 bar, 9% O₂ case, yet OH* is more sensitive to R2 at
534 the location of interest. Looking at the locations of the peaks of R1 and R2 (mixture-
535 fraction-space plots of which are included in Figure A5 of the Supplementary Material),
536 and that of the global OH* peak, it is apparent that the maximum concentration is
537 almost coincident with the peak production rate of R2; this suggests that the quenching
538 effect is stronger in the region of the flame where reaction R1 predominately takes place.

539 In terms of OH* formation, the key question which remains is the cause of the much
540 lower relative rate of reaction R1 predicted by the CFD compared with the laminar flame
541 simulations. The differences in terms of the prominence of the formation reactions can
542 be investigated by comparing the concentrations of the underlying species, that is, H
543 and O for reaction R1 and CH and O₂ for reaction R2. This is shown for the 9% O₂,
544 1 bar case in Figure 8, with the radial species profiles evaluated at an axial distance of
545 $x = 30$ mm for the CFD results.

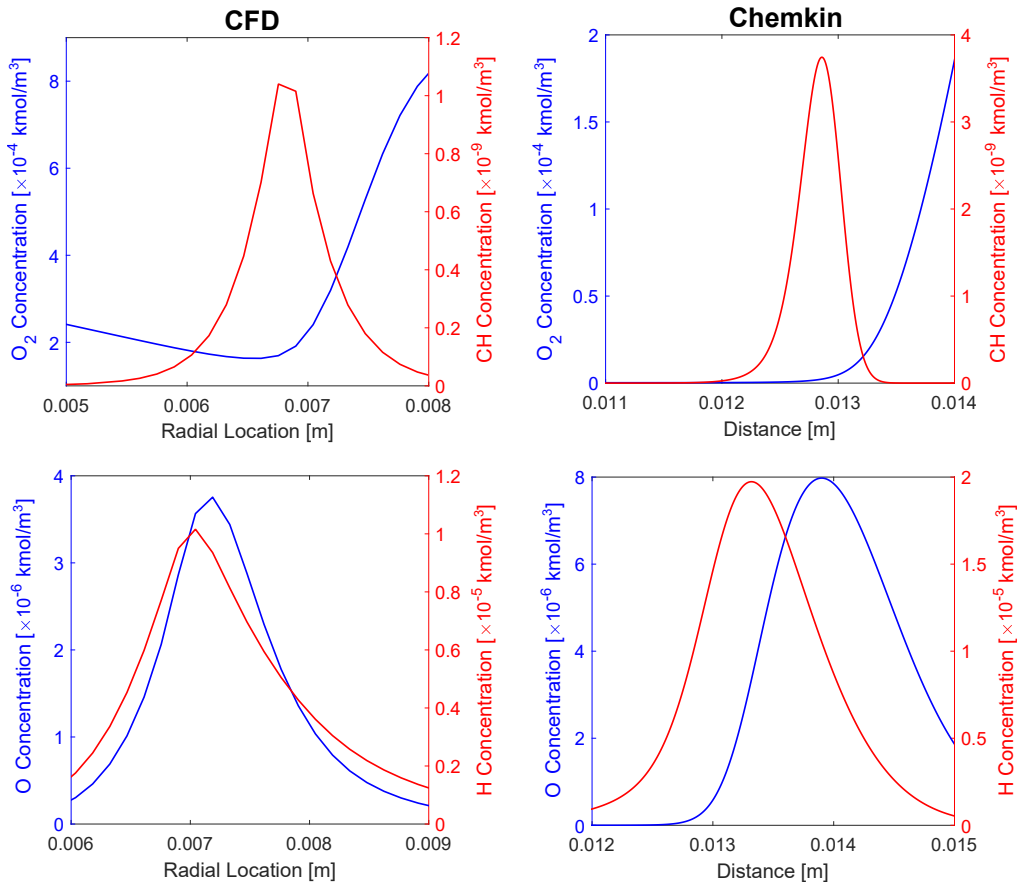


Figure 8: Comparison of underlying species profiles (O_2 , CH, O, H) for CFD and Chemkin results at 1 bar with a 9% O_2 oxidant stream. Note that the 2-D CFD simulation results are evaluated along a radial profile 30 mm from the jet exit plane.

546 The species profiles in Figure 8 indicate that the radical species concentrations are
 547 generally lower for the CFD results, but of similar order of magnitude to that of the 1-D
 548 simulations, and the relative magnitudes of the O, H, and CH species are also similar.
 549 Interestingly, however, the CFD model predicts a significantly higher concentration of
 550 O_2 in the region near the CH peak in comparison to the Chemkin simulations, which is
 551 likely the cause of the relative dominance of the R2 pathway in the CFD modelling. It is
 552 particularly interesting to observe that the O_2 concentration behaves non-monotonically
 553 as a function of the distance from the centreline, since it is expected that the O_2 con-
 554 centration would increase monotonically from zero on the fuel side to 9% (in this case)

555 on the oxidant side for a nonpremixed flame. This indicates that a non-negligible por-
556 tion of the O_2 from the coflow is entrained and transported to the fuel-rich side without
557 being completely consumed by the reaction, as indicated by the 2-D colour-map shown
558 in Figure A6 of the Supplementary Material. This O_2 then continues to react, such that
559 oxidant is supplied to the reaction zone from both sides and the O_2 concentration de-
560 creases to a minimum at the location where CH is at a maximum. Importantly, the fact
561 that the CFD and Chemkin modelling predict similar behaviour in terms of the radical
562 species, yet produce such different results in terms of OH^* , again highlights the extreme
563 sensitivity of chemiluminescence modelling to the underlying flow-field in these flames.

564 The mean formation rates for CH^* from the CFD and Chemkin simulations are
565 shown in Figure 9, again evaluated for $x/D < 10$ for the CFD. In this figure, the three
566 different coflow O_2 concentrations are shown in a single plot, and the formation rate is
567 calculated from the forward rate of reaction R3. It is worth noting that the mean rate of
568 consumption was also calculated via the summation of the various quenching reactions,
569 and this was found to be equivalent to the mean formation rate (as expected since it
570 is an intermediate species). Comparing Figures 7 and 9, it is interesting to note that
571 the CH^* formation rate (and quenching rate) shows an increase with pressure for all O_2
572 concentrations (for both the CFD and Chemkin plots), while the OH^* rates showed a
573 general reduction with pressure, with some cases displaying non-monotonic trends. In
574 terms of CH^* formation, the increase is a consequence of greater concentrations of the
575 C_2H radical as the pressure is increased, while the CH concentration (which leads to
576 OH^* formation via the R2 pathway) decreases with pressure as mentioned previously.
577 Referring back to Figure 6, the CH^* concentrations predicted by the CFD do not show
578 any clear pressure-dependence, while the Chemkin simulations predict a weak negative
579 correlation between pressure and the mean CH^* concentration; this suggests that the
580 increase in quenching at elevated pressures counteracts the increased formation rate
581 which is evident in Figure 9.

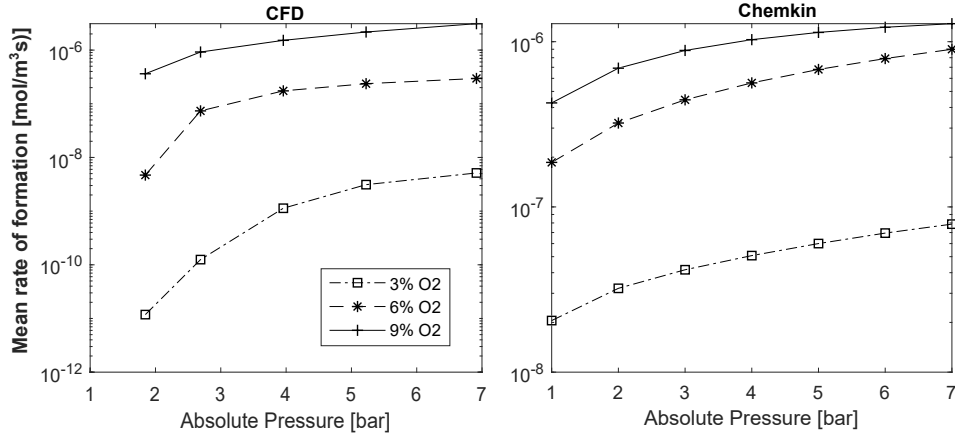


Figure 9: Rates of formation for CH^* via reaction R3, for both the CFD and Chemkin results (evaluated for axial distances $x/D < 10$ for the CFD). Note that the mean quenching rates are essentially identical to the respective formation rates when shown on this scale, and are therefore not included.

582 It is also interesting to observe in Figure 9 that the CH^* concentration shows a
 583 much greater sensitivity to the O_2 concentration for the CFD results in contrast to the
 584 Chemkin simulations, noting the different vertical-axis scales. This difference is also
 585 evident for the OH^* rates in Figure 7, albeit to a lesser extent. The difference is possibly
 586 a consequence of the reaction zone shifting radially outwards as the O_2 is decreased in
 587 the CFD simulations, such that there is a change in the local strain rate which is likely
 588 to have a significant effect on the composition of the radical pool, and therefore on the
 589 relative rates of the chemiluminescence reactions.

590 In the context of the experimental observations, the results presented in this section
 591 offer some important insights. In particular, they highlight the complex interactions
 592 between chemistry and flow-field effects, which lead to some interesting behaviour as the
 593 pressure and coflow O_2 concentration are varied. The general trend observed based on the
 594 experimental chemiluminescence images is a reduction in both OH^* and CH^* intensity
 595 with increasing pressure and decreasing O_2 , as well as a shift towards a more stable
 596 flame base at elevated pressures. While the CFD model appears to predict the general
 597 flame structure reasonably well for the various cases, there is disagreement between the
 598 experimental and CFD results in terms of the relative change in intensity/concentration

599 with both pressure and O_2 . Additionally, the Chemkin simulations suggest that these
600 differences are not solely a consequence of the chemical kinetics mechanism. In terms
601 of OH^* , the modelling results suggest that there is a general reduction in the presence
602 of the CH radical which leads to a reduction in OH^* formation with pressure, although
603 there are also competing effects at play in terms of the spatial overlap with O_2 . The
604 reduced concentration of CH ultimately leads to a more rapid reduction in OH^* with
605 pressure than would be expected simply due to increased quenching. This result is
606 particularly noteworthy, since a previous experimental investigation involving laminar
607 diffusion flames observed that the OH^* signal decay with pressure was less than what
608 would be expected due to quenching effects, suggesting an increased OH^* formation rate
609 as the pressure is increased [48]. Since the CFD model over-predicts the reduction in
610 OH^* with pressure (see Figure 6), it is possible that there is indeed a shift towards an
611 additional OH^* formation mechanism at pressure, which is not captured in the kinetics
612 model. It is also worth noting that the R1 OH^* formation pathway does not show
613 this same pressure-sensitivity, so it is possible that the CFD modelling fails to capture
614 accurately the relative contributions of the two formation reactions and how these vary
615 with pressure. Interestingly, for the CH^* results, there is an increased rate of formation
616 which is approximately balanced by the increase in quenching rate, such that—according
617 to the CFD model—there is no noticeable pressure dependence from a chemical kinetics
618 perspective. The chemiluminescence imaging, however, shows a general reduction in
619 intensity with pressure, and the Chemkin analysis also suggests a modest reduction in
620 the mean CH^* concentration with pressure, which appears to be related to increased
621 quenching rates.

622 5. Conclusions

623 The effect of pressure on the structure and chemiluminescence behaviour of tur-
624 bulent flames under hot and low-oxygen combustion conditions has been investigated.
625 Experimental imaging of OH^* and CH^* in a confined and pressurised jet-in-hot-coflow

626 combustor was complemented by CFD modelling using a validated, atmospheric-pressure
627 model based on the JHC burner. The model geometry and boundary conditions were up-
628 dated to match those of the CP-JHC, and initial comparisons were made in terms of the
629 jet-spreading rate. The experimental chemiluminescence imaging results were presented
630 and analysed in conjunction with the numerically-derived OH* and CH* concentrations,
631 based on both the CFD modelling and laminar, opposed-flow flame simulations. Ul-
632 timately it was found that, although the modelling predicts certain trends such as a
633 reduction in OH* with both pressure and coflow O₂ concentration, there is a clear need
634 to further develop the mechanisms in order to reproduce the experimental results. Fur-
635 ther analysis of both sets of numerical modelling results revealed that there is a reduction
636 in the mean concentration of the CH radical with pressure which leads to a reduction in
637 OH* formation via the reaction R1: $\text{CH} + \text{O}_2 \rightleftharpoons \text{OH}^* + \text{CO}$, which is the dominant path-
638 way at all pressures and coflow O₂ concentrations considered in the CFD analysis. This
639 result is particularly interesting, since previous observations of reduced OH* intensity at
640 elevated pressures are generally attributed to the increased quenching rates at elevated
641 pressure. The comparisons between the CFD and Chemkin results also indicate that the
642 relative dominance of the R1 pathway—as well as the non-monotonic trends observed at
643 lower pressures—are related to slight changes in the spatial overlap of CH and O₂. This
644 emphasises the need to accurately capture both the overall flow behaviour, particularly
645 in the stabilisation region, as well as the precise location and concentration of key inter-
646 mediate species in order to predict the trends in chemiluminescence behaviour. This is
647 particularly important from a practicality perspective, since chemiluminescence imaging
648 is a widely used experimental technique, and if computational models can accurately
649 predict the behaviour seen for the flames in the current experiments, then it gives good
650 confidence in the suitability of the model.

651 6. Acknowledgements

652 The authors would like to acknowledge the multitude of individuals and groups who
653 have contributed to the design, construction and commissioning of the CP-JHC appa-
654 ratus. The generous financial support from the Australian Research Council (ARC),
655 the United States Asian Office for Aerospace Research and Development (AOARD), the
656 Future Fuels Cooperative Research Centre (FF-CRC), and the Australian Government
657 Research Training Program Scholarship (RTPS) is also gratefully acknowledged.

658 References

- 659 [1] S. Hochgreb, Mind the gap: Turbulent combustion model validation and future needs, *Proceedings*
660 *of the Combustion Institute* 37 (2019) 2091–2107.
- 661 [2] A. Perpignan, A. Gangoli Rao, D. Roekaerts, Flameless combustion and its potential towards gas
662 turbines, *Progress in Energy and Combustion Science* 69 (2018) 28–62.
- 663 [3] W. Boyette, A. Elbaz, T. Guiberti, W. Roberts, Experimental investigation of the near field in
664 sooting turbulent nonpremixed flames at elevated pressures, *Experimental Thermal and Fluid*
665 *Science* 105 (2019) 332–341.
- 666 [4] F. Joos, P. Brunner, B. Schulte-Werning, K. Syed, A. Eroglu, Development of the Sequential
667 Combustion System for the ABB GT24/GT26 Gas Turbine Family, in: *Volume 4: Heat Transfer;*
668 *Electric Power; Industrial and Cogeneration*, AMSE, Birmingham, UK, 1996.
- 669 [5] G. H. Abd-Alla, Using exhaust gas recirculation in internal combustion engines: A review, *Energy*
670 *Conversion and Management* 43 (2002) 1027–1042.
- 671 [6] A. Cavaliere, M. de Joannon, Mild Combustion, *Progress in Energy and Combustion Science* 30
672 (2004) 329–366.
- 673 [7] M. J. Evans, P. R. Medwell, H. Wu, A. Stagni, M. Ihme, Classification and lift-off height prediction
674 of non-premixed MILD and autoignitive flames, *Proceedings of the Combustion Institute* 36 (2017)
675 4297–4304.
- 676 [8] B. Dally, A. Karpetsis, R. Barlow, Structure of turbulent non-premixed jet flames in a diluted hot
677 coflow, *Proceedings of the Combustion Institute* 29 (2002) 1147–1154.
- 678 [9] P. Medwell, P. Kalt, B. Dally, Simultaneous Imaging of OH, Formaldehyde, and Temperature of
679 Turbulent Nonpremixed Jet Flames in a Heated and Diluted Coflow, *Combustion and Flame* 148
680 (2007) 48–61.

- 681 [10] R. Cabra, T. Myhrvold, J. Chen, R. Dibble, A. Karpetsis, R. Barlow, Simultaneous laser raman-
682 rayleigh-lif measurements and numerical modeling results of a lifted turbulent H₂/N₂ jet flame in
683 a vitiated coflow, *Proceedings of the Combustion Institute* 29 (2002) 1881–1888.
- 684 [11] R. Gordon, A. Masri, E. Mastorakos, Simultaneous Rayleigh temperature, OH- and CH₂O-LIF
685 imaging of methane jets in a vitiated coflow, *Combustion and Flame* 155 (2008) 181–195.
- 686 [12] R. Lückerkath, W. Meier, M. Aigner, FLOX[®] Combustion at High Pressure With Different Fuel
687 Compositions, *Journal of Engineering for Gas Turbines and Power* 130 (2008) 011505.
- 688 [13] J. Ye, P. Medwell, E. Varea, S. Kruse, B. Dally, H. Pitsch, An experimental study on MILD
689 combustion of prevaporised liquid fuels, *Applied Energy* 151 (2015) 93–101.
- 690 [14] K. Peter Geigle, R. Hadeif, W. Meier, Soot Formation and Flame Characterization of an Aero-
691 Engine Model Combustor Burning Ethylene at Elevated Pressure, *Journal of Engineering for Gas
692 Turbines and Power* 136 (2013).
- 693 [15] Engine Combustion Network, <https://ecn.sandia.gov/>, 2022. [Accessed: 18/10/2022].
- 694 [16] M. Meijer, B. Somers, J. Johnson, J. Naber, S.-Y. Lee, L. M. C. Malbec, G. Bruneaux, L. M.
695 Pickett, M. Bardi, R. Payri, T. Bazyn, Engine combustion network (ECN): Characterization and
696 comparison of boundary conditions for different combustion vessels, *Atomization and Sprays* 22
697 (2012).
- 698 [17] W. Boyette, T. Guiberti, G. Magnotti, W. Roberts, Structure of turbulent nonpremixed syngas
699 flames at high pressure, *Proceedings of the Combustion Institute* 37 (2019) 2207–2214.
- 700 [18] T. F. Guiberti, W. R. Boyette, W. L. Roberts, Height of turbulent non-premixed jet flames at
701 elevated pressure, *Combustion and Flame* 220 (2020) 407–409.
- 702 [19] R. J. Roby, A. J. Hamer, E. L. Johnson, S. A. Tilstra, T. J. Burt, Improved Method for Flame
703 Detection in Combustion Turbines, *Journal of Engineering for Gas Turbines and Power* 117 (1995)
704 332–340.
- 705 [20] D. M. Brown, E. Downey, J. Kretchmer, G. Michon, Emily Shu, D. Schneider, SiC flame sensors
706 for gas turbine control systems, *Solid-State Electronics* 42 (1998) 755–760.
- 707 [21] N. Docquier, S. Belhafaoui, F. Lacas, N. Darabiha, C. Rolon, Experimental and numerical study of
708 chemiluminescence in methane/air high-pressure flames for active control applications, *Proceedings
709 of the Combustion Institute* 28 (2000) 1765–1774.
- 710 [22] B. Higgins, M. Q. McQuay, F. Lacas, S. Candel, An experimental study on the effect of pressure
711 and strain rate on CH chemiluminescence of premixed fuel-lean methane/air flames, *Fuel* 80 (2001)
712 1583–1591.
- 713 [23] F. Guethe, D. Guyot, G. Singla, N. Noiray, B. Schuermans, Chemiluminescence as diagnostic tool
714 in the development of gas turbines, *Applied Physics B* 107 (2012) 619–636.
- 715 [24] W. McCord, M. Gragston, Y. Wu, Z. Zhang, P. Hsu, K. Rein, N. Jiang, S. Roy, J. R. Gord,

- 716 Quantitative fuel-to-air ratio determination for elevated-pressure methane/air flames using chemi-
717 luminescence emission, *Applied Optics* 58 (2019) C61–C67.
- 718 [25] V. Nori, J. Seitzman, Evaluation of Chemiluminescence as a Combustion Diagnostic Under Varying
719 Operating Conditions, in: 46th AIAA Aerospace Sciences Meeting and Exhibit, American Institute
720 of Aeronautics and Astronautics, 2008.
- 721 [26] S. Sardeshmukh, M. Bedard, W. Anderson, The use of OH* and CH* as heat release markers in
722 combustion dynamics, *International Journal of Spray and Combustion Dynamics* 9 (2017) 409–423.
- 723 [27] Y. Liu, J. Tan, H. Wang, L. Lv, Characterization of heat release rate by OH* and CH* chemilu-
724 minescence, *Acta Astronautica* 154 (2019) 44–51.
- 725 [28] B. Higgins, M. Q. McQuay, F. Lacas, J. C. Rolon, N. Darabiha, S. Candel, Systematic measurements
726 of OH chemiluminescence for fuel-lean, high-pressure, premixed, laminar flames, *Fuel* 80 (2001) 67–
727 74.
- 728 [29] L. Merotto, M. Sirignano, M. Commodo, A. D’Anna, R. Dondè, S. De Iuliis, Experimental Char-
729 acterization and Modeling for Equivalence Ratio Sensing in Non-premixed Flames Using Chemi-
730 luminescence and Laser-Induced Breakdown Spectroscopy Techniques, *Energy & Fuels* 31 (2017)
731 3227–3233.
- 732 [30] D. B. Proud, M. J. Evans, Q. N. Chan, P. R. Medwell, Characteristics of turbulent flames in a
733 confined and pressurised jet-in-hot-coflow combustor, *Journal of the Energy Institute* (2022).
- 734 [31] F. C. Christo, B. B. Dally, Modeling turbulent reacting jets issuing into a hot and diluted coflow,
735 *Combustion and Flame* 142 (2005) 117–129.
- 736 [32] B. Magnussen, On the structure of turbulence and a generalized eddy dissipation concept for
737 chemical reaction in turbulent flow, in: 19th Aerospace Sciences Meeting, Aerospace Sciences
738 Meetings, American Institute of Aeronautics and Astronautics, 1981.
- 739 [33] S. R. Shabaniyan, P. R. Medwell, M. Rahimi, A. Frassoldati, A. Cuoci, Kinetic and fluid dynamic
740 modeling of ethylene jet flames in diluted and heated oxidant stream combustion conditions, *Applied
741 Thermal Engineering* 52 (2013) 538–554.
- 742 [34] M. J. Evans, P. R. Medwell, Z. F. Tian, Modeling Lifted Jet Flames in a Heated Coflow Using
743 an Optimized Eddy Dissipation Concept Model, *Combustion Science and Technology* 187 (2015)
744 1093–1109.
- 745 [35] A. Mardani, Optimization of the Eddy Dissipation Concept (EDC) model for turbulence-chemistry
746 interactions under hot diluted combustion of CH₄/H₂, *Fuel* 191 (2017) 114–129.
- 747 [36] S. B. Pope, An explanation of the turbulent round-jet/plane-jet anomaly, *AIAA Journal* 16 (1978)
748 279–281.
- 749 [37] B. B. Dally, D. F. Fletcher, A. R. Masri, Flow and mixing fields of turbulent bluff-body jets and
750 flames, *Combustion Theory and Modelling* 2 (1998) 193–219.

- 751 [38] J. M. Hall, E. L. Petersen, An optimized kinetics model for OH chemiluminescence at high temper-
752 atures and atmospheric pressures, *International Journal of Chemical Kinetics* 38 (2006) 714–724.
- 753 [39] R. M. I. Elsamra, S. Vranckx, S. A. Carl, CH(A₂Δ) Formation in Hydrocarbon Combustion: The
754 Temperature Dependence of the Rate Constant of the Reaction C₂H + O₂ → CH(A₂Δ) + CO₂,
755 *The Journal of Physical Chemistry A* 109 (2005) 10287–10293.
- 756 [40] M. Tamura, P. A. Berg, J. E. Harrington, J. Luque, J. B. Jeffries, G. P. Smith, D. R. Crosley, Colli-
757 sional Quenching of CH(A), OH(A), and NO(A) in Low Pressure Hydrocarbon Flames, *Combustion
758 and Flame* 114 (1998) 502–514.
- 759 [41] M. T. Lewandowski, Z. Li, A. Parente, J. Pozorski, Generalised Eddy Dissipation Concept for
760 MILD combustion regime at low local Reynolds and Damköhler numbers. Part 2: Validation of the
761 model, *Fuel* 278 (2020) 117773.
- 762 [42] M. K. Le, S. Kook, Q. N. Chan, E. R. Hawkes, Comparison between OH* Chemiluminescence and
763 OH Planar Laser-Induced Fluorescence Images in a Light-Duty Optical Diesel Engine (2014) 4.
- 764 [43] N. Maes, M. Meijer, N. Dam, B. Somers, H. Baya Toda, G. Bruneaux, S. A. Skeen, L. M. Pickett,
765 J. Manin, Characterization of Spray A flame structure for parametric variations in ECN constant-
766 volume vessels using chemiluminescence and laser-induced fluorescence, *Combustion and Flame*
767 174 (2016) 138–151.
- 768 [44] R. Weber, J. P. Smart, W. vd Kamp, On the (MILD) combustion of gaseous, liquid, and solid fuels
769 in high temperature preheated air, *Proceedings of the Combustion Institute* 30 (2005) 2623–2629.
- 770 [45] M. de Joannon, P. Sabia, G. Cozzolino, G. Sorrentino, A. Cavaliere, Pyrolytic and Oxidative
771 Structures in Hot Oxidant Diluted Oxidant (HODO) MILD Combustion, *Combustion Science and
772 Technology* 184 (2012) 1207–1218.
- 773 [46] J. Ye, P. R. Medwell, B. B. Dally, M. J. Evans, The transition of ethanol flames from conventional
774 to MILD combustion, *Combustion and Flame* 171 (2016) 173–184.
- 775 [47] M. J. Evans, A. Chinnici, Water vapour effects on temperature and soot loading in ethylene flames
776 in hot and vitiated coflows, *Proceedings of the Combustion Institute* 38 (2021) 5383–5391.
- 777 [48] D. Escofet-Martin, Y.-C. Chien, D. Dunn-Rankin, PLIF and chemiluminescence in a small laminar
778 coflow methane-air diffusion flame at elevated pressures, *Combustion and Flame* (2022) 112067.

1 Pressurised combustion in hot and low-oxygen environments:
2 chemiluminescence imaging and modelling

3 Douglas B. Proud^{a,*}, M.J. Evans^{a,b}, J.A. Kildare^a, Q.N. Chan^c, P.R. Medwell^a

4 ^a*School of Mechanical Engineering, The University of Adelaide, Adelaide, SA 5005, Australia*

5 ^b*UniSA STEM, University of South Australia, Mawson Lakes, SA 5095, Australia*

6 ^c*School of Mechanical and Manufacturing Engineering, University of New South Wales, Sydney, NSW 2052, Australia*

7 **Supplementary Material**

8 *1. CFD model validation*

9 As mentioned in the main text, the CFD modelling results were compared to the “HM2” and “HM3”
10 open-JHC flames. Figure A1 displays this comparison, in the form of radial plots of the OH species at axial
locations of 30 mm and 60 mm from the jet exit plane.

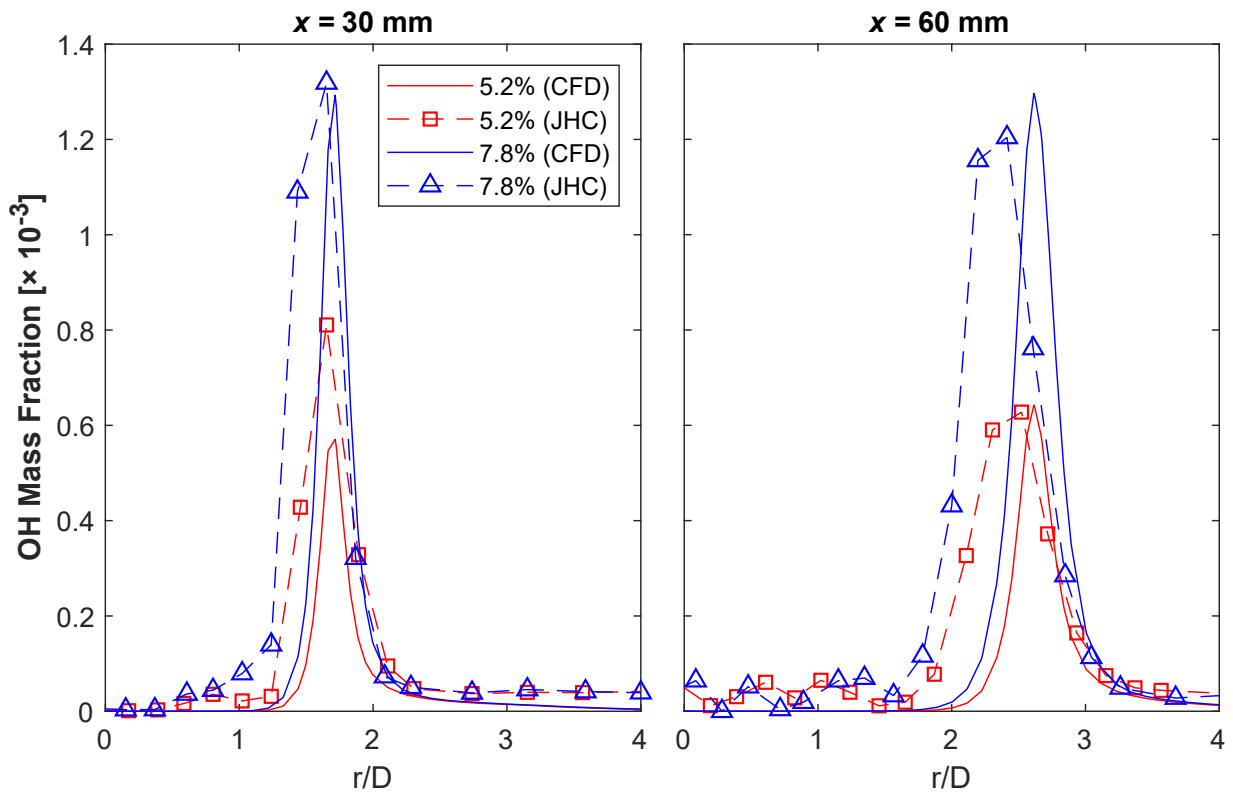


Figure A1: Comparison of radial profiles of OH concentration at axial locations (x) of 30 mm and 60 mm, for CFD modelling and experimental results. Experimental OH profiles obtained from Dally et al. [?].

11

*Corresponding author. E-mail: douglas.proud@adelaide.edu.au

12 1. Unfiltered jet flame imaging

13 Unfiltered images of the 3, 6 and 9% O₂ flames at absolute pressures of 1 bar and 7 bar are shown in
14 Figure A2, displaying the broadband radiation characteristics. As mentioned in the text, the flames are
15 virtually indistinguishable from the background luminescence at 3 and 6% O₂, while the 9% O₂, 7 bar case
displays evidence of soot formation.

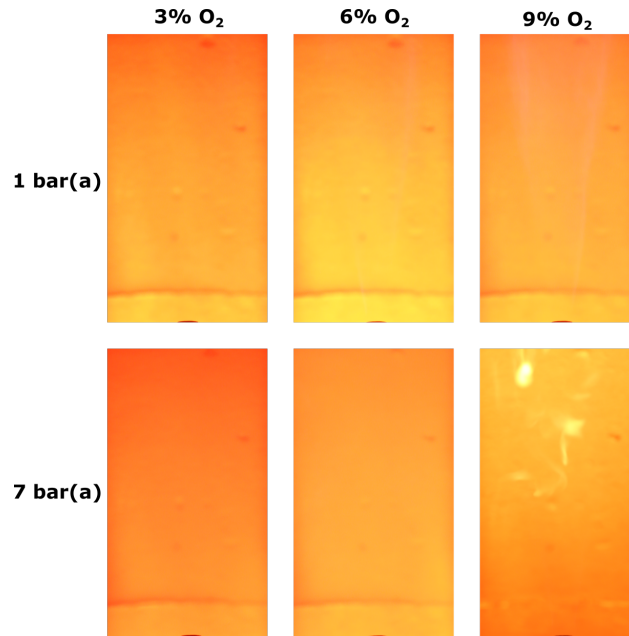


Figure A2: Unfiltered photographs of jet flames for the 3%, 6% and 9% O₂ coflows at absolute pressures of 1 and 7 bar. All images were captured with an exposure time of 1/125 s and 3200 ISO, with the exception of the 9% O₂, 7 bar case, which was captured with 400 ISO.

17 2. Additional modelling results: CFD and laminar flame simulations

18 In the analysis of the CFD results (§4.4), it was observed that the rate of reaction R1 displayed a non-
 19 monotonic behaviour as the pressure was increased. Figure A3 shows that, although the concentration of CH
 20 decreases consistently with increasing pressure for each of the cases, the overlap between CH and O₂—given
 21 by the product [CH]×[O₂]—initially increases at lower pressures for the 6% and 3% O₂ cases.

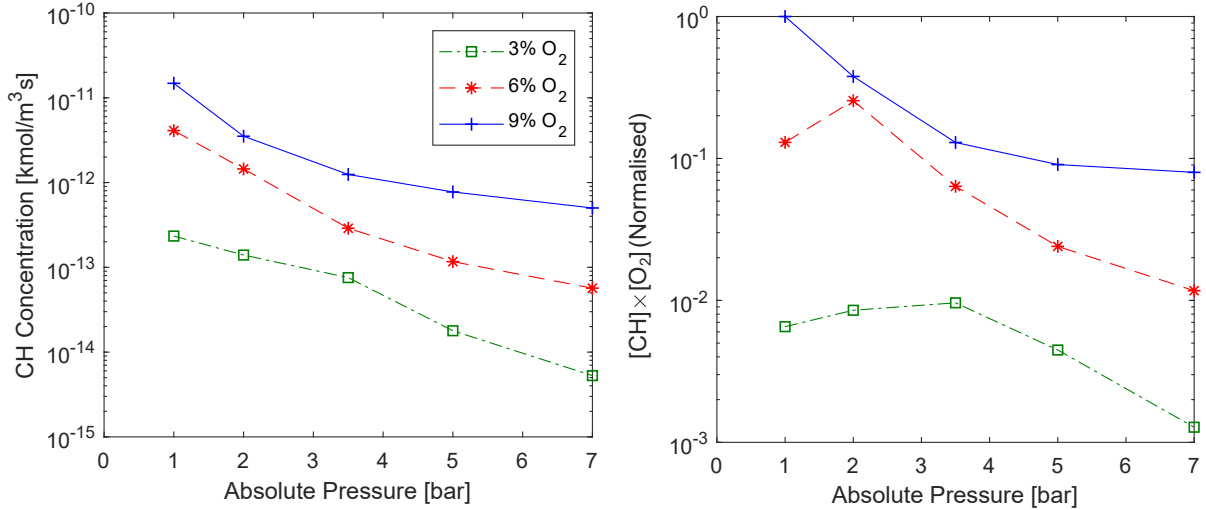


Figure A3: Plots of CH concentration and overlap of CH and O₂ (i.e. [CH]×[O₂]) as a function of pressure for the 3, 6 and 9% O₂ cases, from CFD modelling results.

22 In terms of the Chemkin simulations, the normalised sensitivity values are particularly useful for identify-
 23 ing the key reactions involved and their relative importance. Figure A4 shows the sensitivity results for OH*
 24 at the location of maximum OH* concentration, with the 1 bar results shown in the left column and 7 bar
 25 on the right, with separate columns for each O₂ concentration. Essentially, this provides an overview of the
 26 reactions which lead to both formation (positive) and consumption/quenching (negative) at this particular
 27 location.

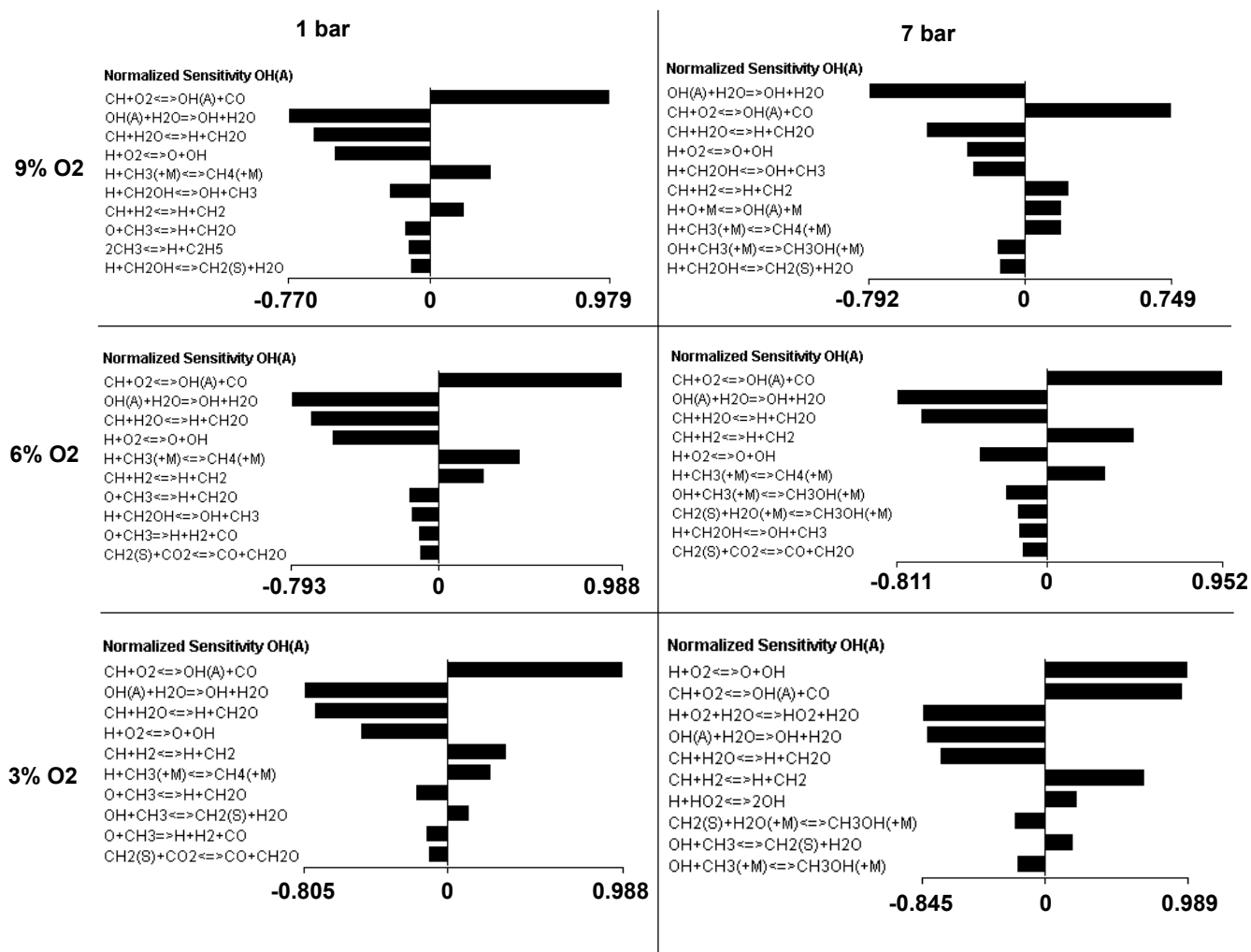


Figure A4: Normalised sensitivities of OH* to various reactions at 3, 6 and 9% O₂ and 1 and 7 bar(a), at the location of maximum OH* concentration based on the Chemkin simulations.

28 To provide further insight regarding how the underlying reactions R1 and R2 contribute to the overall
 29 presence of OH* in the laminar flame simulations (i.e. the Chemkin analysis), Figure A6 displays the mixture-
 30 fraction space profiles of these two reactions along with the OH* concentration on a separate vertical axis. It
 31 is interesting to note that, for the 1 and 3 bar cases, the profile for [OH*] essentially follows the profile of R1
 32 until it reaches the location at which that reaction rate peaks, after which it follows very closely the profile
 33 of R2. The 5 and 7 bar cases are similar; however, due to the reduced spatial separation between the two
 34 reactions, the [OH*] profile deviates away from the R1 curve prior to the peak location of that reaction—this
 35 is particularly evident for the 7 bar case.

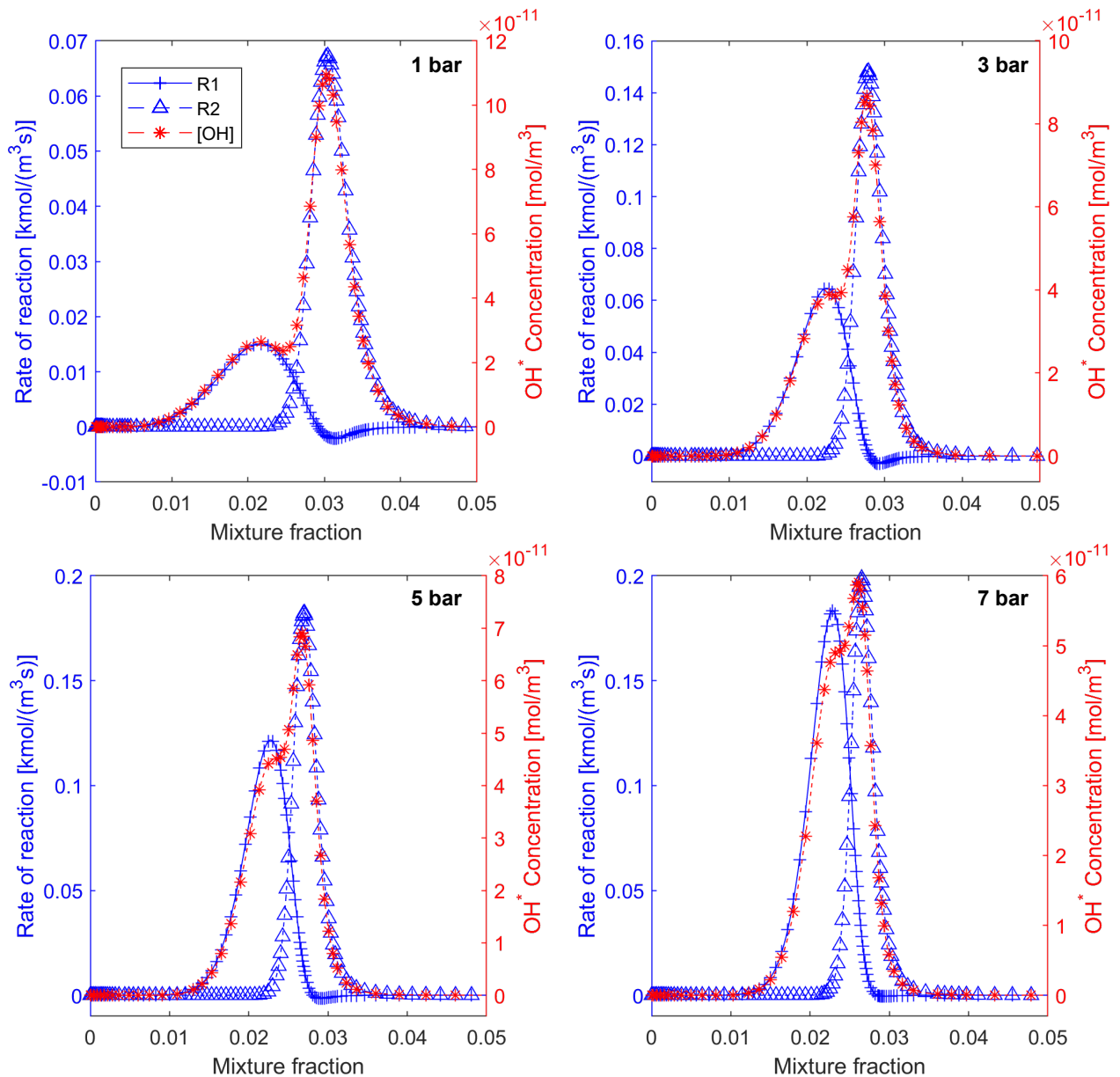


Figure A5: Mixture-fraction space profiles of reactions R1 and R2 (shown on left axis in blue) superimposed with OH concentration (shown on right axis in red).

36 It was also shown in §4.4 that the reason for the relative dominance of reaction R2 in the CFD modelling
 37 compared to the Chemkin simulations—particularly at 9% O_2 —is due to a higher O_2 concentration at the
 38 location of maximum CH concentration. The radial profile of O_2 concentration 30 mm downstream of the
 39 jet exit plane also showed a non-monotonic behaviour with respect to radial location, whereas it is expected
 40 that the O_2 concentration would increase monotonically from 0 on the fuel side to 9% (in this case) on the
 41 oxidant side for a nonpremixed flame. The fact that there is a relatively high O_2 concentration on the “fuel”
 42 side (which decreases to a minimum when CH is at a maximum), indicates that the O_2 from the coflow is
 43 not completely consumed by the reaction (or is entrained upstream before the flame is stabilised), and then
 44 continues to react, such that O_2 is supplied to the reaction zone from both sides.

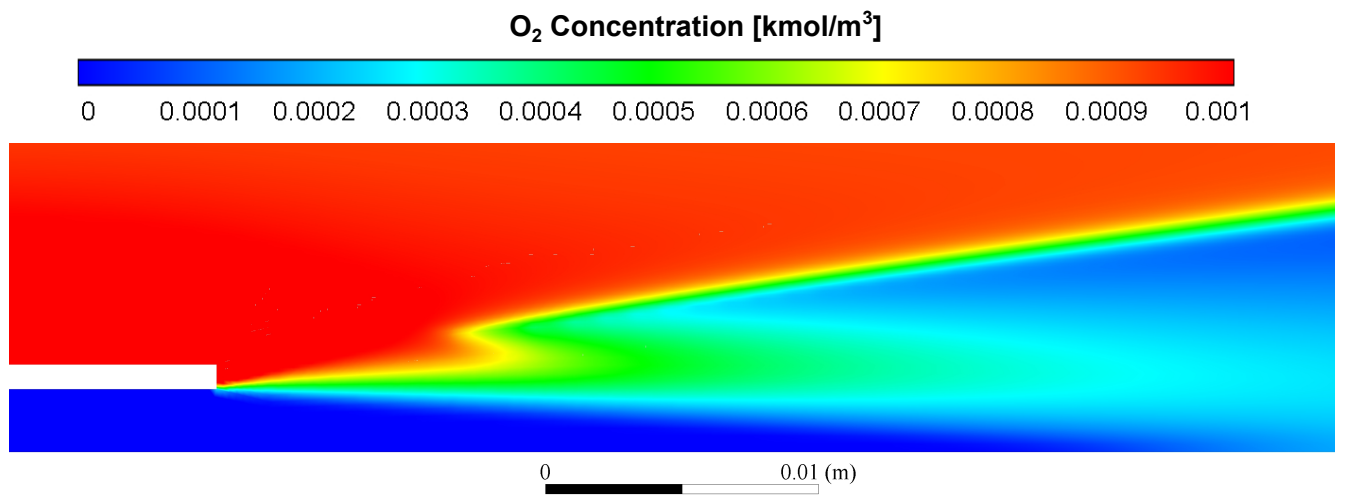


Figure A6: 2-D colour map of O₂ concentration from the CFD simulation of the 9% O₂, 1 bar case, highlighting the transport of O₂ to the fuel-rich side of the reaction zone.


Chapter 6

Experimental Investigation of the Flame Structure of Dilute Sprays Issuing into a Hot and Low-oxygen Coflow

Statement of Authorship

Title of Paper	Experimental investigation of the flame structure of dilute sprays issuing into a hot and low-oxygen coflow.
Publication Status	<input checked="" type="checkbox"/> Published <input type="checkbox"/> Accepted for Publication <input type="checkbox"/> Submitted for Publication <input type="checkbox"/> Unpublished and Unsubmitted work written in manuscript style
Publication Details	D. B. Proud , M. J. Evans, P. R. Medwell & Q. N. Chan (2021). " Experimental investigation of the flame structure of dilute sprays issuing into a hot and low-oxygen coflow." <i>Combustion and Flame</i> 230, Article 111439.

Principal Author

Name of Principal Author (Candidate)	Douglas B. Proud		
Contribution to the Paper	Conceived and set-up experimental configuration in coordination with supervisory team. Coordinated the operation of pulsed lasers and detectors (e.g. tuning of wavelengths, power/beam profile measurements, timing of pulses from different lasers, camera triggering) to achieve simultaneous imaging of spray droplets, intermediate species and soot. Performed experiments and data collection, processed data via the application of image processing techniques, analysed and interpreted data, generated figures from data and wrote manuscript.		
Overall percentage (%)	75		
Certification:	This paper reports on original research I conducted during the period of my Higher Degree by Research candidature and is not subject to any obligations or contractual agreements with a third party that would constrain its inclusion in this thesis. I am the primary author of this paper.		
Signature		Date	18-OCT-2022

Co-Author Contributions

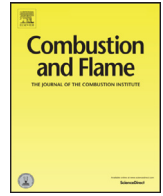
By signing the Statement of Authorship, each author certifies that:

- the candidate's stated contribution to the publication is accurate (as detailed above);
- permission is granted for the candidate to include the publication in the thesis; and
- the sum of all co-author contributions is equal to 100% less the candidate's stated contribution.

Name of Co-Author	Michael J. Evans		
Contribution to the Paper	Supervised the initial design/setup of the experimental apparatus and diagnostics, provided guidance with data analysis, provided feedback on manuscript.		
Signature		Date	17-Oct-2022

Name of Co-Author	Paul R. Medwell		
Contribution to the Paper	Supervised overall research direction and helped in identifying the purpose/scope of the experiments and techniques to be used. Assisted in data processing and provided feedback on manuscript.		
Signature		Date	17-OCT-2022

Name of Co-Author	Qing N. Chan		
Contribution to the Paper	Assisted in implementing image processing/filtering techniques. Provided feedback on manuscript relating to discussion and presentation of results.		
Signature	.	Date	17/10/2022



Experimental investigation of the flame structure of dilute sprays issuing into a hot and low-oxygen coflow

Douglas B. Proud^{a,*}, Michael J. Evans^{a,b}, Paul R. Medwell^a, Qing N. Chan^c

^aSchool of Mechanical Engineering, The University of Adelaide, Adelaide SA 5005, Australia

^bUniSA STEM, University of South Australia, Mawson Lakes SA 5095, Australia

^cSchool of Mechanical and Manufacturing Engineering, University of New South Wales, Sydney NSW 2052, Australia

ARTICLE INFO

Article history:

Received 25 October 2020

Revised 24 March 2021

Accepted 25 March 2021

Available online 21 April 2021

Keywords:

Spray combustion

Mild combustion

Laser diagnostics

Autoignition

Flame stabilisation

ABSTRACT

The combustion of liquid fuels in a hot and low-oxygen environment is commonly encountered in a range of practical situations. To enable investigation of the fundamental combustion processes relating to such applications, liquid fuels were injected into the reaction zone as dilute sprays in this study. Droplets of ethanol, *n*-heptane, and *n*-heptane/toluene blends were produced via an ultrasonic nebuliser, and were carried by air through a central jet to a hot coflow of combustion products. The resulting flames were then analysed using four simultaneous laser diagnostic techniques. Planar laser-induced fluorescence (PLIF) was implemented to perform imaging of key intermediate species, including hydroxyl (OH) and formaldehyde (CH₂O), while the Mie scattering technique was used to detect the location of droplets. The sooting behaviour of these flames was also investigated, via the laser-induced incandescence (LII) technique. The existence of distinct inner and outer reaction zones is a key feature of all of the flames studied, and this “double flame structure” was found to be related to partial premixing of air and fuel, as well as penetration of droplets into the inner reaction zone. A change in the stabilisation of the inner flame front was observed with variations in fuel type, with a greater likelihood of ignition kernels in the case of the *n*-heptane and *n*-heptane/toluene flames, whereas the equivalent ethanol flame displays a bifurcation structure. Variations in the jet Reynolds number and liquid fuel loading were also found to have a notable impact on the distribution and evaporation of droplets, which was in turn found to affect the formation of the double flame structure. Due to the complex coupling between turbulence, chemistry and droplet evaporation in these flames, the accurate prediction of such results *a priori* is not within the limits of current modelling capabilities. These findings provide a valuable insight to enable future advancements in spray combustion modelling and the design of practical combustion devices.

© 2021 The Combustion Institute. Published by Elsevier Inc. All rights reserved.

1. Introduction

The combustion of liquid fuels accounts for approximately 35% of the primary energy consumption in the modern world. Liquid fuels are typically injected in the form of a spray, to accelerate the evaporation and subsequent combustion of the fuel [1,2]. Despite the widespread use of liquid sprays in combustion devices such as gas turbines and reciprocating engines, current understanding of the behaviour of liquid spray flames remains incomplete, particularly in regards to the development and validation of accurate and efficient computational models [3]. This is largely due to the complex nature of the coupled interactions between spray break-up and evaporation, combustion chemistry, and turbulence.

In broad terms, a spray—or a certain region of a spray—can be classified as being either “dense” or “dilute”. For classification purposes, a spray can be considered dilute when the liquid loading is less than approximately 1% by volume and the interactions between droplets are negligible [4,5]. In practical situations, liquid fuels are typically injected as a dense spray, which subsequently breaks-up and evaporates, forming a dilute spray [6]. In order to focus on the fundamental combustion processes relating to fuel droplets in an experimental context, a dilute spray can be directly formed and transported into the reaction zone via a carrier gas. Detailed measurements of reactive scalars and droplet fields have previously been obtained for dilute sprays [5,7], as part of the International Workshop on Turbulent Combustion of Sprays (TCS), which is aimed at providing insight for the development of practical models. Despite this, there still remains a lack of detailed data for certain types of flames, particularly in conditions related to

* Corresponding author.

E-mail address: douglas.proud@adelaide.edu.au (D.B. Proud).

sequential gas turbines and engines using exhaust gas recirculation (EGR) [8,9].

Liquid sprays reacting in a high-temperature, low-oxygen environment are commonly encountered in combustion devices which use techniques such as EGR and mild combustion [10,11]. These methods enable improvements in efficiency and combustion stability, along with emissions reductions [12,13]. The term “mild” has been used here to encapsulate the features of moderate or intense low-oxygen dilution combustion, a particular regime with very high dilution by hot combustion products, characterised by distributed reaction zones, lower peak temperatures, and significant reductions in emissions of NO_x, CO and soot [14].

The behaviour of flames under mild combustion conditions is significantly different to that of conventional flames [15]. The reduced concentration of O₂ results in longer chemical time-scales [16], and a change in the stabilisation mechanism of visually lifted flames has been observed [17]. To examine the fundamental physical and chemical processes which govern flames in this regime, and to facilitate the development of numerical models, most studies have been focussed on relatively simple, gaseous fuels. Many of these fundamental experimental studies have been carried out using a type of burner commonly referred to as a “jet in hot cross/co-flow” (JHC) configuration [18–21], which allows the fuel composition and flow rate to be varied independently of the temperature and O₂ concentration of the oxidant stream, and also facilitates the use of laser diagnostic techniques.

The behaviour of liquid fuels in the mild combustion regime has also been investigated. To study the chemical effects in isolation, a series of experiments were performed with a JHC configuration using pre-vaporised fuels, including ethanol and blends of *n*-heptane/toluene [22,23]. A change in flame structure was observed when the O₂ concentration was increased from 3% to 9%, suggesting a shift away from the mild combustion regime [22]. An analysis of reaction fluxes indicated a fundamental change in chemical kinetics, with greater sensitivity to fuel-specific reactions in the 9% O₂ case [22]. A significant increase in soot formation with addition of toluene to the fuel was also observed, which was found to have a notable impact on the flame temperature [23]. Measurements of the gas, droplet and temperature fields were attained for the “Delft spray in hot coflow” (DSHC) flames [24], which uses a pressure-swirl atomiser to generate droplets. These experiments highlighted a change in spray break-up and evaporation processes when comparing spray flames in a coflow of air versus a hot-diluted coflow. This change was found to have a large impact on the flame structure and temperature field, with the rapid spray break-up and vaporisation in the hot coflow leading to a reduction in peak temperatures and a more uniform distribution. The temperature profiles also indicated the presence of separate inner and outer reaction zones for both coflow conditions, although this was most obvious in the case of an air coflow.

The existence of multiple reaction zones is a commonly observed feature of spray flames. In a simplified numerical analysis of a counterflow spray configuration, two distinct flame zones were predicted to occur under certain conditions; this was attributed to the flame exhibiting both premixed and diffusion-like characteristics, with a merging of the two zones at high strain rates [25]. This “double flame” structure has been observed in other experiments involving sprays [26,27], and has also been reproduced via large-eddy simulation (LES) [28]. This latter study found that there were actually up to four distinct reaction regions in the case of an air coflow, despite the associated experimental results suggesting a double flame structure [28]. Additionally, the formation of these multi-flame structures was found to be very sensitive to the relative evaporative and chemical time-scales, highlighting the complexity involved in the modelling of dual-phase combustion [28]. The flame structure has also been investigated using a

RANS approach, where bifurcating flame fronts were found to occur at lower coflow temperatures [29]. Although the presence of multi-flame structures (i.e. flames with distinct reaction zones) has been observed both experimentally and numerically, the underlying mechanisms which lead to these structures requires further investigation to enable robust and efficient numerical models to be developed.

To bridge the gap between the understanding of gaseous fuels undergoing autoignition in a hot coflow and the experiments performed with piloted dilute sprays [30], a dilute spray burner for studying spray flames in a hot and low-oxygen coflow was developed [31]. Imaging of the hydroxyl (OH) radical was performed to study the formation of ignition kernels, and it was found that auto-ignition occurs in a relatively gradual manner and over a larger range of distances compared with gaseous flames [31]. In a separate study with the same burner configuration [32], a double flame structure was observed when air was used as the carrier gas, which was hypothesised to be a result of vaporised liquid mixing with air to produce localised, ignitable mixtures. Another important feature of these flames was the presence of formaldehyde (CH₂O) prior to OH formation, highlighting the importance of this radical in the autoignition process. Heat release rate was also examined qualitatively in this study, using the product [OH]×[CH₂O] as a marker [32]. A limitation of these studies [31,32], and indeed all of those involving sprays in hot and vitiated coflows, is the lack of simultaneous imaging of both droplets and chemical species, which has been performed in previous studies involving dilute spray burners [5,33].

The present study aims to extend the understanding of spray combustion in a hot and low-oxygen environment, using a dilute spray burner in a JHC configuration. The stabilisation mechanisms and near-field flame structure are of particular focus, along with the distribution of fuel droplets and the effect that this has on the flame further downstream. The results presented correspond to constant coflow conditions, while a range of jet boundary conditions and fuel compositions are investigated. A series of simultaneous laser diagnostic techniques are implemented, providing a unique insight into the structure of these flames and facilitating future development of spray combustion models. Planar laser-induced fluorescence (PLIF) is performed to allow imaging of the hydroxyl (OH) and formaldehyde (CH₂O) radicals, while the Mie scattering technique is used to capture the location of droplets. Additionally, laser-induced incandescence (LII) is performed to measure the soot volume fraction, and how this varies with fuel composition.

2. Methodology

2.1. Spray burner description

The spray burner used in this study shares several features with well-studied JHC and dilute spray burners, which have been used to study both piloted and autoignitive flames [18,22,30–32,34]. The burner and laser diagnostics configuration is equivalent to that which has previously been used to study hydrogen flames with toluene addition, albeit without a hot coflow [34]. A schematic of this burner is shown in Fig. 1. Fuel droplets with minimal initial momentum are generated using an ultrasonic nebuliser, with an estimated Sauter mean droplet diameter (SMD) of 30 μm at the nebuliser head. This estimate is based on data from the manufacturer (Sonotek), in conjunction with a commonly used correlation for the diameter of droplets (d_{SMD}) generated via ultrasonic nebulisation [35]:

$$d_{SMD} = c \left(\frac{8\pi\sigma}{\rho f^2} \right)^{1/3}, \quad (1)$$

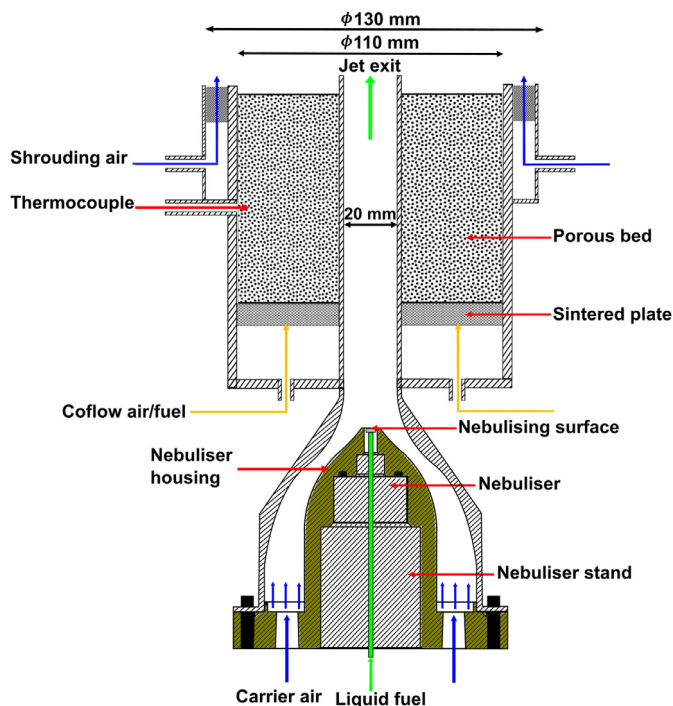


Fig. 1. Schematic cross-section of spray burner and nebuliser (not to scale).

where c is an empirically derived constant which depends on the specific nebuliser used, f is the vibrational frequency of the nebuliser, and σ and ρ are the surface tension and density of the liquid being used, respectively. The viscosity (μ) of the liquid is also known to have an effect on the atomisation process, although previous findings suggest that this effect only becomes significant for $\mu > 10$ mPa·s [36], which is an order of magnitude greater than the viscosity of the liquids used in this investigation.

The nebuliser is located inside a brass housing which has a smooth, tapered exterior, which is in turn contained within a smooth, stainless steel internal contraction. Carrier air flows around the outside of the brass housing, to collect the droplets at the nebulising surface, which is flush with the top of the brass housing. These droplets are then carried by air to the jet exit, which is located approximately 270 mm downstream of the nebuliser. The jet diameter (D) is 20 mm (ID), while the surrounding coflow diameter is 110 mm. The hot coflow is produced via the lean premixed combustion of natural gas and air, stabilised on a porous bed burner positioned 10 mm upstream of the jet exit plane. The porous bed has a depth of 90 mm, containing flint clay with a maximum flint size of 5 mm. The coflow conditions were held constant, with a temperature of 1690 K and a calculated O_2 concentration of 7.5% (by volume). These coflow conditions were selected to enable comparisons with previous studies involving prevaporised fuels [23,37]. Air at room temperature issues from a 130 mm (OD) annulus surrounding the coflow with a velocity of 0.4 m/s, to reduce mixing of the jet and coflow with the surrounding quiescent air.

Four different liquid fuel compositions were used in this study; namely ethanol, n -heptane, and 3:1 and 1:1 blends of n -heptane and toluene (n -heptane:toluene, by liquid volume). These were selected to allow the effects of fuel chemistry to be analysed, particularly in regards to soot formation, as well as the potential for comparison against previous results. Additionally, the variation in physical properties of the different liquids is considered when comparing the flame cases. For the ethanol flames, the flow rates of both the carrier gas (air) and the liquid fuel were also inde-

Table 1

Table of flame cases, indicating the fuel composition, fuel loading (\dot{m}_f), jet equivalence ratio (Φ_{jet}) and Reynolds number (Re_{jet}).

Case	Fuel composition	\dot{m}_f [g/s]	Φ_{jet}	Re_{jet}
E15-5	Ethanol	0.15	0.95	5000
E21-5	Ethanol	0.21	1.3	5000
E27-5	Ethanol	0.27	1.7	5000
E21-3	Ethanol	0.21	2.2	3000
E21-6	Ethanol	0.21	1.1	6000
H21-5	n -heptane	0.21	2.2	5000
HT21-5	3:1 n -heptane:toluene	0.21	2.2	5000
TH21-5	1:1 n -heptane:toluene	0.21	2.1	5000

pendently varied. These correspond to changes in the jet Reynolds number (Re_{jet}) and the liquid fuel loading (\dot{m}_f), respectively, noting that the changes in \dot{m}_f have a negligible impact on the bulk volumetric flow rate through the jet.

The operating conditions and the name of their associated flame cases are listed in Table 1, along with the values of equivalence ratio for each case, based on the total mass of fuel and carrier air. The cases are named according to the type of fuel used (E \equiv ethanol, H \equiv n -heptane, T \equiv toluene), the liquid fuel flow rate, and the jet Reynolds number. For example, case "E21-5" refers to an ethanol flame with 0.21 g/s liquid fuel loading and Reynolds number of 5000. To differentiate between the 3:1 and 1:1 n -heptane/toluene blends, "HT" is used for the 3:1 blend, while "TH" is used for the 1:1 blend. The surface tension (σ), vapour pressure (P_v) and boiling point (T_b) of the pure liquid fuels used are shown in Table 2, in addition to the values of ρ and μ for all fuel compositions.

2.2. Diagnostic techniques

The optical diagnostics configuration used in this study was identical to that which was used in a previous study with a similar spray burner [34]. Simultaneous imaging of soot volume fraction, fuel droplets, hydroxyl radicals (OH) and formaldehyde (CH_2O) was achieved using four separate laser diagnostic techniques. Three Nd:YAG lasers and one Nd:YAG-pumped dye laser were used to produce vertical sheets of 10 Hz pulsed laser light of different wavelengths, each with a nominal height of 15 mm. The burner was traversed vertically through the laser sheet to measure different heights (x) in the flame, ranging from the jet exit plane to 112 mm downstream ($x/D = 5.6$). This range allows the near-field flame structure to be analysed, in terms of flame stabilisation and the existence of multiple reaction zones. For each diagnostic, sets of 255 images were captured for each flame case and measurement location, allowing both instantaneous and time-averaged analyses to be performed.

The frequency-doubled output of an Nd:YAG laser (532 nm) was used to observe fuel droplets via the Mie scattering technique. The laser was operated with an energy of 0.5 mJ/pulse, and the scattered light was detected using a CCD camera through an $f/5.6$ lens with a 500 ns gate width. The lens was fitted with a band-pass filter centred at 532 nm with a FWHM of 10 nm and transmission $> 85\%$, to prevent interference from other signals.

Planar laser-induced fluorescence (PLIF) was used for imaging of both OH and CH_2O . For the OH-PLIF, a frequency-doubled dye laser was tuned to a wavelength of 282.927 nm to excite the $Q_1(6)$ transition of the OH radicals. The $Q_1(6)$ transition was selected due to its relatively low sensitivity to temperature fluctuations in the range of interest, and the fact that it provides a stronger signal in comparison to the $Q_1(7)$ transition. The output of the dye laser had a measured energy of approximately 1 mJ/pulse, and it was pumped by a frequency-doubled Nd:YAG laser. The resulting fluorescence of OH radicals was imaged using an ICCD camera oper-

Table 2

Table of liquid fuel properties. All properties correspond to a pressure of 1 bar and temperature of 20°C, with mixture properties calculated based on empirical correlations for binary mixtures [38,39].

Fuel Composition	ρ [kg/m ³]	μ [mPa·s]	σ [mN/m]	P_v [kPa]	T_b [°C]
Ethanol	789	1.2	22.4	6.0	78.4
<i>n</i> -heptane	684	0.41	20.1	5.3	98.4
Toluene	867	0.59	28.5	2.9	110.6
3:1 <i>n</i> -heptane:toluene	728	0.44			
1:1 <i>n</i> -heptane:toluene	774	0.47			

ated with a gate width of 100 ns, with an $f/3.5$ UV lens. A 310 nm bandpass filter (10 nm FWHM, peak transmission > 70%) was fitted to the UV lens.

For the CH₂O-PLIF, the third harmonic (355 nm) of an Nd:YAG laser was used, with a measured energy of 120 mJ/pulse. An ICCD camera (100 ns gate width) was used for CH₂O imaging, with a bandpass filter centred at 410 nm (10 nm FWHM, transmission > 45%), along with an $f/1.2$ lens. It should be noted that UV excitation is known to cause broadband fluorescence of a range of carbonaceous species in a flame, including polyaromatic hydrocarbons (PAH). In most of the results presented, particularly for measurements made near the flame base, CH₂O is expected to dominate the signal, as has been observed in previous studies of similar flames stabilised via autoignition [5]. However, since there is some interference, particularly for the *n*-heptane/toluene flames and in the downstream locations, the results presented in this paper refer to the signal detected from the 355 nm laser using the label of “UV” to account for this. This scalar measurement is indicative of precursor reactions, whether the collected signal is CH₂O or other species which fluoresce in the detected UV region.

Laser-induced incandescence (LII) was used to measure the soot volume fraction (f_v), using the fundamental output (1064 nm) of an Nd:YAG laser with a fluence of 800 mJ/cm²/pulse at the detection location. This ensures that the measurements correspond to the “plateau region”, in which the LII signal is less sensitive to fluctuations in the laser power [40–42]. The incandescence from the soot particles was observed through an ICCD camera with an $f/1.8$ lens and a gate width of 100 ns. The camera was also fitted with a bandpass filter, with peak transmission of 45% at 430 nm and FWHM of 10 nm. In order to quantify the soot measurements, calibration was performed against extinction measurements in a premixed, laminar flame (ethylene-air, $\Phi = 2.4$) stabilised on a McKenna burner, similar to previous studies [23,34,43].

The timing of the lasers and cameras was controlled using a combination of delay/pulse generators, configured such that all laser pulses were within 400 ns of each other. The 1064 nm LII pulse occurred last, to avoid interference from the broadband incandescent radiation. It should be noted that despite the Mie scattering camera being operated with a gate width of 500 ns, such that there was overlap with the 1064 nm pulse, there was no appreciable interference from LII, due to the strength of the Mie scattering signal. Images were corrected for dark charge, vignetting, and any background signal present, and the OH-PLIF signals were also corrected to account for the variation in intensity of the laser sheet in the vertical direction. Images were spatially matched to sub-pixel accuracy, with a pixel size of $\sim 130\mu\text{m}$. A 3×3 median filter was applied to the raw PLIF and LII images to improve the signal-to-noise ratio, while the Mie scattering images were left unfiltered. Out-of-plane resolution (i.e. sheet thickness) has been estimated to be approximately 400 μm .

Additional processing of the Mie scattering images was performed in order to extract data related to the number of droplets and their spatial distributions. A counting algorithm based on the binarised Mie scattering images was implemented, to determine the number and location of droplets in each instantaneous image.

A radial weighting was also applied, such that the droplet count is scaled relative to the distance from the centreline, to account for cylindrical integration of the planar measurements. This process was applied to a set of 255 images for each case, and these values were then averaged following the removal of any outliers, ensuring statistical convergence of the mean data. For $x/D < 3.0$, the uncertainty in these measurements ranges from 2% to 6%, while the uncertainty across all axial locations and flame cases is less than 10%. To analyse the droplet distributions with respect to the underlying flame structure, the UV-PLIF signal was used as a spatial threshold for the Mie scattering images, such that the droplets could be divided into those which occur inside the continuous CH₂O layer, and those which occur outside. In order to isolate the continuous structures in the UV-PLIF images, a combination of image processing techniques were implemented, following a similar method to that which has previously been used to detect primary particles in images of soot aggregates [44–46]. Specifically, the process involved dilation and erosion of the images, and the resulting structures were filtered by size and eccentricity. The division of the images into “inner” and “outer” regions is further discussed in context with the structure of the flames in Section 3.3.

Photographs of the flames were captured using a DSLR camera, with exposure times ranging from 30 s to 250 μs , although long exposures were not achievable for certain cases due to saturation. The photographs presented in this paper were all captured with an f -number of 16 and an ISO value of 100, with manual focus and white balance.

3. Results and discussion

3.1. Visual observations

Photographs of the eight different flames, corresponding to changes in fuel loading, Reynolds number and fuel composition, are shown in Fig. 2. For the ethanol flames, the photographs shown have exposure times of 4 s, while the *n*-heptane and *n*-heptane/toluene flames have exposures of 0.5 s; these different exposures were required due to the differences in flame luminosities resulting from the increased soot loading of the *n*-heptane and *n*-heptane/toluene flames. All other camera settings were held constant for the different cases. The boxed region in the images represents the range of heights at which laser diagnostic data were collected in this study.

The increase in luminosity for the *n*-heptane and *n*-heptane/toluene flames is clearly evident in the photographs (particularly taking the different exposures into account), which is attributed to higher levels of soot in these flames. Looking at the ethanol flames alone, there also appears to be an increase in luminosity with increasing fuel loading, and decreasing Re_{jet} (which also corresponds to increasing equivalence ratio). With the exception of the *n*-heptane/toluene flames (cases HT21-5 and TH21-5), a blue inner cone can also be observed at the base of the flames. A fainter blue region can be observed outside of the inner cone near the base of some of the flames (particularly the E21-3 flame), which transitions to a yellow/orange flame further

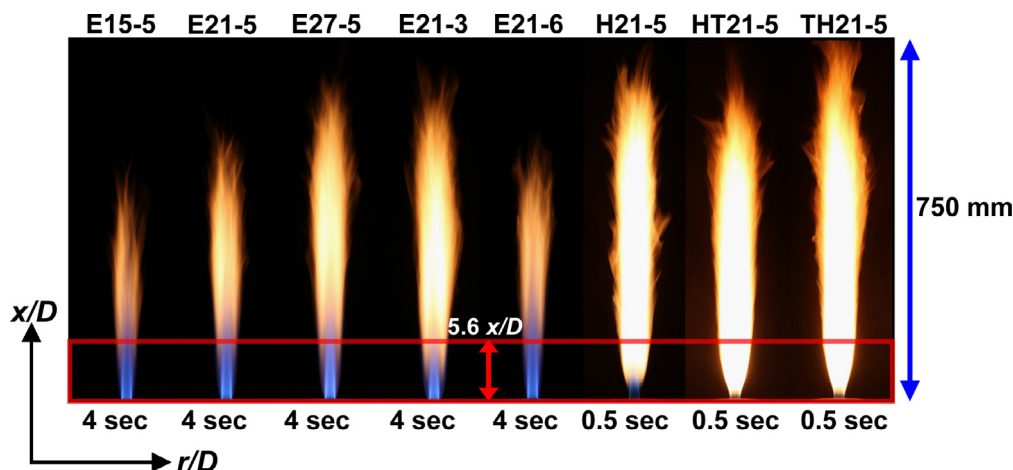


Fig. 2. Flame photographs captured with a DSLR camera with exposure times as shown, with an f-number of 16 and ISO of 100.

downstream, suggesting a double flame structure. The near-field flame structure has a significant impact on the overall appearance of these flames—this is further discussed in Sections 3.4 and 3.5.

The photographs show noticeable changes in the visible flame length for the different cases. The first three images, looking from left-to-right, show a consistent increase in flame length with fuel loading. Since the flow rate of carrier air is held constant for these cases (i.e. Re_{jet} is constant), Φ_{jet} is also directly proportional to the fuel loading, as shown in Table 1. Comparing the photos of the E21-6 and E21-3 flames, it can be seen that Re_{jet} also has an impact on flame length, with a noticeable increase in length when the Reynolds number is decreased from 6000 to 3000. Once again, it should be noted that the change in Re_{jet} is accompanied by a change in Φ_{jet} ; in this case the two are inversely proportional. It can also be seen that the *n*-heptane and *n*-heptane/toluene flames have a longer flame length than the ethanol flame with the equivalent fuel and air flow rates (E21-5). Comparing them to the E21-3 flame, however, the flame lengths are approximately the same, and these flames all have approximately the same value of Φ_{jet} . These observations suggest that there is a relationship between flame length and Φ_{jet} , noting that the equivalence ratio is based on the central jet alone. It is therefore hypothesised that partial premixing between fuel and oxidant in the jet is of importance in these flames, as has been suggested in a previous study of dilute sprays carried by air [32].

3.2. Instantaneous OH-PLIF, UV-PLIF and Mie scattering signals

To analyse the flame structure in detail, imaging of OH-PLIF, UV-PLIF and droplet Mie scattering was performed at axial locations ranging from the jet exit plane to $x/D = 5.6$. Figure 3 displays selected instantaneous images and a superimposed image of the three different signals, for the E21-5 flame with the laser sheets centred at $x/D = 3.0$. These images were selected as they were deemed to be representative of the “typical” instantaneous signals obtained, and they display several key features of the flames studied. Also shown in the superimposed image is the overlap between the OH and UV signals (shown in dark blue), which was determined based on the product $[OH] \times [UV]$.

As suggested by the photographs in Fig. 2, a double flame structure is evident from the OH-PLIF images, with two distinct OH layers on either side of the centreline, although the outer layer is significantly less intense (by a factor of approximately two). An additional regional region of OH can be seen on the inside, which corresponds to a separate reaction zone around an individual fuel droplet. The

product $[OH] \times [UV]$ indicates that there is some overlap between OH and CH_2O in this region, which is indicative of local heat release [47]. The presence of an inner and outer flame front has been observed previously for similar flames [24,26], where it is said to be caused by larger droplets being transported into the coflow, while smaller droplets (i.e. those with a small Stokes number) follow the flow field and move closer to the centreline. However, in a previous study with the same burner as that used in the current study, it was found that droplets tend to cluster near the pipe walls prior to exiting the jet [34]. This was attributed to the phenomena of Saffman lift and turbophoresis [48], which are associated with low Stokes number flow, suggesting that smaller droplets are more likely to be situated further from the centreline. Interestingly, while there is some evidence of fuel droplets penetrating the inner OH layer in Fig. 3, the Mie scattering signal is low in this region—indicating that the droplets exist between the two flame fronts further upstream and have evaporated by $x/D = 3.0$. The distribution of droplets with respect to the two flame fronts is further explored in Section 3.4.

In Fig. 3, the label of “UV” has been used to refer to the CH_2O -PLIF signal, as discussed in Section 2.2. The UV signal that lies just inside of the inner OH layer indicates the presence of intermediate species associated with the preheat region—the same being true for the region enclosing the OH layer around the reacting droplet. In the region circled in Fig. 3(d), an isolated region of UV-PLIF can be observed. Some high-intensity circular regions of UV-PLIF can also be seen in Fig. 3, which at first glance appear to be related to interference caused by Mie scattering of the 355 nm light by droplets. However, further analysis of the UV images (for a range of axial locations and cases), in conjunction with the Mie scattering images from the 532 nm laser, indicates that interference from Mie scattering signal in the UV images is not significant. It is instead hypothesised that these high-intensity regions are related to pre-ignition reactions taking place around evaporating droplets; this is supported by the fact that these structures are observed more often in the regions corresponding to the formation of intermediate species.

To further illustrate the key features of these flames, Fig. 4 shows an additional superimposed image, centred at $x/D = 1.5$, with labels to highlight particular aspects of the flame. Also included in Fig. 4 is a post-processed version of the UV-PLIF image from the same instantaneous shot, where the continuous CH_2O structure on either side of the centreline has been isolated, as discussed in Section 2.2. This is particularly useful for analysing the spatial distribution of droplets, which is explored in Section 3.4.

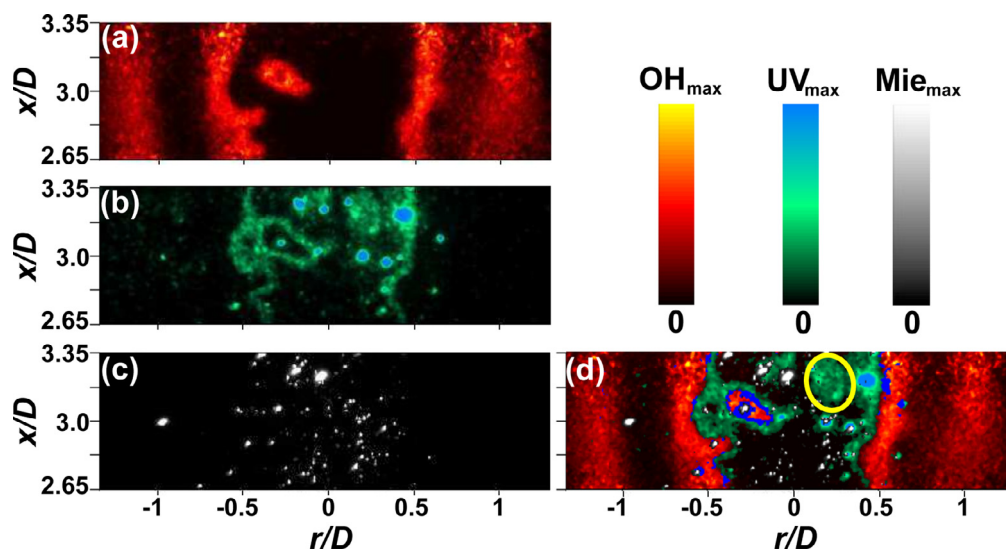


Fig. 3. Selected instantaneous spatially and temporally matched images of (a) OH-PLIF, (b) UV-PLIF (CH_2O) and (c) Mie scattering, and (d) the three signals superimposed. Signal overlap ($[\text{OH}] \times [\text{UV}]$) is shown in dark blue. Flame case E21-5, centred at $x/D = 3.0$. (For interpretation of the references to color in this figure legend, the reader is referred to the web version of this article.)

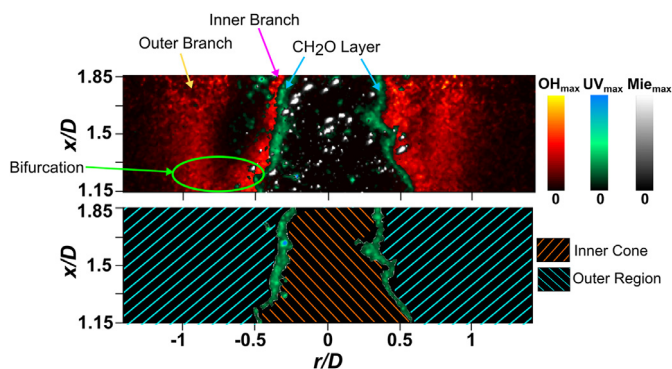


Fig. 4. Instantaneous superimposed images OH-PLIF, UV-PLIF and Mie scattering, with key features as indicated. Flame case E21-5, centred at $x/D = 1.5$.

3.3. Instantaneous flame structure

To provide an insight into the near-field flame structure for the different cases, a series of superimposed images near the jet exit are shown in Fig. 5. These images are centred at an axial location of approximately 7 mm above the jet exit ($x/D = 0.35$), such that the bottom of the laser sheet is aligned with the jet exit plane. It is evident from Fig. 5 that all of the flames are attached, at least in terms of their outer flame front. The bifurcation of the flame into an inner and outer front can also be seen in some of the cases in Fig. 5—this is most noticeable on the left-hand side of the E15-5 flame case. The CH_2O layer lies along the inside of this inner flame front (overlap is shown in blue), and in the cases where the “branching off” of the flame takes place, there appears to be no UV-PLIF signal corresponding to the outer branch. This can also be seen in Figs. 3 and 4, where the UV-PLIF signal lies within the inside OH layer. This suggests that the inside flame front is the result of some of the fuel becoming prevaporised and mixing with the carrier air, since the concentration of CH_2O , and hence the UV-PLIF signal, is expected to be significantly higher under partially premixed conditions [49].

An interesting structure can be observed in the images in Fig. 5(c), where there is no indication of an inner OH layer, yet the CH_2O layer appears to be branching away from the OH, as in-

dicated by the lack of $[\text{OH}] \times [\text{UV}]$ signal in the upper regions of the images (particularly on the right-hand side of both images). This is indicative of pre-ignition reactions of the prevaporised fuel, leading to a lifted inner flame further downstream [32]. To further illustrate this, selected instantaneous UV- and OH-PLIF images for the H21-5 case, centred at $x/D = 0.75$, are shown in Fig. 6.

Distinct ignition kernels can be observed in the OH signals in Fig. 6; these are accompanied by the presence of CH_2O , which represents the preheat region prior to autoignition. It should be mentioned that due to the turbulent nature of the flames, out-of-plane effects could lead to apparent “discontinuities” in the OH sheet which are not actually present; however, there are several reasons why this is unlikely to be the case. First of all, these flames are dominated by streaming flow in the axial direction, such that out-of-plane effects are not expected to be significant. If out-of-plane effects were responsible for the OH structures observed, then the CH_2O layer would be expected to show the same discontinuity, which is not the case. Additionally, the fact that the discontinuities are accompanied by CH_2O , and in some cases surrounded by it, further indicates that they are in fact ignition kernels, since this has been observed in previous studies involving autoignition and local extinction events [15,47]. Finally, the discontinuities occur with much greater frequency for the *n*-heptane and *n*-heptane/toluene flames as opposed to the ethanol flames, and fuel type would not be expected to have a significant impact on out-of-plane effects. Therefore, it can be concluded that the isolated OH structures do indeed represent ignition kernels.

In each of the instantaneous images shown in Fig. 6, the ignition kernels can be seen to form along the continuous CH_2O layer; more specifically, they tend to form on the outside of this layer—examples of this are labelled as A in Fig. 6. Analysis of a series of images for this particular case revealed that when ignition kernels are detected (approximately 60% of images at $x/D = 0.75$), there is a 75% probability that they occur along the outside of the CH_2O layer, while the remaining 25% are enclosed within a layer of CH_2O (see the features labelled B in Fig. 6). The fact that there is always UV-PLIF signal on the inside of the ignition kernels (in a radial sense) is an important observation, as it shows that the formation of intermediate species (including CH_2O) within the inner, partially premixed region is crucial to the formation of the inner flame structure.

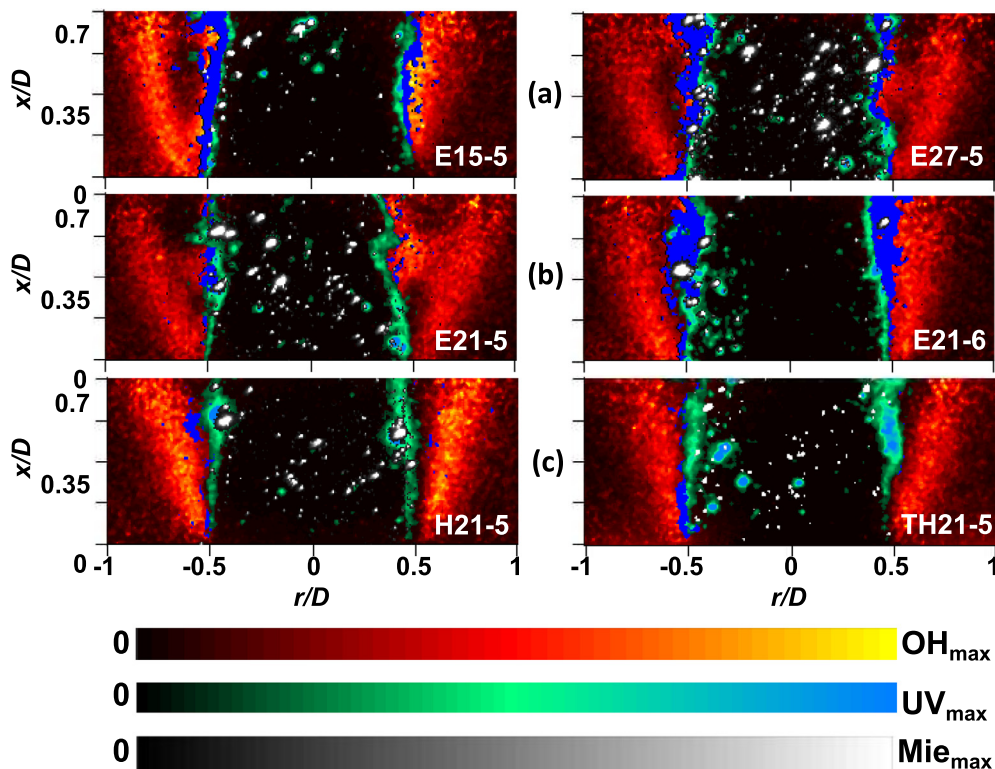


Fig. 5. Superimposed signals from fuel droplets, OH and CH_2O for ethanol and *n*-heptane/toluene flames, centred at $x/D = 0.35$. Row (a) shows variation of fuel loading, row (b) shows variation of Re_{jet} , and row (c) shows the effect of toluene addition. $[\text{OH}] \times [\text{UV}]$ is included in dark blue. (For interpretation of the references to color in this figure legend, the reader is referred to the web version of this article.)

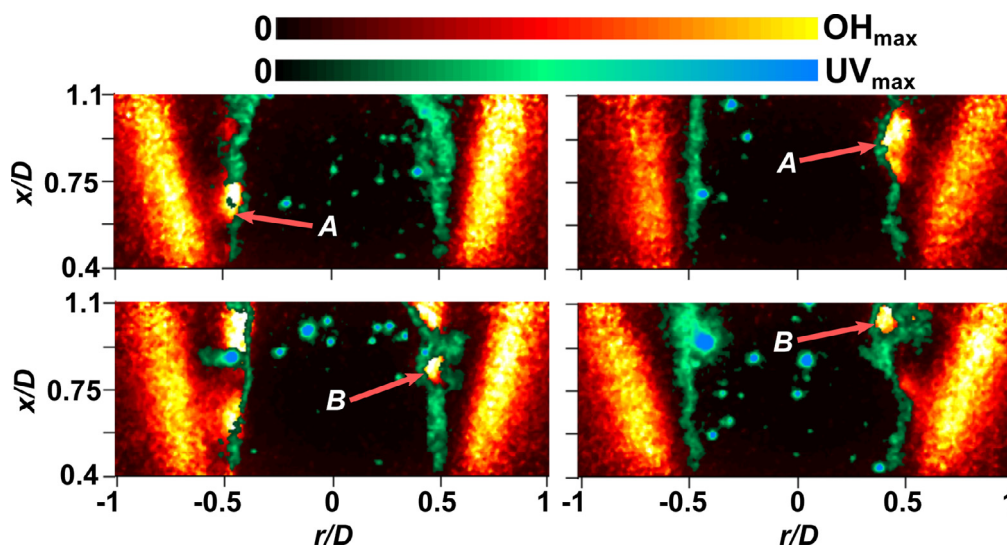


Fig. 6. Selected instantaneous, superimposed images of OH- and UV-PLIF for the H21-5 flame, centred at $x/D = 0.75$.

The occurrence of ignition kernels at $x/D = 0.75$ was also detected for the *n*-heptane/toluene flames, while the ethanol flames did not show this feature consistently at this axial location. In the equivalent ethanol case (E21-5), the inner OH layer begins to form nearer to the jet exit, where bifurcations in the OH layer are more likely to occur, rather than isolated ignition kernels further downstream. In previous experiments using prevaporised fuels under similar conditions [50], an increase in lift-off height has been observed for *n*-heptane flames in comparison with ethanol. In the context of the current study, this suggests that the increased tendency for ethanol to ignite near the jet exit leads to the in-

ner flame branching off from the stabilised, outer structure (i.e. a bifurcation), whereas for the *n*-heptane and *n*-heptane/toluene flames, distinct ignition kernels are more likely to occur since the outer OH layer has greater separation further downstream. In addition, the lower boiling point and higher vapour pressure of ethanol (see Table 2) could also contribute to the inner flames stabilising nearer to the jet in these cases. A change in the autoignition process of ethanol droplets in comparison to *n*-heptane has been previously observed [51], where it was found that the lower volatility of *n*-heptane leads to the formation of flames around individual droplets. It is also worth mentioning that the stoichiometric mix-

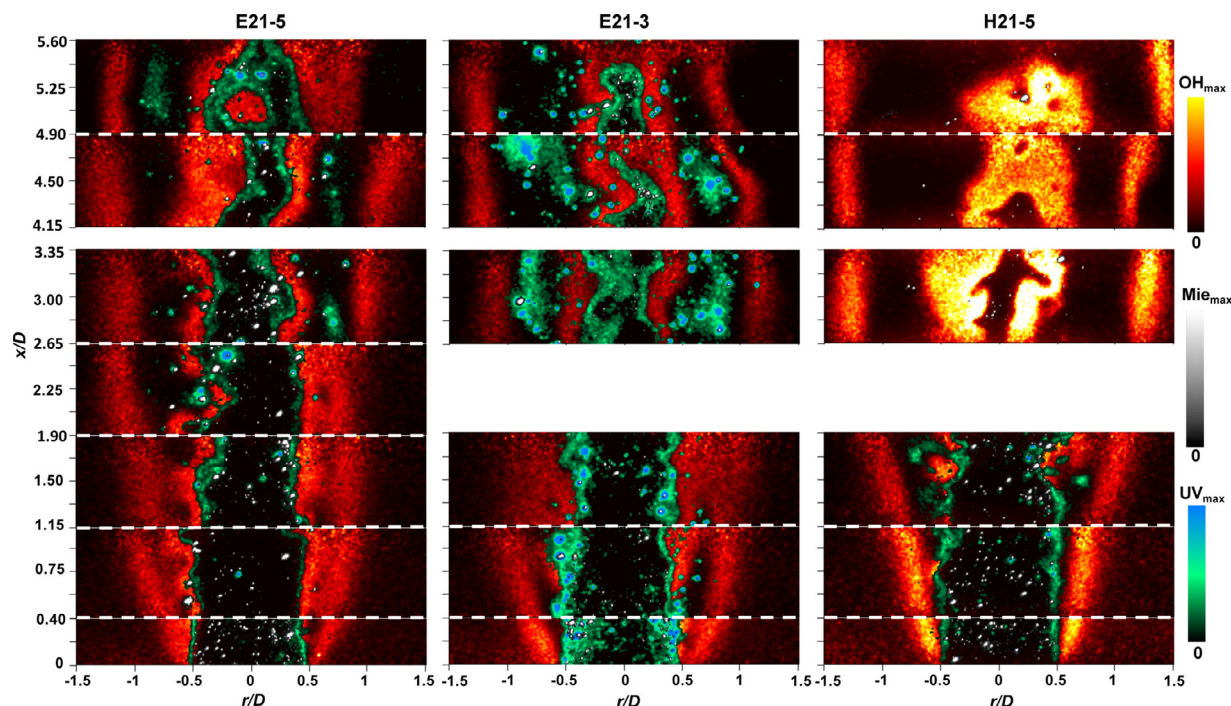


Fig. 7. Stacked images at axial locations from the jet exit to $x/D = 5.6$, for flame cases E21-5, E21-3 and H21-5 (data were not collected for cases E21-3 and H21-5 at $x/D = 2.25$). Note: Images shown at different axial locations are not temporally matched.

ture fraction is shifted toward the oxidant side (i.e. the coflow) for the *n*-heptane and *n*-heptane/toluene flames, which further separates the two structures. For the ethanol flames with greater values of Φ_{jet} (namely cases E21-3 and E27-5), there is an increased likelihood of ignition kernels being detected in the images centred at $x/D = 0.35$. While only a single case is shown in Fig. 6, the Supplementary Material includes the statistical data relating to the detection of ignition kernels for the various cases, along with additional instantaneous images at $x/D = 0.35$. Intermittency plots of the OH signal are also included in the Supplementary Material, indicating a less stabilised inner structure in the near-field for the *n*-heptane and *n*-heptane/toluene flames—this is further explored in Section 3.6.

Figure 7 provides an overview of the flame structures from the jet exit up to $x/D = 5.3$, in the form of stacked, instantaneous, superimposed images, for the E21-5, E21-3 and H21-5 cases. Note that there are no images corresponding to the location $x/D = 2.25$ for the E21-3 and H21-5 cases in Fig. 7. It should also be noted that the UV-PLIF signal has been removed from the *n*-heptane images for $x/D \gtrsim 2$, due to significant interference from LII resulting from the relatively high levels of soot in this region. The stacked images highlight the development of the inner and outer flame fronts and how this varies between the different cases. While the two flame fronts are clearly distinguishable in all cases, there is also significant interaction between them, particularly for the ethanol flames, where the inner and outer OH layers can be seen to form a single structure in some of the instantaneous images. This is a common occurrence in flames with multiple reaction zones [52], and is related to thermal “back-support” between the two flame fronts, leading to a build-up of intermediate species and the merging of the two reaction zones in some instances. These images also show that the inner flame structure closes out nearer to the jet exit for the *n*-heptane case, despite initially forming further downstream. This is likely a consequence of increased premixing in the case of *n*-heptane due to the delayed ignition time.

Some droplets can be seen to penetrate the inner OH layer in Fig. 7, although the majority are enclosed within the inner cone,

particularly for the E21-5 case. It can also be seen that there are still liquid droplets present as the inner, partially premixed flame front begins to “close out” at $x/D \approx 5.6$. Additionally, some droplets can be seen to penetrate into the OH layer in this region. It is worth noting that this closing out of the inner flame front corresponds to the tip of the blue inner cone, as seen in the photographs of the ethanol flames in Fig. 2 (this is less clear in the *n*-heptane flame, due to increased luminosity from soot). In the photographs, a change in colour from a blue/violet shade to a yellow/orange in the inner region of the ethanol flames can be seen at the tip of the inner cone, which is attributed to the droplets penetrating into and through the tip of the inner flame front, where they evaporate and react as a diffusion flame, forming soot. Additionally, isolated regions of UV-PLIF are detected between the two flame fronts from $x/D \gtrsim 2.5$ (for the ethanol flames), which are associated with the onset of the sooting region that is characteristic of conventional diffusion flames [53]. This is particularly evident in the E21-3 images, where the UV-PLIF signal between the two flame fronts in the images centred at $x/D = 3.00$ and $x/D = 4.5$ is attributed to the presence of soot precursors (such as PAHs); this is consistent with the increased luminosity of this flame. It is worth noting here that the level of soot in the ethanol flames was below the LII detection threshold.

While only a limited set of results have been shown in this section, it was observed that the fuel loading and Reynolds number have a noticeable effect on the instantaneous flame structure. Specifically, the merging of the two flame fronts tends to become more frequent both at higher values of Re_{jet} , and lower values of \dot{m}_f —further evidence is included in the Supplementary Material, where additional instantaneous OH-PLIF images are shown for the different cases at a range of axial locations. The effect of Re_{jet} is expected, since the increased turbulence in the case of higher Re_{jet} promotes the transport of both heat and intermediate species between the two reaction zones. The trend observed with the change in fuel loading is attributed to a reduction in the number of droplets which penetrate the inner reaction zone, leading to a less pronounced double flame structure.

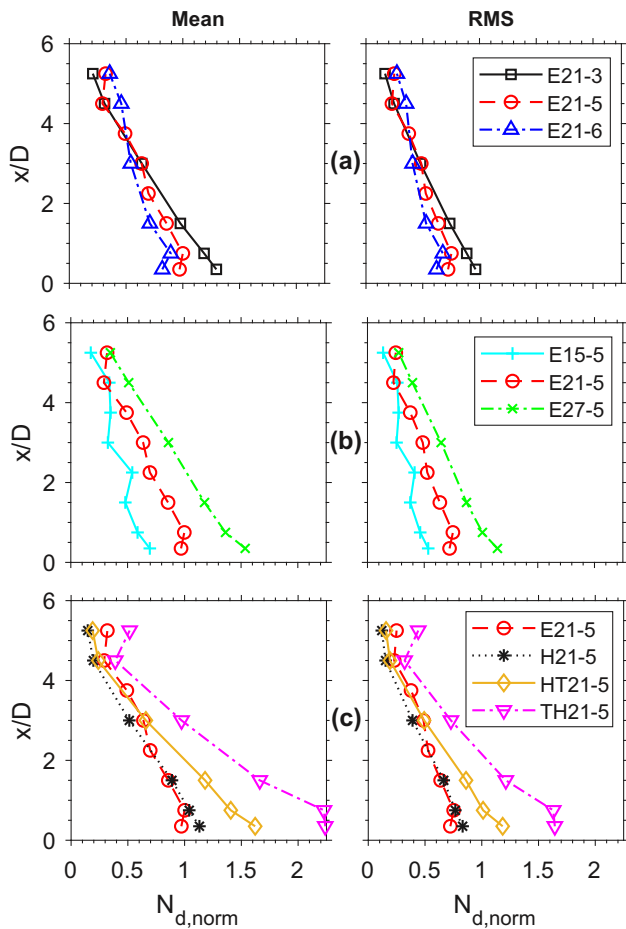


Fig. 8. Radially-weighted axial profiles of mean droplet number counts with variations in (a) jet Reynolds number, (b) fuel loading and (c) fuel composition, normalised against the maximum droplet count from the E21-5 case.

In the stacked images in Fig. 7, the high-intensity circular regions in the UV signal are much more noticeable for the E21-3 case in comparison to the other cases shown. As mentioned in Section 3.2, these structures are attributed to pre-ignition reactions around evaporating droplets. This suggests that there is increased evaporation of droplets in the near-field for the E21-3 case; this is further explored in the following section.

3.4. Droplet behaviour

To further investigate the distribution of droplets and how this relates to the overall flame structure, a useful measure is the droplet number count. Figure 8 displays the normalised droplet number counts with respect to axial location, with three separate plots to independently show the effects of variations in Reynolds number, fuel loading and fuel type. The number of droplets at each location was determined using a computational algorithm, based on the radially weighted Mie scattering signal over the height of the laser sheet and averaged over a set of 255 images for each case, as described in greater detail in Section 2.2. Also shown is the root-mean-square (RMS) values of the droplet counts, to provide an indication of the variability of the measurements. The mean and RMS plots were normalised against the maximum average droplet count from the E21-5 case, which is included in all plots as a reference case.

In Fig. 8(a), a more gradual decay profile with increasing Re_{jet} is evident, with the E21-6 case ($Re_{jet} = 6000$) having the lowest droplet count in the near-field region, and the highest value fur-

ther downstream at $x/D = 5.3$, compared to the $Re_{jet} = 5000$ and $Re_{jet} = 3000$ cases. Considering the difference in bulk flow rates, the greater average number density near the jet exit for the case of lower Re_{jet} is expected. The difference in slopes between the three cases is a less obvious result, and indicates a significant increase in the evaporation of droplets in the near-field for the E21-3 case. This can be attributed to the droplets having greater momentum in the axial direction when Re_{jet} is higher, such that they tend to remain clustered towards the central axis, whereas there is an increased radial distribution of droplets towards the hot coflow when Re_{jet} is lower, leading to increased evaporation. This is supported by analysis of the Mie scattering images in terms of the signal intermittencies, which are included in the Supplementary Material and show an increased radial spread of droplets when Re_{jet} is lower. This result is interesting, since an increase in turbulence could be expected to promote the radial transport of droplets towards the coflow, increasing the rate of evaporation. The fact that the opposite effect has been observed indicates that the magnitude of the turbulent fluctuations does not have a significant effect on the droplet dynamics, at least at the values of Re_{jet} used in this study.

As expected, Fig. 8(b) shows that an increase in fuel loading leads to a general increase in the droplet count, although there are noticeable fluctuations with respect to axial location for the E15-5 case. Comparing (a) and (b) in Fig. 8, and noting the fact that all of the plots are normalised against the E21-5 case, it is interesting to observe that cases E21-3 and E27-5 have very similar droplet counts, particularly in the near-field. Recalling the flame photographs, these two cases are very similar in terms of their visual appearance, which further highlights the influence of droplets in the near-field on the overall evolution of these flames, and also emphasises the need to be able to accurately predict droplet-combustion interactions in numerical modelling of spray flames.

The effect of fuel composition on the number of droplets is shown in Fig. 8(c). There is a noticeable increase in the droplet number count as toluene is added to the fuel (HT21-5 and TH21-5 cases). This trend is likely a consequence of the lower volatility of toluene in comparison to ethanol and *n*-heptane. Specifically, toluene has a significantly lower vapour pressure and a higher boiling point (Table 2), thus a decreased rate of droplet evaporation for the *n*-heptane/toluene blends is expected. Furthermore, the fact that this increase in droplet count can be seen at the jet exit indicates that there is significant prevaporisation of the liquid droplets prior to exiting the jet.

As alluded to in Section 3.3, it is also of interest to investigate the radial location of droplets, particularly with regards to the penetration of droplets into the reaction zone. As discussed in Sections 2.2 and 3.2, the Mie scattering images were spatially filtered with respect to the UV-PLIF signal, to divide the droplets into those which occur within the “inner cone” and those which occur in the “outer region” (see Fig. 4). These “inner” and “outer” droplet counts are shown as ratios in Fig. 9, focussing on the near-field region for variations in fuel loading.

In Fig. 9, it can be seen that droplets are consistently detected outside of the inner cone for all fuel loadings and axial locations shown. The proportion of droplets which exist outside of the inner cone (i.e. those labelled as “outer”) ranges from approximately 15–25% of the total droplet count. Interestingly, the outer fraction can be seen to generally increase with distance from the jet exit for each of the cases. It should be mentioned that droplets which are outside of the inner cone would evaporate relatively quickly, due to the influence of both the hot coflow and the inner flame front. Therefore, the fact that the outer ratio increases suggests that droplets from the inner cone are consistently transported through the preheat region, and penetrate into the inner OH layer.

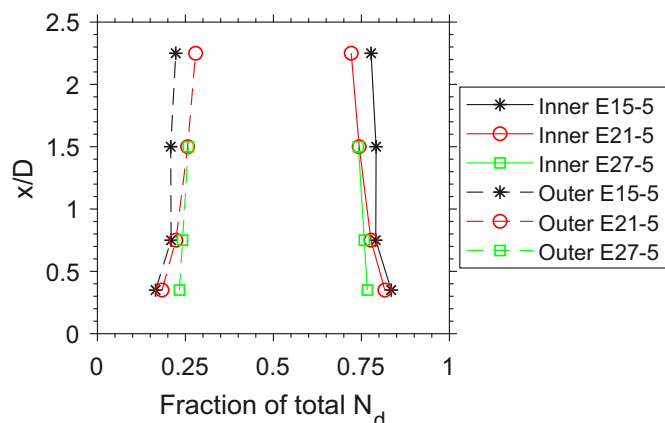


Fig. 9. Proportion of droplets occurring inside and outside of the continuous CH_2O layer, for a range of fuel loadings and axial locations.

As mentioned in Section 3.3, the instantaneous images showed a higher degree of separation between the inner and outer flame structures with an increase in fuel loading. In previous experiments involving pressure-swirl atomised spray flames [24], the divergence between the inner and outer flame fronts was found to be related to the radial spreading of droplets, such that the outer flame is sustained by the vaporisation of larger droplets. Within the context of the droplet fractions displayed in Fig. 9, in conjunction with the normalised number counts shown in Fig. 8(b), it can be seen that there is an increase in both the number and proportion of droplets which penetrate through the inner preheat layer for the E27-5 flame. Although there are key differences between the flames being studied here and those of Rodrigues et al. [24], the findings indicate that the radial distribution of droplets is a crucial factor leading to the development of a dual flame structure, in addition to the partial premixing of prevaporised fuel.

3.5. Mean flame structure: ethanol flames

To further investigate the flame structure and the effects of fuel loading and Reynolds number, radial plots of the time-averaged OH and UV signals at four different axial locations are shown in Figs. 10 and 11. The laser sheets were centred at the axial heights stated in the figures, and the radial signals correspond to a horizontal line at these heights. The averaged OH and UV plots are respectively normalised against the maximum average OH and UV signal intensity from all cases involving ethanol flames; that is, the same normalising value has been used for the different cases shown in Figs. 10 and 11. In addition to time averaging, the signals on either side of the centreline were also averaged to produce the plots.

The plots shown in Figs. 10 and 11 display the OH and UV profiles side-by-side, noting that the OH profiles have been reflected about the vertical axis. From Fig. 10, the mass loading of liquid fuel can be seen to have a noticeable impact, particularly in regards to the formation of a double flame structure. This is highlighted by the OH plots, which show two distinct peaks at all locations for the highest fuel loading case (E27-5), while the E15-5 signals only show a single peak. The intermediate case, E21-5, can also be seen to have a secondary peak, although it is much less defined than the E27-5 case. It should be mentioned that due to turbulent fluctuations in the flames, the averaging process leads to a “blurring” effect, such that some structures cannot be distinguished. At $x/D = 4.5$ (and to a lesser extent at $x/D = 3.0$) the OH signal for the E15-5 case displays a “shoulder” feature rather than a peak, indicating that there is an inner and outer flame front present, but

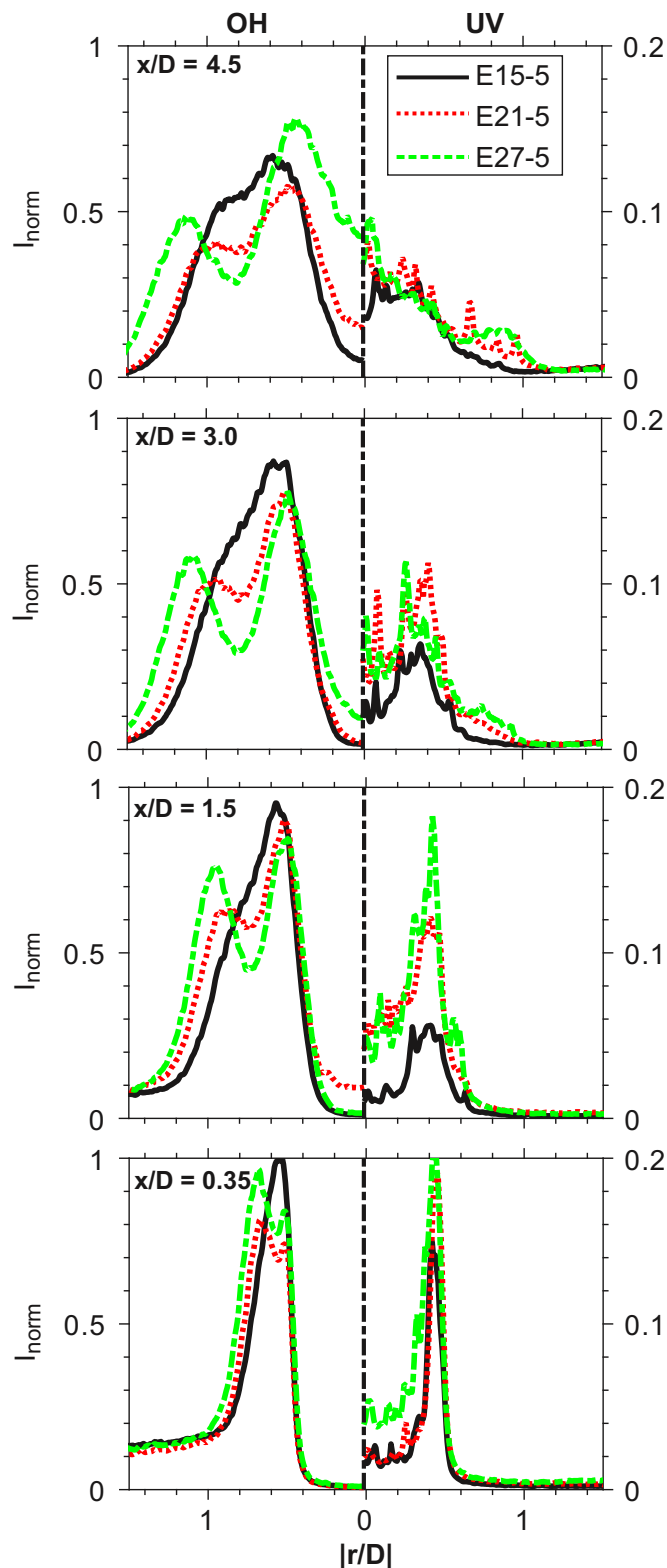


Fig. 10. Radial profiles of normalised OH-PLIF (left) and UV-PLIF (right) signals, at a range of axial locations for ethanol flames with three different fuel loadings.

this double flame structure is less pronounced and is somewhat obscured by the averaging process. It can also be seen that the radial location of the OH peak in the E15-5 case approximately aligns with the inside peaks of the two higher fuel loading cases at all locations, indicating that the inner flame front is more dominant when the fuel loading is lower. This is likely due to the re-

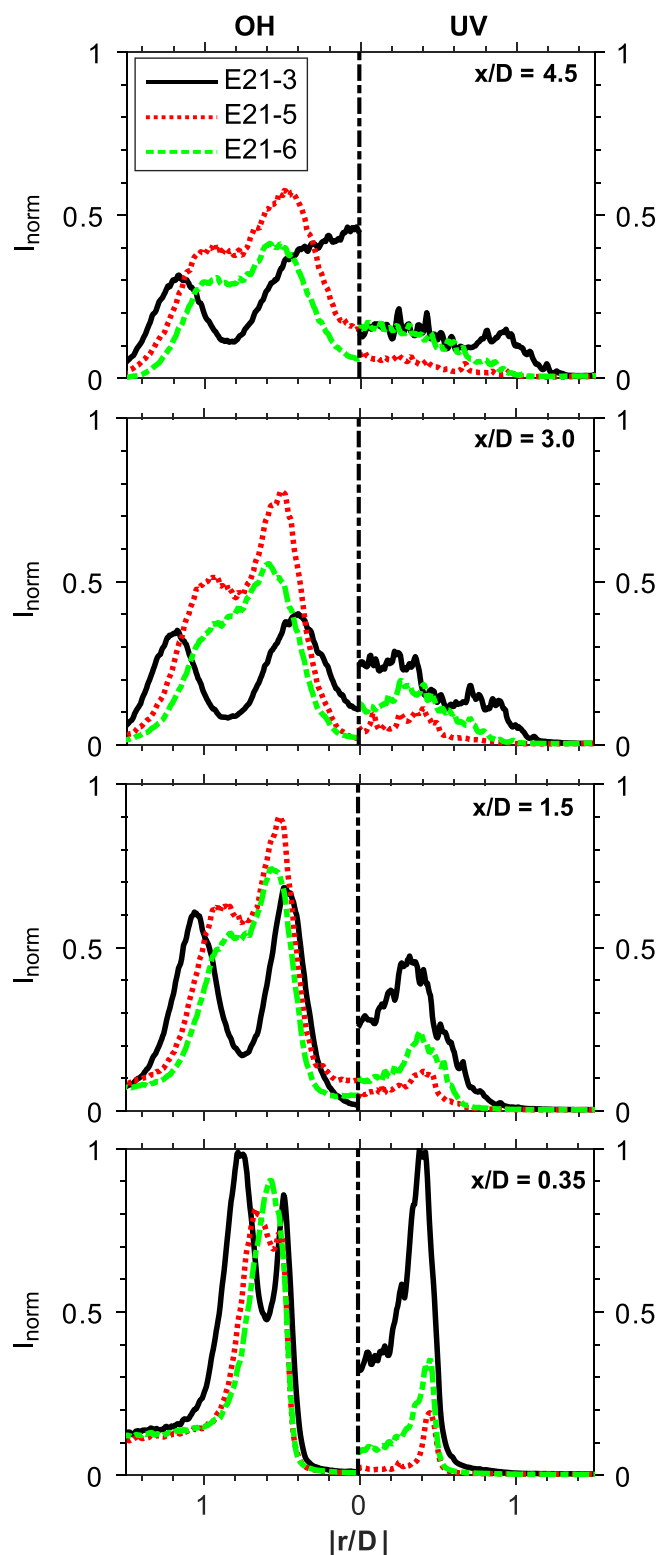


Fig. 11. Radial profiles of normalised OH-PLIF (left) and UV-PLIF (right) signals, at a range of axial locations for ethanol flames with three different Reynolds numbers.

duced number of droplets penetrating the inner flame front and reacting with the hot coflow in the E15-5 flame, as shown by the droplet counts in Fig. 9.

For all cases in Fig. 10, the UV signal can be seen to reach its maximum within $r/D < 0.1$ at $x/D = 4.5$, representing the beginning of the tip of the inner flame. The UV plots show a similar

shape for the three fuel loadings, with the magnitude generally showing an increase with increasing fuel loading, although this change is relatively small at most locations. The non-zero centreline UV signal near the jet exit is related to the isolated regions of UV-PLIF discussed in Section 3.2, and this appears to increase with fuel loading.

In Fig. 11, Re_{jet} can also be seen to have a significant impact on the flame structure. Specifically, the double flame structure is much more pronounced for the $Re_{jet} = 3000$ case, with separate OH layers evident in the near-field. At $x/D = 4.5$, the inner OH layer can be seen to reach its maximum at the centreline for this case, representing the tip of the inner flame front at this axial location. In contrast, the inner peaks of the OH signals in the E21-5 and E21-6 cases at $x/D = 4.5$ occur at radial positions of approximately $r/D = 0.4$ and $r/D = 0.5$, respectively. This indicates that the inner flame front persists further downstream for the higher Re_{jet} cases.

It is interesting to note that the total flame length decreases with increasing Re_{jet} for these flames (see Fig. 2), while the inner flame structure is shown to have the opposite relationship (Fig. 11). When Re_{jet} is higher, the rate of evaporation in the jet increases, leading to an increased degree of premixing such that the flame favours the partially premixed mode (i.e. the inner cone). When Re_{jet} is lower, there is less partially premixed fuel to sustain the inner flame front downstream, with a greater number of droplets evaporating in the presence of the hot coflow and reacting as a diffusion flame, hence a greater flame length. This also explains the decrease in flame luminosity as Re_{jet} is increased (Fig. 2), since an increase in the degree of partial premixing generally suppresses soot formation, provided that Φ_{jet} is sufficiently low ($\lesssim 10$) [54,55]. Previous numerical work has indicated that the formation of a double (or triple) flame structure is very sensitive to the evaporative time scale [28]. In the context of the current findings, this emphasises the importance of droplet evaporation and the near-field structure on the overall behaviour of the flame.

Another observation from Fig. 11 is that the intermediate case with $Re_{jet} = 5000$ (E21-5) has the highest magnitude in terms of OH signal at all locations, except for $x/D = 0.35$, at which point it has the lowest signal. First of all, it should be noted that due to the qualitative nature of the results, it is difficult to directly compare signal magnitudes, because they could be affected by changes in signal quenching in the different flames. Nevertheless, this apparent non-monotonic behaviour with respect to Re_{jet} highlights the complex nature of turbulent and transitional spray flames, in terms of the competing effects of droplet residence time and mixing/evaporation processes. It can also be seen that this case has the lowest UV signal at all locations. The E21-3 case has a significantly higher UV signal, particularly near the jet exit, and the high magnitude at the centreline for this case is also worth noting. This would seem to indicate that interference from droplets is responsible (since the E21-3 case has a greater number of droplets in the near-field); however, if this were the case then the centreline signal would be expected to be higher for the E21-5 case compared with the E21-6 case (see Fig. 9), while the opposite is true. Although this indicates that the change in UV signal intensity is not a direct result of interference from droplets, the signal magnitudes at the centreline suggest that it is also not solely a result of increased concentration of CH_2O in the preheat region. At this stage it is not possible to determine an exact cause, although the instantaneous images show that there is a greater proportion of high-intensity, circular structures in the UV-PLIF signal for the E21-3 and E21-6 cases, which, as discussed in Section 3.2, is indicative of pre-ignition reactions surrounding droplets.

In the E21-3 case, peaks in the UV-PLIF signal can also be seen between the two OH layers (at $r/D \approx 0.8$) at the axial locations of $x/D = 4.5$ and $x/D = 3.0$. Referring back to Fig. 10, this feature

is also evident for the E27-5 flame (and to a lesser extent the E21-5 flame) at $x/D = 4.5$. These two cases (i.e. E27-5 and E21-3) also have the most pronounced double flame structure, as evidenced by the OH profiles. Referring again to the droplet plots (Figs. 8 and 9), both of these cases have a relatively high number of droplets near the jet exit, with the majority having evaporated by $x/D = 4.5$. While the inner and outer droplet profiles are not included for the E21-3 case, Fig. 9 shows that there is a significant number of droplets outside of the inner cone in the near-field for the E27-5 case, and it is reasonable to extend this reasoning to the E21-3 flame. Therefore, this secondary peak in the UV-PLIF signal is attributed to the increased proportion of droplets penetrating through the inner preheat region, and subsequently evaporating and reacting with the hot coflow as a diffusion flame. This is also consistent with the increased luminosity of these flames, and the change in colour at approximately $x/D = 4.5$, indicating the presence of nascent soot.

3.6. Effect of fuel type

To analyse the effect of toluene addition on flame structure in the near-field, shared radial plots of OH- and UV-PLIF for cases H21-5, HT21-5 and TH21-5 are shown in Fig. 12, along with the E21-5 case for reference, from $x/D = 0.35$ to $x/D = 1.5$. Once again, the plotted data are averaged, normalised signals, using the maximum average intensity from the three axial locations as the normalising value. At the location nearest to the jet exit ($x/D = 0.35$), a single OH structure is evident in all of the *n*-heptane/toluene cases, which develops into a double flame structure with two distinguishable peaks further downstream. All three of the cases with *n*-heptane have very similar OH profiles, with the radial location of the peaks coinciding with each other at each of the heights, indicating that the addition of toluene does not significantly affect the near-field flame structure. In saying this, the magnitude of the OH peaks can be seen to decrease with toluene addition, particularly for the outer peaks (when multiple peaks are present). Again referring to the droplet plots, this difference is attributed to the decreased rate of evaporation which occurs with toluene addition, which results in a lower concentration of radicals near the jet exit.

For the UV plots, the data have been omitted for $x/D = 1.5$, due to significant interference from LII, particularly in the cases containing toluene. The increased intensity of the UV-PLIF signal with addition of toluene is thus likely a result of increased levels of PAH when toluene is added, which is consistent with previous findings based on prevaporised *n*-heptane/toluene flames under similar conditions [23,56]. It is interesting to note that the UV signal intensity for the two cases containing toluene is very similar at $x/D = 0.35$, despite the TH21-5 case having twice the concentration of toluene and a significantly higher intensity at $x/D = 0.75$. Previous results relating to prevaporised fuels indicate that as the proportion of toluene is increased, the concentration of PAH increases at all axial locations where PAH is present [56]. It is therefore hypothesised that the amount of vaporised toluene is approximately the same for both cases at $x/D = 0.35$, which is supported by the higher droplet count for the TH21-5 case (see Fig. 8(c)).

It is interesting to note the difference in the OH profiles between the *n*-heptane/toluene cases and the ethanol case. For the ethanol flame, the inner peak can be seen to occur nearer to the jet exit, while it only becomes prominent at $x/D = 1.5$ for the other cases. At this location, the signal corresponding to the inner peak is considerably lower than the outer peak for the cases with *n*-heptane, while the opposite is true for the E21-5 case, along with the remainder of the ethanol flames (Figs. 10 and 11). Interestingly, the instantaneous images show that the OH signal intensity is actually higher in the inner region for all cases—examples at $x/D = 1.5$ are included in the Supplementary Material. The rea-

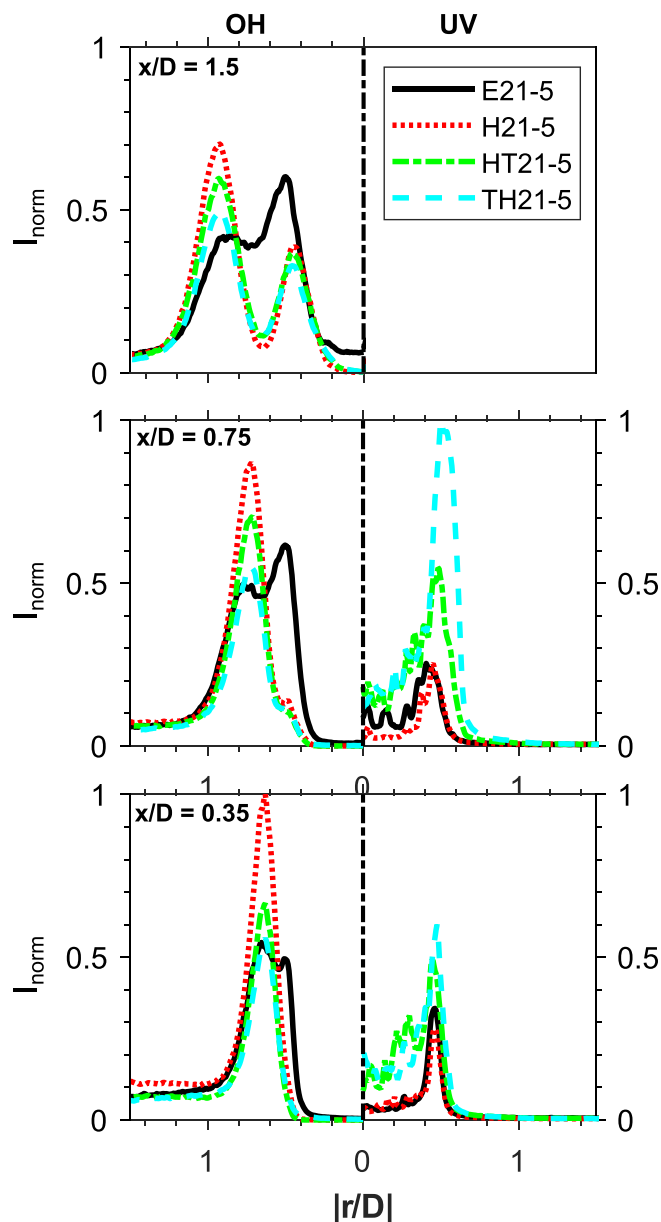


Fig. 12. Radial profiles of OH and CH_2O in the near-field for flames of varying fuel composition.

son that the averaged profiles show a greater outer peak for the *n*-heptane and *n*-heptane/toluene cases is that for these flames, the signal is less consistent in the near-field, suggesting a less stabilised inner flame structure, which is supported by the OH intermittency images shown in the Supplementary Material.

To investigate the formation of soot and how it relates to the flame structure, radial profiles of the average soot volume fraction (f_v) at a range of axial locations are shown alongside normalised signals of OH-PLIF in Fig. 13. In these plots, results correspond to the two *n*-heptane/toluene blends and the purely *n*-heptane case, at the three furthest-downstream axial locations. Note that none of the ethanol cases are included, since the level of soot in these flames was below the LII detection threshold.

A consistent increase in soot volume fraction with toluene addition is noticeable in Fig. 13, with very low levels of soot detected for the *n*-heptane flame. This is due to the relatively high sooting propensity of toluene, as has been well-documented in the literature [23,57]. For both the HT21-5 and TH21-5 cases, the LII sig-

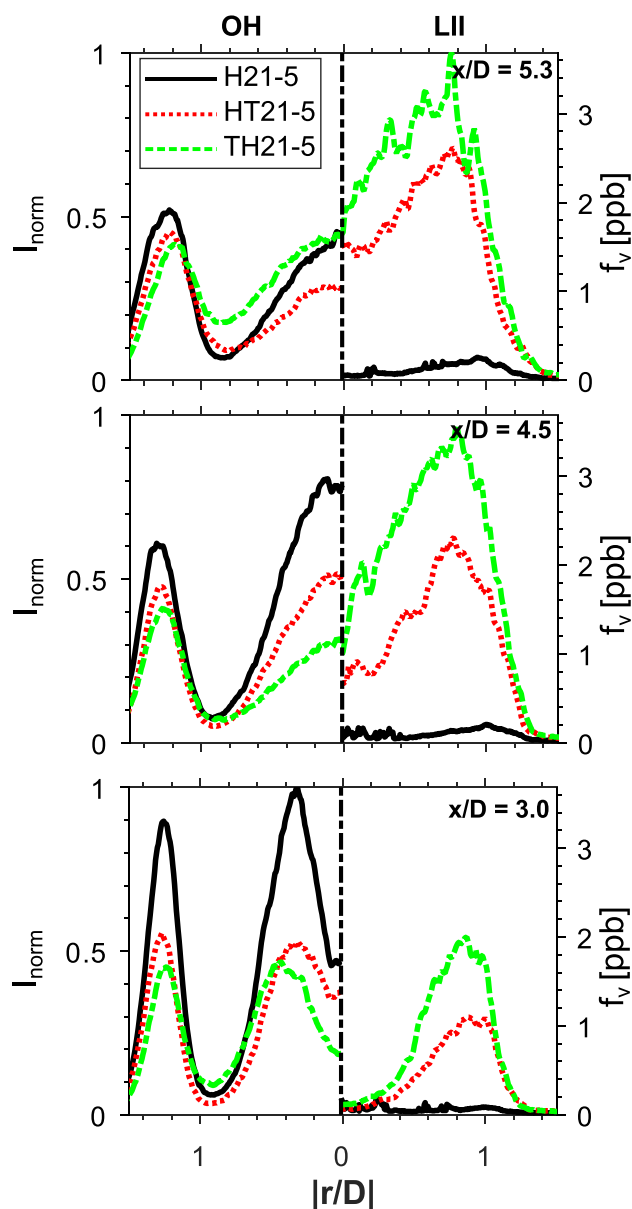


Fig. 13. Radial profiles of OH-PLIF and f_v for the *n*-heptane flame (H21-5), and the 1:3 (HT21-5) and 1:1 (TH21-5) *n*-heptane/toluene flames from $x/D = 3.0$ to $x/D = 5.3$.

nal can be seen to peak at approximately $r/D = 0.8$, which corresponds to the region between the two flame fronts, where the OH is at a minimum. There is a sharp drop in f_v for $r/D > 1$, corresponding to the outer peak in the OH signal, suggesting that the soot is oxidised by the outer flame front, noting that OH is known to oxidise soot [58]. It should be noted that much of the soot occurring between the two flame at the locations shown in Fig. 13 is convected further downstream, where further mixing between soot and OH leads to oxidation of the soot [59].

4. Conclusions

The structure of dilute spray flames in a hot and low-oxygen environment has been studied using a combination of laser diagnostic techniques. Fuel composition, jet Reynolds number and fuel loading were independently varied, and a number of key findings were obtained:

- All flames exhibited a so-called “double-flame” structure to some extent, which is associated with prevaporisation of fuel, along with the penetration of droplets through the inner reaction zone.
- The inner flame structure either “branches away” from the outer structure as a bifurcation, or undergoes a separate auto-ignition process, accompanied by distinct ignition kernels. It was found that ignition kernels are much more likely to occur for the *n*-heptane and *n*-heptane/toluene cases in comparison to the ethanol flame with equivalent fuel loading and Reynolds number. A reduction in Reynolds number and an increase in fuel loading also leads to an increased likelihood of kernel formation as opposed to bifurcations, which is related to an increased equivalence ratio in the jet.
- The distribution of droplets in the near-field was found to have a significant impact on the overall evolution of the flames. Analysis of the Mie scattering signals, in conjunction with simultaneous CH_2O imaging, revealed that droplets are consistently transported through the initial preheat region and into the inner OH structure, which plays an important role in the formation of a double flame structure.
- Analysis of the mean signals indicates that the double flame structure is more pronounced for lower Reynolds numbers and higher fuel loadings, with two distinct peaks in the OH signals evident in some instances.
- Toluene addition was found to have little effect on the overall flame structure, despite the increase in soot volume fraction. Combined analysis of the mean soot volume fraction and radial OH-PLIF signal indicates that soot is formed between the two flame fronts, and is oxidised in the outer reaction zone.

These findings provide a valuable insight into the underlying mechanisms which lead to the complex structures observed in spray flames in a hot and low-oxygen environment. While flames with similar structures have been studied previously, the parametric nature of this study—in terms of the independent variation of a range of jet boundary conditions—is an important distinction. This allows direct comparisons to be made between the various cases in order to better understand the factors which influence the flame structure. This is particularly important, since it is difficult to predict the effect of such changes in boundary conditions in turbulent spray flames, due to the coupled interactions between turbulence, chemistry and droplet evaporation. Although primarily qualitative in nature, the results presented here are of particular importance for the prediction of bifurcating flame structures and the presence of ignition kernels under varying conditions. This is an important step towards the development of more efficient and robust numerical models of spray combustion, which will in turn enable improvements in the efficiency of practical combustion devices.

Declaration of Competing Interest

The authors declare that they have no known competing financial interests or personal relationships that could have appeared to influence the work reported in this paper.

Acknowledgments

The authors would like to thank Dr Jingjing Ye for her contribution in the design of the burner used for these experiments, and Dr Thomas Kirch for his assistance with data collection. The support from the University of Adelaide is acknowledged, along with the financial support provided by the Australian Research Council (ARC) and the Future Fuels Cooperative Research Centre (CRC); Project RP1.10-04.

Supplementary material

Supplementary material associated with this article can be found, in the online version, at [10.1016/j.combustflame.2021.111439](https://doi.org/10.1016/j.combustflame.2021.111439)

References

- [1] P. Jenny, D. Roekaerts, N. Beishuizen, Modeling of turbulent dilute spray combustion, *Prog. Energy Combust. Sci.* 38 (2012) 846–887.
- [2] G.M. Faeth, Current status of droplet and liquid combustion, *Prog. Energy Combust. Sci.* 3 (1977) 191–224.
- [3] S. Hochgreb, Mind the gap: turbulent combustion model validation and future needs, *Proc. Combust. Inst.* 37 (2019) 2091–2107.
- [4] G.M. Faeth, Mixing, transport and combustion in sprays, *Prog. Energy Combust. Sci.* 13 (1987) 293–345.
- [5] A.R. Masri, Turbulent combustion of sprays: from dilute to dense, *Combust. Sci. Technol.* 188 (2016) 1619–1639.
- [6] R. Lebas, T. Menard, P.A. Beau, A. Berlemont, F.X. Demoulin, Numerical simulation of primary break-up and atomization: DNS and modelling study, *Int. J. Multiphase Flow* 35 (2009) 247–260.
- [7] Experiments and Numerical Simulations of Diluted Spray Turbulent Combustion, in: B. Merci, D. Roekaerts, A. Sadiqi (Eds.), *ERCOFTAC Series*, 17, Springer, Netherlands, Dordrecht, 2011.
- [8] M. Zheng, G.T. Reader, J.G. Hawley, Diesel engine exhaust gas recirculation—a review on advanced and novel concepts, *Energy Convers. Manag.* 45 (2004) 883–900.
- [9] A.A.V. Perpignan, A. Gangoli Rao, D.J.E.M. Roekaerts, et al., Flameless combustion and its potential towards gas turbines, *Prog. Energy Combust. Sci.* 69 (2018) 28–62.
- [10] I.I. Enagi, K.A. Al-attab, Z.A. Zainal, Liquid biofuels utilization for gas turbines: a review, *Renew. Sustain. Energy Rev.* 90 (2018) 43–55.
- [11] V. Mahendra Reddy, S. Kumar, Development of high intensity low emission combustor for achieving flameless combustion of liquid fuels, *Propul. Power Res.* 2 (2013) 139–147.
- [12] N. Ladommatos, S. Abdelhalim, H. Zhao, The effects of exhaust gas recirculation on diesel combustion and emissions, *Int. J. Engine Res.* 1 (2000) 107–126.
- [13] A. Cavaliere, M. de Joannon, Mild combustion, *Prog. Energy Combust. Sci.* 30 (2004) 329–366.
- [14] M. de Joannon, G. Langella, F. Beretta, A. Cavaliere, C. Noviello, Mild combustion: process features and technological constraints, *Combust. Sci. Technol.* 153 (2000) 33–50.
- [15] P.R. Medwell, P.A.M. Kalt, B.B. Dally, Simultaneous imaging of OH, formaldehyde, and temperature of turbulent nonpremixed jet flames in a heated and diluted coflow, *Combust. Flame* 148 (2007) 48–61.
- [16] C. Galletti, A. Parente, L. Tognotti, Numerical and experimental investigation of a mild combustion burner, *Combust. Flame* 151 (2007) 649–664.
- [17] P.R. Medwell, P.A.M. Kalt, B.B. Dally, Imaging of diluted turbulent ethylene flames stabilized on a jet in Hot Coflow (JHC) burner, *Combust. Flame* 152 (2008) 100–113.
- [18] B.B. Dally, A.N. Karpetsis, R.S. Barlow, Structure of turbulent non-premixed jet flames in a diluted hot coflow, *Proc. Combust. Inst.* 29 (2002) 1147–1154.
- [19] R. Cabra, T. Myhrvold, J.Y. Chen, R.W. Dibble, A.N. Karpetsis, R.S. Barlow, Simultaneous laser raman-rayleigh-lif measurements and numerical modeling results of a lifted turbulent H₂/N₂ jet flame in a vitiated coflow, *Proc. Combust. Inst.* 29 (2002) 1881–1888.
- [20] J. Sidey, E. Mastorakos, Visualization of MILD combustion from jets in cross-flow, *Proc. Combust. Inst.* 35 (2015) 3537–3545.
- [21] C.M. Arndt, M.J. Papageorge, F. Fuest, J.A. Sutton, W. Meier, M. Aigner, et al., The role of temperature, mixture fraction, and scalar dissipation rate on transient methane injection and auto-ignition in a jet in hot coflow burner, *Combust. Flame* 167 (2016) 60–71.
- [22] J. Ye, P.R. Medwell, K. Kleinheinz, M.J. Evans, B.B. Dally, H.G. Pitsch, Structural differences of ethanol and DME jet flames in a hot diluted coflow, *Combust. Flame* 192 (2018) 473–494.
- [23] M.J. Evans, P.R. Medwell, Z. Sun, A. Chinnici, J. Ye, Q.N. Chan, B.B. Dally, Downstream evolution of n-heptane/toluene flames in hot and vitiated coflows, *Combust. Flame* 202 (2019) 78–89.
- [24] H.C. Rodrigues, M.J. Tummers, E.H. van Veen, D.J.E.M. Roekaerts, Spray flame structure in conventional and hot-diluted combustion regime, *Combust. Flame* 162 (2015) 759–773.
- [25] G. Continillo, W.A. Sirignano, Counterflow spray combustion modeling, *Combust. Flame* 81 (1990) 325–340.
- [26] F. Shum-Kivan, J. Marrero Santiago, A. Verdier, E. Riber, B. Renou, G. Cabot, B. Cuenot, Experimental and numerical analysis of a turbulent spray flame structure, *Proc. Combust. Inst.* 36 (2017) 2567–2575.
- [27] S.K. Marley, E.J. Welle, K.M. Lyons, W.L. Roberts, Effects of leading edge entrainment on the double flame structure in lifted ethanol spray flames, *Exp. Therm Fluid Sci.* 29 (2004) 23–31.
- [28] L. Ma, D. Roekaerts, Numerical study of the multi-flame structure in spray combustion, *Proc. Combust. Inst.* 36 (2017) 2603–2613.
- [29] H.K. Motaalegh Mahalegi, A. Mardani, Investigation of fuel dilution in ethanol spray MILD combustion, *Appl. Therm. Eng.* 159 (2019) 113898.
- [30] J.D. Gounder, A. Kourmatzis, A.R. Masri, Turbulent piloted dilute spray flames: flow fields and droplet dynamics, *Combust. Flame* 159 (2012) 3372–3397.
- [31] W. O'Loughlin, A.R. Masri, A new burner for studying auto-ignition in turbulent dilute sprays, *Combust. Flame* 158 (2011) 1577–1590.
- [32] W. O'Loughlin, A.R. Masri, The structure of the auto-ignition region of turbulent dilute methanol sprays issuing in a vitiated co-flow, *Flow Turb. Combust.* 89 (2012) 13–35.
- [33] A.R. Masri, J.D. Gounder, Turbulent spray flames of acetone and ethanol approaching extinction, *Combust. Sci. Technol.* 182 (2010) 702–715.
- [34] M.J. Evans, D.P. Proud, P.R. Medwell, H. Pitsch, B.B. Dally, Highly radiating hydrogen flames: effect of toluene concentration and phase, *Proc. Combust. Inst.* (2021) In press.
- [35] R.J. Lang, Ultrasonic atomization of liquids, *J. Acoust. Soc. Am.* 34 (1962) 6–8.
- [36] R. Rajan, A.B. Pandit, Correlations to predict droplet size in ultrasonic atomization, *Ultrasonics* 39 (2001) 235–255.
- [37] S. Kruse, J. Ye, Z. Sun, A. Attili, B. Dally, P. Medwell, H. Pitsch, Experimental investigation of soot evolution in a turbulent non-premixed prevaporized toluene flame, *Proc. Combust. Inst.* 37 (2019) 849–857.
- [38] M.J. Mussche, L.A. Verhoeve, Viscosity of ten binary and one ternary mixtures, *J. Chem. Eng. Data* 20 (1975) 46–50.
- [39] A.M. Velásquez, B.A. Hoyos, Viscosity of heptane-toluene mixtures. Comparison of molecular dynamics and group contribution methods, *J. Mol. Model.* 23 (2017) 58.
- [40] P.O. Witze, S. Hochgreb, D. Kayes, H.A. Michelsen, C.R. Shaddix, Time-resolved laser-induced incandescence and laser elastic-scattering measurements in a propane diffusion flame, *Appl. Opt.* 40 (2001) 2443–2452.
- [41] N.H. Qamar, Z.T. Alwahabi, Q.N. Chan, G.J. Nathan, D. Roekaerts, K.D. King, Soot volume fraction in a piloted turbulent jet non-premixed flame of natural gas, *Combust. Flame* 156 (2009) 1339–1347.
- [42] Q.N. Chan, P.R. Medwell, P.A.M. Kalt, Z.T. Alwahabi, B.B. Dally, G.J. Nathan, Simultaneous imaging of temperature and soot volume fraction, *Proc. Combust. Inst.* 33 (2011) 791–798.
- [43] B. Axelsson, R. Collin, P.-E. Bengtsson, Laser-induced incandescence for soot particle size measurements in premixed flat flames, *Appl. Opt.* 39 (2000) 3683.
- [44] Q.N. Chan, P.R. Medwell, G.J. Nathan, et al., Algorithm for soot sheet quantification in a piloted turbulent jet non-premixed natural gas flame, *Exp. Fluids* 55 (2014) 1827.
- [45] S. Kook, R. Zhang, Q.N. Chan, T. Aizawa, K. Kondo, L.M. Pickett, E. Cenker, G. Bruneaux, O. Andersson, J. Pagels, E.Z. Nordin, Automated detection of primary particles from transmission electron microscope (TEM) images of soot aggregates in diesel engine environments, *SAE Int. J. Engines* 9 (2015) 279–296.
- [46] C. Wang, Q.N. Chan, R. Zhang, S. Kook, E.R. Hawkes, G.H. Yeoh, P.R. Medwell, Automated determination of size and morphology information from soot transmission electron microscope (TEM)-generated images, *J. Nanopart. Res.* 18 (2016) 127.
- [47] R.L. Gordon, A.R. Masri, E. Mastorakos, et al., Heat release rate as represented by [OH] × [CH₂O] and its role in autoignition, *Combust. Theor. Model.* 13 (4) (2009) 645–670.
- [48] T.C.W. Lau, G.J. Nathan, Influence of Stokes number on the velocity and concentration distributions in particle-laden jets, *J. Fluid Mech.* 757 (2014) 432–457.
- [49] B.A.V. Bennett, C.S. McEnally, L.D. Pfefferle, M.D. Smooke, M.B. Colket, Computational and experimental study of axisymmetric coflow partially premixed ethylene/air flames, *Combust. Flame* 127 (2001) 2004–2022.
- [50] J. Ye, P.R. Medwell, M.J. Evans, B.B. Dally, Characteristics of turbulent n-heptane jet flames in a hot and diluted coflow, *Combust. Flame* 183 (2017) 330–342.
- [51] R.L. Gordon, E. Mastorakos, Autoignition of monodisperse biodiesel and diesel sprays in turbulent flows, *Exp. Therm Fluid Sci.* 43 (2012) 40–46.
- [52] M.S. Mansour, I. Alkhesho, S.H. Chung, Stabilization and structure of n-heptane flame on CWJ-Spray burner with kHz SPIV and OH-PLIF, *Exp. Therm Fluid Sci.* 73 (2016) 18–26.
- [53] J. Du, R.L. Axelbaum, The effect of flame structure on soot-particle inception in diffusion flames, *Combust. Flame* 100 (1995) 367–375.
- [54] G. De Falco, M. Sirignano, M. Commodo, L. Merotto, F. Migliorini, R. Dondè, S. De Iulius, P. Minutolo, A. D'Anna, Experimental and numerical study of soot formation and evolution in co-flow laminar partially premixed flames, *Fuel* 220 (2018) 396–402.
- [55] A. Mitrovic, T.W. Lee, Soot formation characteristics of laminar partially premixed flames, *Combust. Flame* 115 (1998) 437–442.
- [56] S. Park, Y. Wang, S.H. Chung, S.M. Sarathy, Compositional effects on PAH and soot formation in counterflow diffusion flames of gasoline surrogate fuels, *Combust. Flame* 178 (2017) 46–60.
- [57] A.E. Daca, O.L. Gülder, Soot formation characteristics of diffusion flames of methane doped with toluene and n-heptane at elevated pressures, *Proc. Combust. Inst.* 36 (2017) 737–744.
- [58] M. Stöhr, K.P. Geigle, R. Hader, I. Boxx, C.D. Carter, M. Grader, P. Gerlinger, et al., Time-resolved study of transient soot formation in an aero-engine model combustor at elevated pressure, *Proc. Combust. Inst.* 37 (2019) 5421–5428.
- [59] S.-Y. Lee, R.J. Turns, R.J. Santoro, et al., Measurements of soot, OH, and PAH concentrations in turbulent ethylene/air jet flames, *Combust. Flame* 156 (2009) 2264–2275.

Experimental investigation of the flame structure of dilute sprays issuing into a hot and low-oxygen coflow

Douglas B. Proud^{a,*}, Michael J. Evans^{a,b}, Paul R. Medwell^a, Qing N. Chan^c

^a*School of Mechanical Engineering, The University of Adelaide, Adelaide, SA 5005, Australia*

^b*University of South Australia, Mawson Lakes, SA 5095, Australia*

^c*School of Mechanical and Manufacturing Engineering, University of New South Wales, Sydney, NSW 2052, Australia*

*Corresponding author. E-mail: douglas.proud@adelaide.edu.au

Supplementary Material

1. Ignition kernels and bifurcations: statistical data and instantaneous images

As mentioned in Section 3.3, the *n*-heptane and *n*-heptane/toluene flames tend to feature ignition kernels at the axial location of $x/D = 0.75$, while bifurcations are more common for the ethanol flames. The percentage of instantaneous images in which these features are observed for the various cases is shown in Table 1. It should be noted that in some instances, neither ignition kernels nor bifurcations are present, either because the inner flame is stabilised further upstream, or because there is no inner flame front present. Additionally, some of the instantaneous images display both bifurcations and ignition kernels in a single shot.

Table 1: Percentage of instantaneous images displaying ignition kernels and bifurcations at $x/D = 0.75$.

Case	Bifurcations [%]	Ignition Kernels [%]
E15-5	35	1
E21-5	63	8
E27-5	27	18
E21-3	28	20
E21-6	36	5
H21-5	23	60
HT21-5	24	55
TH21-5	36	49

As discussed, it is evident from Table 1 that ignition kernels are much more likely to be detected for the *n*-heptane and *n*-heptane/toluene cases. It is worth mentioning that for the E21-3 and E27-5 cases, a significant portion ($\sim 50\%$) of the images at $x/D = 0.75$ indicated that the inner flame front was stabilised further upstream, such that the ignition kernel/bifurcation could not be detected within the height of the laser sheet. For these cases, it is therefore of interest to further analyse the structure at $x/D = 0.35$, which captures the jet exit plane.

Figure 1 displays instantaneous images of OH- and UV-PLIF for cases E21-3 and E27-5, as well as E21-5 for comparison, centred at $x/D = 0.35$.

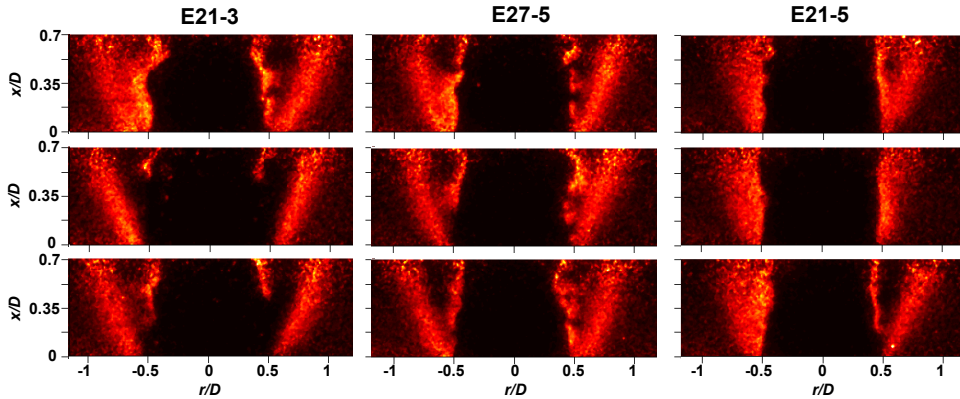


Figure 1: Selected instantaneous OH-PLIF images for cases E21-3, E27-5 and E21-5.

From Figure 1, both bifurcations and ignition kernels can be seen to occur near the jet exit for the E21-3 and E27-5 cases. Although one of the E21-5 images shows a bifurcation structure, there is generally less separation between the inner and outer flames fronts for this case, and ignition kernels are rarely detected. The increased separation for the E21-3 and E27-5 cases is attributed to the outer flame front developing further away from the central axis, recalling that these cases have the highest values of Φ_{jet} amongst the ethanol flames, such that the stoichiometric mixture fraction is shifted towards the oxidant side.

Figure 2 shows the signal intermittencies for a range of cases at $x/D = 0.75$ and $x/D = 1.5$, in order to highlight the differences in the stability of the inner flame front as the fuel is changed. In these images, the probability of detection of a signal greater than 10% of the maximum over the height of the laser sheet is shown. Results are shown for three different fuel compositions (E21-5, H21-5 and TH21-5), as well as a case with a lower Re_{jet} (E21-3) for comparison. From Figure 2, it can be seen that there is a much lower probability of OH being detected in the inner region for the H21-5 and TH21-5 flames, while for the ethanol flames the detection frequency is more uniform between the two structures. This is attributed to the greater separation between the inner

and outer flame fronts in the cases involving *n*-heptane, resulting in a greater likelihood of ignition kernels (see Figure ??) and local extinction events, in contrast with the more continuous structures which are present for the E21-5 and E21-3 flames. It is worth noting the similarities in the H21-5 and TH21-5 cases, which indicates that the *n*-heptane in the 1:1 blend dominates the flame structure in the near-field. This is attributed to the higher volatility of *n*-heptane, such that it evaporates and subsequently reacts in preference to toluene near the jet exit. Note that for case TH21-5, at the axial location $x/D = 0.75$, there appear to be some irregularities in the signal intermittency, specifically on the right-hand side at the top and bottom of the image. This is related to interference from the relatively high luminosity of this particular flame case, resulting in the signal in this region being above the 10% threshold in certain frames.

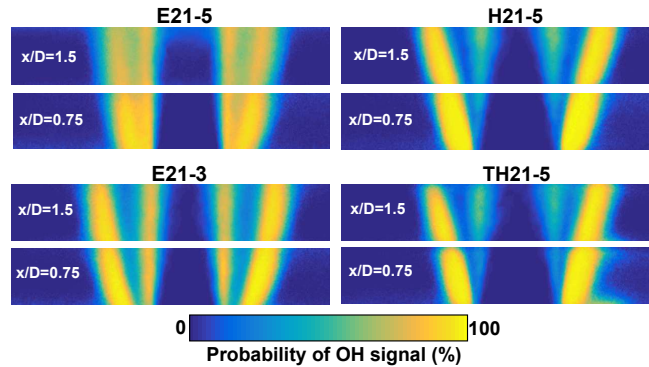


Figure 2: Probability of OH signal detection for four different flame cases.

2. Additional instantaneous OH-PLIF images

To provide further insight into the effects of Re_{jet} and \dot{m}_f on the flame structure, additional OH-PLIF images, centred at $x/D = 3.0$, are shown in Figure 3. Images are shown for cases E21-3, E21-6, E15-5 and E27-5, and three instantaneous images are shown for each case—these were selected to be representative of the “typical” structures for each case and to highlight the differences between cases.

As discussed in Section 3.3, the inner and outer flame structures tend to merge together more frequently for the cases with higher Re_{jet} and lower \dot{m}_f . It can also be seen in Figure 3 that the outer OH structure for the E21-3 case is generally further away from the centreline in comparison with the E21-6 case, and this is reflected in the mean radial plots shown in Section ??.

It was also highlighted in Section 3.6 that the inner peak in the mean OH profiles was lower than the outer peak for the *n*-heptane and *n*-heptane/toluene flames, with the opposite being true for the ethanol flames. This is despite the signal corresponding to the inner OH structures in the instantaneous images being higher in all cases, indicating a less stabilised inner structure in the *n*-heptane and *n*-heptane/toluene flames. This is shown in Figure 4, in which a selection of instantaneous images for four different cases centred at $x/D = 1.5$ are included.

3. Droplet intermittency plots

To provide a visual indication of the statistical behaviour of droplets in the near-field, and how this varies with Re_{jet} , intermittency plots showing the probability of detecting droplets at a given location are shown in Figure 5. The results are shown for the three axial locations nearest to the jet exit, for three different values of Re_{jet} .

As discussed in Section 3.4, the images in Figure 5 show a greater likelihood of droplets in the near-field for the E21-3 case. It can also be seen that droplets are more likely to spread in the radial direction for the E21-3 case; this is most evident in the $x/D = 0.75$ image, where there is a wider spread angle in comparison to the cases with higher Re_{jet} . At $x/D = 1.5$, the E21-3 case can be seen to again have a greater spread in the radial direction, despite being more concentrated in the inner region.

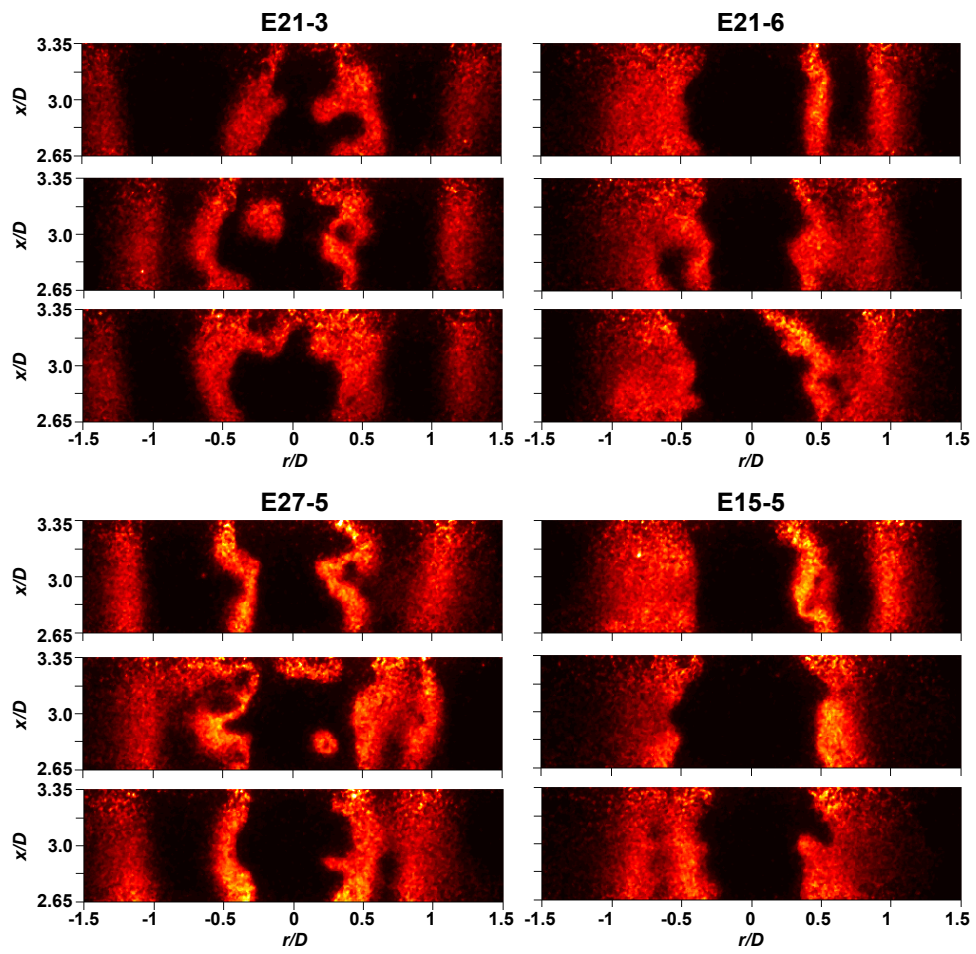


Figure 3: Selected instantaneous OH-PLIF images showing the effects of Re_{jet} and \dot{m}_f .

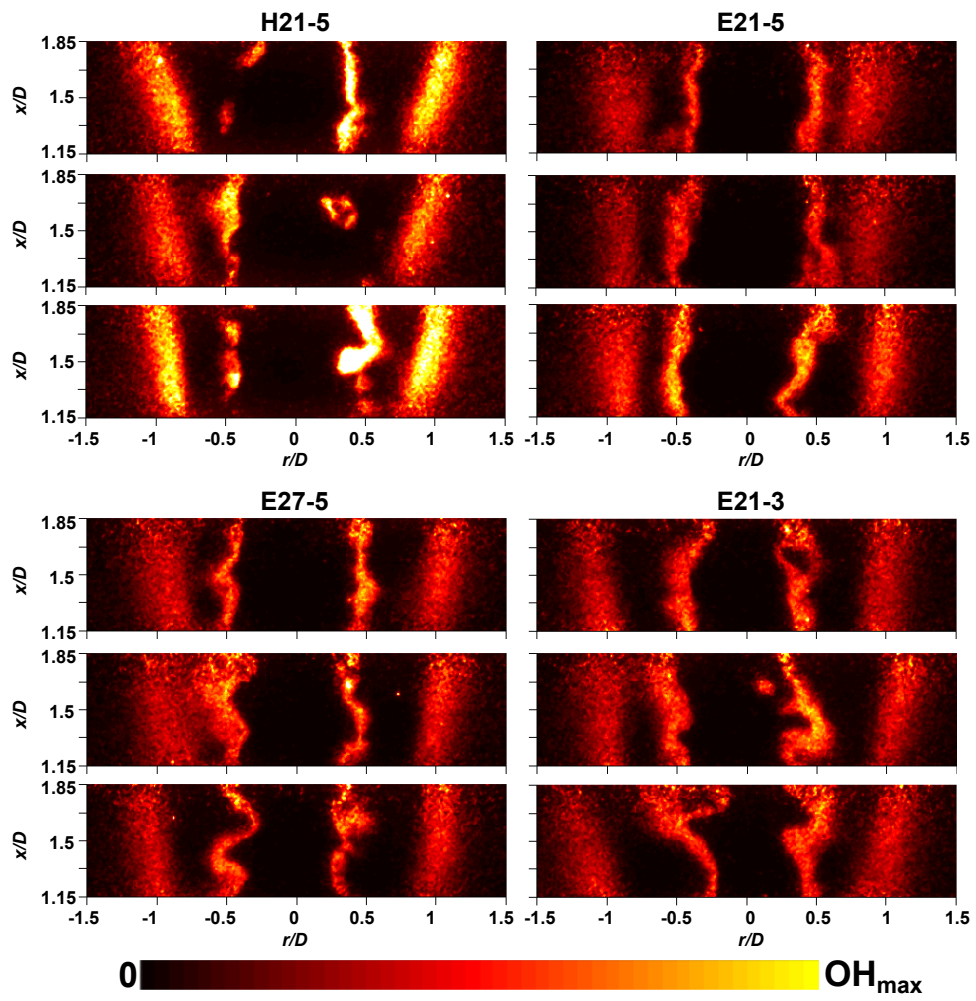


Figure 4: Selected instantaneous OH-PLIF images at $x/D = 1.5$.

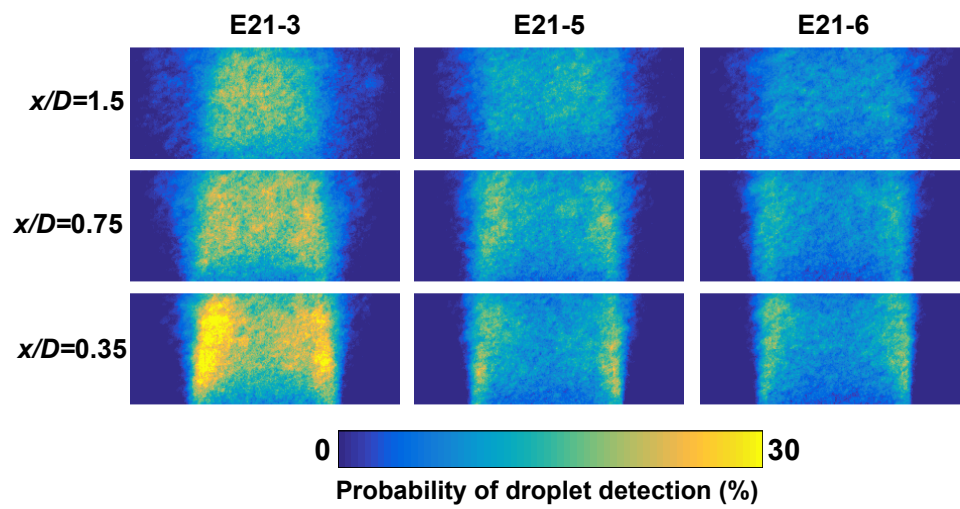


Figure 5: Probability of detection of droplets in Mie scattering signal, for three axial locations and three different Re_{jet} .


Chapter 7

Dilute Spray Flames of Ethanol and *n*-heptane in the Transition to Mild Combustion

Statement of Authorship

Title of Paper	Dilute spray flames of ethanol and <i>n</i> -heptane in the transition to mild combustion.		
Publication Status	<input checked="" type="checkbox"/> Published	<input type="checkbox"/> Accepted for Publication	
	<input type="checkbox"/> Submitted for Publication	<input type="checkbox"/> Unpublished and Unsubmitted work written in manuscript style	
Publication Details	D. B. Proud, M. J. Evans, Q. N. Chan & P. R. Medwell (2022). " Dilute spray flames of ethanol and <i>n</i> -heptane in the transition to mild combustion." <i>Combustion and Flame</i> 238, Article 111918.		

Principal Author

Name of Principal Author (Candidate)	Douglas B. Proud		
Contribution to the Paper	Conceived and set-up experimental configuration in coordination with supervisory team. Coordinated the operation of pulsed lasers and detectors (e.g. tuning of wavelengths, power/beam profile measurements, timing of pulses from different lasers, camera triggering) to achieve simultaneous imaging of spray droplets and intermediate species. Performed experiments and data collection, processed data via the application of image processing techniques, analysed and interpreted data, generated figures from data and wrote manuscript.		
Overall percentage (%)	75		
Certification:	This paper reports on original research I conducted during the period of my Higher Degree by Research candidature and is not subject to any obligations or contractual agreements with a third party that would constrain its inclusion in this thesis. I am the primary author of this paper.		
Signature		Date	24-OCT-2022

Co-Author Contributions

By signing the Statement of Authorship, each author certifies that:

- i. the candidate's stated contribution to the publication is accurate (as detailed above);
- ii. permission is granted for the candidate to include the publication in the thesis; and
- iii. the sum of all co-author contributions is equal to 100% less the candidate's stated contribution.

Name of Co-Author	Michael J. Evans		
Contribution to the Paper	Supervised the initial design/setup of the experimental apparatus and diagnostics, provided guidance with data analysis, provided feedback on manuscript.		
Signature		Date	17-Oct-2022

Name of Co-Author	Qing N. Chan		
Contribution to the Paper	Assisted in implementing image processing/filtering techniques. Provided feedback on manuscript relating to discussion and presentation of results.		
Signature	,	Date	17/10/2022

Name of Co-Author	Paul R. Medwell		
Contribution to the Paper	Supervised overall research direction and helped in identifying the purpose/scope of the experiments and techniques to be used. Assisted in data processing and provided feedback on manuscript.		
Signature		Date	17-OCT-2022



Contents lists available at ScienceDirect

Combustion and Flame

journal homepage: www.elsevier.com/locate/combustflame

Dilute spray flames of ethanol and *n*-heptane in the transition to mild combustion

Douglas B Proud^{a,*}, Michael J Evans^{a,b}, Qing N Chan^c, Paul R Medwell^a^aSchool of Mechanical Engineering, The University of Adelaide, Adelaide, SA 5005, Australia^bUniSA STEM, University of South Australia, Mawson Lakes, SA 5095, Australia^cSchool of Mechanical and Manufacturing Engineering, University of New South Wales, Sydney, NSW 2052, Australia

ARTICLE INFO

Article history:

Received 29 June 2021

Revised 25 November 2021

Accepted 26 November 2021

Available online 15 December 2021

Keywords:

Spray combustion

Mild combustion

Laser diagnostics

Flame stabilisation

ABSTRACT

The structure and stabilisation mechanisms of ethanol and *n*-heptane spray flames are investigated in this study. The burner configuration involves a dilute spray of dispersed droplets which is produced and transported via a carrier gas stream of air to the reaction zone, where the flames are stabilised by a hot coflow of combustion products. A range of coflow conditions were implemented for the different flame cases, allowing the effects of the coflow oxygen (O₂) concentration and temperature to be examined independently. The resulting flames were analysed using three simultaneous laser diagnostic techniques, enabling the combined planar imaging of the hydroxyl (OH) and formaldehyde (CH₂O) radicals, along with the location of droplets. For both fuel types, a noticeable shift in stabilisation behaviour was observed with a variation in the coflow O₂ concentration from 11% to 3%, while the coflow temperature was not seen to have a significant impact. These flames also show an interesting departure from the typical behaviour observed for gaseous and prevaporised flames in a similar configuration, particularly for coflow conditions that are typically associated with the transition to the mild combustion regime.

© 2021 The Combustion Institute. Published by Elsevier Inc. All rights reserved.

1. Introduction

The use of spray-injected liquid fuels is widespread in practical combustion devices, particularly in applications where a high energy density is a priority, such as the transport and aerospace sectors. Injection of liquids in the form of a spray enhances the combustion process, by increasing the rate of fuel evaporation and improving the mixing between fuel and air. In order to develop low-emissions and fuel-flexible technologies, the ability to accurately predict spray combustion phenomena under a range of conditions is a necessity [1,2]. This requires a comprehensive understanding of the physical and chemical processes which take place in spray flames, including turbulence-chemistry interactions, droplet evaporation, and spray break-up.

In practical burners, liquid fuels are typically injected directly into the reaction zone in the form of a “dense” spray, in which droplets are clustered together. This dense region then undergoes spray break-up, with droplets becoming smaller and more dispersed, ultimately evaporating before the fuel burns. This dispersed region of the spray—in which interactions between individual droplets are negligible—is referred to as a “dilute” spray [3]. In

order to focus on the fundamental combustion processes in spray flames in an experimental setting, it is useful to form a dilute spray directly, as this facilitates the use of non-intrusive laser diagnostic techniques [4].

A range of detailed measurements have previously been obtained using a dilute spray configuration, providing important insights into the structure and behaviour of spray flames. Experimental findings based on a piloted, dilute spray burner highlighted the complexity of the reaction zones and ignition modes in such flames, with particular focus on the sensitivity to the boundary conditions [5]. Due to this sensitivity, there has been a conscious effort to obtain experimental results for flames with well-characterised initial conditions, forming a major focus of the Workshop on Turbulent Combustion of Sprays (TCS) [6,7]. These efforts have in turn enabled the development of more accurate and efficient numerical models [8,9], by providing a detailed database for model validation. However, a lack of understanding regarding the structure and stabilisation of dilute spray flames still persists, particularly in relation to “non-conventional” combustion regimes, such as those encountered in sequential gas turbines and burners featuring recirculation of exhaust products [1].

The dilution of air with exhaust gases—either via recirculation or sequential combustion—can provide increased performance in a range of practical applications. The excess heat from the combus-

* Corresponding author.

E-mail address: douglas.proud@adelaide.edu.au (D.B. Proud).

tion products enables preheating of the reactants, facilitating an increase in thermal efficiency and improved combustion stability [10]. Additionally, the reduced O_2 concentration resulting from the dilution leads to a less intense combustion process, limiting the increase in temperature and allowing a reduction of CO, NO_x and soot emissions under certain conditions [11,12]. A particular combustion regime which is of interest in this regard is “mild” combustion, which, in addition to describing the nature of the combustion process, stands for moderate or intense low-oxygen dilution combustion [13]. While initially developed and studied for implementation in furnaces, there is also potential to extend this combustion technique to both land-based and aerospace gas turbines, particularly in applications where greater flexibility is required, both in terms of operating conditions and fuel type [1].

Much of the fundamental experimental work on mild combustion has been carried out using a “jet in hot cross-/co-flow” (JHC) burner configuration [14–17]. This type of burner enables the temperature and O_2 concentration of the oxidant stream to be controlled and adjusted independently of the fuel composition and flow rate, allowing the transition to the mild regime to be studied. In the context of gaseous flames, several interesting findings have previously been made regarding the change in stabilisation and lift-off behaviour with variations in the coflow properties [18–21]. It has been observed that there is a fundamental shift in the stabilisation mechanism of visually lifted flames in the mild regime in comparison with conventional lifted, autoignitive flames, with pre-ignition reactions being detected upstream of the apparent lift-off height [18], and formation of ignition kernels playing a key role in flame stabilisation [19]. This behaviour has been found to be very sensitive to the fuel composition, as well as the coflow temperature and O_2 level [20]. It is important to note that the JHC configuration essentially emulates the conditions required for mild combustion in a simplified configuration, such that the overall appearance of the resulting flames tends to be different to that which is observed under more practical implementations of mild combustion, particularly in downstream locations where the controlled influence of the coflow is diminished [18,22].

While most fundamental studies of mild combustion have been focussed on relatively simple, gaseous fuels, liquid fuels have also been investigated. Pre-vaporised flames of ethanol and dimethyl ether (DME) issuing into a hot coflow were found to exhibit similar structures, particularly at a coflow oxygen concentration of 3% by volume, with an increased sensitivity to fuel type at higher O_2 concentrations [23]. In the same experimental configuration, *n*-heptane flames were found to exhibit a significantly different behaviour to pre-vaporised ethanol and other gaseous flames, with a general deviation away from the mild regime even at very low oxygen concentrations [24]. This was attributed to the more complex chemistry of *n*-heptane and the increased tendency for pyrolysis to occur.

Several studies of mild/flameless combustion of liquid fuels have also been carried out using an enclosed or confined burner configuration. While these configurations typically do not facilitate the analysis of the flame structure and stabilisation mechanisms in as much detail as open flames, the transition to the mild combustion regime can be examined via temperature measurements and analysis of the flue gas composition, in addition to visual observations. Experiments with ethanol in liquid form were performed using a confined burner with recirculation of flue gases and a “blurry injector” configuration to generate a spray, with reduced pollutant emissions and uniform temperatures observed under certain operating conditions corresponding to a range of excess air coefficients [25]. Experiments involving a cyclonic flow configuration emphasised the flexibility of mild combustion, with steady operation spanning across different equivalence ratios and heat inputs for three low-molecular-weight alcohol fuels, while maintaining

complete fuel conversion and low pollutant emissions [26]. While these investigations—and indeed others based upon EGR configurations [27,28]—are very useful for studying the limits of mild combustion in a practical environment under various conditions, it is difficult to draw fundamental conclusions from them with regards to ignition processes and flame structure, largely due to a lack of optical access and challenges with quantifying the level of recirculation in many cases [1]. Thus, while such studies offer important insights which cannot be ascertained from JHC-type experiments, their limitations also emphasise the importance of studying liquid fuels in a JHC configuration, particularly with regards to the development of numerical models.

Liquid sprays issuing into a hot and low-oxygen coflow have also been investigated previously. Measurements of droplet location and gas temperature were obtained for the “Delft spray in hot coflow” (DSHC) flames [29], using a pressure-swirl atomiser to generate droplets. A much more rapid spray break-up and evaporation of droplets was observed for sprays in a hot-diluted coflow compared with a coflow of air. The change in coflow conditions was also found to have a noticeable impact on the underlying flame structure, with a more uniform temperature distribution resulting in lower peak temperatures for the hot-diluted coflow. The existence of distinct inner and outer reaction zones was another important feature of these flames, attributed to the transport of larger droplets away from the spray axis and the flame propagation of a droplet-vapour-air mixture towards the centreline [29]. This “double flame” structure was found to be weakened in the presence of a hot and low-oxygen coflow, due to a less pronounced inner flame resulting from a richer gaseous mixture. This structure has also been investigated for pressure-swirl-atomised spray flames in coflows of room-temperature air at a range of coflow velocities (including no coflow) [30,31], with a transition to a single reaction zone for high coflow velocities. For these flames, partial premixing was found to be crucial to the development of the inner flame structure [31]. The structure of the DSHC flames was also reproduced via large-eddy simulation (LES), in which the formation of multiple flame structures was found to be very sensitive to evaporation rates and chemical time-scales [32], emphasising the importance of understanding these phenomena to further develop modelling capabilities.

A double flame structure has also been identified in a dilute spray configuration [33] which is similar to that used in the current study. For the case of fuel droplets carried by air, it was hypothesised that vaporisation of droplets prior to ignition leads to partial premixing and the formation of locally ignitable mixtures, resulting in an unsteady inner flame front and a broadening of the OH layer [33]. This behaviour was not observed with nitrogen as the carrier gas, with the flame exhibiting a more typical diffusion-like behaviour. The effect of jet boundary conditions and fuel composition has also been investigated using a dilute spray burner, in which simultaneous imaging of fuel droplets and OH/ CH_2O -PLIF was performed [34]. While a double flame structure was a consistent feature of all flames studied, a change in behaviour from a bifurcating structure to the occurrence of distinct ignition kernels was identified for ethanol and *n*-heptane flames. While these studies reveal important details of the structure and stabilisation of spray flames in a hot and low-oxygen environment, an open question remains regarding the effect of the coflow conditions, particularly at reduced O_2 concentrations, such that the transition towards the mild regime is realised.

This study builds upon previous experimental work performed with the same burner configuration [34]. While the aforementioned study [34] presented results and analysis related to the overall evolution of the flame structures for a range of jet boundary conditions, the current paper is focussed on investigating the stabilisation mechanisms of the flames, and the impact of the

Table 1

Table of flame cases, indicating the jet and coflow properties. Numbers in case names represent the rounded molar percentage of O₂ in the coflow, while the letter “H” in the suffix denotes the higher temperature (1690 K) coflow.

Case	Jet Properties			Coflow Properties				
	Fuel	Re_{jet}	Φ_{jet}	X_{O_2}	X_{H_2O}	X_{CO_2}	X_{N_2}	T_{cofl} [K]
HEP-03	<i>n</i> -heptane	5000	2.2	0.030	0.11	0.036	0.83	1400
HEP-08	<i>n</i> -heptane	5000	2.2	0.075	0.11	0.036	0.78	1400
HEP-11	<i>n</i> -heptane	5000	2.2	0.11	0.11	0.036	0.75	1400
HEP-H08	<i>n</i> -heptane	5000	2.2	0.075	0.12	0.061	0.74	1690
ETH-03	Ethanol	5000	1.3	0.030	0.11	0.036	0.83	1400
ETH-11	Ethanol	5000	1.3	0.11	0.11	0.036	0.75	1400

coflow composition and temperature on these mechanisms. The burner used is based upon the well-established JHC configuration, allowing the independent effects of coflow temperature and O₂ concentration to be determined while the jet boundary conditions are held constant. Two different liquid fuels are considered in this study; namely ethanol and *n*-heptane, facilitating additional analysis in terms of the effects of chemistry. These two fuels are also of significant importance in practical combustion applications; ethanol has been identified as a promising low-carbon fuel for the transport sector [35], while *n*-heptane is commonly used as a primary reference fuel for the analysis of internal combustion engines [36]. An ultrasonic nebuliser is implemented to generate a dispersed droplet field, with simultaneous imaging of fuel droplets via Mie scattering, and key intermediate flame species (predominately OH and CH₂O) via planar laser-induced fluorescence (PLIF). This offers a unique insight into the stabilisation and propagation of dilute sprays reacting under conditions relevant to practical, low-emissions and fuel-flexible combustion devices. In particular, an interesting change in the stabilisation behaviour is observed as the O₂ concentration is reduced from 11% to 3%, and fundamental differences in the behaviour of the ethanol and *n*-heptane flames are examined. In addition to developing a deeper understanding of the mechanisms involved in spray combustion, these results also provide a challenging target to test the predictive capabilities of numerical models under a range of boundary conditions.

2. Methodology

2.1. Spray burner description

The burner configuration implemented in this study is identical to that which has been used previously to investigate the effect of jet boundary conditions on spray flames in a hot and low-oxygen coflow [34]. The burner shares many characteristics with the well-studied JHC configuration (e.g. [14,37]), while also incorporating the features of dilute spray burners which have previously been used to study piloted flames [6,38]. An ultrasonic nebuliser is used to generate fuel droplets with a nominal Sauter mean diameter of 30 μm. These droplets have minimal initial momentum, and are transported to the jet exit via a carrier gas stream of air. The jet has an exit inner diameter (D) of 20 mm, and the Reynolds number based on this diameter (Re_{jet}) for all flame cases was 5000. Both ethanol and *n*-heptane were used as the liquid fuel for different flame cases, with the mass loading of liquid held constant at 0.21 g/s. The hot coflow is produced by the lean premixed combustion of natural gas, H₂ and air in varying quantities, with dilution via N₂ to control the concentration of O₂ in the coflow stream. Further details and a schematic of the burner and nebuliser configuration have been presented in a previous publication [34].

By varying the flow rates of natural gas, H₂, N₂ and air into the porous bed, four different coflow conditions were produced. These consist of three coflows with different O₂ concentrations (all

with the same temperature), and two coflows with different temperatures and the same O₂ concentration, enabling the effects of these two parameters to be investigated independently. For the results presented in this paper, the *n*-heptane flames cover all four coflow conditions, while for the ethanol flames only two different coflow conditions are considered. Table 1 displays the various cases for which results are presented, and their corresponding jet and coflow boundary conditions. Also shown in Table 1 is the overall jet equivalence ratio (Φ_{jet}), which is based on the total flowrates of liquid fuel and carrier air in the main fuel tube. It should be noted that some evaporation of the liquid fuel occurs within this tube, that is, between the nebulising surface and the jet exit. Since air is used as the carrier gas, this pre-vaporised fuel undergoes pre-mixing within the pipe. In a previous study using a similar dilute spray configuration, the extent of droplet evaporation within the pipe was found to depend on the relative flow of the liquid and carrier gas [6]. Based on these results, it is estimated that approximately 40% of the liquid fuel undergoes evaporation prior to reaching the jet exit plane.

The flame cases described in Table 1 all correspond to a fuel mass flowrate of 0.21 g/s. As a result, the mixture in the jet (i.e. liquid fuel and carrier air) is overall rich for all cases studied, with $\Phi_{jet} = 2.2$ for the *n*-heptane flames and $\Phi_{jet} = 1.3$ for the ethanol flames, noting that this difference is due to the lower stoichiometric air-fuel ratio for ethanol. In a previous study with the same burner [34], flames with different equivalent ratios were analysed, and it was found that the flame structure was very sensitive to these conditions. In particular, leaner mixtures tend to favour the propagation of the inner flame front due to the influence of the air in the jet, with a less prominent double flame structure present. It then follows that the stabilisation and overall evolution of these flames would be less sensitive to the influence of the coflow, hence the focus on rich mixtures in the current study.

2.2. Diagnostic techniques

Three laser diagnostic techniques were implemented simultaneously in this study, to enable combined imaging of the flame boundary and intermediate species, along with the location of fuel droplets. Planar imaging through the central axis of the burner was performed, using vertical sheets of pulsed laser light with a frequency of 10 Hz and a nominal height of 15 mm. Two Nd:YAG lasers and one Nd:YAG-pumped dye laser were used to generate the three laser sheets of different wavelengths. Different axial locations (x) within the flames were captured by traversing the burner in the vertical direction, ranging from the jet exit ($x = 0$) to 112 mm above the jet ($x/D = 5.6$). A set of 255 images were collected for each diagnostic at each location, facilitating the analysis of the mean flame structure in addition to capturing instantaneous features.

To study the boundary of the reaction zone, the hydroxyl (OH) radical was imaged via the planar laser-induced fluorescence (PLIF) technique. A dye laser, pumped by the 532 nm output of an

Nd:YAG laser, was tuned to a wavelength of 282.927 nm to excite the $Q_1(6)$ transition of the OH radicals. This transition was selected as it has a relatively low sensitivity to temperature fluctuations in the range of interest, and provides a stronger signal in comparison to the $Q_1(7)$ transition. The dye laser was operated with an energy of 0.8 mJ/pulse, and the fluorescence from the OH was imaged onto an ICCD camera through an $f/3.5$ UV lens, with a gate width of 100 ns. The camera lens was fitted with a bandpass filter centred at 310 nm, with a peak transmission $> 70\%$ and FWHM of 10 nm. An additional processing step was applied to the OH-PLIF images to facilitate the separate analysis of the inner and outer branches of the flames. This involved the implementation of an algorithm to find the peaks in the radial OH profile for each image, in conjunction with a shape filter for the OH structures, allowing the statistical behaviour of the reaction zone to be explored in more detail.

The PLIF technique was also implemented to detect intermediate species associated with fuel decomposition and pre-ignition reactions, in particular the formaldehyde (CH_2O) species. This was performed using the third harmonic (355 nm) of an Nd:YAG laser, with a measured energy of 125 mJ/pulse. It is important to note that excitation in the UV region is known to lead to the fluorescence of several intermediate species in a flame, leading to difficulty in attributing the signal to a specific chemical species in some instances. A narrow-range bandpass filter was used to filter out interference from unwanted sources, where possible. This bandpass filter was centred at 410 nm with a FWHM of 10 nm (transmission $> 45\%$), allowing fluorescence from the CH_2O species to be targeted. Consequently, the signal associated with the 355 nm laser is expected to be dominated by CH_2O -PLIF, particularly in the near-field region where the flame undergoes stabilisation, as has been observed previously for similar flames stabilised via autoignition [4]. There is, however, the potential for a non-negligible contribution to the detected signal from other sources which warrants careful discussion. One particular source of interference is from polyaromatic hydrocarbons (PAHs), which are key precursors to the formation of soot, and are therefore expected to contribute to the signal in the furthest-downstream locations where soot begins to form in the *n*-heptane flames. The presence of droplets can also lead to interferences due to both elastic and inelastic scattering. The elastically scattered 355 nm light is expected to be effectively attenuated by the bandpass filter, which has an optical density of approximately 7.5 at 355 nm, such that the intensity of light transmitted at this wavelength is reduced by a factor of greater than 1×10^7 . In terms of inelastic Raman scattering from the fuel, the wavelength of the scattered light can be estimated from the Raman shift corresponding to the CH bonds, for both ethanol and *n*-heptane [39,40]. Based on a shift value of 2900 cm^{-1} , the wavelength of the first-order Raman-scattered light is approximately 396 nm. Despite the narrow range of the bandpass filter, the optical density at this wavelength is slightly lower with a value of 3.3, such that the intensity is reduced by a factor of around 2000. While this means that this interference is significantly reduced by the filter, a low-level signal from fuel Raman can be expected. To account for these interferences, the results presented herein refer to the signal resulting from excitation at 355 nm as "UV-PLIF", and the source of the signal is discussed where appropriate. The UV-PLIF signal was detected using a separate ICCD camera with a 100 ns gate width, fitted with an $f/1.2$ lens.

Imaging of fuel droplets was performed via the Mie scattering technique, using the frequency-doubled 532 nm output of an Nd:YAG laser. The measured energy of the laser was 0.6 mJ/pulse, and the scattered light from droplets was collected on a CCD camera, operated with a gate width of 500 ns. The camera was fitted with an $f/5.6$ lens and a bandpass filter with a FWHM of

10 nm centred at 532 nm, allowing $> 85\%$ transmission at the target wavelength. Additional processing of the Mie scattering images was performed in order to extract the intermittency data relating to the droplet distributions. This involved converting the Mie scattering signal to a binarised image, representing the presence or absence of a droplet at any given location in the detection range. To generate the mean radial droplet distributions, this binarised signal was averaged over a row of 30 pixels centred at each axial location, and a full set of images was then averaged for each case and axial location, yielding the mean probability of droplets being detected at each location. Statistical convergence studies were performed for the radially-integrated droplet probabilities, with results indicating an uncertainty ranging from 1 to 3% for $x/D < 3.0$, and less than 5% for any given measurement. The mean data for all other results presented were found to have uncertainties lower than that of the droplet probabilities.

The timing of the laser pulses and camera gates were controlled using a combination of delay/pulse generators, to ensure that each camera detected the signal associated with a single laser only. The OH-PLIF laser pulse occurred first in the sequence; this was followed by the UV-PLIF pulse with a separation of 100 ns, with the Mie scattering pulse delayed by a further 100 ns, such that all laser pulses occurred within 200 ns of each other. The triggering of the camera shutters was synchronised with the corresponding laser pulse for each camera, such that the beginning of each detection in the sequence was also separated by approximately 100 ns from the preceding detection, noting that the Mie scattering camera gate width was 500 ns. It is worth noting that these timescales (that is, of the order of 500 ns) are much shorter than the flow and chemical timescales within the flames, such that the detections can effectively be considered simultaneous [41,42]. Dark charge, vignetting, and background signal corrections were performed for all imaging techniques, and a beam-profile correction was also carried out for the OH-PLIF signals. Images were spatially matched to sub-pixel accuracy, with each pixel representing $\sim 130 \mu\text{m}$, while the out-of-plane resolution has been estimated to be approximately $400 \mu\text{m}$. A 3×3 median filter was applied to the OH- and UV-PLIF images to improve the signal-to-noise ratio, while the Mie scattering images were left unfiltered.

Photographs of the flames were captured using a DSLR camera, with exposure times ranging from 30 s to 250 μs , although long exposures were not achievable for certain cases due to saturation. The photographs presented in this paper were all captured with an *f*-number of 16 and an ISO value of 100, with manual focus and white balance.

3. Results and discussion

3.1. Visual observations

Photographs of the six flames in this study are shown in Fig. 1. The photographs show the visual appearance of the entire length of these flames, as well as close-up images to highlight the features at the base of the flames. The exposure times used for the photographs are also shown in Fig. 1. It is worth noting that the difference in exposures between the *n*-heptane and ethanol flames is a consequence of the increased luminosity of the *n*-heptane flames due to their increased soot loading. Also shown in Fig. 1 is the region in which laser diagnostics were performed, from the jet exit plane to $x/D = 5.6$.

In Fig. 1(a), the change in coflow conditions does not appear to have a significant impact on the overall appearance of the flames. For the *n*-heptane flames, there is little difference in flame luminosity with variations in O_2 concentration or coflow temperature, while there appears to be a slight increase in luminosity as the concentration of O_2 is increased for the ethanol flames. The *n*-

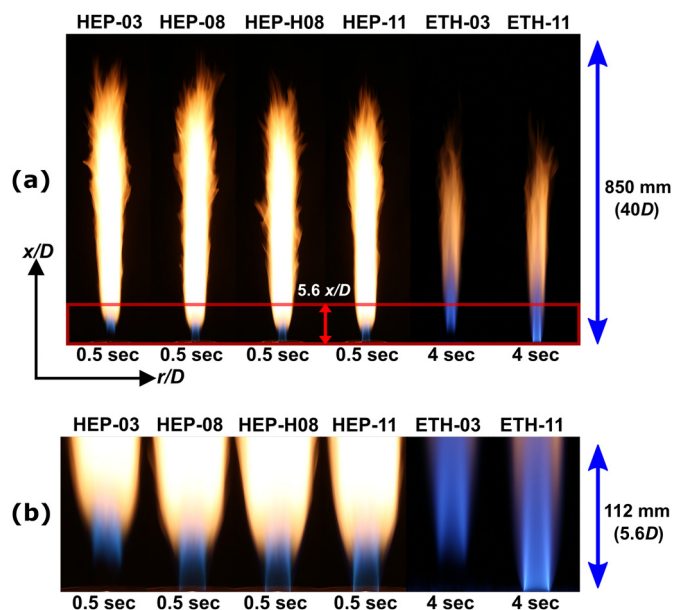


Fig. 1. Photographs of flames captured with a DSLR camera, with exposure times as shown. Subfigure (a): full photographs of flames, with box indicating region in which laser diagnostics were performed. Subfigure (b): Near-field images, from jet exit to 112 mm ($x/D = 5.6$).

heptane flames all appear to feature a “double flame” structure, with a yellow sooting region which branches away from the blue inner cone in the near-field. This structure has previously been observed for similar flames under a variety of jet boundary conditions [34], and has been attributed to premixing of prevaporised fuel with the carrier air upstream of the jet exit (as described in Section 2.1), along with the radial transport of droplets into the hot coflow. In a previous study involving both air and nitrogen as carriers [33], double reaction zones were only observed for cases with an air carrier, further validating this assumption. The ethanol flames also appear to feature an inner and outer reaction zone; this is most apparent in the ETH-11 case, although it is more difficult to distinguish in comparison to the *n*-heptane cases due to the reduction in soot leading to a less luminous outer flame.

It is worth noting that the influence of the hot coflow extends approximately 100 mm downstream from the jet exit plane ($x/D \approx 5$), after which the surrounding air begins to mix with the jet and coflow and influences the appearance of the flames. With this in mind, it can be seen that for the *n*-heptane flames, soot forms within the hot coflow-controlled region ($x/D \lesssim 5$), which is in contrast to previous studies involving a JHC configuration [18,22,24]. This difference is attributed to the presence of carrier air in the jet for these flames, which results in an increase in O_2 concentration as this air mixes with the coflow, leading to an earlier onset of the sooting region than would otherwise be expected for a purely non-premixed flame in a hot and low-oxygen coflow. It should be mentioned that in one of the aforementioned studies (namely [18]), flame cases with air in the central jet were in fact included, using ethylene as the fuel. Again, soot was not observed for these flames in the coflow-controlled region, although an earlier onset of soot in comparison to the case with nitrogen instead of air was observed. Prevaporised *n*-heptane flames carried by air have also been studied [24], where it was again observed that no soot was present in the coflow-controlled region. A key difference, however, is the fact that the fuel-air mixture in the jet was purely gaseous in these studies [18,24], whereas the presence of droplets leads to a change in behaviour for the *n*-heptane flames in the present study. This effect was also observed for toluene-doped H_2 flames, where

the use of toluene in liquid form was found to lead to increased soot formation in comparison to prevaporised toluene, due to the presence of local fuel-rich regions around individual droplets [43].

An important observation from the photographs in Fig. 1(b) is the apparent change in lift-off behaviour under the different coflow conditions. The HEP-03 and ETH-03 flames—which correspond to the 3% O_2 coflow—appear to be lifted, while the flames with 7.5% and 11% O_2 in the coflow can be seen to be attached. It is worth noting that previous findings related to prevaporised ethanol flames show a non-monotonic trend in lift-off height as the O_2 in the coflow is varied, with an initial increase in lift-off as the level of O_2 is increased [24]. This behaviour is thought to be related to a shift in the location of the most reactive mixture fraction in relation to the shear layer, which plays an important role in flame stabilisation in the mild regime [20]. While it is difficult to draw conclusions from the two ethanol flames included here, it appears that an increase in O_2 causes the flame to stabilise nearer to the jet, suggesting a different stabilisation process due to the presence of droplets.

In addition to the change in lift-off behaviour, the close-up images indicate that the onset of the luminous, sooting region occurs closer to the jet exit for the cases with increased O_2 in the coflow. This is particularly evident for the ethanol flames, where a transition to an orange flame can be seen in the ETH-11 close-up image, while this transition occurs further downstream for the ETH-03 case. It is also worth noting the differences in the intensity of the blue region near the flame base in the different cases. For the 3% O_2 cases, this region is relatively faint compared with the higher O_2 cases, with a less clearly defined structure. This result is interesting, since the blue region of the flame is thought to correspond to combustion of the prevaporised fuel [33,34,44], which mixes with the carrier air upstream of the jet exit to form a premixed stream and appears to be stabilised by autoignition at the flame base. However, if this were the case, then the temperature of the coflow would be expected to be the dominant factor in the appearance and lift-off behaviour of this blue region in the near-field, rather than O_2 concentration. Comparing the HEP-08 and HEP-H08 flames, although there is a slight increase in intensity for the case with higher coflow temperature (HEP-H08), it does not seem to have a significant impact on the flame structure in the near-field. This behaviour is further explored in the context of the laser diagnostics results in the following sections.

3.2. Instantaneous OH-PLIF, UV-PLIF and Mie scattering signals

To allow the structure and stabilisation of the flames to be examined, simultaneous OH-PLIF, UV-PLIF and Mie scattering signals were obtained. This facilitates the instantaneous visualisation of the reaction zone boundaries, along with the formation of flame precursor species and the location of fuel droplets. Figure 2 displays typical single-shot images of these signals for the HEP-08 case at an axial location of $x/D = 1.5$, in addition to a superimposed image showing the spatially matched signals together.

Focussing on the OH signal in Fig. 2, the formation of a double flame structure can be seen, with inner and outer reaction zones evident on either side of the centreline. The inner flame front appears to be less stable, with discontinuities in the OH signal which suggests the presence of local extinction and/or ignition events—this is particularly evident on the left-hand side of Fig. 2(a). It should be noted that it is unlikely that these discontinuities are a result of out-of-plane wrinkling of the flame, due to the continuous nature of the UV-PLIF signal which lies inside of the inner OH layer, and the fact that these flames are dominated by streaming flow in the axial direction. It is also worth noting that there is background OH signal resulting from the equilibrium OH in the coflow, although this cannot be observed in Fig. 2 due to the much

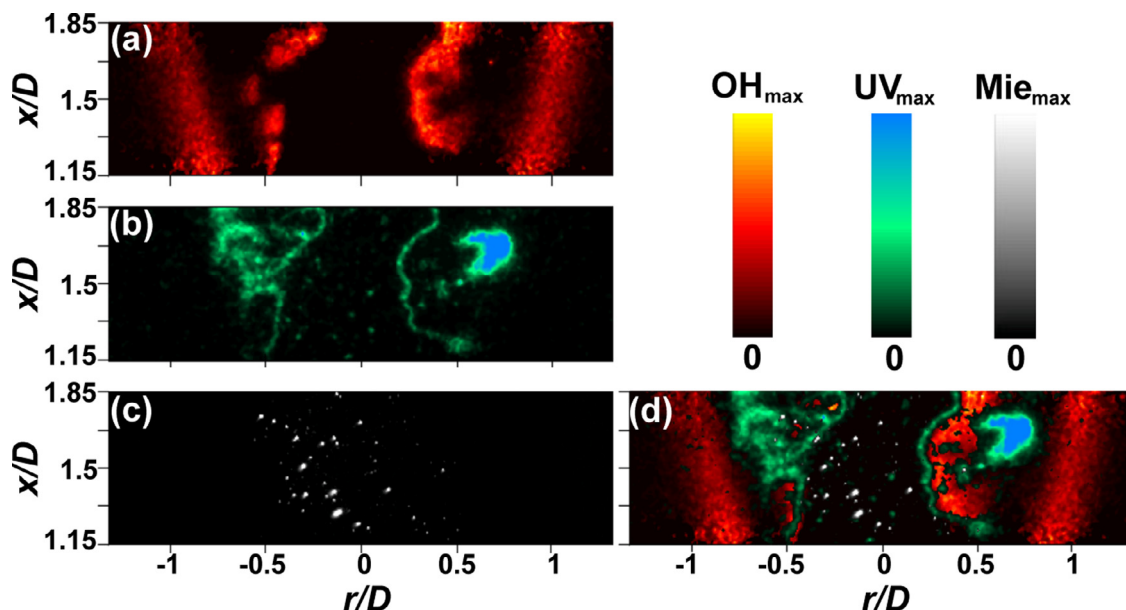


Fig. 2. Typical instantaneous signals of (a) OH-PLIF, (b) UV-PLIF and (c) Mie scattering, and (d) the three signals superimposed. Images correspond to flame case HEP-08 and are centred at $x/D = 1.5$.

Table 2

Frequency of detection of different OH structures (as shown in Fig. 3) for the different flame cases at $x/D = 1.5$.

Case	Type A [%]	Type B [%]	Type C [%]	Type D [%]
HEP-03	11	18	8	63
HEP-08	19	8	29	45
HEP-11	37	2	28	32
HEP-H08	45	1	31	23
ETH-03	17	81	2	0
ETH-11	37	63	0	0

higher signal from the flame fronts. This “coflow OH” concentration is higher in regions closer to the jet exit, with an estimated mole fraction of 3×10^{-5} for the 1400 K coflows and 3×10^{-4} for the 1690 K coflow, based on equilibrium calculations.

Another interesting feature, apparent in Fig. 2, is the overlap between the OH and UV signals, particularly in locations where there are discontinuities in the inner OH layer. This supports the notion that the isolated regions of OH represent ignition kernels, with the UV signal corresponding to the build-up of pre-ignition species. The broader regions of UV-PLIF which can be seen between the inner and outer flame fronts are also worth noting; these are associated with the formation of soot precursors in the outer diffusion flame, hence the very strong signal on the right-hand side of Fig. 2(b). There is also evidence of some interference in the UV-PLIF signal from the presence of fuel droplets in Fig. 2(b). This is represented by the distinct “spots” in the UV-PLIF image, which appear to share some spatial overlap with the Mie scattering signal in the superimposed image. This is hypothesised to be a result of Raman scattering from fuel droplets, which, as discussed in Section 2.2, is expected to produce some low-level interference in the UV-PLIF signal.

To examine the behaviour of the double flame structure in greater detail, it is useful to analyse separately the OH signal corresponding to the inner and outer reaction zones. This in turn enables quantification of the statistical features relating to the flame structures, and facilitates comparisons between different cases. This analysis involves the classification of the instantaneous OH signals into four separate categories, as shown in Fig. 3. Table 2 presents the statistical data relating to the occurrence of these

structures for the different flame cases at various axial locations, in terms of the frequency of detection over a series of images.

From Table 2, it is evident that the coflow conditions have an impact on the formation of the different OH structures shown in Fig. 3. For the 3% O_2 *n*-heptane case (HEP-03), the majority of frames displayed an outer OH layer only, with a relatively large number of instances in which there was a “merged” structure (i.e. Type B). The prevalence of a distinct and stabilised inner OH layer (Type A) can be seen to increase with O_2 concentration and coflow temperature, accompanied by a decreased likelihood of merged flame structures. The presence of ignition kernels—characterised by the Type C structures—can be seen to increase significantly from the 3% to 7.5% O_2 *n*-heptane case, while a further increase in O_2 does not have a noticeable effect. The ethanol flames can be seen to display a significantly different behaviour, which is characterised by an increased tendency of a merged/bifurcating flame structure (i.e. Type B), and a negligible percentage of frames which display either ignition kernels or an outer OH structure only. Similar to the *n*-heptane flames, the increase in O_2 leads to an increased likelihood of a distinct inner and outer reaction zone. The frequency of the occurrence of these different structures is further discussed in the following sections in the context of the stabilisation mechanisms and mean flame structures.

3.3. Flame stabilisation

To illustrate the stabilisation mechanisms of the flames in this study, Figure 4 displays the OH, UV and Mie scattering signals at the flame base for the various cases. The superimposed images are centred at $x/D = 0.35$, with the laser sheet extending from the jet exit to $x/D = 0.7$. Images were selected based on being representative of typical images for each case.

In Fig. 4, the HEP-03 case can be seen to have much lower OH-PLIF signal in comparison to the other cases. This is consistent with the flame photographs shown in Fig. 1, where the HEP-03 flame appears lifted from the jet exit. In saying this, the presence of UV-PLIF signal in Fig. 4 suggests that there are in fact reactions taking place in the visually lifted region for the HEP-03 flame. It should be noted that there is also OH-PLIF signal in the HEP-03 image in Fig. 4, although it is difficult to distinguish from the coflow equi-

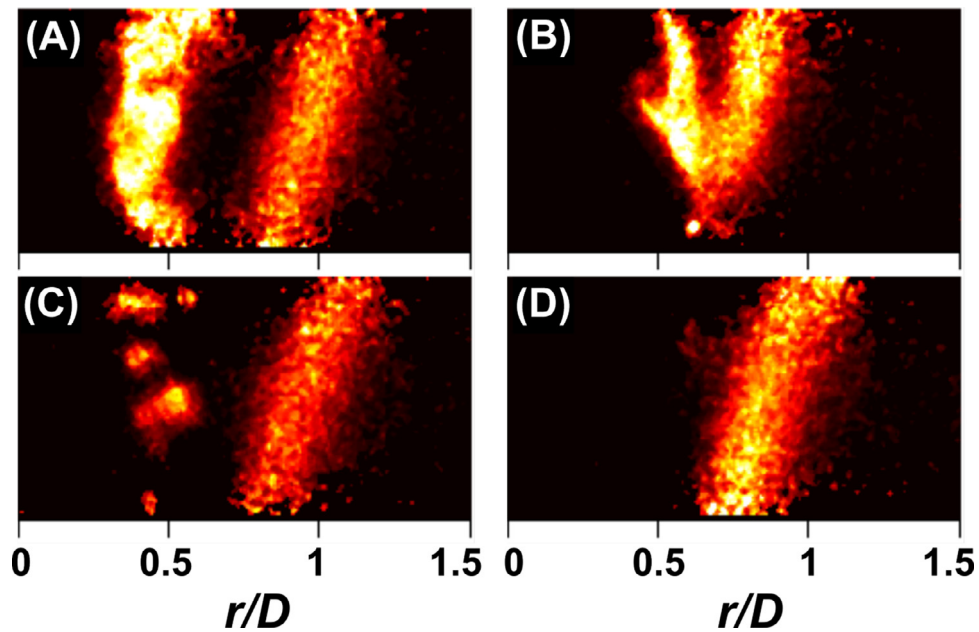


Fig. 3. OH-PLIF images displaying four different types of behaviour; (A) continuous and distinct inner and outer structures, (B) merged/bifurcating inner and outer structures, (C) unsteady inner structure/ignition kernels, and (D) outer OH structure only. Images correspond to flame case HEP-08 and are centred at $x/D = 1.5$.

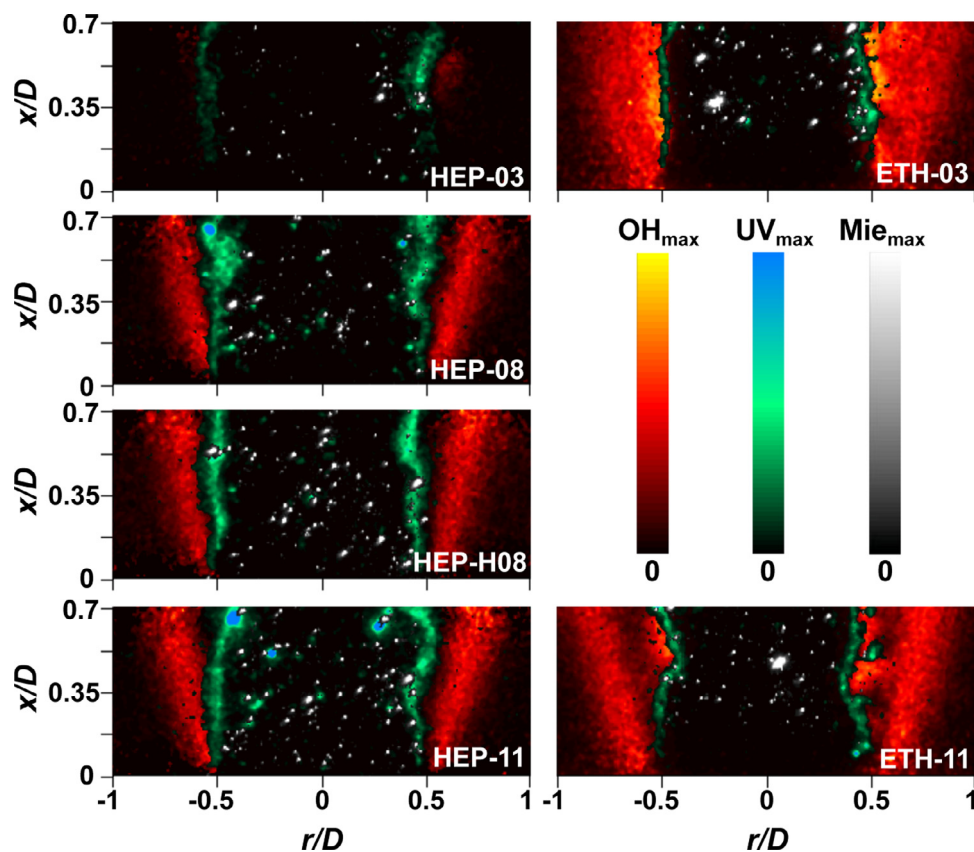


Fig. 4. Instantaneous, superimposed images of OH-PLIF, CH_2O -PLIF and Mie scattering, for the six different flames at $x/D = 0.35$.

librium OH. Interestingly, the equivalent ethanol flame (ETH-03)—which is also visually lifted—has quite a strong OH signal at the jet exit. It has previously been observed that *n*-heptane has a greater tendency for lift-off in comparison to ethanol [24], which would explain the difference in the OH signals between the two fuels in Fig. 4.

With the exception of the HEP-03 flame, Figure 4 indicates that the flames are stabilised at the jet exit. It is interesting to note that, for the *n*-heptane flames and the 11% O_2 ethanol flame, the OH structure which is stabilised at the jet exit appears to correspond to the “outer” flame; this is substantiated by the fact that the continuous OH layer can be seen to spread radially outward

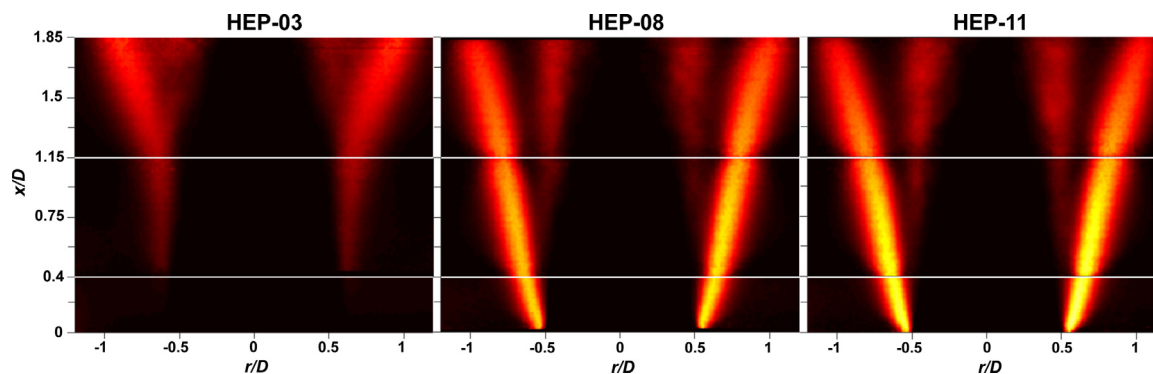


Fig. 5. Averaged OH images for the HEP-03, HEP-08 and HEP-11 cases, from the jet exit to $x/D = 1.85$.

in the images. Referring back to the flame photographs (Fig. 1), the inner blue cone is always angled towards the centreline, and the outer structure is not visible until further downstream. The OH-PLIF imaging therefore reveals that the flames are actually stabilised by the outer reaction zone, which is barely visible in the photographs even in the cases with 11% O_2 , at least with the exposure times shown in Fig. 1. The fuel within the inner region then undergoes ignition, supported by the heat release and radical build-up from the outer flame.

In the ETH-11 image in Fig. 4, the bifurcation of the flame into an inner and outer reaction zone can be seen. The CH_2O layer lies within the inner region, which is consistent with this inner flame front being related to mixing of the prevaporised fuel and the carrier air, as observed in previous studies of similar spray flames [33,34]. In contrast, the *n*-heptane flames only feature a single OH structure on either side of the centreline. However, the CH_2O layer can be seen to branch away from the OH layer at the flame base (for all *n*-heptane cases except for HEP-03, as previously discussed), which indicates that the prevaporised fuel within the inner region has begun to thermally decompose. This fuel in the inner region then undergoes ignition further downstream; this can be seen for the HEP-08 case in Fig. 2.

To further explore the formation and stabilisation of the double flame structure for the various cases, Figure 5 displays the averaged OH-PLIF signal, from the jet exit to $x/D = 1.85$ for the *n*-heptane cases with varying O_2 concentrations (averaged images for the ethanol flames are included in the Supplementary Material). These images highlight the change in flame structure for the 3% O_2 coflow case (HEP-03) in comparison to the other two *n*-heptane flames at the same coflow temperature. The HEP-08 and HEP-11 cases appear very similar, with a consistent outer flame front stabilised at the jet exit, and a less prominent inner flame which begins to branch away at approximately $x/D = 1$. The HEP-03 case, in contrast, does not show a stabilised outer flame until approximately $x/D = 1.15$, which is consistent with the apparent liftoff height (Fig. 1(b)). Interestingly, there is in fact OH signal upstream of this location, albeit at a much lower magnitude relative to the HEP-08 and HEP-11 cases. This low-magnitude signal, which can be seen from approximately $x/D = 0.4$ in Fig. 5, does not appear to spread radially outward in the same way as the outer flame front for the cases with more O_2 in the coflow. This difference can be explained by changes in droplet evaporation as the concentration of O_2 is varied, which is explored in Section 3.4. For the HEP-08 and HEP-11 cases, droplets which are transported radially into the hot coflow begin to evaporate and burn rapidly, forming radicals and releasing heat, such that the increased temperature causes more evaporation and leads to a stabilised diffusion flame at the jet exit. For the 3% O_2 case, the droplets still evaporate at a similar rate initially; however, the low level of O_2 leads to slower chemical timescales and a reduced tendency for droplets to react near the

jet. As a result, the flame corresponding to the prevaporised fuel in the inner region is stabilised prior to the formation of an outer diffusion flame for the HEP-03 case. For the equivalent ethanol case (ETH-03), a weakened outer flame front is again apparent, with a relatively strong signal from the inner flame near the jet exit. This emphasises the importance of the carrier air on the stabilisation of these flames, particularly under highly vitiated conditions.

Referring again to the prevaporised flames of Ye et al. [24], some interesting comparisons can be made regarding the flame structure. One of the key findings of the aforementioned study [24] was the observation that the *n*-heptane flames maintained a “transitional” flame structure as the O_2 concentration was varied from 9% to 3%, characterised by the presence of a weak OH signal below the apparent lift-off height. This was in contrast to the ethanol flames (along with ethylene and natural gas), for which this structure was only observed for the 9% O_2 cases. This transitional structure is considered to be indicative of a shift away from the mild regime [24,45], suggesting a greater difficulty in achieving mild combustion for *n*-heptane. In the present study, the 3% O_2 cases show similarities with the corresponding prevaporised cases [24], with the HEP-03 flame displaying a very weak OH signal upstream of the apparent lift-off height, while the ETH-03 case has a relatively strong signal (Fig. 4). As the concentration of O_2 in the coflow is increased, however, a change in behaviour is observed due to the presence of droplets, resulting in the flames being stabilised by the outer reaction zone at the jet exit.

3.4. Droplet evaporation and distribution

It has previously been observed that the behaviour of droplets in the near-field can have a significant impact on the overall structure of a spray flame [34]. It is therefore crucial to predict these features in order to enable accurate modelling of these flames. To analyse the distribution and evaporation of droplets under the different coflow conditions, Figure 6 displays the radial profiles of droplet intermittency for the various cases, with results corresponding to different axial locations grouped together. These plots are generated based on the probability of droplet detection from the Mie scattering signal, as outlined further in Section 2.2.

In Fig. 6, the droplet distributions at the four axial locations can be seen to follow a similar overall behaviour with variation in the coflow conditions. This is to be expected, since all cases had the same initial fuel loading and jet Reynolds number. A noticeable feature for all cases is the tendency for droplets to cluster near the pipe walls at the jet exit, as shown by the peaks at $|r/D| = 0.5$. This has been observed previously for similar conditions, and is related to the low-Stokes flow phenomena of Saffman lift and turbophoresis [46]. These droplets are immediately exposed to the hot coflow after exiting the jet, and proceed to evaporate relatively quickly, as evidenced by the rapid decrease in droplets at this radial lo-

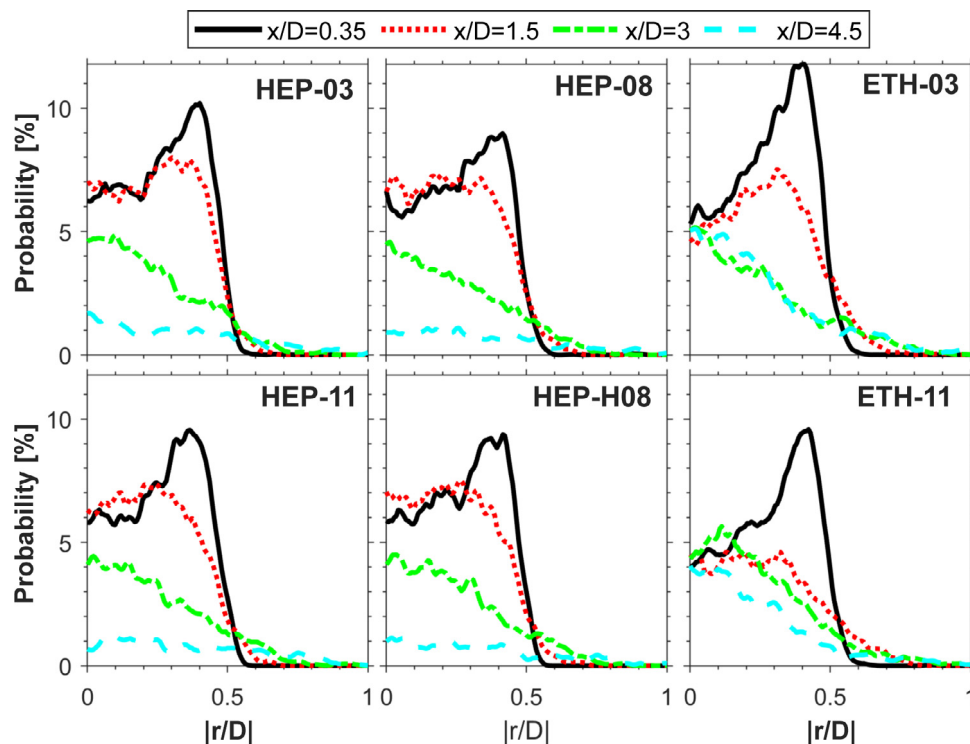


Fig. 6. Radial distribution of droplets at a range of axial locations, for all flame cases.

cation. An interesting difference in the HEP-03 plot in comparison to the other *n*-heptane cases is the fact that the peak at approximately $|r/D| = 0.5$ remains evident at $x/D = 1.5$ (red dotted line), while the profiles have flattened out at this location for the other cases. This supports the explanation from Section 3.3 regarding the change in the flame stabilisation mechanism for the HEP-03 case, in which it was theorised that the slower chemistry and reduced temperatures in the case of lower oxygen leads to a reduction in droplet evaporation and combustion in the near-field, which leads to the premixed portion of the fuel undergoing ignition prior to the formation of the outer flame structure. This difference is also evident for the ethanol cases, where an increase in droplets in general can be observed for the ETH-03 case.

An interesting difference between the *n*-heptane and the ethanol droplet distributions can be observed for the downstream plots, in particular at $x/D = 4.5$. In all of the *n*-heptane cases, there is a sharp reduction in the presence of droplets from $x/D = 3.0$ to $x/D = 4.5$, whereas droplets near the central axis are shown to persist further downstream in the case of ethanol. In fact, for the ethanol cases, the likelihood of droplets being detected along the centreline does not appear to decrease at all with increasing axial location; this is also the case for the *n*-heptane profiles at $x/D = 0.35$ and $x/D = 1.5$, where there even appears to be a slight increase in probability. It should be mentioned that this does not mean that there is no evaporation occurring along the central axis; rather, it suggests that the majority of the droplets have not yet undergone complete evaporation by $x/D = 4.5$ for the ethanol cases, whereas the droplets evaporate more rapidly from $x/D = 1.5$ to $x/D = 4.5$ in the case of *n*-heptane. This is further discussed in the context of the flame structure in the following section.

3.5. Mean flame structure: radial profiles

To investigate the effect of the coflow O_2 concentration on the near-field flame structure, Figure 7 displays the mean radial pro-

files of OH- and UV-PLIF up to $x/D = 1.5$, for the 3% and 11% O_2 ethanol and *n*-heptane cases. The radial signals are generated via the averaging of 15 rows of pixels, centred at the heights stated in the figures. The OH and UV signals are respectively normalised against the maximum average OH and UV signal intensity from each “pair” of cases, at all axial locations up to $x/D = 1.5$. A single normalising value is therefore used for each of the *n*-heptane cases shown in Fig. 7, while a separate value is used for the ethanol cases. In addition to time averaging, the signals on each side of the centreline were also averaged.

A noticeable change in the near-field flame structure with variation in the coflow O_2 concentration is apparent in Fig. 7. For both the *n*-heptane and ethanol cases, distinct peaks in the OH signal can be seen at $x/D = 1.5$ for the 11% O_2 cases, while only a single peak is present for the 3% cases. This confirms that there are distinct, stabilised inner and outer reaction zones for the HEP-11 and ETH-11 cases at this location, while this double reaction zone is less prominent for the 3% O_2 cases. Previously, temperature measurements of ethanol spray flames in air and hot-diluted coflows have been attained [29], with distinct local maxima in the radial profiles observed for the case of an air coflow, suggesting the presence of separate inner and outer reaction zones. For the hot and diluted coflow cases in the same study, the results suggested that a double reaction zone still exists, but with a reduced-intensity inner flame front due to the reduced stoichiometric mixture fraction and hence richer local mixture [29]. In the plots shown in Fig. 7, it is interesting to note the location of the peaks in the OH profiles for the ETH-03 case. At each of the three axial locations shown, the peak occurs at approximately $|r/D| = 0.5$. This peak corresponds to the inner, partially premixed flame front, since the radial location coincides with the inner peaks in the ETH-11 case, and a slight irregularity in the OH profile can be seen at greater radial locations (i.e. at $r/D \approx 0.9$ for $x/D = 0.75$ and $x/D = 1.5$), representing the outer flame front. This indicates that the inner flame is dominant in the near-field for the ETH-03 case, contrasting with the results

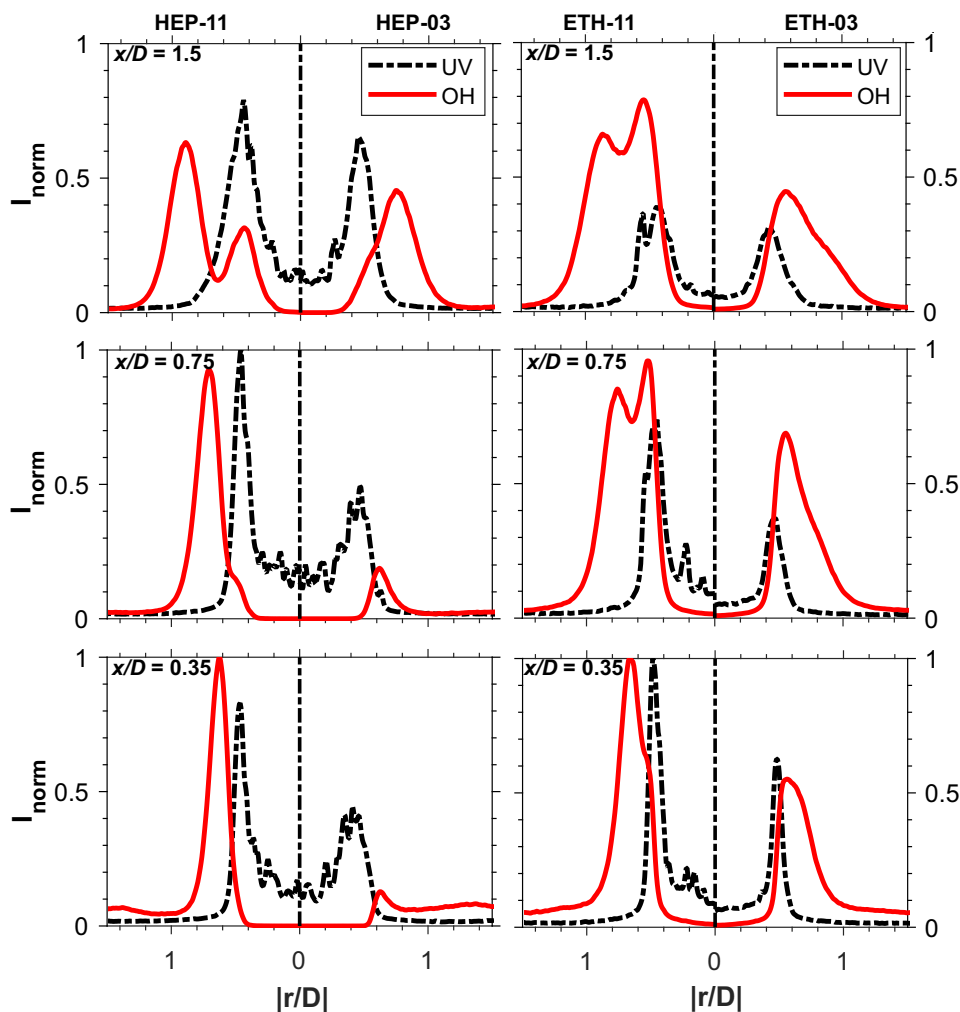


Fig. 7. Mean radial profiles of OH- and UV-PLIF for cases HEP-11, HEP-03, ETH-11 and ETH-03, from $x/D = 0.35$ to $x/D = 1.5$. Signals are normalised against the maximum OH- or UV-PLIF intensity amongst cases of the same fuel type.

of Rodrigues et al. [29]. It should, however, be noted that the results being compared against were obtained with a pressure-swirl atomiser to generate the spray without an air carrier, such that there is not expected to be any partial premixing between fuel and oxidant. This again emphasises the role of partial premixing on the formation of the inner flame front—and in turn the double flame structure—with the burner configuration implemented in the current investigation.

Another important observation from Fig. 7 is the difference between the HEP-03 and ETH-03 cases. Recalling from Fig. 1 that both of these flames are visually lifted to a height of approximately $x/D = 1$, the radial OH- and UV-PLIF profiles centred at $x/D = 0.35$ show that there is in fact a flame below this apparent lift-off height for both cases. This is much more noticeable for the ETH-03 case, which displays an appreciable signal above that of the coflow OH, and of comparable magnitude to the ETH-11 case. The HEP-03 case can also be seen to show a peak in the OH, although this signal is only marginally above that which corresponds to the coflow equilibrium OH, and much lower than the 11% O_2 case. The HEP-03 OH signal is also relatively low at $x/D = 0.75$, after which it can be seen to increase significantly, which is consistent with the apparent lift-off height. It is interesting to note that at $x/D = 0.75$, the location of the OH peak is closer to the centreline for the HEP-03 case compared with the HEP-11 case, indicating that the outer flame is stabilised further downstream for the 3% case; this is also

evident in Fig. 5. At $x/D = 1.5$, the HEP-03 peak can be seen to shift radially outwards to $r/D \approx 0.8$, suggesting that the outer flame is stabilised at this point. At the same axial location, the HEP-11 case shows two distinct peaks in the OH profile, with the outer peak occurring at $r/D \approx 0.9$ and the inner peak at $r/D \approx 0.4$. Similar to the ETH-03 case, the HEP-03 profile also displays an asymmetric shape in the OH profile at $x/D = 1.5$. A key difference, however, is that the ETH-03 case displays a dominant “inner peak” with a broadening of the curve at greater radial distances, whereas the opposite is true for the HEP-03 case. This is consistent with the results displayed in Table 2, which shows that the merged or bifurcating OH structure is the most prevalent for ETH-03 flame (occurring in 81% of frames), while the HEP-03 flame is most likely to feature an outer reaction zone only, with a smaller percentage of frames in which an inner flame is detected. Importantly, the shift in the location of the peak at $x/D = 1.5$ for the HEP-03 case, and the broadening of the profile in the ETH-03 case at the same location, indicates that the visually lifted nature of the 3% O_2 flames can be attributed to the lack of a stabilised outer flame front upstream of this location.

Similarly to Fig. 7, radial profiles of the mean OH and UV signals for cases HEP-H08 and HEP-08 are shown in Fig. 8, highlighting the effect of the coflow temperature on the near-field flame structure. The coflow temperature can be seen to have a relatively minor effect on the flame structure compared with the O_2 con-

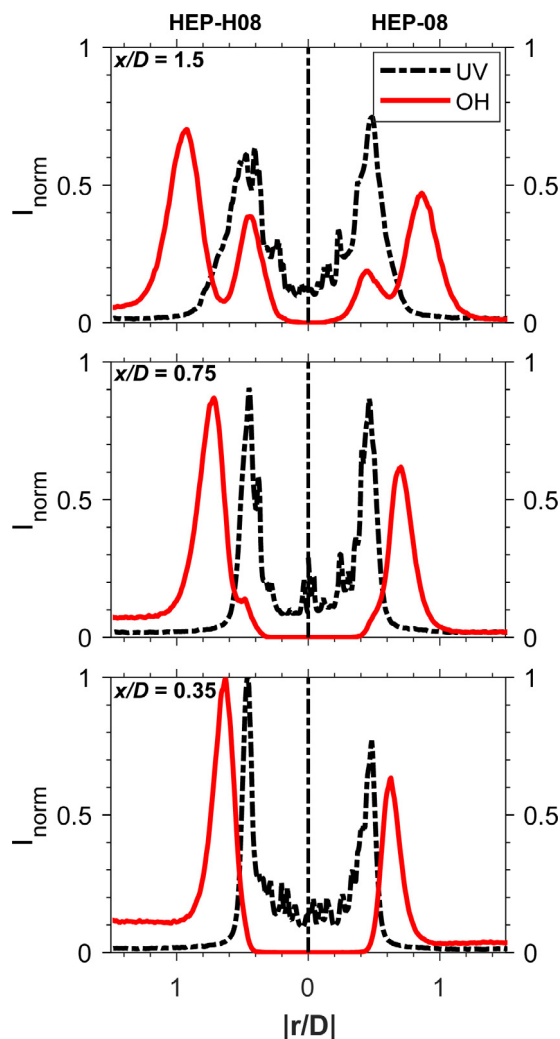


Fig. 8. Mean radial profiles of OH- and UV-PLIF for cases HEP-H08 and HEP-08, from $x/D = 0.35$ to $x/D = 1.5$. Signals are normalised against the maximum OH- or UV-PLIF intensity from both cases.

centration, with the HEP-08 and HEP-H08 profiles showing a similar behaviour. For both cases, the UV signal can be seen to peak radially inward with respect to the OH layer at $x/D = 0.35$, suggesting pre-ignition reactions of the prevaporised fuel, as discussed in Section 3.3. Once the inner flame is established further downstream (i.e. at $x/D = 1.5$), the radial location of the peak in the UV can be seen to coincide with the inner peak in the OH signal, again highlighting the strong overlap between OH and CH_2O during the autoignition stage. It is worth noting that this behaviour is also evident for the HEP-11 flame (Fig. 7), while the UV signal peak at $x/D = 1.5$ for the ETH-11 case occurs closer to the centreline in relation to the inner OH peak. This difference can be attributed to the change in the stabilisation of the inner flame front between the *n*-heptane and ethanol flames. Rather than undergoing spontaneous ignition, the inner flame tends to branch away from the outer flame front near the jet exit for the ETH-11 case, forming a bifurcating structure (see Fig. 4). Consequently, the inner OH structure is more stable for the ethanol flame, and there is less overlap between the OH and CH_2O in this region.

Although the radial profiles are very similar for the HEP-H08 and HEP-08 cases, a difference in the OH structure can be seen at $x/D = 0.75$ in Fig. 8. For both cases, the outer OH structure is dominant, with the peaks occurring at a similar radial location (approximately $|r/D| = 0.7$). For the higher temperature case (HEP-H08), a

slight peak in the OH profile can be observed at $|r/D| = 0.5$, indicating that the inner flame is at least partially stabilised at this axial location. The HEP-08 case, on the other hand, only features a single peak in the OH profile, indicating that the inner flame is stabilised further downstream. This behaviour is to be expected, since the lower coflow temperature leads to a delayed ignition of the prevaporised fuel mixture. It should be noted that, due to the averaging process and the turbulent nature of the flames, the occurrence of a single peak in the OH profile does not necessarily dictate that there is no inner flame front at $x/D = 0.75$ for the HEP-08 case; rather, it shows that there is a less prominent double flame structure, with the outer flame dominating the OH profile.

To show the structure of the flames further downstream, Figure 9 displays the OH profiles for all cases, from $x/D = 3.0$ to $x/D = 5.3$. The plots are grouped in pairs, to show separately the effects of coflow oxygen concentration (for both fuel types) and temperature (for *n*-heptane). It is interesting to note that, despite the clear difference in near-field flame structure between the HEP-03 and HEP-11 cases as seen in Fig. 7, the two appear to exhibit similar overall structures for $x/D \geq 3.0$, with distinct inner and outer reaction zones present for both cases. In saying this, there are some important differences to note between the two cases. While it is not possible to directly compare the signal magnitudes between cases due to varying quenching effects, it is possible to compare the relative magnitudes between the inner and outer peaks at different axial locations. With this in mind, it can be seen at $x/D = 3.0$ that the inner and outer OH peaks are approximately equal in magnitude for the 11% O_2 case, whereas the inner OH peak is greater for the 3% O_2 case. This indicates that the outer reaction zone is significantly less intense for the HEP-03 flame, consistent with previous findings for gaseous flames under similar conditions [14]. For both cases, the centreline OH signal can be seen to peak at $x/D = 4.5$, representing the tip of the inner flame. This is consistent with the droplet distribution plots shown in Fig. 6, which showed a sharp reduction in the presence of droplets at $x/D = 4.5$, indicating that there is rapid evaporation of droplets in this region due to the influence of the inner flame. Although both cases reach their peak centreline OH magnitude at $x/D = 4.5$, there is a much more rapid reduction in OH from $x/D = 4.5$ to $x/D = 5.3$ for the HEP-11 case, highlighted by the reversal in the relative magnitudes of the OH peaks between these two axial locations which is not the case for the HEP-03 flame. This suggests that the tip of the inner flame occurs slightly further downstream for the HEP-03 flame, which is likely a result of the reduced thermal back-support from the weakened outer flame front.

Comparing the HEP-H08 and HEP-08 profiles in Fig. 9, the ≈ 300 K difference in coflow temperature does not appear to have a major impact on the downstream flame structure. Although the OH signal magnitude is significantly higher for the higher temperature coflow (HEP-H08), as expected, the relative magnitudes between the inner and outer OH structures can be seen to be consistent between the two cases at each of the axial locations. Similarly to the 3% and 11% O_2 cases, the peak centreline OH occurs at approximately $x/D = 4.5$, with the outer flame dominating further downstream. In general, the flame structure at $x/D \geq 3.0$ is shown to be very consistent across all of the *n*-heptane flames in Fig. 9. In a previous study of similar flames with varying jet boundary conditions and constant coflow conditions [34], the downstream behaviour—in particular the presence of a double flame structure—was shown to be very sensitive to the initial conditions. This highlights the relative dominance of the jet boundary conditions on the overall structure of these flames, despite the change in stabilisation and near-field structure.

For the ethanol cases shown in Fig. 9, the OH profiles indicate a clear change in behaviour in comparison with the *n*-heptane

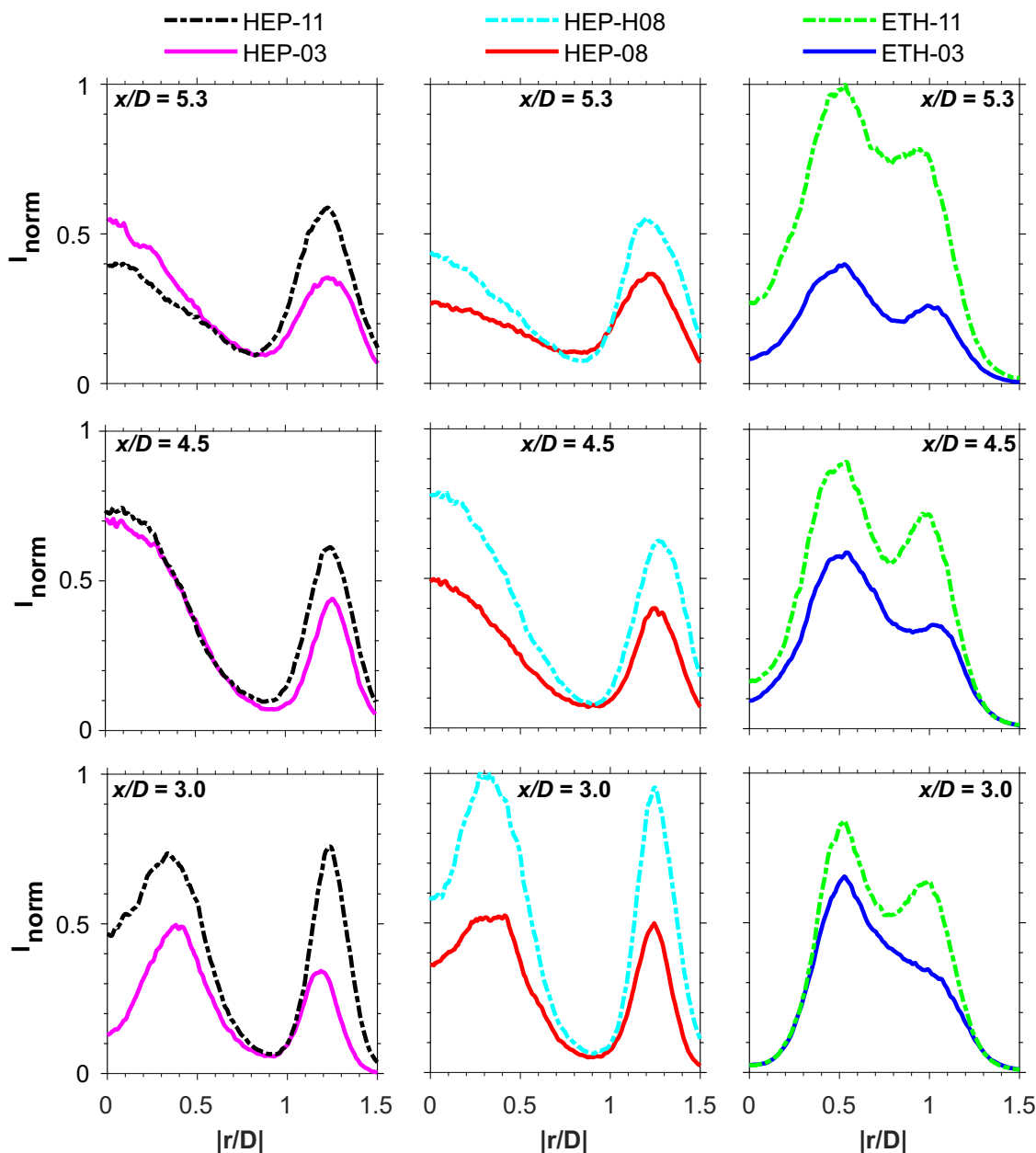


Fig. 9. Mean radial profiles of OH-PLIF from $x/D = 3.0$ to $x/D = 5.3$. Plots are grouped to show the effect of coflow oxygen concentration and temperature separately.

flames. For both the ETH-11 and ETH-03 cases, the inner and outer flame fronts are noticeably less distinct, with the inner OH peak occurring at an increased radial distance and the outer peak closer to the centreline, relative to the *n*-heptane flames at the equivalent axial location. It is interesting to note that in the near field—specifically at $x/D = 0.35$ in Fig. 7—the location of the OH peaks for the ETH-11 and HEP-11 cases is seen to coincide. This suggests that the difference observed in Fig. 9 is not a result of a shift in the stoichiometric mixture fraction (as has been hypothesised previously [34]), since this difference would manifest itself at the point of stabilisation. It can instead be concluded that the change in shape of the OH profiles is a result of increased interaction between the two flame fronts in the case of ethanol, with thermal back-support and the transport of radicals leading to the two structures stabilising closer to one another. The absence of an OH peak at the centreline for the ethanol cases also suggests that the inner reaction

zone persists further downstream in comparison to the *n*-heptane cases. Referring again to the droplet distributions shown in Fig. 6, the lack of centreline decay of droplets in the case of ethanol can be linked with the inner flame front occurring at a greater radial location.

Similarly to the *n*-heptane flames, the reduction in the coflow O_2 concentration can again be seen to cause a weakening of the outer reaction zone in terms of the relative peak signal magnitudes for the ethanol flames. This is particularly evident at $x/D = 3.0$ in Fig. 9, where the inner flame front dominates the OH profile and only a single peak is observed for the ETH-03 case. This indicates that the change in O_2 concentration has an increased effect for the ethanol flames compared with *n*-heptane, in terms of the formation of the double flame structure. Once again, it should be stressed that the lack of a separate outer peak at $x/D = 3.0$ for the ETH-03 case does not disprove the presence of separate inner and

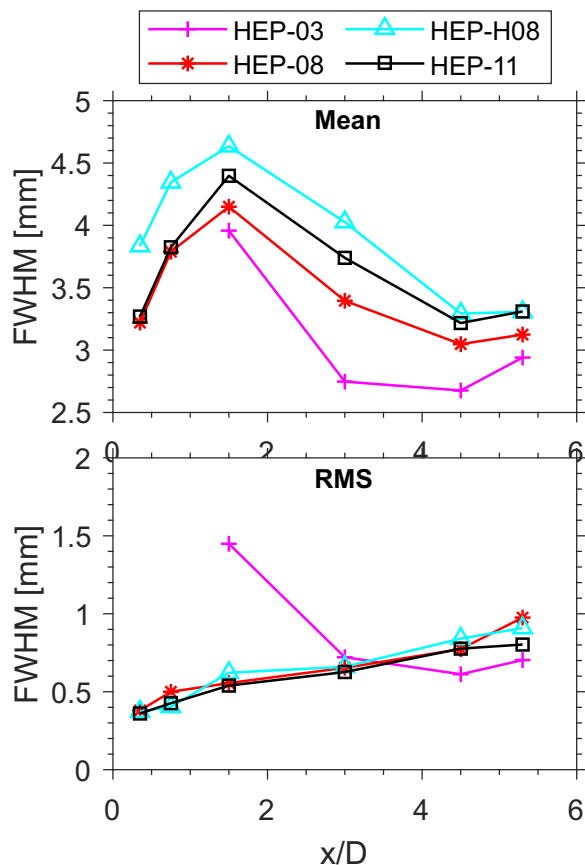


Fig. 10. Mean and RMS values of the FWHM reaction zone thickness for the *n*-heptane cases, from $x/D = 0.35$ to $x/D = 5.3$.

outer reaction zones for this case, rather than these two structures are less distinct, such that the two structures become “blurred” in the mean profile.

It is evident from the profiles shown in Figs. 7–9 that the averaging process leads to a “blurring” effect, such that the variation in the position of the reaction zone due to turbulent fluctuations leads to the inner and outer structures being difficult to distinguish in some instances. To examine the flame structure for the different cases in a more quantitative sense, it is therefore useful to perform calculations on the instantaneous images prior to averaging. As mentioned in the Methodology, an algorithm was developed to separate the inner and outer OH structures in the instantaneous images. Using this method, it is then possible to calculate the width of the outer reaction zone for the different cases. For this analysis, the full-width at half maximum (FWHM) value of the radial OH signal was used to provide a measure of the reaction zone thickness, similar to previous studies [37,47]. For further details regarding this process the reader is directed to the Supplementary Material, where an example of the separation between the inner and outer structures and the subsequent analysis are provided. The FWHM results are plotted against the axial location in Fig. 10, for the *n*-heptane flames from the jet exit to $x/D = 5.3$. For the HEP-03 case, the results are only included for $x/D \geq 1.5$, since the lack of a stabilised outer flame upstream of this point prevents a meaningful analysis of the flame width.

The FWHM values displayed in Fig. 10 highlight some key differences between the flame cases, which are not evident from the mean profiles alone. From the mean FWHM plots, it can be seen that a reduction in O_2 concentration leads to a narrowing of the outer reaction zone, with the HEP-03 case in particular having a noticeably narrower reaction zone in comparison to the higher O_2

cases for $x/D \geq 3$. This is an interesting result, since previous studies of mild combustion have found that the reaction zone tends to become wider as the O_2 concentration is reduced, which is attributed to a shift in the stoichiometric mixture fraction towards the oxidant side resulting in lower strain rates [37]. The change in behaviour observed in the current study is likely due to the presence of the inner reaction zone, which influences the outer flame front differently in the various cases. Recalling from Fig. 7 and the accompanying discussion that the HEP-03 case only displays a single peak in the mean OH profile at $x/D = 1.5$ while the HEP-11 case features distinct peaks, it follows that the double flame structure is less prominent for the 3% case, with increased interaction between the two reaction zones in the HEP-03 case; this is substantiated by the increased likelihood of the merged flame structures being detected for this case (Table 2). Somewhat paradoxically, this merging of the inner and outer structures leads to a broadening of the reaction zone when it occurs, hence the much higher RMS values for the HEP-03 case at $x/D = 1.5$. However, it should be noted that this behaviour only accounts for approximately 18% of the images analysed, while the majority show only a stabilised outer flame. It is therefore hypothesised that the presence of a stabilised and distinct inner reaction zone corresponds with a broadening of the outer flame front, whereas the lack of a stabilised inner flame for the HEP-03 case results in a build-up of radicals within the inner region which supports the outer reaction zone, ultimately leading to a narrowing of the OH structures. This behaviour is also consistent with the shift in the OH peak towards the centreline for the HEP-03 radial profiles at $x/D = 1.5$ in Fig. 7 and at $x/D = 3.0$ in Fig. 9. This also explains the increased width for the HEP-H08 case, for which the inner flame was shown to have greater stability and separation from the outer structure in Table 2 and Fig. 8.

The change in the reaction zone width with increasing distance from the jet exit is also interesting to note. For the cases with $> 3\%$ O_2 , there is an initial increase in the FWHM values from the jet exit to $x/D = 1.5$, followed by a narrowing of the reaction zone up to $x/D = 4.5$, after which the width appears to increase again. The broadening observed in the near-field region is likely a result of the radially outward shift of the outer reaction zone (shown in Figs. 7 and 8), which is accompanied by reduced strain rates. Interestingly, the reaction zone continues to move radially outwards up until $x/D \approx 3.0$, yet there is a sharp reduction in the reaction zone width from $x/D = 1.5$ to $x/D = 3.0$ for all cases. This is consistent with the explanation that the presence of the inner reaction zone leads to a broadening of the outer flame, with the increased separation further downstream leading to a narrower outer structure. As mentioned, the tip of the inner flame is reached at approximately $x/D = 4.5$ for the *n*-heptane cases, which is consistent with the increase in the outer reaction zone width downstream of this location.

4. Conclusions

The stabilisation features and flame structures of dilute sprays of ethanol and *n*-heptane have been experimentally analysed under a range of coflow conditions. Three laser diagnostic techniques were performed simultaneously, enabling the combined visualisation and analyses of the reaction zones and droplet distributions. This work highlights the complex nature of the reaction zones and stabilisation processes for spray combustion, specifically under highly vitiated coflow conditions which are typical of the mild combustion regime. A transition from a stabilised flame base at the jet exit to a visually lifted flame was observed with reduction in the coflow O_2 concentration to 3%, for both *n*-heptane and ethanol flames. The instantaneous imaging, however, revealed the occurrence of flame radicals and intermediate species in this apparently lifted region, indicating the presence of a relatively weak reaction

zone extending to the jet exit for the 3% O₂ cases. Analysis of the radial droplet distributions revealed that there is a tendency for droplets to cluster near the pipe walls at the jet exit, after which they undergo rapid evaporation in the presence of the hot coflow. This leads to a stabilised diffusion flame at the jet exit for coflows with >3% O₂ concentrations, with the heat release in this region leading to increased evaporation rates in comparison to the reduced O₂ cases. Droplets were found to persist further downstream in the ethanol cases, which is attributed to the increased interaction between the inner and outer flame fronts which results in the inner flame propagating further radially from the central axis in comparison to the *n*-heptane flames.

The mean OH- and UV-PLIF results revealed interesting changes in the structures of the flames studied. The 3% O₂ cases were found to display a less prominent double flame structure, particularly in the near field, due to the weakened outer flame front which is stabilised further downstream. A broadening in the mean radial OH profile was observed near the apparent lift-off height, for both the HEP-03 and ETH-03 cases, suggesting that the lack of a stabilised “outer flame” at the jet exit is responsible for the visually lifted nature of the flames. It was also observed that there is an increased probability of merging between the inner and outer flame fronts for the HEP-03 case in comparison to the other *n*-heptane flames, leading to greater variability in the reaction zone width for this case in the near-field. Interestingly, and in apparent contrast to gaseous flames in similar configurations, the reduction in O₂ was found to lead to a narrowing of the mean outer reaction zone, and the cases with higher O₂ concentrations displayed a non-monotonic behaviour with respect to the axial location. This indicates that the presence of a stabilised inner reaction zone leads to a broadening of the outer reaction zone, which is in competition with the reduced strain rate at greater axial locations.

Declaration of Competing Interest

The authors declare that they have no known competing financial interests or personal relationships that could have appeared to influence the work reported in this paper.

Acknowledgments

The authors thank Dr Jingjing Ye for her contribution in the design of the burner used for these experiments, and Dr Thomas Kirch for his assistance with data collection. The support from the University of Adelaide is acknowledged, along with the financial support provided by the Australian Research Council (ARC) and the Future Fuels Cooperative Research Centre (CRC): Project RP1.10-04.

Supplementary material

Supplementary material associated with this article can be found, in the online version, at doi:[10.1016/j.combustflame.2021.111918](https://doi.org/10.1016/j.combustflame.2021.111918).

References

- [1] A.A.V. Perpignan, A. Gangoli Rao, D.J.E.M. Roekaerts, Flameless combustion and its potential towards gas turbines, *Prog. Energy Combust. Sci.* 69 (2018) 28–62.
- [2] A.E.E. Khalil, A.K. Gupta, Fuel flexible distributed combustion for efficient and clean gas turbine engines, *Appl. Energy* 109 (2013) 267–274.
- [3] G. Faeth, Mixing, transport and combustion in sprays, *Prog. Energy Combust. Sci.* 13 (4) (1987) 293–345.
- [4] A.R. Masri, Turbulent combustion of sprays: from dilute to dense, *Combust. Sci. Technol.* 188 (10) (2016) 1619–1639.
- [5] A.R. Masri, A. Kourmatzis, W. O'Loughlin, J.D. Gounder, From dilute to dense turbulent sprays: combustion, auto-ignition and atomization, in: B. Merci, E. Gutheil (Eds.), *Experiments and Numerical Simulations of Turbulent Combustion of Diluted Sprays*, ERCOFTAC Series, Springer International Publishing, Cham (2014), pp. 1–29.
- [6] J.D. Gounder, A. Kourmatzis, A.R. Masri, Turbulent piloted dilute spray flames: flow fields and droplet dynamics, *Combust. Flame* 159 (11) (2012) 3372–3397.
- [7] Experiments and numerical simulations of turbulent combustion of diluted sprays, in: B. Merci, E. Gutheil (Eds.), ERCOFTAC Series, volume 19, Springer International Publishing, Cham, 2014.
- [8] P. Jenny, D. Roekaerts, N. Beishuizen, Modeling of turbulent dilute spray combustion, *Prog. Energy Combust. Sci.* 38 (6) (2012) 846–887.
- [9] S. Hochgreb, Mind the gap: turbulent combustion model validation and future needs, *Proc. Combust. Inst.* 37 (2) (2019) 2091–2107.
- [10] M. Katsuki, T. Hasegawa, The science and technology of combustion in highly preheated air, *Symp. (Int.) Combust.* 27 (2) (1998) 3135–3146.
- [11] J.A. Wünnig, J.G. Wünnig, Flameless oxidation to reduce thermal NO-formation, *Prog. Energy Combust. Sci.* 23 (1) (1997) 81–94.
- [12] M. de Joannon, G. Langella, F. Beretta, A. Cavaliere, C. Noviello, Mild combustion: process features and technological constraints, *Combust. Sci. Technol.* 153 (1) (2000) 33–50.
- [13] A. Cavaliere, M. de Joannon, Mild combustion, *Prog. Energy Combust. Sci.* 30 (4) (2004) 329–366.
- [14] B.B. Dally, A.N. Karpets, R.S. Barlow, Structure of turbulent non-premixed jet flames in a diluted hot coflow, *Proc. Combust. Inst.* 29 (1) (2002) 1147–1154.
- [15] R. Cabra, T. Myhrvold, J. Chen, R. Dibble, A. Karpets, R. Barlow, Simultaneous laser Raman-Rayleigh-Lif measurements and numerical modeling results of a lifted turbulent H₂/N₂ jet flame in a vitiated coflow, *Proc. Combust. Inst.* 29 (2) (2002) 1881–1888.
- [16] J. Sidey, E. Mastorakos, Visualization of MILD combustion from jets in cross-flow, *Proc. Combust. Inst.* 35 (3) (2015) 3537–3545.
- [17] C.M. Arndt, M.J. Papageorge, F. Fuest, J.A. Sutton, W. Meier, M. Aigner, The role of temperature, mixture fraction, and scalar dissipation rate on transient methane injection and auto-ignition in a jet in hot coflow burner, *Combust. Flame* 167 (2016) 60–71.
- [18] P.R. Medwell, P.A.M. Kalt, B.B. Dally, Imaging of diluted turbulent ethylene flames stabilized on a jet in hot coflow (JHC) burner, *Combust. Flame* 152 (1) (2008) 100–113.
- [19] E. Oldenhof, M. Tummers, E. van Veen, D. Roekaerts, Ignition kernel formation and lift-off behaviour of jet-in-hot-coflow flames, *Combust. Flame* 157 (6) (2010) 1167–1178.
- [20] M.J. Evans, A. Chinnici, P.R. Medwell, J. Ye, Ignition features of methane and ethylene fuel-blends in hot and diluted coflows, *Fuel* 203 (2017) 279–289.
- [21] M.J. Evans, P.R. Medwell, H. Wu, A. Stagni, M. Ihme, Classification and lift-off height prediction of non-premixed MILD and autoignitive flames, *Proc. Combust. Inst.* 36 (3) (2017) 4297–4304.
- [22] M.J. Evans, P.R. Medwell, Z. Sun, A. Chinnici, J. Ye, Q.N. Chan, B.B. Dally, Downstream evolution of *n*-heptane/toluene flames in hot and vitiated coflows, *Combust. Flame* 202 (2019) 78–89.
- [23] J. Ye, P.R. Medwell, K. Kleinheinz, M.J. Evans, B.B. Dally, H.G. Pitsch, Structural differences of ethanol and DME jet flames in a hot diluted coflow, *Combust. Flame* 192 (2018) 473–494.
- [24] J. Ye, P.R. Medwell, M.J. Evans, B.B. Dally, Characteristics of turbulent *n*-heptane jet flames in a hot and diluted coflow, *Combust. Flame* 183 (2017) 330–342.
- [25] C.G. de Azevedo, J.C. de Andrade, F. de Souza Costa, Flameless compact combustion system for burning hydrous ethanol, *Energy* 89 (2015) 158–167.
- [26] G.B. Ariemma, P. Bozza, M. de Joannon, P. Sabia, G. Sorrentino, R. Ragucci, Alcohols as energy carriers in MILD combustion, *Energy Fuels* 35 (9) (2021) 7253–7264.
- [27] S. Kruse, B. Kerschgens, L. Berger, E. Varea, H. Pitsch, Experimental and numerical study of MILD combustion for gas turbine applications, *Appl. Energy* 148 (2015) 456–465.
- [28] J. Ye, P.R. Medwell, E. Varea, S. Kruse, B.B. Dally, H.G. Pitsch, An experimental study on mild combustion of prevaporised liquid fuels, *Appl. Energy* 151 (2015) 93–101.
- [29] H.C. Rodrigues, M.J. Tummers, E.H. van Veen, D.J.E.M. Roekaerts, Spray flame structure in conventional and hot-diluted combustion regime, *Combust. Flame* 162 (3) (2015) 759–773.
- [30] J.A. Friedman, M. Rensizbulut, Investigating a methanol spray flame interacting with an annular air jet using phase-Doppler interferometry and planar laser-induced fluorescence, *Combust. Flame* 117 (4) (1999) 661–684.
- [31] S.K. Marley, E.J. Welle, K.M. Lyons, W.L. Roberts, Effects of leading edge entrainment on the double flame structure in lifted ethanol spray flames, *Exp. Therm. Fluid Sci.* 29 (1) (2004) 23–31.
- [32] L. Ma, D. Roekaerts, Numerical study of the multi-flame structure in spray combustion, *Proc. Combust. Inst.* 36 (2) (2017) 2603–2613.
- [33] W. O'Loughlin, A.R. Masri, The structure of the auto-ignition region of turbulent dilute methanol sprays issuing in a vitiated co-flow, *Flow Turbul. Combust.* 89 (1) (2012) 13–35.
- [34] D.B. Proud, M.J. Evans, P.R. Medwell, Q.N. Chan, Experimental investigation of the flame structure of dilute sprays issuing into a hot and low-oxygen coflow, *Combust. Flame* 230 (2021) 111439.
- [35] N. Leplat, P. Dagaut, C. Togbé, J. Vandooren, Numerical and experimental study of ethanol combustion and oxidation in laminar premixed flames and in jet-stirred reactor, *Combust. Flame* 158 (4) (2011) 705–725.
- [36] H.J. Curran, P. Gaffuri, W.J. Pitz, C.K. Westbrook, A comprehensive modeling study of *n*-heptane oxidation, *Combust. Flame* 114 (1) (1998) 149–177.
- [37] P.R. Medwell, P.A. Kalt, B.B. Dally, Simultaneous imaging of OH, formaldehyde, and temperature of turbulent nonpremixed jet flames in a heated and diluted coflow, *Combust. Flame* 148 (1–2) (2007) 48–61.

- [38] A.R. Masri, J.D. Gounder, Turbulent spray flames of acetone and ethanol approaching extinction, *Combust. Sci. Technol.* 182 (4–6) (2010) 702–715.
- [39] H. Zheng, E. Qiao, Y. Yang, T. Duan, Determination of inner pressure for fluid inclusions by Raman spectroscopy and its application, *Geosci. Front.* 2 (3) (2011) 403–407.
- [40] T. Müller, G. Grünefeld, V. Beushausen, High-precision measurement of the temperature of methanol and ethanol droplets using spontaneous Raman scattering, *Appl. Phys. B* 70 (1) (2000) 155–158.
- [41] M.J. Evans, P.R. Medwell, Understanding and interpreting laser diagnostics in flames: a review of experimental measurement techniques, *Front. Mech. Eng.* 5 (2019) 65.
- [42] S.M. Mahmoud, G.J. Nathan, P.R. Medwell, B.B. Dally, Z.T. Alwahabi, Simultaneous planar measurements of temperature and soot volume fraction in a turbulent non-premixed jet flame, *Proc. Combust. Inst.* 35 (2) (2015) 1931–1938.
- [43] M.J. Evans, D.B. Proud, P.R. Medwell, H. Pitsch, B.B. Dally, Highly radiating hydrogen flames: effect of toluene concentration and phase, *Proc. Combust. Inst.* 38 (1) (2021) 1099–1106.
- [44] Y.K. Jeong, C.H. Jeon, Y.J. Chang, Evaluation of the equivalence ratio of the reacting mixture using intensity ratio of chemiluminescence in laminar partially premixed CH₄-air flames, *Exp. Therm. Fluid Sci.* 30 (7) (2006) 663–673.
- [45] P.R. Medwell, B.B. Dally, Experimental observation of lifted flames in a heated and diluted coflow, *Energy Fuels* 26 (9) (2012) 5519–5527.
- [46] T.C.W. Lau, G.J. Nathan, Influence of Stokes number on the velocity and concentration distributions in particle-laden jets, *J. Fluid Mech.* 757 (2014) 432–457.
- [47] E.J. Welle, W.L. Roberts, C.D. Carter, J.M. Donbar, The response of a propane-air counter-flow diffusion flame subjected to a transient flow field, *Combust. Flame* 135 (3) (2003) 285–297.

Dilute spray flames of ethanol and *n*-heptane in the transition to mild combustion

Douglas B. Proud^{a,*}, Michael J Evans^{a,b}, Qing N Chan^a, Paul R Medwell^c

^a*School of Mechanical Engineering, The University of Adelaide, Adelaide, SA 5005, Australia*

^b*UniSA STEM, University of South Australia, Mawson Lakes, SA 5095, Australia*

^c*School of Mechanical and Manufacturing Engineering, University of New South Wales, Sydney, NSW 2052, Australia*

Supplementary Material

1. Averaged OH-PLIF images for ethanol

Figure 1 shows the mean flame structure from the jet exit to $x/D = 1.85$, in the form of the averaged OH-PLIF images stacked together. This figure complements what was shown in the radial plots, allowing the flame behaviour to be better visualised. As mentioned in the main text, the outer flame can be seen to be significantly weakened for the 3% case, with a much less clearly defined structure, which supports the analysis of the radial plots in Section 3.5.

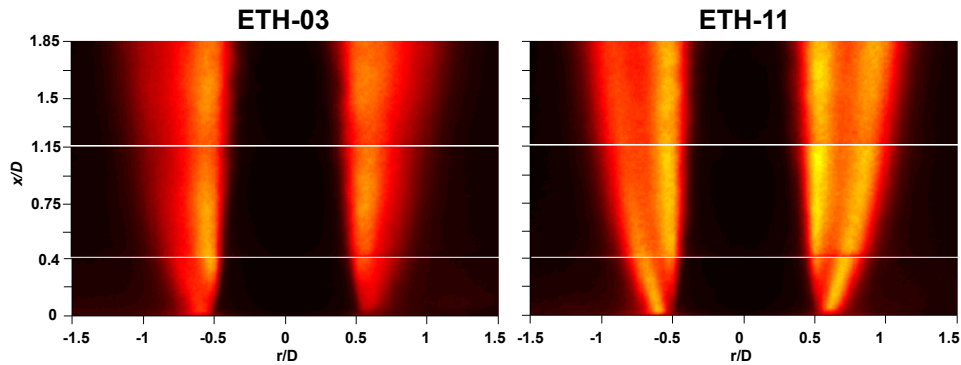


Figure 1: Averaged OH-PLIF images from the jet exit to $x/D = 1.85$ for cases ETH-03 and ETH-11.

*Corresponding author. E-mail: douglas.proud@adelaide.edu.au

2. Additional OH processing and FWHM calculation

To analyse the behaviour of the inner and outer reaction zones separately, a spatial filtering algorithm was applied to the instantaneous OH-PLIF images. Essentially this algorithm was based on identifying the radial locations of the peak OH signal, as well as the minimum value between these peaks, which is used as a boundary to separate the inner and outer structures. An example of this is shown in Figure 2 for the HEP-11 case, including the definition of the FWHM for the outer OH structure.

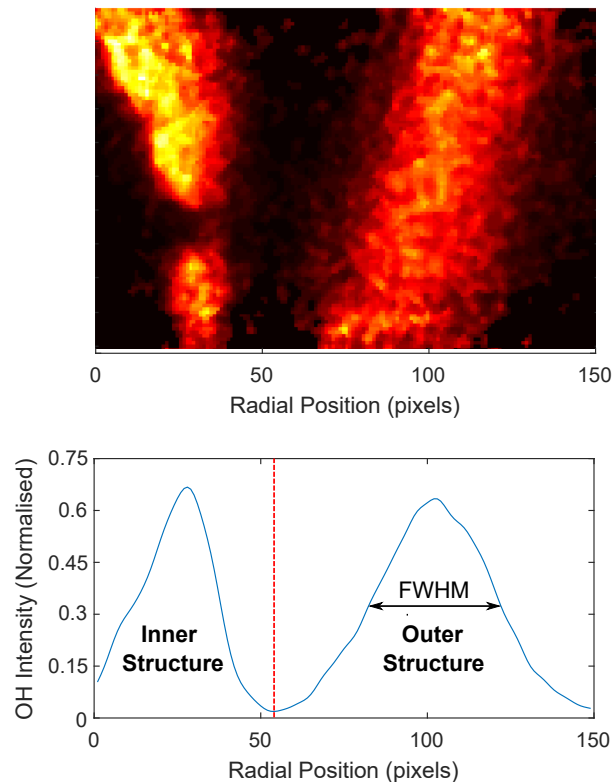


Figure 2: Example of separation of inner and outer OH structures based on radial profile, for case HEP-11 at $x/D = 1.5$. Right-hand side only shown.

In the event that there was no clearly defined boundary between the two structures (i.e. two separate peaks could not be identified or the minimum value between peaks was greater than the FWHM), then the shape of the OH structure was identified, to determine which of the four categories (see Section 2.2) the image belonged to. The inner structures of images with a clearly defined boundary were also analysed in terms of their shape, to determine if the inner structure was continuous or featured ignition kernels.

Chapter 8

Effect of Dopants on Hydrogen Flames for Improved Safety and Performance

Statement of Authorship

Title of Paper	Effect of Dopants on Hydrogen Flames for Improved Safety and Performance.
Publication Status	<input checked="" type="checkbox"/> Published <input type="checkbox"/> Accepted for Publication <input type="checkbox"/> Submitted for Publication <input type="checkbox"/> Unpublished and Unsubmitted work written in manuscript style
Publication Details	D. B. Proud , P. R. Medwell, N. Smith & M. J. Evans (2022), "Effect of Dopants on Hydrogen Flames for Improved Safety and Performance." Report published by Future Fuels Cooperative Research Centre (Project RP1.10-04).

Principal Author

Name of Principal Author (Candidate)	Douglas B. Proud		
Contribution to the Paper	Carried out a detailed literature review to identify challenges and opportunities related to the use of hydrogen as a substitute for natural gas, and the potential for using a hydrocarbon dopant to improve combustion properties. Developed and implemented an experimental test program to compare the characteristics of pure and toluene-doped hydrogen flames with natural gas flames; set-up diagnostic techniques and identified specific cases to be investigated. Processed and analysed data, presented and discussed results in a technical report.		
Overall percentage (%)	80		
Certification:	This paper reports on original research I conducted during the period of my Higher Degree by Research candidature and is not subject to any obligations or contractual agreements with a third party that would constrain its inclusion in this thesis. I am the primary author of this paper.		
Signature		Date	18-OCT-2022

Co-Author Contributions

By signing the Statement of Authorship, each author certifies that:

- the candidate's stated contribution to the publication is accurate (as detailed above);
- permission is granted for the candidate to include the publication in the thesis; and
- the sum of all co-author contributions is equal to 100% less the candidate's stated contribution.

Name of Co-Author	Paul R. Medwell		
Contribution to the Paper	Supervised the initial direction of the research and helped to refine the scope of the investigation. Supervised the design/setup of the experimental apparatus and techniques, and provided feedback on report.		
Signature		Date	17-OCT-2022

Name of Co-Author	Neil Smith		
Contribution to the Paper	Assisted in defining the initial research goals and provided insight regarding the relevance to industry stakeholders. Provided additional raw experimental data.		
Signature		Date	18-OCT-2022

Name of Co-Author	Michael J. Evans		
Contribution to the Paper	Involved in concept generation, performed a related set of experiments which informed the research direction.		
Signature		Date	17-Oct-2022



Effect of Dopants on Hydrogen Flames for Improved Safety and Performance: Report #2

31st January 2022

Project number: RP1.10-04

Effect of Dopants on Hydrogen Flames for Improved Safety and Performance

Authors:

Douglas Proud

Project team:

Douglas Proud (School of Mechanical Engineering, The University of Adelaide)

Paul Medwell (School of Mechanical Engineering, The University of Adelaide)

Neil Smith (School of Chemical Engineering and Advanced Materials, The University of Adelaide)

Michael Evans (UniSA STEM, University of South Australia)



Australian Government
**Department of Industry, Science,
Energy and Resources**

Business
Cooperative Research
Centres Program

This work is funded by the Future Fuels CRC, supported through the Australian Government's Cooperative Research Centres Program. We gratefully acknowledge the cash and in-kind support from all our research, government and industry participants.

IMPORTANT DISCLAIMER

Future Fuels CRC advises that the information contained in this report comprises statements based on research. Future Fuels CRC makes no warranty, express or implied, for the accuracy, completeness or usefulness of such information or represents that its use would not infringe privately owned rights, including any parties intellectual property rights. To the extent permitted by law, Future Fuels CRC (including its employees and Participants) excludes all liability to any person for any consequences, including but not limited to all losses, damages, costs, expenses and any other compensation, arising directly or indirectly from using this report (in part or in whole) and any information or material contained in it.

© Copyright 2021 Future Fuels CRC. All Rights Reserved

ACKNOWLEDGEMENT

This work is funded by the Future Fuels CRC, supported through the Australian Governments' Cooperative Research Centres Program. The cash and in-kind support from the industry participants is gratefully acknowledged.

PROJECT INFORMATION	
Project number	RP1.10-04
Project title	Effect of Dopants on Hydrogen Flames for Improved Safety and Performance
Research Program	Program 1: Future Fuel Technologies, Systems and Markets
Milestone Report Number	2 (Addresses Deliverables 3 and 4)
Description	Literature review and presentation of experimental results, including flame photography, heat flux measurements and spectral imaging of pure and toluene-doped hydrogen flames. These experimental results address Aims 1, 2 and 3 of the project, which correspond to Deliverables 3 and 4.
Research Provider	The University of Adelaide
Project Leader and Team	Douglas Proud, Paul Medwell, Neil Smith, Michael Evans
Industry Proponent and Advisor Team	
Related Commonwealth Schedule	<p>RP1.1.3 [Report on future fuels for decarbonisation of industrial, residential (heat), electricity, and other sectors delivered]</p> <p>RP1.3.2 [Novel concepts and/or prototypes of innovative process technology for future fuels in end-use applications developed]</p> <p>RP1.4.1 [Report demonstrating compatibility of low-carbon fuels with appliances and equipment used in Australia delivered]</p> <p>RP1.4.2 [Solutions for new/modified household appliances and meters to allow for a broader range of fuel compositions delivered]</p> <p>RP1.4.4 [Provision of recommendations, based on research into modification needs for appliances and equipment, for updates of appliance standards]</p>
Project start/completion date	Feb 2020/ Feb 2023
IP Status	Owned by Future Fuels CRC
Approved by	
Date of approval	

Table of Contents

Important Disclaimer	3
Acknowledgement	3
Project Information.....	4
Summary of Report.....	7
1. Introduction	8
2. Literature Review	9
2.1 Hydrogen Flame Visibility	9
2.1.1 Importance of Flame Visibility.....	9
2.1.2 Pure Hydrogen Flames.....	9
2.1.3 Improving Visibility of Hydrogen Flames	11
2.2 Heat Radiation from Hydrogen Flames.....	11
2.2.1 Importance of Radiative Heat Transfer.....	11
2.2.2 Improving Heat Radiation of Hydrogen Flames.....	11
2.3 Olfactory Detection of Hydrogen Gas	12
2.3.1 Odorant Addition in Conventional Fuels.....	12
2.3.2 Issues for Implementation in Hydrogen Pipelines.....	12
2.3.3 Alternative Odorants for Hydrogen	13
3. Methodology	15
3.1 Experimental overview	15
3.2 Burner Configurations and Boundary Conditions	16
4. Results and Discussion	18
4.1 Visible Emissions from Pure Hydrogen Flames	18
4.2 Flame Photography.....	19
4.2.1 Simple Jet Configuration.....	19
4.2.2 BBQ Ring Burner Configuration.....	19
4.2.3 Stove-top Burner Configuration.....	21
4.3 Heat Flux Measurements	22
4.4 Spectral Measurements of Natural Gas/Hydrogen Flames	23
4.5 Olfactory Detection: Toluene and Other Potential Dopants.....	27
4.5.1 Toluene as an Odorant	27
4.5.2 Practical Considerations and Alternative Dopants	27
5. Conclusions	29

6. Implications and Recommendations for Industry	29
7. Future Work	30
8. Reference List	31

Summary of Report

This report presents a description of some of the issues and challenges relating to the use of hydrogen in domestic settings, and the feasibility of addressing these issues through the use of a fuel additive. Specifically, the potential for blending a small amount of a highly sooting liquid hydrocarbon (referred to as a dopant) with hydrogen is investigated, with the aim of simultaneously improving the flame visibility and thermal radiation, as well as facilitating leak detection via odourisation of the gas. A comprehensive literature review is provided, including a discussion of the visibility of pure hydrogen flames and the need for improving visibility, and potential solutions for improving both the visible and radiative properties of hydrogen flames. The issues surrounding the olfactory detection of gas leaks are also presented in this literature review, including potential solutions for a 100% hydrogen gas network.

A series of experiments based on the use of toluene as a dopant were carried out for this project, and the key experimental results are presented in this report. Experiments were carried out for three different burner configurations, and the flames were analysed based on their visual appearance (flame photography), thermal radiation (heat flux measurements), and visible and infra-red emissions (spectral imaging). These experiments involved both pure and toluene-doped hydrogen, with dopant concentrations up to 1% by mole. Comparisons were also made against natural gas flames of equivalent heat input. Interestingly, the visible emissions from the pure hydrogen flames were observed to be stronger than expected, and the spectral imaging revealed that the visible light emissions were dominated by sodium excitation at 589 nm. Analysis of previous results for natural gas and blends of natural gas and hydrogen indicated that this sodium excitation was not unique to hydrogen, although the intensity tends to increase at higher concentrations of hydrogen, and sensitivity to the burner configuration was also observed. A noticeable increase in both visibility and thermal radiation was observed with increasing toluene addition, due to the formation of soot which is then oxidised within the flame. Qualitative observations and theoretical calculations concerning the olfactory properties of toluene were also made, to assess the potential of such a dopant in the context of leak detection. The experimental results presented in this report address Aims 1, 2 and 3 of the project, which correspond to Deliverables 3 and 4.

While the findings suggest that doping with toluene has the potential to address the three issues identified, it is unlikely to be a feasible solution in practice, particularly in the context of distribution throughout the network. However, if it were derived from a sustainable source, or if a similar highly sooting and pungent dopant which is carbon-neutral were to be implemented, then it could become a viable option. This is particularly true if alternative, sulphur-free odorants are not feasible (for economic reasons, for example), or if removal of traditional odorants upstream of fuel cells is cost-prohibitive. Additionally, the use of a dopant to enhance safety and performance at the appliance side, such as within the internal pipework of a gas cooktop, appears to be a feasible option for manufacturers to consider in comparison to alternative methods of flame supervision.

1. Introduction

As society moves away from the combustion of fossil fuels and towards clean, renewable sources of energy, the role of hydrogen will become increasingly important [1]. Not only can hydrogen be used to power fuel cells to generate electricity, it can also be used directly as a fuel in combustion applications, ranging from domestic appliances to large-scale industrial boilers, engines and gas turbines [2, 3]. One particular area in which hydrogen is well-positioned to displace fossil fuels is in existing gas networks [4]. The addition of hydrogen to the natural gas pipeline in relatively low proportions has been trialled and successfully implemented in several networks globally, and studies indicate that most pipelines can accommodate addition of hydrogen up to 10% (by volume), with only slight modifications to the distribution system required [5]. Ultimately, the aim is to extend this to achieve a zero-carbon gas pipeline of 100% hydrogen, which can be used as a fuel for combustion appliances and to power fuel cells. There are, however, a number of safety concerns which must be addressed when implementing hydrogen as a fuel source, particularly with regards to pure or near-pure hydrogen.

Many of the safety concerns pertaining to hydrogen (H_2) are related to the fact that hydrogen molecules are both extremely small (in fact, the smallest [6]) and very reactive. The small molecular size means that hydrogen is more susceptible to leaking than other substances and can result in material defects in metal alloys [7]. Additionally, the high reactivity means that small leaks have a greater likelihood of leading to explosions compared with conventional fuels [8]. From an end-use perspective, a major issue is the lack of a clearly visible flame for the case of 100% hydrogen as a fuel source [9], which presents an obvious safety hazard. Additionally, radiative heat transfer is of importance to the operation of many combustion appliances, and the heat radiated from a flame is often coupled with the visibility of the flame.

Another practical issue surrounding the use of hydrogen is related to the detection of leaks and unburnt gas at the user end. While hydrogen detectors have been developed [10], these involve a significant financial cost and regular maintenance; therefore, alternatives will be required at the domestic scale if an economically feasible hydrogen pipeline is to be implemented. In the natural gas network, an important method of detecting leaks is through olfactory detection—that is, the sense of smell—via the addition of an odorant (often also referred to as a stenching agent). While the odorant can vary depending on the pipeline, a form of sulphur-based compound known as a mercaptan is typically used, as these compounds provide a characteristic smell that can be detected at very low concentrations—typically less than 1.0 ppb (parts per billion) in air [11]. If an odorant were to be added to an otherwise pure hydrogen network, it would not only need to be compatible with hydrogen, but it would also need to be compatible with hydrogen fuel cells, or alternatively, it would need to be easily removed upstream of the fuel cell or be added close to appliances.

The current project is focussed on assessing the feasibility of improving the safety and performance of hydrogen as a fuel via the addition of a small amount of a hydrocarbon, herein referred to as a dopant. Specifically, the potential for such a dopant to act as both an odorant (for leak detection) and as a colourant (for flame observation) is examined, with practical considerations discussed where appropriate. An in-depth review of the literature is initially presented, covering the topics of hydrogen flame visibility and radiative properties, as well as the issues surrounding leak detection and odorisation within the context of the current natural gas standards and regulations. This literature review also identifies a range of potential dopants, and compares their viability in a pragmatic sense. Experimental results based on toluene as a dopant are then presented, including flame photography for various burners and lighting conditions, radiative heat flux measurements, and spectral imaging measurements. Finally, the recommendations to industry and end-users are provided, and the future directions of this research are discussed.

2. Literature Review

2.1 HYDROGEN FLAME VISIBILITY

2.1.1 Importance of Flame Visibility

Before discussing the visibility of hydrogen flames and methods for improvement, it is important to understand under what scenarios flame visibility is relevant from both a safety and operational perspective. In terms of safety, the lack of a visible flame can present a hazard both from the user not being aware of when the flame is lit, and equally, being unaware when the flame is extinguished. In the context of a kitchen cooktop burner, for example, an “invisible flame” would present an obvious burn hazard when lit, particularly for users who are accustomed to a conventional natural gas cooktop. Such a flame would also present an increased risk of a dangerous build-up of gas, since the user would be more likely to leave the gas turned on following the accidental extinguishing of the flame. This latter concern is partially addressed by the fact that modern cooktops typically feature some form of flame supervision device (e.g. via a thermoelectric valve), which is interlocked with the gas supply to shut-off the gas flow in the case of the flame being extinguished. However, it should be noted that these systems are intended to be used as a back-up feature, and tend to involve a significant delay prior to activation of the shut-off valve. A potential option to enable a cooktop burner to be safely operated without a visible flame is to provide an alternative method of flame supervision, which is coupled with a flame indicator (e.g. an LED light), such that the user can determine if the flame is extinguished without a significant delay. One option in this regard is the use of an ultra-violet (UV) sensor to detect the flame rather than a temperature sensor, as mentioned in a recent Hy4Heat report on colourants [12], although this would incur additional costs to be passed on to appliance manufacturers and hence consumers.

In addition to safety, the lack of a visible flame also has implications from a user-friendliness and social acceptance perspective. For example, it is common for end-users to determine their required heat input or turn-down settings based on the visual appearance of the flame(s) for both gas cooktops and gas fires [12]. Again, a potential work-around could be in the form of a separate visual indicator to gauge the input settings; however, to maximise the social acceptance of hydrogen in domestic settings, it would be desirable to maintain a similar behaviour to that of existing natural gas appliances. It is also worth mentioning that for some domestic applications, such as water heaters and ducted space heaters, flame visibility is less important since the flame is enclosed within the device itself and cannot be seen. It should be noted, however, that the lack of a visible flame would still have implications for some boilers in which flame checks are performed during maintenance and installation [13], although this could be addressed through appropriate training of technicians and/or the use of additional instrumentation. Since water heaters and ducted space heaters typically account for the majority of residential gas consumption in Australia [14], it would be economical to administer a colourant to hydrogen at the appliance (or just upstream of it) so that it is only used when required, such as when an open flame is present. This is of course only relevant under the assumption that the colourant is not distributed throughout the entire network, and would also likely depend on whether the colourant also provides other benefits, as explored in this project.

2.1.2 Pure Hydrogen Flames

It is widely known that flames resulting from pure hydrogen combustion in air typically produce low levels of visible radiation, compared with the conventional combustion of hydrocarbons [9, 15]. A common misconception, however, is that hydrogen flames are invisible. A faint blue colour has consistently been observed under low-light conditions [9, 16], as well as a red “tail” to the flame in some cases [9, 17], although the exact source of these visible emissions remains a subject of debate. Some early sources claim that the only source of visible emissions in pure hydrogen-air flames is that which stems from the hydroxyl (OH) bands, which are primarily in the UV but have slight overlap in the blue end of the visible spectrum [15, 18]. The presence of additional radiation has often been attributed to impurities, including sodium, calcium and sulphur [15]. To examine the impact of impurities, hydrogen at both 99% and 99.999% purity has been tested [9], and no discernible difference in the flame spectrum was observed. Additionally, pure oxygen mixed with argon was used as the “air” mixture, and once again there was no effect. With impurities ruled out, the reddish appearance of these flames is attributed to the vibrational excitation of water molecules within the flame. A relatively weak continuum at the blue end of the visible spectrum was also observed in the experiments with high-purity hydrogen [9], which is thought to be a result of reactions involving OH radicals and atomic hydrogen (H), although the exact mechanism behind this observation remains unclear.

It should be mentioned that in the experiments of Schefer et al. (i.e. Ref. [9]), the reddish colour which was observed was very faint, with the flames clearly visible only under reduced-light conditions. This behaviour is expected, since the excitation of water molecules results in relatively low emissions of light in the visible region, with peaks in the near infra-red [16]. Other experiments and trials, however, have reported a relatively strong red-to-orange appearance of hydrogen flames, such that the flames are visible even under well-lit conditions. Most notably, a recent demonstration project by Northern Gas Networks in the UK displays a hydrogen cooktop burner with a distinct orange flame colour, as shown in Figure 1. While there are no specific details relating to the configuration of this burner, a media release [19] states that the flames correspond to 100% H₂, without any mention of the intentional addition of a colourant.



Figure 1: Hydrogen cookers from Northern Gas Network's demonstration project. Image sourced from Hydrogen-Central.com [20]

Since the presence of this relatively bright “orange” colour appears to vary depending on the laboratory or apparatus in which the experiments/trials are conducted, the logical conclusion is that these higher-intensity visible emissions are indeed related to the presence of impurities. It has been suggested that these impurities stem from hydrogen embrittlement during storage/transportation, which leads to the presence of metal or metal oxide particles within the fuel stream [16]. This was supported by experiments performed with and without a 0.5- μm filter installed on the fuel line, which showed a statistically significant reduction in intensity based on digital photographs. Electron microscopy revealed the presence of iron, sodium and calcium in the fuel stream, leading to the authors to conclude that the impurities are related to particle deposition following embrittlement, since this is the likely source of the iron, which was present in a relatively high concentration. While these results show that the colour is at least partially related to the presence of filterable particles in the hydrogen, it does not confirm that the particles which produce this colour stem from embrittlement. This is because the filtering process also removes sodium, which is unlikely to stem from embrittlement, and the lack of spectral measurements makes it impossible to ascertain the source of the visible emissions. It is also worth mentioning that sodium impurities have been found to contribute to the emission spectra in previous flame spectroscopy studies [21, 22], with a strong peak at 589 nm which corresponds to a distinctive yellow/orange colour, similar to that seen in Figure 1. The effect of impurities in the context of the current investigation is further discussed in Section 4.1.

It should be noted that, although visible emissions can be detected from hydrogen flames, the intensity of these emissions is in general much lower than comparable hydrocarbon flames. While some studies indicate that impurities could lead to a flame of similar visibility to natural gas, it is not clear if this can be relied upon to produce a consistently observable flame in all situations. Since domestic appliances involving an open hydrogen flame (i.e. excluding boilers and ducted space heaters) would typically be operated in a well-lit environment (e.g. a kitchen stovetop), the visibility of a hydrogen flame should also be assessed with this in consideration. Ultimately, for hydrogen to be safely used in appliances, the visibility achieved must be similar to or greater than

that of a natural gas flame, particularly when taking into account the increased flammability of hydrogen and therefore the elevated risks associated with leaks.

2.1.3 Improving Visibility of Hydrogen Flames

As noted in the previous subsection, the presence of certain impurities has been found to significantly increase the visibility of hydrogen flames. The addition of metal oxide nanoparticles to increase radiative heat transfer in flames has been investigated previously, in the context of improving the efficiency of gas-fired furnaces [23]. It was found that the addition of inert alumina particles to LPG fuel leads to a significant increase in flame luminosity and a larger visible flame area. For domestic applications, it would likely be more practical to introduce the metal oxides in a solution rather than as a powder, to reduce the emission of particulates (e.g. PM_{2.5}) [12]. In saying this, the use of a solution (such as sodium chloride dissolved in water) would still produce solid particles following combustion which could form deposits on appliances and lead to corrosion, as well as negatively impacting the indoor air quality, particularly in the case of flueless heaters [12]. It should also be mentioned that the use of a metal oxide colourant would not be compatible with injection throughout the gas network, since it would either form deposits in the pipeline or be filtered out at various points throughout the network [24].

The addition of hydrocarbons in relatively low proportions—herein referred to as “doping”—is another method of increasing the visibility of hydrogen flames. In conventional hydrocarbon fuels, much of the radiative flux—and therefore much of the visible light—stems from soot particles, which produce high levels of broadband radiation in a flame [25]. Due to the importance of soot formation in applications such as furnaces, along with the need to suppress it in other devices such as gas turbines, the physical and chemical processes relating to soot formation have been studied in depth over the years. The tendency to form soot varies greatly depending on the initial fuel composition, and a useful method of comparing and quantifying the sooting propensity of different fuels is through the Yield Sooting Index (YSI) [26]. This index is based on measurements of the soot volume fraction in methane flames doped with 400 ppm of the hydrocarbon of interest. In general, it is understood that aromatic hydrocarbons, such as toluene, tend to have relatively high YSIs due to the presence of a benzene ring and the associated high carbon-to-hydrogen ratio [27]. By selecting dopants with high YSIs, there is potential to significantly enhance the visibility of hydrogen flames, even at very low concentrations of dopant.

Another attractive feature of using high YSI hydrocarbon fuels as a dopant for hydrogen flames is the fact that these fuels typically exist in the liquid state at standard conditions [26]. This offers a range of benefits over gaseous additives in terms of transportation and storage, since pressurisation is not necessary and leak prevention is less problematic. This makes it feasible to inject the dopant much closer to the end use side, or even within the plumbing configuration of individual appliances, allowing pure hydrogen to still be used for other applications, such as in fuel cells. Additionally, if the dopant were to be injected into the pipeline as a vapour upstream of a fuel cell, the relatively high boiling point would enable it to be separated from hydrogen via a condenser.

2.2 HEAT RADIATION FROM HYDROGEN FLAMES

2.2.1 Importance of Radiative Heat Transfer

Along with convection and conduction, heat transfer via radiation is an important mechanism for the efficient performance of many combustion devices. The importance of radiation varies depending on the application, for example, stove top burners operate primarily through conduction and convection, whereas the performance of boilers and some gas heaters is largely dependent on radiant heat [28, 29].

Radiative heat transfer can also impact safety, in both a positive and negative manner. For example, it is desirable to have a flame which emits enough thermal radiation such that the flame can be sensed from a safe distance, to prevent a user accidentally coming into contact with the flame itself. On the other hand, an excessive amount of radiated heat would pose additional hazards, such as causing ignition of surrounding objects, or potentially causing skin burns [30]. Therefore, it is important to have an understanding of the radiant heat generated by pure and doped hydrogen flames, and how this compares to the properties of comparable natural gas flames.

2.2.2 Improving Heat Radiation of Hydrogen Flames

In addition to visibility, heat radiation is another aspect of hydrogen flames which differs from conventional hydrocarbon flames. Although hydrogen flames are known to emit radiation in the infra-red [9] (due to excitation

of H₂O as noted in Section 2.1.2), the total radiative heat flux is much lower than an equivalent natural gas flame [25]. The heat that is radiated from a pure hydrogen flame can be classed as being non-luminous, or banded, meaning that the spectrum is composed of narrow bands which are a result of energy released from vibrational and rotational transitions in the gaseous molecules [25]. The most effective way of improving the amount of heat radiated from a flame is by increasing the amount of luminous radiation produced—that is, broadband radiation due to the presence of solid particles in the flame, namely soot particles.

Although it is well-known that the addition of hydrogen can suppress the formation of soot in predominantly hydrocarbon flames [31], there is comparatively little information relating to the reverse case; that is, when highly sooting fuels are added to hydrogen in low proportions. The addition of hydrocarbons to increase the luminous radiation in otherwise non-luminous flames has been proposed previously, in the context of both hydrogen- and natural gas-fired furnaces [25, 32]. For hydrogen flames, it was suggested that the addition of pulverised bituminous coal would be most effective [25], and a later study found that addition of carbon particles can lead to a noticeable increase in radiative flux [33]. In terms of liquid and gaseous hydrocarbon dopants, it has been stated that hydrogen-hydrocarbon flames are luminous even for very low levels of hydrocarbon [34], although this area has remained unexplored in the literature, at least in regards to measurements of radiative heat flux.

As one might expect, the methods involved in improving the heat radiation in hydrogen flames are typically accompanied by an increase in flame visibility. Therefore, it is possible to address two concerns of hydrogen as a fuel with a single solution. In this study, a third challenge is also hoped to be addressed with this same solution, and this relates to the detection of leaks via an odorant.

2.3 OLFACTORY DETECTION OF HYDROGEN GAS

2.3.1 Odorant Addition in Conventional Fuels

Fuels which are commonly used in domestic applications (predominately natural gas and LPG in Australia) require an odorant to be added to them to enable leaks to be detected, since they are otherwise odourless. While the exact requirements surrounding odourisation vary between states in Australia, the general stipulation for pipeline gas is that the gas must have an odour that is “distinctive and unpleasant” and be discernible at “one-fifth of the lower explosive limit (LEL) of the gas” [35, 36]. The LEL of methane (the main component of natural gas) in air is approximately 4.4% (by volume), which implies that the natural gas mixture following odorant addition must be able to be detected at volumetric concentrations below 0.9% in air.

The Australian Energy Market Operator (AEMO) states that the preferred odorant is a blend of 70% THT (tetrahydrothiophene) and 30% TBM (tertiary butyl mercaptan). This blend is typically injected into the pipeline in proportions between 7.0–14.0 mg/m³, although other chemicals and concentrations which comply with the legislation [35, 36] are accepted [37]. These chemicals are used in most gas networks throughout Australia, with additional blending with IPM (isopropyl mercaptan) in WA. Both THT and TBM are sulphur-based compounds which have characteristic odours which can be detected by humans at less than 1 ppb, and they have properties that are generally favourable for use in gas networks, including resistance to oxidation in the pipeline [38]. However, TBM has a relatively high freezing point of 1 °C, while THT has poor soil penetration, hence the preference for blending the two together [38]. It is also worth mentioning that these types of sulphur-based compounds were initially selected for odourisation not only due to the aforementioned properties, but because they produce an odour similar to that of the previously used town gas, which tended to naturally consist of a number of sulphur impurities which produced the typical “gassy” odour [38].

2.3.2 Issues for Implementation in Hydrogen Pipelines

Like methane, hydrogen is also a colourless and odourless gas, so an odorant must be added for safe use. The obvious choice would be to use the same blend (or a similar one) to that which is currently used in gas networks, since end users are familiar with this odour and automatically associate it with a “gassy” smell. This is the suggested option for trials involving the blending of hydrogen with natural gas in low proportions, where the end use is solely for combustion devices [4].

In the context of 100% hydrogen pipelines, odorants which are currently in use would likely not be suitable. This is because a key end-use application of hydrogen is in fuel cells, and many of the sulphur-based odorants—including THT and TBM—can lead to poisoning of PEM fuel cells, and more generally fuel cells involving reduced metal catalysts such as nickel and cobalt [39, 40]. While there are ongoing studies into the development of sulphur-resistant PEM fuel cells, these do not yet have commercial outcomes [41-43]. Therefore, if traditional

odorants such as THT and TBM are to be used in a 100% hydrogen network, these would have to be removed from the hydrogen upstream of the fuel cell. It should be mentioned that filtration systems to enable desulphurisation have been developed and are an active area of research [39, 44]. Although their implementation has been shown to be feasible—for example, in residential systems in Japan [45]—this presents an additional cost in the transition to a 100% hydrogen network. Due to this additional cost and the scale at which the desulphurisation systems would need to be implemented, it would be advantageous to use an odorant which is compatible with hydrogen fuel cells, or can be added to and/or removed from the pipeline relatively easily and economically.

2.3.3 Alternative Odorants for Hydrogen

Alternative odorants for use in hydrogen gas pipelines have been investigated, although there is currently no widely accepted option which is compatible with fuel cells [4, 46, 47]. In saying this, sulphur-free odorants which do not degrade fuel cells have been developed and are another active area of investigation. The recently published Hy4Heat odorant report compares the feasibility of five different odorants in the context of a 100% hydrogen network, including two sulphur-free compounds which are believed to be suitable for fuel cell applications [48]. One of these sulphur-free odorants was deemed inappropriate due to concerns regarding the nature of the odour (i.e. it did not have a characteristic “unpleasant” odour), while the other—namely “Gasodor S-Free”—was found to be particularly promising. The economic assessment in this report found that this odorant would incur additional costs over existing options, although it also mentions that if the sulphur-free odorant can be used with fuel cells without any purification then the economics could shift in favour of this option, assuming that fuel cells make up a relatively large proportion of end-use applications. Ultimately, it is recommended that further studies should be performed on the long-term compatibility of this alternative odorant with use in fuel cells without any purification. Another complication is that odorants are expected to present additional challenges in terms of their storage. Specifically, many hydrogen storage options would result in the odorant being separated from hydrogen during storage, which could lead to a non-uniform distribution of odorant in the gas pipeline downstream [10].

As mentioned in Section 2.2.2, the focus of the current project is to address the challenges surrounding visibility, radiation and olfactory detection via a single solution. As mentioned previously, aromatic hydrocarbons (which are based on a cyclic benzene ring structure) typically lead to significant soot formation during combustion, which is of relevance for addressing the issues of visibility and radiation. Additionally, aromatic hydrocarbons—and indeed many other volatile organic compounds—tend to be very pungent, particularly those with long carbon chains [49, 50]. The name “aromatic” might suggest that these chemicals tend to produce a pleasant aroma, and while this is the case for certain aromatic hydrocarbons, it is not true in general [50].

To gauge the feasibility of various sooting hydrocarbons (and other organic compounds such as alcohols) as potential odorants, it is worthwhile to compare the detection thresholds of some of these compounds against traditional odorants. Depending on the relevant legislation, the ability to simply detect a chemical based on odour is not the only requirement for an odorant; it must also have an “unpleasant” smell according to certain regulatory frameworks [36]. Table 1 displays the odour detection thresholds for a range of selected chemicals, using the results of an exhaustive study carried out at the Environmental Sanitation Center in Japan [11]. Also shown in Table 1 are descriptions of the odours based on various sources shown in the footnotes, although descriptions were not available for all chemicals. Additionally, the rows in the table are shaded to identify different compound groups. The chemicals included in Table 1 were selected based on either being used as existing odorants, having a relatively high sooting propensity, or being of practical relevance in other ways (for example, commonly occurring in liquid biofuels).

Table 1: Odour detection thresholds and descriptions for various chemicals, grouped by family (yellow: sulphur-based odorants, orange: aromatic hydrocarbons, blue: alcohols). Threshold data sourced from Abraham et al. [11].

Name of Chemical	Odour Detection Threshold (ppm)	Description of Odour	Chemical Family
THT (Tetrahydrothiophene)	0.00062	Unpleasant, rotten eggs [51]	Sulphur-based odorants
TBM (Tertiary Butyl Mercaptan)	0.000029	Skunk-like, offensive [52]	
Methyl Acrylate	0.0035	Acrid, pungent [52]	Esters
Ethyl Acrylate	0.00026	Acrid, pungent, sour [52]	
Toluene	0.33	Solvent, paint [53]	Aromatic hydrocarbons
Styrene	0.035	Sweet/floral, unpleasant in high concentrations [52]	
p-Diethylbenzene	0.00039	Gasoline-like [54]	
n-Octanol	0.0027	Penetrating, orange [52]	Alcohols
n-Decanol	0.00077	Fat-like, waxy [52]	
Limonene	0.038	Citrus, lemon [53]	Other
Isoprene	0.048	Petroleum-like [52]	
Pyridine	0.063	Foul, unpleasant, fishy [52]	
Skatole	0.0000056	Putrid, faecal [52]	
1-Nonene	0.00054	Gasoline, rancid [52]	

From Table 1, it appears that some of the selected chemicals are able to be detected at comparable concentrations to traditional, sulphur-based odorants, particularly THT which has a higher threshold than TBM. It is worth noting that the two acrylates shown in Table 1 are the main constituents of the previously mentioned GasOdor-S-Free odorant, hence their inclusion in the table. It is also worth mentioning that the odour detection thresholds shown are indicative only, and their values are known to vary depending on the methods used for determination [11]. Additionally, while this threshold represents the concentration at which the odour can be detected, the change in odour intensity with increasing concentration above this threshold is known to vary between different chemicals, with highly nonlinear behaviour for some substances [47]. The odour descriptions are also indicative, and the perception of certain odours is known to change depending on concentration [47]. For example, many of the sources cited contained a number of different descriptions for the same chemical, which often appeared contradictory. This emphasises the importance of conducting screening tests with different human subjects prior to implementing an alternative odorant. The potential of these substances to be used as an odorant in practice, in addition to improving flame visibility and radiative properties, is further discussed in Section 4.5.

3. Methodology

3.1 EXPERIMENTAL OVERVIEW

For the experimental investigation in this project, the focus is on the feasibility of using toluene as a dopant. Toluene was selected primarily due to its very high sooting propensity which has been investigated in the context of turbulent hydrogen flames previously [55], in addition to its physical properties making it suitable for injection as a liquid. Therefore, if the experimental results indicate that toluene addition does not improve flame visibility and/or radiation at sufficiently low dopant concentrations, then other dopants are unlikely to be viable either. Toluene is also known to be formed as an intermediate species (along with other aromatic hydrocarbons) during the combustion of common biodiesel blends [56], so it can be considered a surrogate fuel to enable consistent experimental measurements in this sense. In a practical implementation, it is unlikely that the use of toluene would be widespread, particularly in domestic settings; this is also discussed further in Section 4.5.

To investigate the effect of toluene addition on the visibility and radiative characteristics of hydrogen flames, a comprehensive experimental campaign was carried out. Pure and toluene-doped hydrogen flames, in addition to natural gas flames, were analysed using a combination of flame photography, spectral imaging and thermal radiation measurements. Toluene vapour was produced via a controlled evaporator and mixing (CEM) unit, allowing a homogeneous mixture of hydrogen and toluene to be generated. Very low liquid flowrates of toluene into the CEM unit were achieved using a low-flow metering valve in conjunction with a Coriolis flow-meter, while the bulk gas flowrate was controlled with a thermal mass flow controller. A schematic of the experimental setup is shown in Figure 2.

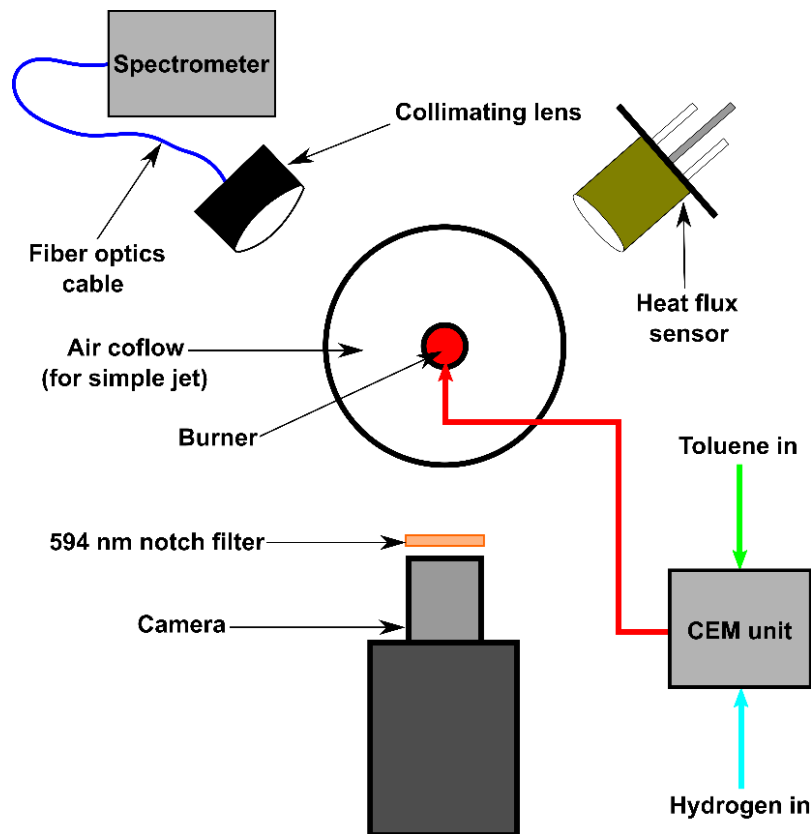


Figure 2: Top-view schematic of experimental setup.

Flame photography was performed using a DSLR camera, operated with an exposure time of $1/5^{\text{th}}$ of a second for the photographs presented in this report. The photographs were all captured with an f-number of 1.8 and an ISO value of 100, except where otherwise stated, with manual focus and white balance. The camera was also fitted with a notch filter centred at a wavelength of 594 nm with a FWHM of 23 nm. This was necessary to remove the effect of emissions from sodium excitation in the flame, as further discussed in Section 4.1. Unless otherwise stated, the flame photographs presented herein were captured with the notch filter fitted to the camera. In order

to assess the visibility of the flames in different environments, photographs were captured with both an optically-absorbing (black velvet) background and a glossy white background, in both a dark and a well-lit room.

The thermal radiation from the flames was measured using a Medtherm 64-series heat flux sensor. This sensor is fitted with a sapphire window attachment for the elimination of convective heat transfer from the flames, ensuring that the radiative heat flux alone is measured. For each measurement, the reading was monitored to ensure that a steady value was being recorded, and the data were obtained over a period of 30 s to account for any unsteady effects, using a sampling rate of 5 kHz. For consistency, the sensor was oriented normal to the central axis of the flames, and held at a constant height and distance from the burner throughout the experiments.

To further analyse the visible and infra-red emissions from the various flames, spectral imaging of the flames was performed using an Ocean Optics Red Tide USB650 spectrometer. This spectrometer was coupled to an optical fibre, which was in turn fitted to a collimating lens to increase the signal-to-noise ratio of the spectral data. These measurements provide a resolution to the nearest nm, with transmission ranging from the visible to near-IR region (approximately 400 – 850 nm). The flame spectra were collected under dark background conditions, and background noise corrections were also performed. A minimum of 30 spectral measurements were recorded for each flame case, which were then averaged to better identify the peaks in the signal.

3.2 BURNER CONFIGURATIONS AND BOUNDARY CONDITIONS

To study the effect of toluene addition under different scenarios, three different burner configurations were implemented in this investigation. A simple jet configuration was the initial focus, to simplify the analysis and enable future comparisons with numerical simulations. The burner was operated in non-premixed mode, with fuel issuing from an 8.0 mm I.D. jet into a coflow of room-temperature air. A single volumetric flowrate (\dot{V}) of hydrogen was used, along with a natural gas case with equivalent heat input (Q_{in}) for comparison. A range of toluene mass flowrates (\dot{m}_{tol}) were also implemented, corresponding to a mole fraction (X_{tol}) of toluene in the fuel mixture which ranged from 0–1%. The various flame cases and corresponding boundary conditions for the simple jet configuration are shown in Table 2.

Table 2: Flame cases for 8-mm-diameter simple jet, including toluene mole fraction (X_{tol}) as a percentage of the total fuel stream.

Case	\dot{V}_{H_2} [SLPM]	\dot{V}_{NG} [SLPM]	\dot{m}_{tol} [mg/s]	X_{tol} [%]	Re_{jet}	Q_{in} [kW]
JET-T0	10	0	0	0.0	280	1.80
JET-T1	10	0	1.7	0.25	304	1.87
JET-T2	10	0	3.4	0.5	327	1.94
JET-T3	10	0	5.2	0.75	351	2.01
JET-T4	10	0	6.9	1.0	374	2.08
JET-NG	0	3.4	0	0	560	1.80

In addition to the simple jet flames, two typical domestic appliance burners were studied; namely a portable barbeque burner (GasMate) and a traditional gas stove-top burner (Bellini). These burners are designed to operate in premixed mode, using a passive air entrainment mechanism involving a fuel injection nozzle and air inlet regions. Due to the much higher flame speed of hydrogen and its propensity for flashback, the burners designed for natural gas had to be modified to prevent premixing from occurring when using hydrogen. Since it is of interest to compare the pure and doped hydrogen flames to the premixed natural gas flames for which these appliances are designed, data were collected for the premixed natural gas case prior to modifying the burners. The toluene concentration was again varied from 0–1% for both burners, and the hydrogen flowrates were assigned based on the rated heat input for the appliances. The boundary conditions and case names for the barbeque (BBQ) and stove (STV) burners are shown in Table 3.

Table 3: Flame cases for BBQ and STV burners, including toluene mole fraction (X_{tol}) as a percentage of the total fuel stream.

Case	\dot{V}_{H_2} [SLPM]	\dot{V}_{NG} [SLPM]	\dot{m}_{tol} [mg/s]	X_{tol} [%]	Q_{in} [kW]
BBQ-T0	8.5	0	0	0.0	1.53
BBQ-T1	8.5	0	2.0	0.35	1.61
BBQ-T2	8.5	0	2.9	0.5	1.65
BBQ-T4	8.5	0	5.9	0.75	1.71
BBQ-NG	0	2.9	0	0.0	1.53
STV-T0	9.1	0	0	0.0	1.64
STV-T1	9.1	0	1.6	0.25	1.70
STV-T2	9.1	0	3.1	0.5	1.76
STV-T4	9.1	0	6.3	0.75	1.83
STV-NG	0	3.2	0	0.0	1.64

4. Results and Discussion

4.1 VISIBLE EMISSIONS FROM PURE HYDROGEN FLAMES

As mentioned in Section 2.1, it is often stated that pure hydrogen burns colourlessly and that the flames are “invisible”, although this is not strictly true. The primary source of visible emissions in pure hydrogen flames is from excited H_2O molecules, which produce a weak reddish appearance under certain conditions, along with a relatively weak blue continuum from reactions involving the OH and H radicals. During the current experiments, however, a relatively bright yellow-to-orange colour was observed for the supposedly pure hydrogen flames, often appearing in distinct streaks. This has also been observed previously (see Section 2.1), and is often attributed to excitation of sodium, whose emission spectrum is dominated by the D-lines at 589.0 and 589.6 nm. To verify the source of the colour observed, spectral imaging of the “pure” hydrogen flames was performed. Figure 2 displays the spectrum that was attained for the “BBQ-T0” flame, corresponding to the 1.5 kW hydrogen flame (without toluene addition) stabilised on a BBQ ring burner.

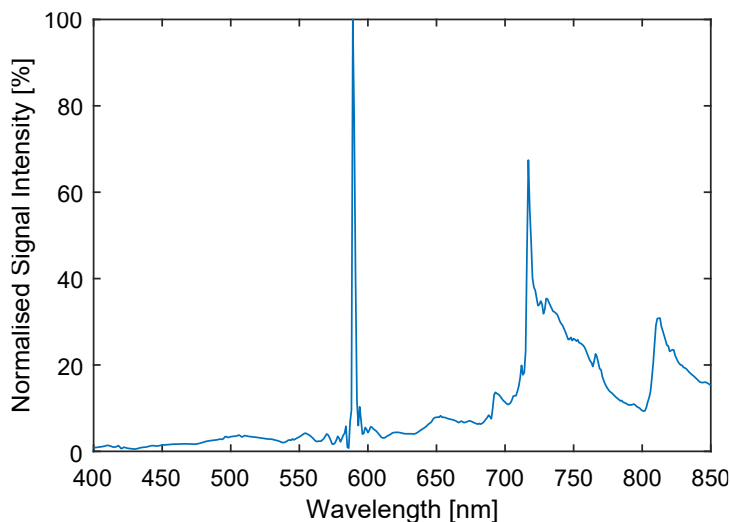


Figure 3: Visible and near-IR spectrum for undoped H_2 barbeque burner flame (BBQ-T0).

The spectrum shown in Figure 3 shows a dominant peak at approximately 589 nm, confirming that the characteristic orange colour is indeed from sodium excitation. Also evident in Figure 3 is an increase in intensity in the red/near-IR region with distinct peaks due to the excitation of H_2O molecules, in line with previous observations [9, 15]. It should be mentioned that the visible portion of the spectrum extends to approximately 700 nm, such that the visible emissions due to the excitation of H_2O contribute a relatively small amount to the observed colour. While this confirms that the colour observed is related to the presence of sodium in the flames, it is not immediately clear where this sodium originates from. The orange colour, in addition to the peak at 589 nm, was observed throughout the experiments with varying strength, including for the three different burner types. The plumbing system was also purged with ethanol to ensure that it was not related to impurities within the pipes, with no effect observed. It was initially thought that the sodium could stem from the impurities within the hydrogen itself; however, no obvious difference was observed between industrial grade and ultra-high purity (Grade 5.0) hydrogen. Additionally, the D-lines due to sodium excitation were also observed for the spectra of natural gas flames in some cases; this is further explored in Section 4.4, which also presents results for blends of natural gas and hydrogen. This suggests that the source of sodium is in the air rather than the fuel, although it is possible that there was sodium present in both the hydrogen and the natural gas streams.

Since the presence of sodium is expected to change significantly depending on the surrounding environment, it cannot be consistently relied upon to produce a visible flame. As such, an optical filter was used for the flame photography to block out the light from sodium excitation, as described in Section 3.1. Figure 4 compares photographs captured with and without the filter on the camera for the simple jet configuration, highlighting the profound impact of the sodium emissions on the appearance of the flame. It should be noted that—due to the narrow blocking range of the filter—the use of this filter does not block out any other wavelengths of light which contribute to the colour of the flames other than those from the sodium lines. The remainder of the photographs presented in this report were captured with the notch filter attached.



Figure 4: Photographs captured with and without the notch filter for undoped jet flame (JET-T0).

4.2 FLAME PHOTOGRAPHY

4.2.1 Simple Jet Configuration

Photographs of the simple jet flames are shown in Figure 5, highlighting the change in appearance with addition of toluene. For both hydrogen flowrates, toluene was added to hydrogen in four different concentrations up to 1% (by mole), with the equivalent heat input natural gas flame also included in Figure 5 for comparison. The flame photography results show that addition of toluene does not significantly change the structure of the flames near the jet exit, although the effect further downstream is noticeable.

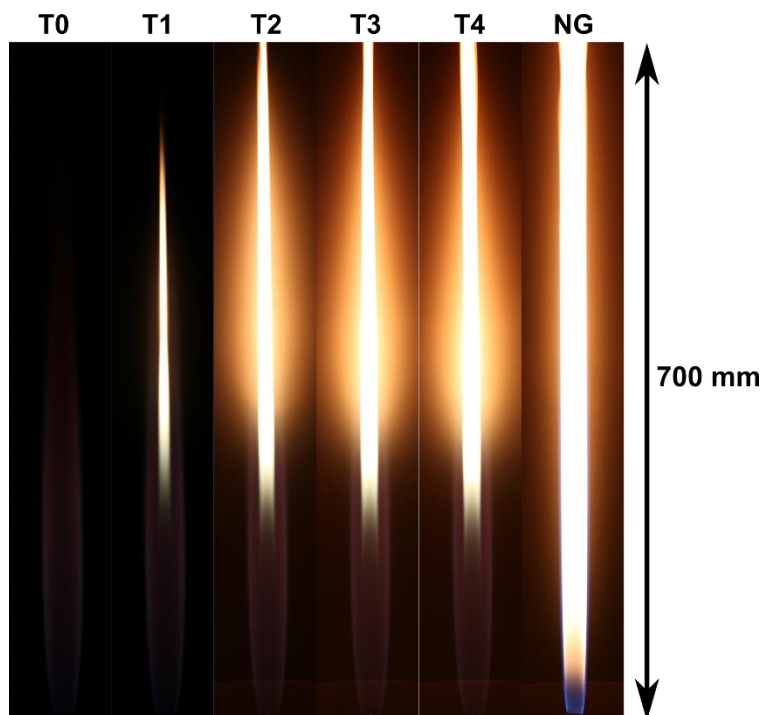


Figure 5: Photographs of simple jet flames with toluene addition from 0 – 1%, and equivalent natural gas flame (refer Table 2). All photographs captured with 1/5 sec exposure time.

For all of the flames with toluene, a luminous sooting region can be seen to form radially inwards from the main flame front. Interestingly, a similar study involving turbulent hydrogen-toluene flames diluted with nitrogen found that significant soot formation did not occur until the toluene concentration was increased to 3% per mole of H_2 [55]. This difference is likely a result of the lack of turbulent mixing and longer residence times for the laminar flames in the current study, which increases the tendency for soot inception since precursor species are less likely to follow the oxidation pathway [57]. The luminous sooting region is relatively narrow for the 0.25% toluene case (T1), and the soot can be seen to be consumed within the frame of the photograph. There is a significant increase in intensity as the toluene concentration is increased to 0.5%, after which the effect of increasing toluene becomes less noticeable. From 0.5% to 1%, a broadening of the sooting region can be seen to occur, as well as a slightly further-upstream onset of soot formation. The sooting region is more uniformly distributed in the case of natural gas, with a reduced intensity from approximately 300 to 600 mm downstream of the jet exit in comparison to the cases with $\geq 0.5\%$ toluene concentration.

4.2.2 BBQ Ring Burner Configuration

Similar to the simple jet flames, a range of toluene concentrations up to 1% by mole were investigated for the BBQ burner configuration. Photographs were captured with three different lighting/background conditions, to highlight the importance of these parameters when studying flame visibility. The different conditions are labelled as L0, L1 and L2, corresponding to lights off with a dark background (L0), lights on with a dark background (L1), and lights on with a white, glossy background (L2). The photography results are shown in Figure 6, for toluene concentrations of 0 (i.e. pure hydrogen), 0.5% and 1%, all operated in nonpremixed mode, while the equivalent natural gas flame shown is premixed. In order to avoid saturation of the images under the L2 condition, the f-number of the camera was increased from 1.8 to 5 for these photographs.



Figure 6: Photographs of “BBQ” flames (refer Table 3) under different lighting and background conditions. Images were captured with 1/5 sec exposure time, with an f-number of 1.8 for L0 and L1 conditions (dark background with lights off and on, respectively) and f-number of 5 for the L2 condition (lights on with white background).

In Figure 6, a significant change in the appearance of the flames can again be seen with addition of toluene due to soot formation. The pure hydrogen flame can be just made out under the “lights off” conditions (top-left frame, column “L0”), with a faint blue region near the burner and a reddish appearance further downstream. With the lights turned on the flame becomes much more difficult to observe; a very faint flame can be seen with the dark background (L1) while the flame appears invisible with the white, glossy background (L2), which simulates a kitchen environment. At 0.5% toluene (T2) there is a luminous sooting region enclosed within the outer structure, which can be clearly seen under the L0 and L1 conditions, while it is much less apparent under the L2 conditions. There is a significant increase in soot formation as the toluene concentration is increased from 0.5% to 1%, with the flame being clearly visible for all three conditions. The difference between the BBQ-T2 and BBQ-T4 flames is an interesting departure from the observations relating to the simple jet configuration, in which the increase from 0.5% to 1% did not have a major impact on the luminosity. This difference is likely a result of the change in the flow-field and mixing processes between the two types of burners. In particular, the ring burner features a number of narrow ports from which the fuel issues, leading to a more complex mixing field and a potential change in soot formation mechanisms. The premixed natural gas flame can also be observed under all three lighting conditions shown in Figure 5. It is worth pointing out, however, that under the L2 conditions, the blue natural gas flame can only be seen against the dark backdrop of the burner body, and is very difficult to distinguish against the white background. These results emphasise the importance of considering the surroundings when evaluating the visibility and safety of flames for domestic applications.

The length of the flames also increases significantly with toluene addition, particularly from the BBQ-T2 to the BBQ-T4 case. It is interesting to note that the pure hydrogen flame displays a similar shape and flame length to the equivalent premixed natural gas flame, despite operating in nonpremixed mode. This suggests that it could be feasible to simply modify these types of burners to prevent premixing to allow them to run on 100% H₂ in practice, although if toluene (or a similar sooting fuel) were to be added then it would need to be appropriately designed in order to prevent flame impingement on the surface being heated.

4.2.3 Stove-top Burner Configuration

Photographs of the flames under the three different lighting/background conditions are shown for the stove-top burner in Figure 7. Once again, the photographs corresponding to the L2 condition were captured with an f-number of 5 instead of 1.8 to prevent saturation of the images. For this burner, results are shown for toluene concentrations of 0, 0.25%, 0.5% and 1%, along with the equivalent heat input premixed natural gas flame. Once again, the pure hydrogen flame is visible under the L0 and L1 conditions, and virtually undetectable with the L2 background. There is again a noticeable increase in soot formation and therefore luminosity as the toluene is added, with the STV-T1 flame displaying a faint sooting region which can be observed under all three conditions, although it is very faint under the L2 condition. Similar to the BBQ burner, the effect of increasing from 0.5 to 1% toluene is significant, with the incandescence from the soot dominating the appearance of the flame for the STV-T4 flame. The natural gas flame can again be seen under all three conditions, although detection against the white background is difficult. These results indicate that addition of toluene at $\geq 0.25\%$ can produce a flame that is of similar or improved visibility to that of natural gas.

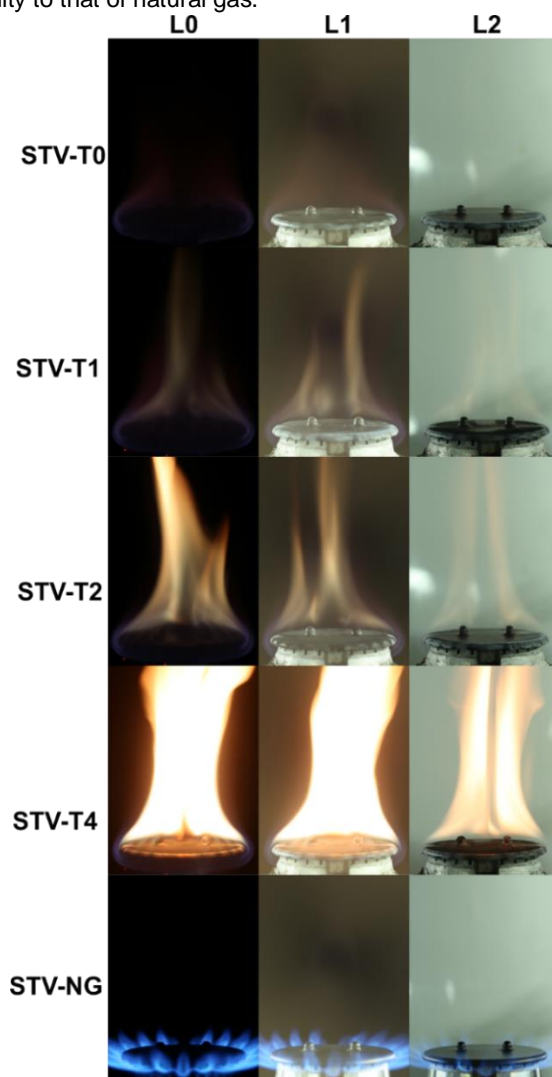


Figure 7: Photographs of “STV” flames (refer Table 3) under different lighting and background conditions. Images were captured with 1/5 sec exposure time, with an f-number of 1.8 for L0 and L1 conditions (dark background with lights off and on, respectively) and f-number of 5 for the L2 condition (lights on with white background).

Comparing the hydrogen/toluene flames with the equivalent natural gas flame in Figure 7, it is evident that the lack of premixing leads to a significant change in the shape and length of the flames. While the pure hydrogen flame showed a similar behaviour to the natural gas flame for the BBQ burner (Figure 6), this is not the case for the stove burner. While the premixed natural gas flame features distinct flamelets which branch outwards from the exit ports, the hydrogen case appears to be stabilised as a single flame with its base below the exit ports and a large “tail” which extends downstream. The flame length then increases significantly with addition of toluene, similar to the observations for the previous burners. This suggests that this type of burner would need to be operated in either premixed or partially-premixed mode, or modifications to the burner geometry would be necessary to enable efficient and safe use with hydrogen as the dominant fuel source if operated in nonpremixed mode. It is also worth noting that these changes would also lead to changes in visibility which would require further investigation.

4.3 HEAT FLUX MEASUREMENTS

Heat flux measurements were obtained to study the effect of toluene addition on the amount of heat radiated from the flames. Results for the simple jet configuration are shown in Figure 8. The data points plotted correspond to the five hydrogen/toluene flames shown in Figure 5, while the dashed horizontal line represents the measured heat flux from the equivalent natural gas flame, against which the results are normalised.

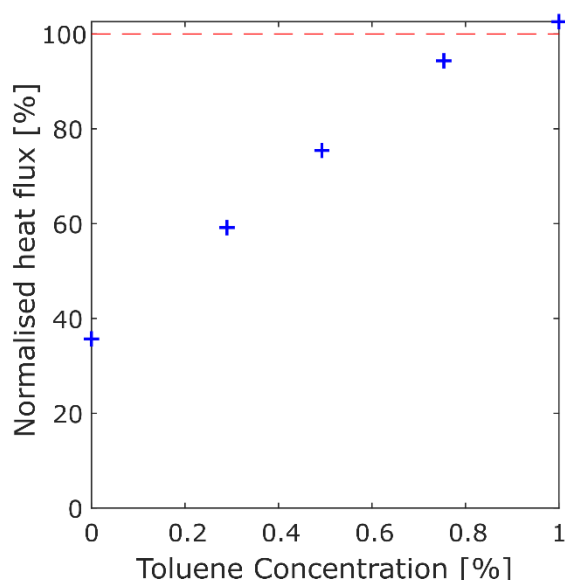


Figure 8: Thermal radiation with addition of toluene for simple jet flames (refer Table 2), normalised against the equivalent heat input natural gas case.

The heat flux results displayed in Figure 8 show a clear trend in the radiative heat flux as toluene is added to hydrogen. For the pure hydrogen flame, the heat radiation measured by the sensor is approximately 35% of that of the equivalent heat input natural gas flame. There is a steady increase in thermal radiation with increasing toluene concentration, which appears to begin to level off from 0.75% to 1%. The approximately 75% increase in heat flux as the toluene is increased from 0.5% to 1% is interesting, since this effect is not immediately noticeable from the flame photographs. At 1% toluene concentration by mole, the measured heat flux is seen to be slightly above that of the natural gas flame. It should be noted that the heat sensor was positioned at a height of 250 mm above the jet exit plane, corresponding to the approximate location of maximum luminosity from soot in the H₂/toluene flames (see Figure 5). While the heat flux sensor captures radiation from the entirety of the flames, radiation which stems from locations nearer to the sensor contributes a greater proportion to the overall measured heat flux, due to the inverse-square law. As a result, the heat flux measurements are somewhat biased toward the H₂/toluene flames, since the luminous region—which is indicative of regions with significant thermal radiation—is more evenly distributed in the natural gas flame.

The heat flux results for the two practical burners, that is, the BBQ and STV series of flames, are shown in Figure 9. Again, the measured values are normalised against the equivalent natural gas flames for each of the burners.

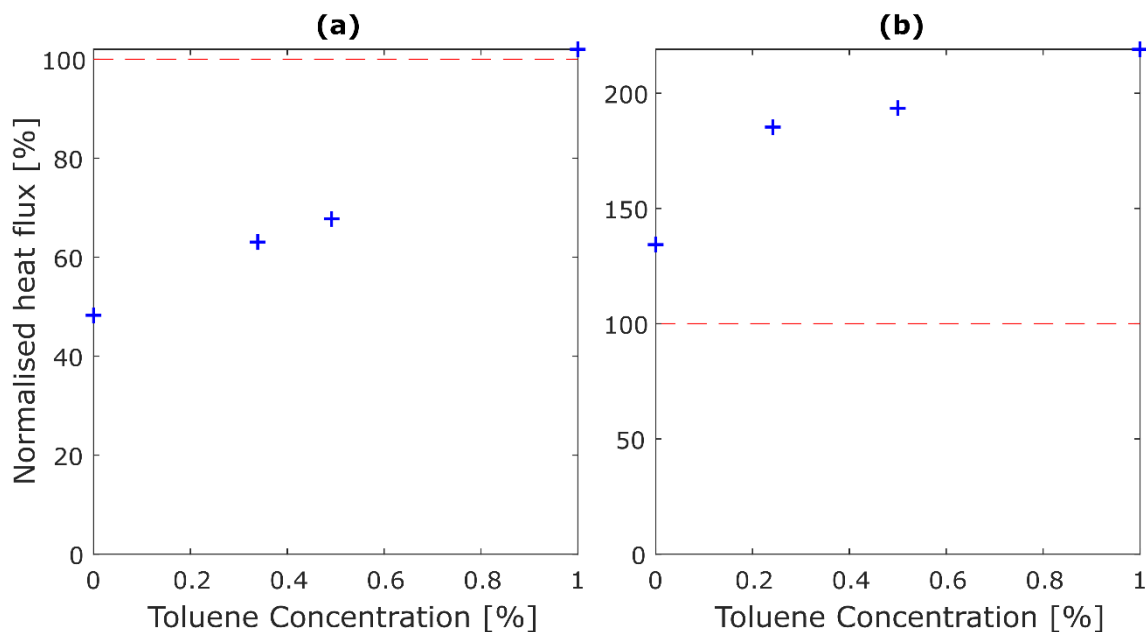


Figure 9: Thermal radiation for (a) BBQ burner flames and (b) stove-top (STV) flames (refer Table 3), normalised against equivalent premixed natural gas cases.

For both of the plots shown in Figure 9, a consistent increase in thermal radiation can again be seen with toluene addition, as expected. A key difference between the results for the BBQ and STV flames is the relative magnitudes in comparison to the equivalent natural gas flames. It should be mentioned that the absolute values of heat flux for the H₂/toluene flames are actually very similar for the two burners (for equivalent toluene concentrations), while the premixed natural gas cases are significantly different, despite having similar heat inputs. Specifically, the heat flux measured for the BBQ-NG case was approximately 1.7 times greater than that of the STV-NG case, such that the normalised values are higher for the STV series of flames shown in Figure 9(b), since the results are normalised against the equivalent natural gas case for each burner.

The difference in radiative heat flux between the BBQ-NG and STV-NG cases is likely a result of the difference in their flame structures, as shown in the photographs in Figures 6 and 7. For the BBQ burner, the fuel/air mixture issues directly upward from the burner body where flamelets are stabilised at the exit ports, and a relatively long flame which extends downstream from the flamelets can be seen. The stove-top burner, on the other hand, displays a much more “compact” structure, with small flamelets which remain close to the exit ports. This is likely a result of differences in air entrainment between the two configurations, as well as the fact that the fuel/air issues horizontally for the stove-top burner rather than vertically. The larger flame volume in the case of the BBQ-NG flame is therefore likely to lead to a larger radiative heat flux in comparison to the STV-NG flame. It is also possible that the convective heating of the burner body due to the flames stabilised at the exit ports leads to radiation from the BBQ burner itself, which could interfere with the flame radiation measurements.

4.4 SPECTRAL MEASUREMENTS OF NATURAL GAS/HYDROGEN FLAMES

As mentioned in Section 4.1, the emission of light due to the excitation of sodium within the hydrogen flames was found to be significant during these experiments. Since the presence of sodium did not appear to change noticeably when using both industrial grade and ultra-high purity hydrogen—nor after purging the piping system—it was hypothesised that the sodium instead stems from the surrounding air. While there is limited data available regarding the presence of sodium in ambient air, it is known to be one of several sources of particulate matter, occurring both naturally from suspended sea salt and due to anthropogenic sources [58]. It is worth mentioning that the current experiments were conducted in relatively close proximity to the ocean within the City of Adelaide, such that both sources of sodium are likely to be significant.

Although the emission of light due to sodium excitation was noticeable for the hydrogen flames, it is interesting to note that this behaviour was not apparent for the natural gas flames, at least based upon qualitative observations by eye. Therefore, spectrometer measurements were performed to determine if this feature was unique to the hydrogen flames. These results are shown for the three different burners in Figure 10.

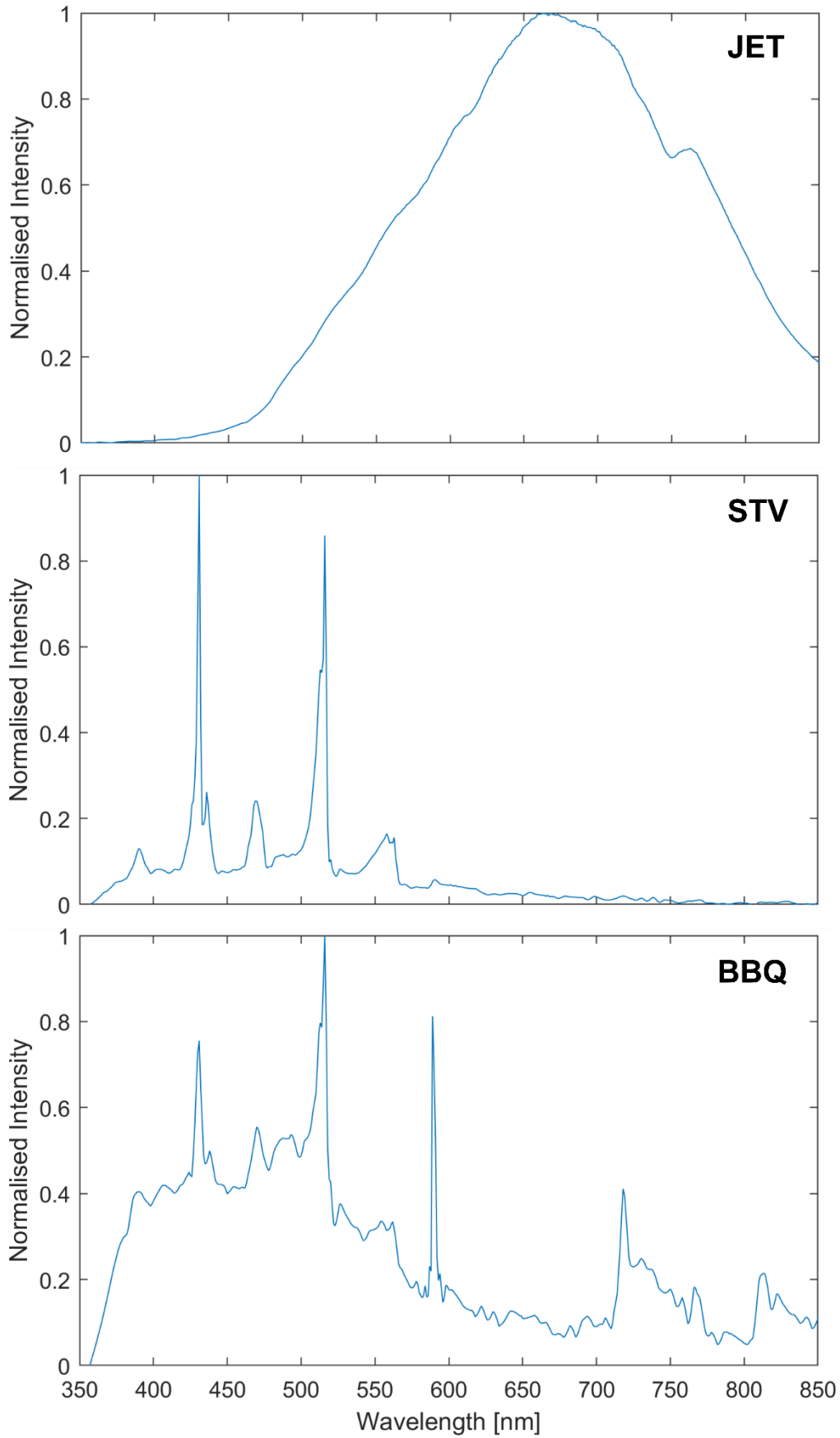


Figure 10: Flame spectra for natural gas flames for the three different burner configurations, for wavelengths ranging from near-UV to near-IR. Note that “JET” case is non-premixed, while “STV” and “BBQ” are premixed.

From Figure 10, it is apparent that the flame emission spectrum is sensitive to the burner configuration that is implemented. First of all, it is important to note that the “JET” spectrum shown corresponds to a non-premixed flame, such that soot formation is significant, as shown in the photograph of this flame in Figure 5. As a result, the spectrum is dominated by black-body radiation due to the high-temperature soot particles, and there is minimal radiation in the 350–450 nm range. The premixed burners, as expected, do not display this broadband radiation, instead showing peaks in the “near-UV/blue” region (i.e. approximately 350–500 nm), which are well-characterised for hydrocarbon flames and correspond primarily to CH* radicals and the C₂ Swan bands [15]. Importantly, it can be seen from the “BBQ” spectrum that there are indeed emissions from excited sodium for this case, with the characteristic peak at 589 nm, similar to the H₂ spectrum shown in Figure 3. There is also a very slight peak in the spectrum of the “STV” flame at 589 nm, although it is much less intense in comparison to the BBQ case and difficult to distinguish in Figure 10. It is also interesting to observe that the BBQ flame displays peaks in the red/near-IR region which are characteristic of excitation of water molecules, similar to the spectrum of the equivalent H₂ flame, while this behaviour is not apparent for the stove-top burner; this is consistent with the difference in the radiative heat flux between these cases as discussed in Section 4.3.

To further explore the source of the sodium emissions, results from a separate set of spectrometer measurements involving blends of H₂ and natural gas (NG) have been analysed. This series of experiments involved flame cases ranging from pure H₂ to pure NG, with eight intermediate NG:H₂ ratios. A stove-top burner configuration was used for these experiments similar to the STV burner discussed throughout this report, although the burner was operated in premixed mode without modification for all flame cases. As a result, the flames transitioned from a conventional stove-top behaviour for low-to-intermediate H₂ concentrations, with flamelets stabilised at the exit ports between the burner crown and the cap, to a “light-back” condition in which the flame burns inside the mixing region, that is, between the fuel injector and the exit ports. Based on qualitative observations, this light-back situation occurred for H₂ concentrations of 80% (by volume) and greater. The spectral imaging results are shown in Figure 11, for a selection of cases shown on a single set of axes, for two different wavelength ranges; specifically, from 350–550 nm and from 580–600 nm, to highlight specific features of the spectra.

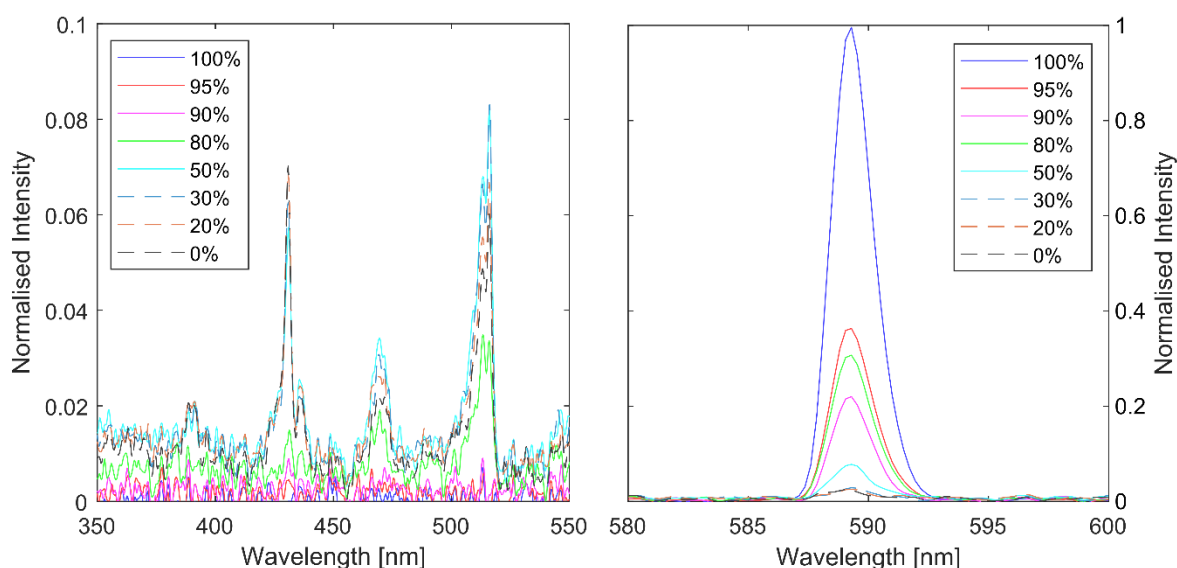


Figure 11: Measured spectra for selected H₂:NG blends from 0% (pure NG) to 100% (pure H₂). Results are shown for two different wavelength ranges to focus on the “blue” region (left) and the sodium emissions (right). Values shown in legend refer to the volume of H₂ as a percentage of the total volume of fuel. Note also the different y-axes for the two plots.

A noticeable change in the spectra of the various blends can be seen for both wavelength ranges shown in Figure 11. The 580–600 nm plots once again show peaks at 589 nm due to sodium excitation, consistent with the spectra shown previously. It is interesting to note the rapid reduction in the intensity of this “sodium peak” as the H₂ concentration is decreased from 100%, even with just 5% NG by volume (that is, the 95% case). While the NG-dominated cases show a greatly diminished peak at this location, the peak still remains present for all cases, and there does not appear to be any noticeable change from 30% H₂ case to the pure NG case. The change in

the intensity of this sodium excitation emission with varying H₂ concentrations is plotted in Figure 11. This figure displays the “normalised peak intensity”, based on the ratio of the maximum intensity value in the 580–600 nm range (that is, at approximately 589 nm) to the mean intensity in the same range, excluding the 586–595 nm range where the peak begins and ends. Note that Figure 12 includes additional H₂ concentrations not included in Figure 11.

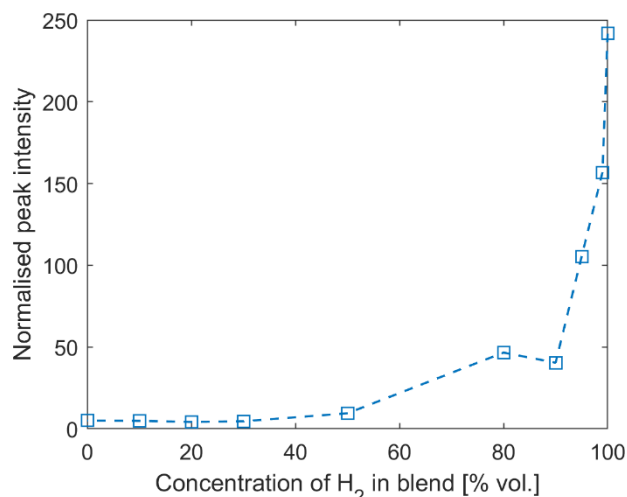


Figure 12: Variation in the peak intensity due to sodium excitation for H₂ concentrations ranging from 0 to 100%.

It is clear from Figure 12 that an increase in the concentration of H₂ leads to more intense emissions from sodium excitation, with the exception of the 90% H₂ case which appears to be an outlier in these measurements. The fact that there is still a slight peak for the NG-dominated flames—coupled with the strong peak observed for the BBQ-NG case (see Figure 10)—indicates that the primary source of the sodium is not from the hydrogen itself. The effect seen in Figures 10 and 11 must therefore be related to a change in flame behaviour as hydrogen is added to natural gas. One factor which likely contributes to this change is the transition from a conventional cooktop flame for the flames with 50% H₂ and less, to a flame which is lit-back for H₂ concentrations of 80% and greater; this would explain the relatively large increase from 50% to 80% H₂. This is also consistent with the spectra from 350–550 nm shown in Figure 11, in which the ≤50% H₂ cases can all be seen to have very similar spectra both in terms of the location of the peaks and their intensities. It should also be noted that these peaks which can be seen in the 350–550 nm range in Figure 11 correspond to the well-characterised emission bands for hydrocarbon flames which are also evident for the STV and BBQ burner spectra shown in Figure 10.

While the light-back effect under sufficiently high H₂ concentrations appears to have an effect on the flame spectrum, this does not completely explain the observations regarding the peak at approximately 589 nm. If the flame being lit-back were the sole cause, then one would not expect the increase in intensity which occurs from 90% to 100% H₂ as shown in Figure 12, nor would it explain the detection of sodium emissions for the simple jet configuration and the BBQ burner, for both nonpremixed hydrogen and premixed natural gas in the case of the BBQ burner. Based on these results, it is likely that there are multiple factors which affect the emission of light at 589 nm due to sodium excitation. Since the behaviour is observed across different burner configurations and plumbing systems, it follows that the sodium either stems from the surrounding air, or it is present in both the natural gas (from the mains network) and the hydrogen (from a compressed cylinder, both industrial grade and UHP). In addition to the source, the actual mechanism which leads to the sodium excitation and emission of light is not clear. While temperature measurements were not performed in this study, an increase in the H₂ concentration is expected to lead to a slightly hotter flame, which could lead to an increased tendency for excitation to occur. In saying this, the temperature difference between the 99% and 100% H₂ flames is unlikely to be significant, yet there is a relatively large increase in intensity. Additionally, the premixed BBQ-NG case was seen to have a strong emission at 589 nm, as well as peaks in the red/near-IR region of the spectrum which align to those observed for the equivalent H₂ flame and are attributed to excitation of water molecules. This suggests a change in behaviour for the premixed BBQ burner in comparison to the stove-top burner, which is likely a result of a change in the entrainment of air and mixing processes. This could in turn lead to a change in temperature and/or oxidation pathways, such that excitation of sodium and water are favoured in the case of the BBQ burner, although this requires further investigation.

4.5 OLFACTORY DETECTION: TOLUENE AND OTHER POTENTIAL DOPANTS

4.5.1 Toluene as an Odorant

In addition to the impact on flame visibility and radiative properties, the potential of using a dopant as an odorant for leak detection is also of interest, as discussed in the Literature Review. While the experimental environment did not facilitate thorough olfactory detection tests in accordance with the relevant standard [AS/NZS 4323.3], some qualitative observations were made regarding the smell of toluene. Due to safety concerns relating to extended exposure to toluene, a face mask was worn when working closely with this substance, affecting observations in this sense. However, during the experiments, the toluene odour could typically still be detected upon removal of the face mask after handling the toluene, even after approximately five minutes in a well-ventilated room. Additionally, the odour could also be detected when a vapourised mixture of toluene and air (0.5% by mole of toluene in the pipe) was allowed to leak at a rate of approximately 9 SLPM for 1 minute, although quantitative measurements of the concentration in the surrounding air at which the “leak” was detected were not possible. With regards to the nature of the odour, the observations were consistent with what was included in Table 1 (i.e. reminiscent of a solvent or paint-thinner), and the odour could also be described as “unpleasant” and “distinct”. While these observations are not intended to be concrete evidence of toluene (and similar chemicals) being suitable for use as an odorant at the concentrations used in the current study, they suggest that it could certainly be viable.

To provide a further indication of toluene’s potential as an odorant, the odour detection threshold based on previous measurements [11] can be used, in conjunction with the requirement of detection of an odourised gas leak at 20% of the LEL in air. Based on the experimental observations, it appears that toluene addition to hydrogen at a concentration of 0.5% by mole can lead to a flame of comparable visibility to that of natural gas. Assuming that addition of toluene at this level does not significantly change the LEL of the mixture, the toluene/hydrogen mixture would need to be detectable at a concentration of 0.8% (by volume of fuel in air), based on an LEL for hydrogen of 4%. Using these details, an indication of the potential for toluene as an odorant can be estimated:

$$\begin{aligned}LEL_{H_2} &= 4\% \\ \therefore C_{crit} &= 0.8\%\end{aligned}$$

Where C_{crit} is the critical concentration at which the hydrogen/toluene mixture must be detectable.

The concentration of toluene in the fuel mixture is assumed to be 0.5% by mole, which is equivalent to the volumetric percentage by the ideal gas law, therefore::

$$\begin{aligned}C_{tol} &= 0.005 \times 0.8\% \\ &= 0.004\% \\ &= 40 \text{ ppm (vol/vol)}\end{aligned}$$

That is, the concentration of toluene in the air at one-fifth (20%) of the LEL of hydrogen in air, based on a dopant concentration of 0.5%, is 40 ppm. Referring back to Table 1, this value is greater than the detection threshold for toluene of 0.33 ppm by a factor of approximately 120. While this certainly indicates that toluene at this concentration would be effective for leak detection, further investigation in the form of olfactory testing of hydrogen/toluene mixtures in air at this concentration would be required to verify this.

4.5.2 Practical Considerations and Alternative Dopants

Although the theoretical calculations suggest that toluene could be used for olfactory detection of leaks at a dopant concentration of 0.5% by mole, there are a number of important practical considerations. First of all, while a concentration of 0.5% by mole may seem like a relatively minor amount, this equates to 18.8% by mass and 7.2% by energy content. This ultimately corresponds to a 92.5% reduction in CO₂ emissions in comparison to natural gas (based on equivalent heat input), from 73.3 g/MJ for natural gas down to 5.53 g/MJ for the hydrogen/toluene mixture. While this is a significant reduction, it is still far from a non-negligible level of CO₂ emissions, particularly if the toluene were to be blended throughout the network. It is worth noting that currently, the major areas of natural gas consumption in domestic settings are for water heating and ducted space heating, and these uses do not, in general, require a visible or highly radiating flame. Therefore, if the use of the dopant were limited to instances in which a visible flame is desired, such as for cooking and heating, then the case for

using a carbon-emitting dopant becomes much more attractive from an emissions perspective. To provide a practical indication, calculations based on the operation of a high heat-input gas cooktop for one hour every day for an entire year, with 0.5% toluene addition to hydrogen, result in a consumption of just 8 L of liquid toluene per year. In terms of emissions, this corresponds to 20 kg of CO₂ emitted annually; this is approximately the same amount of CO₂ emitted from a single 80 km trip in a typical internal combustion engine passenger vehicle [59]. It should also be mentioned that if the use of a dopant was limited to applications such as cookers and visible fires, then it would clearly not address the issue of leak detection in the wider network.

As mentioned earlier, a key reason for the focus on toluene for this investigation was as a surrogate for potential biofuels or biomass-derived substances. If a carbon-neutral dopant were to be implemented, then injection throughout the network could be feasible, at least from an emissions perspective, allowing olfactory detection throughout the wider network. While there is little information in the literature about the olfactory and sooting properties of biofuels themselves (likely due to their variability in terms of composition), there are many substances which can be obtained from the processing of biofuels and biooils, similar to the processing of crude oil. Many of the substances listed in Table 1 can be derived in such a way and are also known to be highly sooting, along with having odour detection thresholds below that of toluene. For example, while benzene and benzene-derivatives (including toluene itself) are typically obtained from crude oil and other industrial processes using fossil-fuel feedstocks, the situation in the future could potentially be very different [60]. It is worth noting that these benzene derivatives (which generally belong to the aromatic hydrocarbon family) often have similar sooting properties to toluene [61] and lower detection thresholds; for example, styrene and p-Diethylbenzene which are listed in Table 1.

5. Conclusions

The use of 100% hydrogen as a fuel for domestic heating applications presents a number of challenges in terms of both safety and performance. Many of these challenges are related to the difference in combustion behaviour of hydrogen in comparison to natural gas. It is well-documented that hydrogen burns with a relatively faint flame due to a lack of soot and carbon-containing species, such that it is often described as being invisible under regular lighting conditions; this presents an obvious safety concern for applications such as cooktop burners. The lack of radiative heat transfer can also inhibit the performance of hydrogen flames in instances where this mode of heat transfer is important, both in domestic and industrial applications. An investigation has therefore been carried out to assess the feasibility of improving flame visibility and radiative heat transfer through the addition of a highly sooting fuel, with the focus on toluene as a surrogate fuel for this project. There is also a potential side-benefit of the addition of such a fuel, in terms of leak detection via olfactory sensation, particularly when considering the complications of using sulphur-based odorants in a pure hydrogen network.

A review of the relevant literature revealed a number of interesting findings with regards to the visible emissions associated with hydrogen flames. An interesting observation was the apparent lack of consensus across different studies, particularly with regards to the “reddish” appearance of hydrogen flames and the effect of impurities. This literature review also encompassed the issues and challenges surrounding the olfactory detection of hydrogen, using the existing standards pertaining to natural gas as a reference. A number of potential dopants were identified, and the potential for these chemicals to act as both a colourant and an odorant was discussed.

Following a comprehensive review of the literature, an experimental study was performed to examine the behaviour of toluene-doped hydrogen flames for three different burner configurations. The flames were analysed via photography under various lighting and background conditions, complemented by radiative heat flux measurements and spectral imaging. A particularly interesting finding was the dominance of the visible emissions from sodium impurities on the visual appearance of the pure hydrogen flames, which necessitated the use of a notch filter for the flame photography in order to capture the visible emissions from the underlying hydrogen flame. Spectral imaging revealed that emissions due to the presence of sodium also occurred for natural gas under certain configurations, although increasing the concentration of hydrogen in the fuel tends to promote sodium excitation. The addition of toluene up to 1% by mole was found to have a significant impact on the visual appearance of the flames, as well as the radiative heat flux. For the two practical burners, photographs were captured under a range of background/lighting conditions which were found to have a notable effect on the visibility, emphasising the importance of these parameters when analysing the safety of flames in domestic applications.

6. Implications and Recommendations for Industry

The experimental results presented in this report provide a number of interesting insights with regards to the implementation of a hydrogen gas network. With regards to the issue of visibility, the solution that is ultimately implemented will likely be determined by the priorities of appliance manufacturers and regulatory bodies. It should be stressed that although there are visible emissions from “pure” hydrogen flames, the results of this investigation indicate that the visibility is significantly reduced in comparison to equivalent natural gas flames. Additionally, when discussing visibility, it is important to understand the effect of impurities and variable environmental conditions on this behaviour. This is in reference to the photographs captured with the notch filter installed to block out the emissions from sodium impurities, which was shown to significantly impact the appearance. It could be argued that, due to the relatively high visibility of the hydrogen flames as a result of sodium excitation (see Figure 4), there is no need to improve flame visibility. Indeed, there have recently been trials and demonstrations overseas—specifically in the UK—where an “orange” hydrogen flame was produced without any additional colourant, which appears to solve the visibility issue. However, as discussed in the literature review, the source of these emissions appears to be related to adventitious impurities (particularly sodium), the reliability of which is likely very sensitive to local environmental conditions. As a result, there is expected to be variation in the appearance of the flames from city to city and even between different homes due to changes in ventilation systems, for example. Furthermore, the current experiments indicate that the light emission from sodium excitation is also dependent on the flame structure and burner configuration, so this must also be considered when assessing the need for a colourant.

Based on the results presented, the addition of a highly sooting fuel (toluene) can be seen to improve both the flame visibility and the radiative heat transfer properties of hydrogen. The flame photography results indicate that

addition of toluene at concentrations of approximately 0.5% by mole can lead to a flame of similar visibility to that of natural gas, although it should be mentioned that modifications to practical burners will be necessary when shifting to predominately hydrogen, and this could in turn affect the visibility. The heat flux measurements suggest that doping with toluene at concentrations of 1% by mole produces a comparable level of radiation to an equivalent heat input natural gas flame, although once again these results were found to be dependent on the burner configuration. Therefore, if the potential to improve performance by doping hydrogen with a biofuel—for example—is to be assessed, then this should be evaluated based on the specific burner configuration that is to be implemented.

The addition of a liquid dopant also offers the potential to resolve the issue of olfactory detection, brought-upon by the fact that common sulphur-based odorants are known to cause degradation of fuel cell electrodes, along with posing challenges in terms of removal from the gas stream. While chemicals such as toluene have higher detection thresholds compared with traditional odorants, they should not be ruled out, since the key factor to consider is whether the mixture with hydrogen is discernible at “one-fifth of the lower explosive limit (LEL) of the gas” [35, 36]. Based on a dopant concentration of 0.5% by volume and an LEL value of 4% by volume (based on pure hydrogen in air), initial calculations show that the concentration of toluene would be approximately 40 ppm at one-fifth of the LEL. This is 120 times the detection threshold of 0.33 ppm for toluene as reported in Table 1, suggesting that this could indeed be a viable option for olfactory detection. In saying this, calculations also indicated that addition of toluene at this concentration would lead to significant CO₂ emissions, particularly if distributed throughout the network, as would be the case if it were to be used as an odorant.

Based on these findings, the ultimate recommendation is against the addition of a fossil-fuel-based dopant throughout an otherwise-100% hydrogen network, for use as both a colourant and an odorant. While a carbon-neutral dopant could be viable for network-wide distribution, this is likely to incur significant costs in the transition to a hydrogen pipeline, and would therefore need to be compared against the option of using existing odorants with desulphurization when necessary, or using an alternative sulphur-free odorant (e.g. GasOdor-S-Free). With regards to injection of a dopant within internal pipework or at specific appliances, it is recommended that this option be explored further. This will require comparison against alternative options such as advanced flame indicators which negate the need for a visible flame (at least from a safety perspective), as well as other colourant options such as metal oxides, or simply relying on the presence of impurities. If a network-wide colourant is not implemented, then the solution to be implemented will likely be appliance-specific and depend on the priorities of the appliance manufacturer.

7. Future Work

While this investigation has provided several key insights with regards to hydrogen flame visibility and the effect of dopants and impurities, it has also raised a number of questions which require further investigation. In addition to the recommendations already mentioned in Section 6, there are some specific research opportunities which will be investigated within the scope of current and commencing Future Fuels CRC projects. Although the source of the orange hydrogen flame colour was verified in this study to stem from sodium, further experiments are necessary to determine the exact source of this sodium and the factors which contribute to its excitation. This will involve spectrometer measurements with a wider range of fuels to assess the effects of chemistry, to be accompanied by temperature measurements. Experiments and numerical analyses will also be performed for more practical burner configurations, to enable partial premixing of hydrogen and air to occur, and the effect of these changes on flame visibility and burner performance will be investigated. Additional heat flux measurements will also be performed; this will include pure and doped hydrogen flames, as well as blends of hydrogen and natural gas, in the context of domestic, commercial, and industrial applications.

8. Reference List

1. G.W. Crabtree, M.S. Dresselhaus, and M.V. Buchanan, *The Hydrogen Economy*, Physics Today, 2004. 57(12): p. 39-44.
2. P.E. Dodds, et al., *Hydrogen and Fuel Cell Technologies for Heating: A Review*, International Journal of Hydrogen Energy, 2015. 40(5): p. 2065-2083.
3. C.M. White, R.R. Steeper, and A.E. Lutz, *The Hydrogen-Fueled Internal Combustion Engine: A Technical Review*, International Journal of Hydrogen Energy, 2006. 31(10): p. 1292-1305.
4. M.W. Melaina, O. Antonia, and M. Penev, *Blending Hydrogen into Natural Gas Pipeline Networks: A Review of Key Issues*, NREL, 2013.
5. R. Judd and D. Pinchbeck, *Hydrogen admixture to the natural gas grid*, in *Compendium of Hydrogen Energy*. 2016. p. 165-192.
6. R.L. DeKock and H.B. Gray, *Chemical Structure And Bonding*. 1989: University Science Books. 516.
7. K. Takai, et al., *Lattice defects dominating hydrogen-related failure of metals*, Acta Materialia, 2008. 56(18): p. 5158-5167.
8. C. Tang, et al., *Explosion characteristics of hydrogen–nitrogen–air mixtures at elevated pressures and temperatures*, International Journal of Hydrogen Energy, 2009. 34(1): p. 554-561.
9. R.W. Schefer, et al., *Visible emission of hydrogen flames*, Combustion and Flame, 2009. 156(6): p. 1234-1241.
10. J. Kopasz, *Fuel cells and odorants for hydrogen*, International Journal of Hydrogen Energy, 2007. 32(13): p. 2527-2531.
11. M.H. Abraham, et al., *An algorithm for 353 odor detection thresholds in humans*, Chem Senses, 2012. 37(3): p. 207-18.
12. DNV, *Hydrogen Colourant - Final Report*, Hy4Heat, 2019. Available from: <https://www.hy4heat.info/s/WP2-Colourant-Report-final-10-May-2021.pdf>.
13. Frazer-Nash Consultancy, *Appraisal of Domestic Hydrogen Appliances*, Department for Business, Energy and Industrial Strategy, 2018.
14. Frontier Economics, *Residential energy consumption benchmarks*, Australian Energy Regulator, 2020.
15. A. Gaydon, *The Spectroscopy of Flames*. 1974: Springer Netherlands.
16. Y. Zhao, et al., *Investigation of visible light emission from hydrogen-air research flames*, International Journal of Hydrogen Energy, 2019. 44(39): p. 22347-22354.
17. A. Choudhuri, *Combustion characteristics of hydrogen–hydrocarbon hybrid fuels*, International Journal of Hydrogen Energy, 2000. 25(5): p. 451-462.
18. P.J. Padley, *The origin of the blue continuum in the hydrogen flame*, Transactions of the Faraday Society, 1960. 56.
19. Northern Gas Networks. *Our Hydrogen Home*. Available from: <https://www.northerngasnetworks.co.uk/current-business-plan/our-hydrogen-home-welcome-to-green-gas/>. Accessed 09/12/2021.
20. Hydrogen Central. *Northern Gas Networks, First Hydrogen Homes open to the Public*, 2021. Available from: <https://hydrogen-central.com/northern-gas-networks-hydrogen-homes-open-public/>. Accessed 22/11/2021.
21. H.A. Webster, *Visible Spectra of Standard Navy Colored Flares*, Propellants, Explosives, Pyrotechnics, 1985. 10(1): p. 1-4.
22. D. Juknelevicius, et al., *A Spectrophotometric Study of Red Pyrotechnic Flame Properties Using Three Classical Oxidizers: Ammonium Perchlorate, Potassium Perchlorate, Potassium Chlorate*, Zeitschrift für anorganische und allgemeine Chemie, 2014. 640(12-13): p. 2560-2565.
23. K. Waheed, et al., *Investigations on Thermal Radiative Characteristics of LPG Combustion: Effect of Alumina Nanoparticles Addition*, Combustion Science and Technology, 2014. 187(6): p. 827-842.
24. AEMO, *GAS QUALITY GUIDELINES*, AEMO, 2017.
25. W. Hutny and G. Lee, *Improved radiative heat transfer from hydrogen flames*, International Journal of Hydrogen Energy, 1991. 16(1): p. 47-53.
26. C. McEnally and L. Pfefferle, *Improved sooting tendency measurements for aromatic hydrocarbons and their implications for naphthalene formation pathways*, Combustion and Flame, 2007. 148(4): p. 210-222.
27. P. Chylek, S.G. Jennings, and R. Pinnick, *SOOT*, in *Encyclopedia of Atmospheric Sciences*, J.R. Holton, Editor. 2003, Academic Press: Oxford. p. 2093-2099.
28. F. Ahmady and S.C. Duvvuri, *Radiant space heater for residential use*, S. United, Editor. 1997, Solaronics Inc.
29. E.P. Keramida, et al., *Radiative heat transfer in natural gas-fired furnaces*, International Journal of Heat and Mass Transfer, 2000. 43(10): p. 1801-1809.
30. Udayraj, et al., *Heat transfer analysis and second degree burn prediction in human skin exposed to flame and radiant heat using dual phase lag phenomenon*, International Journal of Heat and Mass Transfer, 2014. 78: p. 1068-1079.
31. H. Guo, et al., *Numerical study on the influence of hydrogen addition on soot formation in a laminar ethylene–air diffusion flame*, Combustion and Flame, 2006. 145(1-2): p. 324-338.

32. S.H. Pourhoseini and M. Moghiman, *Effect of pulverized anthracite coal particles injection on thermal and radiative characteristics of natural gas flame: An experimental study*, Fuel, 2015. 140: p. 44-49.
33. S.W. Baek, et al., *Effects of Addition of Solid Particles on Thermal Characteristics in Hydrogen-Air Flame*, Combustion Science and Technology, 2002. 174(8): p. 99-116.
34. C. Law, *Effects of hydrocarbon substitution on atmospheric hydrogen-air flame propagation*, International Journal of Hydrogen Energy, 2004. 29(8): p. 867-879.
35. Government of South Australia, *Gas Regulations 2012*, in *Division 2—Gas supply, quality etc.* 2012.
36. Government of Victoria, *Gas Safety (Gas Quality) Regulations 2007*, in *Odour*. 2018.
37. AEMO, *Gas Quality Standard and Monitoring Guidelines (Declared Transmission System)*, in *Gas odourisation*. 2016.
38. D. Tenkrat, T. Hlincik, and O. Prokes, *Natural Gas Odorization*, Natural Gas, 2010.
39. D. Lee, et al., *Adsorptive removal of tetrahydrothiophene (THT) and tert-butylmercaptan (TBM) using Na-Y and AgNa-Y zeolites for fuel cell applications*, Applied Catalysis A: General, 2008. 334(1-2): p. 129-136.
40. J. Dunleavy, *Final Analysis: Sulfur as a Catalyst Poison*, Platinum Metals Review, 2006. 50(2): p. 110-110.
41. V.A. Sethuraman and J.W. Weidner, *Analysis of sulfur poisoning on a PEM fuel cell electrode*, Electrochimica Acta, 2010. 55(20): p. 5683-5694.
42. J. Wu, et al., *A review of PEM fuel cell durability: Degradation mechanisms and mitigation strategies*, Journal of Power Sources, 2008. 184(1): p. 104-119.
43. A. Dushina, et al., *The influence of hydrogen sulphide contamination on platinum catalyst used in polymer electrolyte membrane fuel cells during potential cycling at 0.05–1.05 V vs RHE: An RRDE study*, International Journal of Hydrogen Energy, 2020. 45(60): p. 35073-35084.
44. P.J. de Wild, et al., *Removal of sulphur-containing odorants from fuel gases for fuel cell-based combined heat and power applications*, Journal of Power Sources, 2006. 159(2): p. 995-1004.
45. T. Haneda, et al., *Technological assessment of residential fuel cells using hydrogen supply systems for fuel cell vehicles*, International Journal of Hydrogen Energy, 2017. 42(42): p. 26377-26388.
46. J.R. Anstrom, *Hydrogen as a fuel in transportation*, in *Advances in Hydrogen Production, Storage and Distribution*. 2014. p. 499-524.
47. J. Mouli-Castillo, et al., *Olfactory appraisal of odorants for 100% hydrogen networks*, International Journal of Hydrogen Energy, 2020. 45(20): p. 11875-11884.
48. A. Murugan, *Hydrogen Odorant and Leak Detection Part 1*, Hydrogen Odorant, Hy4Heat, 2020.
49. M. Zarzo, *Effect of functional group and carbon chain length on the odor detection threshold of aliphatic compounds*, Sensors (Basel), 2012. 12(4): p. 4105-12.
50. J.G. Speight, *Chapter 2 - Organic Chemistry*, in *Environmental Organic Chemistry for Engineers*, J.G. Speight, Editor. 2017, Butterworth-Heinemann. p. 43-86.
51. Gasunie, *Working with Odorants (THT)*, N.V. Nederlandse Gasunie, 2015. Available from: [https://www.gasunie.nl/en/organisation/health-safety-environment/corporate-hse-policy/hse-documentation/\\$3951/\\$3980](https://www.gasunie.nl/en/organisation/health-safety-environment/corporate-hse-policy/hse-documentation/$3951/$3980).
52. PubChem. *PubChem*. Available from: <https://pubchem.ncbi.nlm.nih.gov/>. Accessed 18/11/2021.
53. J. Lehtinen and A. Veijanen, *Odour Monitoring by Combined TD–GC–MS–Sniff Technique and Dynamic Olfactometry at the Wastewater Treatment Plant of Low H₂S Concentration*, Water, Air, & Soil Pollution, 2010. 218(1-4): p. 185-196.
54. United States Environmental Protection Agency. *Technical Factsheet on Ethylbenzene*, 2014. Available from: <https://nepis.epa.gov/Exe/ZyPURL.cgi?Dockkey=P1010HXN.txt>. Accessed 18/11/2021.
55. M.J. Evans, et al., *Highly radiating hydrogen flames: Effect of toluene concentration and phase*, Proceedings of the Combustion Institute, 2021. 38(1): p. 1099-1106.
56. H.Y. Kim and N.J. Choi, *Study on Volatile Organic Compounds from Diesel Engine Fueled with Palm Oil Biodiesel Blends at Low Idle Speed*, Applied Sciences, 2020. 10(14).
57. S.M. Mahmoud, et al., *The effect of exit Reynolds number on soot volume fraction in turbulent non-premixed jet flames*, Combustion and Flame, 2018. 187: p. 42-51.
58. A. Ooki, et al., *Sources of sodium in atmospheric fine particles*, Atmospheric Environment, 2002. 36(27): p. 4367-4374.
59. United States Environmental Protection Agency (EPA). *Greenhouse Gas Emissions from a Typical Passenger Vehicle*. Available from: <https://www.epa.gov/greenvehicles/greenhouse-gas-emissions-typical-passenger-vehicle>. Accessed 26/11/2021.
60. Q. Meng, et al., *Sustainable production of benzene from lignin*, Nat Commun, 2021. 12(1): p. 4534.
61. C.S. McEnally, D.D. Das, and L.D. Pfefferle, *Yield Sooting Index Database Volume 2: Sooting Tendencies of a Wide Range of Fuel Compounds on a Unified Scale*. 2017, Harvard Dataverse.

THIS PAGE SHOULD BE LEFT BLANK



Future Fuels CRC

Enabling the Decarbonisation of
Australia's Energy Networks



www.futurefuelscrc.com



info@futurefuelscrc.com



Australian Government
Department of Industry, Science,
Energy and Resources

Business
Cooperative Research
Centres Program

Chapter 9

Discussion

A major challenge in the development of new combustion devices is the requirement of both high thermal efficiency and low emissions of soot, CO and NO_x, while also accommodating different fuel types across a range of operating conditions. In this regard, the concepts of mild and sequential combustion are particularly promising, as discussed in Chapter 2. To apply these concepts to practical devices such as gas turbines—which typically operate at pressures significantly above atmospheric levels and are increasingly required to provide high operational flexibility—a more detailed understanding of the fundamental combustion processes is necessary. There are also unique challenges related to the use of hydrogen as a fuel in combustion devices, which further motivates this work. The research presented in this thesis is an important contribution towards developing a better understanding of combustion for improved fuel-flexibility in practical devices. The key outcomes of Chapters 4–8 are discussed and analysed in this chapter, as framed by three underlying themes which constitute the following section headings.

9.1 Decoupling of boundary conditions for the study of flame stabilisation

One of the key aspects which motivates this research is the importance of improving the operational and fuel flexibility of combustion systems, which is a potential advantage of mild combustion. Consequently, a range of different boundary conditions were investigated within the scope of this project, to assess the sensitivity to changes in these conditions. To facilitate this, a key feature common to both of the novel experimental burners studied as part of this thesis is the ability to isolate the individual effects of different operating conditions. The CP-JHC apparatus, upon which Chapters 4 and 5 are based, enables the pressure to be increased while maintaining a constant mass flowrate of both the fuel and oxidant stream, such that there is a decoupling between the jet Reynolds number (Re_{jet}) and the bulk velocity of the jet and the hot coflow. This configuration also provides the ability to vary the coflow O₂ concentration independently of Re_{jet} , and vice-versa. Similarly, Chapters 6 and 7 relate to the dilute spray burner configuration,

9.1 Decoupling of boundary conditions for the study of flame stabilisation

which is based on the same “jet-in-hot-coflow” (JHC) concept, such that the surrounding O₂ concentration and temperature can be controlled, with additional key variables being the fuel composition and liquid fuel loading.

An important finding from the CP-JHC experiments is the tendency towards increased flame stability as the pressure is increased, likely due to the lower velocity at the jet exit such that the tendency of flame liftoff is reduced. Similarly, an increase in Re_{jet} from 10,000 to 15,000 was seen to promote liftoff and lead to greater fluctuations in the location of the flame base, particularly at lower pressure. Additionally, the comparisons of chemiluminescence intensity for the CP-JHC flames against the numerical modelling results at a range of coflow O₂ concentrations—which are presented in Chapter 5—suggest that the discrepancies between the results of the experiments, CFD modelling and laminar flame simulations can be partially attributed to changes in flame stabilisation and lift-off height.

In the context of the spray flames, the effects of both the jet and coflow boundary conditions on flame stabilisation are examined in Chapters 6 and 7, respectively. A particularly interesting finding from Chapter 6 is the detection of isolated ignition kernels radially inward of the stabilised outer flame front for the *n*-heptane and *n*-heptane/toluene cases, whereas the imaging of the equivalent ethanol flame reveals a bifurcating double flame structure. The simultaneous imaging of OH and CH₂O in the near-field region also showed that the formation of these ignition kernels is supported by the presence of pre-ignition species in the inner, partially premixed region. The results presented in Chapter 7 highlight the importance of the surrounding O₂ level on the near-field flame structure, again providing important insights into the changes in stabilisation mechanisms for such flames. In particular, the simultaneous imaging of fuel droplets and key flame radical species (such as OH) revealed that flames with sufficiently high coflow O₂ concentrations (i.e. $\geq 7.5\%$ O₂) tend to be stabilised by an outer diffusion flame which extends to the jet exit. In contrast, the flames in the 3% O₂ coflow showed a significant departure from this behaviour, with either a more dominant inner flame structure in the case of ethanol, or a significantly weakened reaction zone near the jet exit in the case of *n*-heptane which leads to a visibly lifted flame. Interestingly, the coflow temperature was seen to have a relatively minor impact on the overall structure of these flames, although an increased stability of the inner flame in the near-field region was apparent for the 7.5% O₂ case at the higher coflow temperature.

These findings relating to both gaseous flames at elevated pressures and liquid spray flames in an open burner are an important step towards understanding the fundamental stabilisation behaviour of flames under hot

9.2 Imaging of flame structure and sooting behaviour under variable operating conditions

and low-oxygen combustion conditions. Not only does this research offer important phenomenological insights, the range of boundary conditions studied is of relevance for the development of numerical modelling capabilities, since the flames studied address key gaps in the literature [1, 2]. It is worth noting that, although the imaging of species and chemiluminescence performed for the flames is qualitative in nature, the radial profiles obtained under the various conditions—particularly in regard to the formation of the double flame structure in the context of the spray flames—offers a useful method assessing the validity of a model in terms of its ability to predict the stabilisation features.

9.2 Imaging of flame structure and sooting behaviour under variable operating conditions

In addition to flame stabilisation, the impact of variable operating conditions was studied in terms of the changes in flame structure and appearance more broadly. Once again, this includes the experiments performed in the pressurised combustor and spray burner, as well as the investigation of the characteristics of hydrogen flames with the addition of toluene to the fuel. In these various phases of the project, the imaging of the flames via either filtered or true-colour photography—as well as more detailed laser-based imaging of reaction zone structures in some cases—was a particular focus.

In Chapter 6, the effect of the variation of a number of different jet boundary conditions on the flame structure and sooting behaviour of spray flames was investigated. In terms of flame structure, the laser-based imaging revealed the presence of complex reaction zones in the near-field region which were found to be sensitive to changes in boundary conditions, and appeared to have a significant impact on the overall appearance of the flames. It was also noted that the flame length appeared to be proportional to the equivalence ratio in the jet (based on the total fuel and air flowrates), highlighting the importance of the carrier air stream on the evolution of the flames. Measurements of the soot volume fraction via the laser-induced incandescence (LII) technique highlighted the high sooting propensity of toluene in comparison to *n*-heptane under the conditions of interest, whilst the underlying flame structure remained largely the same.

The high sooting propensity of toluene was also an important factor in investigating the feasibility of using a hydrocarbon dopant to enhance the properties of hydrogen flames. Using a similar experimental configuration to the spray burner (upon which Chapters 6 and 7 are based)—although

with the hot coflow replaced by an air stream—the sooting characteristics and underlying flame structure of a series of toluene-doped hydrogen flames were examined as part of an investigation related to this thesis (included in Appendix A). This study was largely motivated by the practical challenges presented by the low emissivity of hydrogen flames in the context of industrial applications. Extending the scope of this investigation, an additional series of experiments were performed with a focus on the use of hydrogen in domestic combustion appliances. Imaging of these flames revealed notable changes in flame appearance as prevaporised toluene was introduced to the fuel stream, with 0.5% toluene (by mole) in the fuel producing a luminous, sooting flame, in addition to significantly increasing the thermal radiation of the flames in comparison to the pure hydrogen cases.

In addition to chemiluminescence imaging (discussed further in the following section), unfiltered images of the jet flames in the CP-JHC were also captured. These are shown in Figure 6 of Paper 1 (i.e. Chapter 4), and highlight the effect of pressure on soot formation. In particular, there is no indication of any soot formation within the viewing section for this series of flames for $P \leq 3.5$ bar, while the 5 and 7 bar cases show isolated regions of high luminosity due to soot incandescence. The effect of O₂ concentration on soot formation is discussed in Paper 2 (i.e. Chapter 5), in which it is intimated that there is no presence of soot (in the region of interest) at any of the operating pressures for the 3% and 6% O₂ coflows. This behaviour is consistent with the suppression of pyrolytic reactions at low O₂ concentrations, which has been observed in previous studies of mild combustion [3–5].

9.3 Flame spectrometry and chemiluminescence

Many of the key insights presented in the five chapters that compose the body of this thesis are based upon the detection and measurement of the light emitted from a flame in the ultra-violet (UV), visible and infra-red (IR) regions of the electromagnetic spectrum. The radiation emitted from a flame can be very broadly described as being either luminous or non-luminous [6]. In this context, luminous radiation refers to that which is emitted by solid particulates (typically soot in a hydrocarbon flame), producing a continuous (or broadband) emission spectrum, with most of this radiation in the visible and infra-red regions at typical flame temperatures. Non-luminous radiation, conversely, is generally associated with gaseous species within a flame [6]. This non-luminous radiation can be further classified according to the type of spectra produced; specifically, into either a line spectrum or

band spectrum. In general terms, the emission of lines is associated with the electronic excitation of atoms, which release a photon of a particular wavelength upon their transition to a lower energy level, while banded radiation is produced by molecules which emit light via a more complex combination of electronic, vibrational and rotational energy transitions [7]. Within a flame, these molecules can become excited due to the very high temperatures, or alternatively, via chemical reactions—this latter process is referred to as chemiluminescence. As discussed in Section 2 of this chapter, luminous radiation from soot is particularly important from a heat transfer perspective, with the sooting behaviour and resulting thermal radiation forming a common theme between the different phases of this project. Similarly, the investigation of the non-luminous radiation from flames was a central focus of the experiments performed in the CP-JHC and the accompanying numerical modelling, as well as the study of predominately hydrogen flames.

The investigation of the UV and visible light produced via chemiluminescence was a particular focus of the pressurised combustion experiments and numerical analyses. Not only does chemiluminescence imaging (via filtered flame photography) enable the imaging of reaction zones and provide an indication of heat release, an understanding of the sensitivity of this light to surrounding conditions—such as pressure and O₂ concentration—can be particularly useful in the optimisation of practical combustion systems, as discussed in Chapter 2. The comparison between the experimental imaging results, and the trends predicted via laminar flame simulations and CFD modelling, highlighted the importance of accurately modelling both the turbulent flow field and the finite-rate chemistry in order to predict chemiluminescence behaviour.

The chemiluminescence imaging performed for the CP-JHC flames was focussed on the excited state OH* and CH* radicals, in particular on the emission bands with notable peaks at 310 nm and 430 nm, respectively. It is worth noting that the CH* emission centred at approximately 430 nm is primarily responsible for the characteristic, intense blue colour of premixed hydrocarbon flames, such as that produced by a natural-gas-fired cooktop burner. Since there is no carbon present in a pure hydrogen flame to form CH* (or CO, which also tends to produce a less intense blue emission), hydrogen flames display quite a different appearance. As mentioned in Chapter 2, hydrogen flames are often described as invisible or very nearly invisible, with contradictory observations typically attributed to impurities in the fuel or air stream. To address this and to provide additional insight, the flame spectra were measured for pure and toluene-doped hydrogen flames, with these spectra compared against those of natural gas and natural gas/hydrogen

blends. An important outcome of these measurements is the confirmation that the distinct “yellow-orange” appearance of nominally pure hydrogen flames is due to the excitation and subsequent relaxation of sodium, which produces a signature “doublet” emission centred at 589 nm. Interestingly, this characteristic sodium emission was also observed for natural gas flames for one of the practical burners studied, suggesting that the source of this sodium was in the surrounding air rather than stemming from the fuel. The analysis of the spectra of the flames based on H₂/natural blends also showed a very slight peak at 589 nm for natural gas, with hydrogen addition tending to increase the intensity of the emission.

9.4 References

- [1] Hochgreb, S. (2019). “Mind the Gap: Turbulent Combustion Model Validation and Future Needs”. *Proceedings of the Combustion Institute* 37 (2), pp. 2091–2107.
- [2] Perpignan, A. A. V., A. G. Rao, and D. J. E. M. Roekaerts (2018). “Flameless Combustion and Its Potential towards Gas Turbines”. *Progress in Energy and Combustion Science* 69, pp. 28–62.
- [3] de Joannon, M., P. Sabia, G. Cozzolino, G. Sorrentino, and A. Cavaliere (2012). “Pyrolytic and Oxidative Structures in Hot Oxidant Diluted Oxidant (HODO) MILD Combustion”. *Combustion Science and Technology* 184 (7-8), pp. 1207–1218.
- [4] Ye, J., P. R. Medwell, B. B. Dally, and M. J. Evans (2016). “The Transition of Ethanol Flames from Conventional to MILD Combustion”. *Combustion and Flame* 171, pp. 173–184.
- [5] Evans, M. J. and A. Chinnici (2021). “Water Vapour Effects on Temperature and Soot Loading in Ethylene Flames in Hot and Vitiated Coflows”. *Proceedings of the Combustion Institute* 38 (4), pp. 5383–5391.
- [6] Tien, C. L. and S. C. Lee (1982). “Flame Radiation”. *Progress in Energy and Combustion Science* 8 (1), pp. 41–59.
- [7] Gaydon, A. G. (1974). “Flame Spectra”. *The Spectroscopy of Flames*. Ed. by A. G. Gaydon. Dordrecht: Springer Netherlands, pp. 1–13. ISBN: 978-94-009-5720-6.

Chapter 10

Summary

10.1 Conclusions

The combustion of fuels in a hot and low-oxygen environment is an attractive option in the development of practical combustion devices, enabling improvements in both operational and fuel flexibility whilst maintaining low emissions. Such flexibility will facilitate the use of alternative fuels in combustion processes, which is becoming increasingly relevant as various companies, industries and governments seek to reduce carbon emissions. In order to successfully implement this technology and optimise performance, it is necessary to have a deeper understanding of the fundamental behaviour of flames under these conditions of increased temperature and reduced oxygen concentration. The work presented within this thesis offers several important insights in this regard.

One of the major gaps relating to the use of mild combustion in practical devices (such as gas turbines) is the effect of pressure on the behaviour of the flames. In particular, there is a lack of experimental data relating to the structure and stability of elevated-pressure flames under varying boundary conditions, placing a limitation on the development of generalised numerical models which are valid at pressure. A significant portion of this work has therefore been focussed on the imaging of jet flames in a novel experimental burner, which facilitates the independent variation of the surrounding coflow conditions and the operating pressure. Specifically, chemiluminescence imaging—targeting the OH^* and CH^* radicals—was performed at pressures of up to 7 bar for a range of coflow O_2 concentrations, with the results indicating a consistent reduction in chemiluminescence intensity with increasing pressure across the various flame cases. This was complemented by a series of numerical simulations—using both computational fluid dynamics (CFD) and 1-D modelling—which highlighted the importance of accurately predicting both the fluid flow and the finite-rate chemistry for the flames studied. Additionally, the experimental imaging revealed an increased tendency for soot formation to occur as the pressure was increased, which was effectively suppressed with sufficiently low oxygen concentrations.

The combustion of liquid sprays is another area in which there are gaps

in existing knowledge, particularly in terms of mild combustion and similar combustion regimes. To study the complex reaction zone structures and stabilisation mechanisms of liquid sprays under conditions relevant to sequential combustors, a dilute spray burner based on the jet-in-hot-coflow configuration was developed. A combination of laser diagnostic imaging techniques were performed to simultaneously capture the location of key intermediate flame species, fuel droplets, and soot. A key feature of the burner configuration that was implemented is the ability to decouple a range of boundary conditions relating to both the jet and the hot coflow. By independently varying the jet Reynolds number, fuel loading and fuel composition whilst maintaining constant coflow conditions, a detailed understanding of the sensitivity of the near-field flame structure and overall evolution of the flames was obtained. In particular, it was observed that fuel droplets in the near-field region are consistently transported through the preheat region and into the reaction zone, which is accompanied by the formation of distinct inner and outer flame fronts. A range of coflow conditions were also investigated, to enable the exploration of the effects of the surrounding O_2 concentration and temperature on the stabilisation mechanisms of these flames. A notable observation from these experiments was the change in behaviour of the flame base as the O_2 concentration in the coflow was reduced to 3%, whereby a significantly weakened outer flame front was found to lead to a visually lifted flame. The range of boundary conditions studied for these dilute sprays—in addition to the complex flame structures and the detailed imaging that was performed—is particularly relevant in the context of computational modelling, as it provides a useful set of results to test the robustness of various models of spray combustion.

To extend the work based on the experimental JHC-style burners, an additional set of experiments of a more practical nature were performed, using hydrogen as the main fuel component. This was carried out to assess the potential of enhancing the visible and thermal radiation characteristics of hydrogen flames via the introduction of a highly sooting hydrocarbon fuel in relatively low proportion. As part of this investigation, the visibility of supposedly pure hydrogen flames was also examined via flame photography and spectrometry. The addition of toluene to hydrogen at concentrations of up to 1% by mole was observed to significantly increase thermal radiation via soot formation, leading to comparable radiative heat transfer characteristics to natural gas flames of equivalent heat input. The spectral imaging and filtered flame photography also confirmed the presence of sodium impurities from the surrounding air within the flames, the excitation of which leads to the emission of distinct and relatively high-intensity light at 589 nm.

Ultimately, this body of work is an important step towards the development of techniques and technologies which will facilitate the transition towards low-emissions and fuel-flexible combustion devices. The experimental work has largely been focussed on the imaging of flames under practically relevant yet well-defined and controllable boundary conditions, specifically under conditions which have not been studied extensively in the past. These results, in addition to offering several key insights in their own right, will aid in the development of numerical models and help to guide future research directions.

10.2 Future work

While this thesis and the publications it comprises offer several valuable insights and key findings to enable improvements in low-emissions and fuel-flexible combustion technologies, there remains scope for the extension of certain aspects of the work. In particular, the following research avenues to complement the results presented in Chapters 4 to 8 have been identified:

- *Imaging of key intermediate species in hot and low-oxygen, elevated pressure flames.*

While the experiments based on the pressurised combustor (that is, the CP-JHC) and the spray burner configurations were similar in terms of the ability to decouple several boundary conditions, there were key differences in terms of the diagnostics performed. In particular, the spray burner flames were investigated via a suite of laser diagnostic techniques—specifically, planar laser-induced fluorescence (PLIF) targeting the OH and CH₂O flame radicals was performed, along with the detection of soot via laser-induced incandescence (LII) and imaging of droplets via Mie scattering. The techniques involved in the CP-JHC experiments were comparatively less sophisticated, in terms of lacking the ability to isolate specific non-excited species within the flames and resolve their radial location. It would therefore be insightful to extend the optical configuration that was implemented for the spray burner experiments—or rather, the portion that was used for the PLIF imaging (and potentially the LII)—to study the flames within the CP-JHC. An additional diagnostic that is worth consideration in future experiments is the imaging of the CH radical, due to its importance in the formation of OH* and the uncertainty regarding the ability to accurately model changes in this behaviour with pressure and coflow O₂ concentration. It should be noted that PLIF imaging in the CP-JHC is not a trivial task.

Reflection and absorption of both the light from the lasers and that which is produced from the fluorescence/incandescence would need to be minimised and/or accounted for, as well as careful consideration of the effects of beam-steering and signal quenching at elevated pressures. Despite these practical hurdles which would need to be overcome, the measurement of these intermediate species would provide a more comprehensive picture regarding the effect of pressure on flame structure and stabilisation mechanisms, as well as providing additional insights into the chemiluminescence behaviour. It is therefore an activity worth consideration in future endeavours.

- *Investigation of additional fuels and fuel types at elevated pressure.*

While a number of different fuels and fuel types were examined in the various phases of this project, the experiments based on the pressurised combustor apparatus relate to a single fuel composition in the jet; namely, a 1:1 volumetric mixture of hydrogen and natural gas. This was necessary in order to limit the scope of the investigation and to enable the impacts of pressure and coflow properties to be isolated. It would, however, be beneficial to study a range of different fuels in the future in order to develop a more general understanding of the effect of pressure under conditions relevant to practical combustors. A natural next step would be to extend the atmospheric-pressure experiments performed as part of this thesis to the elevated pressure conditions of the CP-JHC. This includes both the dilute spray flames in a hot and low-oxygen coflow, and the pure and toluene-doped hydrogen flames in a coflow of air. It is worth noting that to perform the experiments with liquid sprays, significant modifications would need to be made to the apparatus. While these are achievable, the initial testing could be performed with prevaporised fuel in order to understand the effects of chemistry prior to studying the sprays. Extending the tests to incorporate a range of blending ratios between hydrogen and natural gas would also be of significant practical benefit, particularly in terms of chemiluminescence behaviour. Specifically, the operation of power-generation gas turbines on variable blends of H₂ and NG (up to 100% H₂) would benefit from a quantitative understanding of the changes in OH* and CH* intensity with variations in H₂ content of the fuel, by providing a method of actively adjusting control parameters such as the air-fuel ratio.
- *Continuing to develop modelling capabilities in conjunction with experimental work.*

The CFD and Chemkin modelling results presented in Chapter 7 in-

dicating that improvements are necessary in order to accurately capture certain changes in combustion behaviour—such as chemiluminescence—as the pressure is increased. This is closely related to the first future work suggestion; that is, the measurement and imaging of intermediate flame species such as the OH and CH radicals. Not only would this imaging provide a useful method of validating the reaction zone structures predicted via CFD modelling, the trends observed with increasing pressure would also provide important insights regarding the changes in chemical kinetics. This could in-turn help to explain the differences in chemiluminescence intensity from the modelling and experimental results, enabling improvements upon existing OH* and CH* chemical kinetics mechanisms which has important implications for practical combustion devices, as discussed in §2.3. The importance of developing a robust and efficient CFD model—which is able to accurately predict the structure and intermediate species of the flames in the CP-JHC under conditions of variable pressure, O₂ concentration and temperature—cannot be understated. With confidence in the ability to capture the underlying physics and chemistry with these variations in boundary conditions, the model can then be extended to more realistic geometries and configurations, such as the downstream combustor of a sequential gas turbine, thereby enabling the optimisation of practical combustion devices to achieve reductions in emissions and improvements in fuel flexibility.

Appendix A

Work Related to this Thesis

Journal articles

M. J. Evans, **D. B. Proud**, P. R. Medwell, H. Pitsch, B. B. Dally (2021). "Highly radiating hydrogen flames: Effect of toluene concentration and phase." *Proceedings of the Combustion Institute*, vol. 38, pp.1099-1106.

Conference papers/presentations

D. B. Proud, N. Smith, B. Crossman, P. R. Medwell, P. J. Ashman (2022). "Testing of Legacy Residential Appliances & Small Industrial Burners." Research presented at Future Fuels CRC Research Seminar, Sydney (and online).

D. B. Proud, A. J. Gee, P. R. Medwell, N. Smith M. J. Evans (2021). "Visible and thermal radiation from toluene-doped hydrogen flames." Paper presented at the Australian Combustion Symposium, Toowoomba (and online).

D. B. Proud, M. J. Evans, P. R. Medwell, Q. N. Chan (2021). "Preliminary experiments in a confined and pressurised jet-in-hot-coflow combustor." Paper presented at the Australian Combustion Symposium, Toowoomba (and online).

D. B. Proud, M. J. Evans, P. R. Medwell, Q. N. Chan (2021). "Dilute spray flames of ethanol and n-heptane in the transition to mild combustion." Paper presented at the Australian Combustion Symposium, Toowoomba (and online).

D. B. Proud, M. J. Evans, P. R. Medwell (2021). "Laser-based imaging of ethanol and n-heptane spray flames in the transition to mild combustion." Poster presented at the 38th International Symposium on Combustion, Adelaide (and online).

D. B. Proud, M. J. Evans, P. R. Medwell, F. Vandenbussche (2019). "Numerical modelling of mild combustion at elevated pressures." Paper presented at the Australian Combustion Symposium, Adelaide, 2019.